Ph.D. Dissertation/Tesis Doctoral

Impact of primary and secondary aerosol particles on cloud condensation nuclei activation properties

Andrea Casans Gabasa 2025







PHD. DISSERTATION / TESIS DOCTORAL



Programa de Doctorado en Física y Ciencias del Espacio

Impact of primary and secondary aerosol particles on cloud condensation nuclei activation properties

Andrea Casans Gabasa

Instituto Interuniversitario de Investigación del Sistema Tierra en Andalucía
Departamento Física Aplicada
Universidad de Granada







UNIVERSIDAD DE GRANADA

DEPARTAMENTO DE FÍSICA APLICADA GRUPO DE FÍSICA DE LA ATMÓSFERA

TESIS DOCTORAL

Impact of primary and secondary aerosol particles on cloud condensation nuclei activation properties

Tesis presentada por Dña. Andrea Casans Gabasa para optar al título de Doctora por la Universidad de Granada.

Directoras de la Tesis:

Dra. Gloria Titos Vela Profesora Titular de la UGR Departamento de Física Aplicada Universidad de Granada Dra. Paloma Cariñanos González Profesora Titular de la UGR Departamento de Botánica Universidad de Granada

Granada, marzo de 2025

Editor: Universidad de Granada. Tesis Doctorales

Autor: Andrea Casans Gabasa ISBN: 978-84-1195-862-2

URI: https://hdl.handle.net/10481/106858

El trabajo de investigación que se expone en la presente memoria, titulado: Impact of secondary primary and aerosol particles on cloud condensation nuclei activation properties, para aspirar al título de Doctora por la Universidad de Granada dentro del Programa de Doctorado en Física y Ciencias del Espacio que presenta Dña. Andrea Casans Gabasa, ha sido realizado en la Universidad de Granada en las instalaciones del Instituto Interuniversitario del Sistema Tierra en Andalucía (IISTA) y la Facultad de Ciencias; gracias a la ayuda "Contratos predoctorales de Formación de Personal Investigador (FPI) (PRE2019-090827) " concedida por el Ministerio de Ciencia, Innovación y Universidades, bajo la dirección de:

<u>Directoras de la Tesis / Thesis supervisors</u>

Fdo.: Dra. Gloria Titos Vela Fdo.: Dra. Paloma Cariñanos González

<u>Doctoranda / Doctoral candidate</u>

Fdo.: Dña. Andrea Casans Gabas

La doctoranda / The doctoral candidate Dña. Andrea Casans Gabasa y las directoras de la tesis / and the thesis supervisors Dra. Gloria Titos Vela y Dra. Paloma

Cariñanos González.

Garantizamos, al firmar esta tesis doctoral, que el trabajo ha sido realizado por

la doctoranda bajo la dirección de las directoras de la tesis, y hasta donde nuestro conocimiento alcanza, en la realización del trabajo, se han respetado los derechos

de otros autores a ser citados cuando se han utilizado sus resultados o publicaciones.

Guarantee, by signing this doctoral thesis, that the work has been done by the

doctoral candidate under the direction of the thesis supervisor/s and, as far as our

knowledge reaches, in the performance of the work, the rights of other authors to be cited (when their results or publications have been used) have been respected.

Granada, marzo de 2025

Directoras de la Tesis / Thesis supervisors

Fdo.: Dra. Gloria Titos Vela

Fdo.: Dra. Paloma Cariñanos González

<u>Doctoranda / Doctoral candidate</u>

Fdo.: Dña. Andrea Casans Gabasa

Mi gente luminosa, que me ha regalado su tiempo. Hemos hecho juntos todo este camino.

"Hombro con hombro, bailaremos en mitad de la tormenta" Javier Labandón, "El Arrebato"

Agradecimientos/Acknowledgments

En primer lugar, tengo que agradecer a mis directoras, las Dras. Gloria Titos Vela y Paloma Cariñanos González. Ellas me brindaron la oportunidad de realizar la tesis dentro del marco de una convocatoria FPI, vinculada a su proyecto que abarcaba diversas áreas del conocimiento. Por ello, a Paloma, le tengo que agradecer que nos haya transmitido su conocimiento en botánica, particularmente en el ámbito del polen, que tantos quebraderos de cabeza me ha dado todo este tiempo. En el caso de Gloria, con quien he pasado la mayor parte del tiempo, no sé si soy capaz de expresar con palabras lo agradecida que me siento. Especialmente, por todo el trabajo que te he dado estos últimos meses y lo complicado que ha tenido que ser para ti... Por eso, creo que lo primero que tengo que decirte es LO SIENTO y lo segundo, GRACIAS. Gracias por todo el tiempo que nos dedicas, por enseñarnos a hacer las cosas con rigor científico, por el esfuerzo y trabajo que supone para ti revisar al mínimo detalle todo lo que hacemos, por sentarte en nuestra mesa cuando estamos atascados y en un momento, hacer que veamos las cosas de otro color. Gracias, también a nivel personal, por conocernos y por tratarnos de tal forma que nos ayude a sacar lo mejor de nosotros mismos. Después de cuatro años trabajando contigo, sigo sin entender de dónde sacas el tiempo para dedicarte a nosotros, a tus clases, proyectos, campañas, reuniones, ... Solo puedo decir que para mí eres todo un ejemplo y un referente como científica, profesora, directora y persona. Ojalá algún día pudiera llegar a ser como tú. ¡GRACIAS, Gloria!

A continuación, tengo que agradecer al Catedrático Lucas Alados, cabeza de este grupo de investigación y que ha ejercido como mi tutor durante estos años. Gracias por darme la oportunidad de incorporarme al GFAT y embarcarme en este viaje. Junto a él, tengo que mencionar al resto de Catedráticos, Profesores y Doctores del GFAT. Porque ellos han vivido todo esto antes que nosotros y saben todo lo que conlleva. Nos habláis desde la experiencia y estar con vosotros día a día hace que siempre aprendamos algo nuevo. Gracias también por la dedicación y esfuerzo que ponéis en vuestros proyectos. Al final, sin vosotros, el grupo de GFATILLOS no se hubiera creado.

Entrando al grupo de GFATILLOS, tengo que empezar por el Dr. más reciente, Fernando Rejano. Fernando, gracias por el tiempo que hemos compartido, lo que significa, pasar de los mejores y peores momentos de la tesis. Horas de laboratorio entre risas y lágrimas cada vez que los experimentos fallaban, algún instrumento se estropeaba o los datos no tenían sentido y había que repetir. El cerebro es sabio y decide quedarse sólo con lo bueno así que no puedo evitar soltar una carcajada cada vez que vienen a mi mente frases como "Andrea, ¿sigues en la Facultad?", "A mí no me renta lavarme el pelo" o "Fernando, cuida, porque yo creo que esto Gloria y Juan Andrés no lo harían así..." \(\vec{\text{

Si sigo con Fátima e Inés, hablo de personas maravillosas que aparecen cuando las necesitas. Gracias, Fátima, por todos los momentos juntas y por ser miembro de mi familia andaluza. Gracias por todas las conversaciones, especialmente esa que tuvimos en Suiza y que tanto significó para mí. También por las lágrimas compartidas, situaciones absurdas y noches en nuestro templo. En cuanto a Inés, cuando necesitaba un poco de Norte, llegó el auténtico Norte. Gracias por hacer que los problemas disminuyan su tamaño, por las risas con ese código de programación a compartir y los momentos previos a practicar el bilingüismo. Gracias por los cafés mañaneros en el salón de tu casa y especialmente, por todas esas situaciones tan bien definidas como "MISERIOSAS" que, desde luego, han hecho que esta segunda mitad de tesis sea mucho más llevadera. Gracias también a Elena por su ayuda con el inglés, sus MOMENTAZOS y nuestras miradas cómplices desde el ordenador, que indican cuándo hay que activar el modo motivacional. Gracias a Matheus por sus palabras en "brasiñol" y por estar siempre presente, tanto en el CEAMA como en las anécdotas de fin de semana. Gracias, Pablo por todas esas frases épicas tan granaínas con las que me sigo riendo. También al "Team fumadoras", incluyendo a quienes siguen al pie del cañón y a mi Soledad, que "ha logrado" dejar el vicio. Gracias a todos los GFATILLOS (tanto a los que siguen, como a los que ya no están) por su presencia en esta tesis, ya sea ayudando con Python, informes meteorológicos, avisos de polvo o las misteriosas desapariciones de in-situ (Jesús, sorry solo un poquito 😌). Gracias por las comidas y tapas de los viernes, que nos recuerdan que las penas compartidas, son menos penas. ¡ÁNIMO, PRINGADOS, ya queda menos 😂!

Y dejo para el final a una pieza clave y fundamental para mí todos estos años. Porque cuando te fuiste me entró pánico al ver todos los instrumentos con los que me quedaba. Sin embargo, has hecho que la distancia Helsinki-Granada parezca de 0 km cada vez que un SMPS ha fallado, que una gráfica no ha tenido sentido o no he sabido cómo seguir. Gracias, Juan Andrés, por todo el tiempo que me dedicas, por enseñarme, por todas las revisiones que has hecho, por tu paciencia, por soportar mis "high" y especialmente, mis "low". Gracias por seguir cada vez que, como buena maña, he sido cabezona. Sabes que he escuchado todos tus consejos, he tenido en cuenta tu opinión y (para sorpresa de nadie), finalmente... SIEMPRE he tenido que darte la razón . Gracias, también, por esos "llama..." acompañados de "¿y ahora qué te pasa Andreita?" que han hecho que al día siguiente viera las cosas de otra forma. Creo que no puedo escribir nada que no sepas, así que solo puedo darte las GRACIAS POR ESTAR (incluso a un continente de distancia), personal y académicamente.

I switch to English to thank Dr. Martin Gysel-Beer for giving me opportunity to join his group at PSI during my research stay. I am greatly acknowledged for teaching and helping me to understand much better theoretical and scientific topics about CCNC. I would also like to thank Dra. Barbara Bertozzi and Qizhi Xu for their help, advice and recommendations in Switzerland as well as the good time that we had there and also, here.

Vuelvo a cambiar al español para hacer un repaso y agradecer a todos aquellos que forman parte de mi vida en Zaragoza pero que sin ellos no hubiera llegado hasta aquí. Tengo que empezar por mis amigos, los de toda la vida. Aquellos con los que he crecido y cada vez que estamos juntos es como si volviéramos 15 años atrás. Gracias chamaquitos por la alegría que siento y la fuerza que me dais cada vez que nos vemos. Solamente puedo decir, ¡POR OTROS 30 AÑOS MÁS JUNTOS!

Ahora quiero mencionar a mis amigos de la carrera, con quienes, de alguna manera, comenzó todo esto. Antonio, Franchito, Leyre, Jorge, Ander y María, gracias por haber hecho de todas esas horas en la biblioteca y de los momentos de desesperación en los laboratorios, un bonito recuerdo. Sin duda, un pedacito de cada uno de vosotros está presente en estas páginas. También a otra de esas personas increíbles que descubrí que necesitaba en mi vida. Gracias, Sara, por esos

días de 72 horas en los que siempre había tiempo para todo. Juntas aprendimos que, cuando se quiere, se puede. Los retos y objetivos se afrontan mejor acompañado, y en mi caso, no tengo duda de que tuve LA MEJOR compañía. En esta época también apareció la persona que, sin saberlo, me dio el empujón que necesitaba para llegar aquí. Sevillano, gracias por poder contar contigo. Lo que termina para mí, comienza para ti; así que ánimo porque esto también lo vas a conseguir. Hace unos años cambiaste el verde por el azul, dejaste atrás tu querida infantería; y ya verás que más pronto que tarde, vestido "de bonito" te presentas como Sargento Hermosa, Aviónica.

Finalmente, tengo que agradecer a mi familia. A mis padres y a mis hermanas. A mis padres porque nos han enseñado el valor del esfuerzo, la constancia y saber lo que cuesta conseguir las cosas. Gracias a ellos somos lo que somos. A mis hermanas, porque son el ejemplo para mí de trabajo, superación y disciplina. Hace unos años se dieron las circunstancias para que tomarais, seguramente, una de las decisiones más importantes de vuestra vida. Decisión que hizo posible que yo siguiera en el camino que había escogido. Aunque para mí siempre seréis mi Puchi y mi Saruquen, no sé cómo describir la admiración que siento por vosotras con cada reconocimiento, cada medalla o cada peldaño que subís en ese escalafón interminable. Solo puedo terminar diciendo: A sus órdenes mi Capitán y a sus órdenes mi Teniente.

Contents

INT OBJEC FUN 2.1 2.2	EN	20 23
OBJEC FUN 2.1 2.2 2.2.	TIVES AND OUTLINE	20 23
FUN 2.1 2.2 2.2.	NDAMENTALS	23
2.1 2.2 2.2.	ATMOSPHERIC AEROSOLS	23
2.2 2.2.	CLOUD FORMATION AND KÖHLER THEORY	
2.2.		30
	l Homodeneous nucleation	2.1
つつ		
	2 Heterogeneous nucleation	
	3 κ-Köhler Theory	
3.1	2 Izaña Observatory: IZO	39
3.2	INSTRUMENTATION AND EXPERIMENTAL DATA	41
3.2.	1 Cloud Condensation Nuclei Counter	41
3.2	2 Scanning Mobility Particle Sizer	47
3.2.	3 Aerodynamic Particle Sizer	52
ME	THODOLOGY	55
4.1		
4.3	COMPARISON OF SIZE-RESOLVED AND POLYDISPERSE CCN APPROACHES	60
4.4	POLLEN CHARACTERIZATION	62
4.4.	1 Pollen sampling and SPP generation	62
4.4.	2 Cloud condensation activity of size-selected SPPs	62
4.4.	3 Surface tension analysis	64
4.4.	4 Organic chemical analysis	65
ERRA		
	EXH 3.1 3.1.2 3.2.3 3.2.3 3.2.3 ME 4.1 4.2 JREME 4.3 4.4 4.4.2 4.4.2 4.4.2 CLC	EXPERIMENTAL SITES AND INSTRUMENTATION 3.1 EXPERIMENTAL SITES 3.1.1 Sierra Nevada Station: SNS 3.1.2 Izaña Observatory: IZO

5.3	SURFACE ACTIVITY	79
5.4	IMPACT OF SURFACE TENSION ON HYGROSCOPICITY	85
5.5	Conclusions	89
6. AM	BIENT MEASUREMENTS OF CLOUD CONDENSATION NUCLEI	
ACTIVATION	N PROPERTIES DURING SAHARAN DUST EVENTS	91
6.1	OVERVIEW OF CCN ACTIVATION PROPERTIES AT SNS AND IZO	92
6.2	IDENTIFICATION OF DUST EVENTS AT SNS AND IZO	100
6.3	INFLUENCE OF DUST EVENTS ON CCN CONCENTRATION AND AC	TIVATION
PROPERTIES		108
6.4	Conclusions	118
7. IMI	PACT OF NEW PARTICLE FORMATION ON THE CLOUD	
CONDENSAT	TION NUCLEI BUDGET	121
7.1	NPF EVENTS AT SNS AND IZO STATIONS	122
7.2	NEW METHOD TO ESTIMATE THE NPF CONTRIBUTION TO CCN CONCENTRA	TIONS
		124
7.3	ASSUMPTIONS, LIMITATIONS AND SOURCES OF UNCERTAINTY OF THE NEW M	METHOD.
		132
7.4	CONTRIBUTION OF NPF EVENTS TO CCN CONCENTRATIONS AT SNS AND IZ	ZO 136
7.5	CONCLUSIONS	145
8. GE I	NERAL CONCLUSIONS AND PERSPECTIVES	149
CONCL	USIONES GENERALES Y PERSPECTIVAS	155
APPEND	DIX	161
REFERE	ENCES	173

List of symbols and acronyms

a.s.l.	Above Sea Level
N _{Accumulation}	Accumulation mode concentration
AF	Activation Fraction
Da	Aerodynamic Diameter
APS	Aerodynamic Particle Sizer
ACTRIS	Aerosol, Clouds and Trace gases Infrastructure network
ACI	Aerosol-Cloud Interactions
N ₁₂₋₂₅	Aerosol particle number concentration in the size-range 12-25 nm
N ₂₅₋₁₀₀	Aerosol particle number concentration in the size-range 25-100 nm
N ₁₀₀₋₁₀₀₀	Aerosol particle number concentration in the size-range 100-1000 nm
ARI	Aerosol-Radiation Interactions
N _{Aitken}	Aitken mode concentration
AGORA	Andalusian Global Observatory of the Atmosphere
IISTA	Andalusian Institute for Earth System Research
ABL	Atmospheric Boundary Layer
GFAT	Atmospheric Physics Group
BVOCs	Biogenic Volatile Organic Compounds
к	CCN-derived Hygroscopicity Parameter
κ _{mean}	CCN-derived Hygroscopicity Parameter (averaged at different sizes)

κ ₅₀	CCN-derived Hygroscopicity Parameter (from D ₅₀ size-
	resolved CCN measurements)
$\kappa_{\sigma c/100}$	CCN-derived Hygroscopicity Parameter (concentration diluted 100 times)
	CCN-derived Hygroscopicity Parameter (most concentrated
$\kappa_{\sigma c}$	solution)
	CCN-derived Hygroscopicity Parameter (using water surface
$\kappa_{\sigma w}$	tension)
CCN	Cloud Condensation Nuclei
CCN _{NPF}	CCN Concentration of the NPF mode
$\frac{\text{dCCN}_{\text{NPF}}}{\text{dLogD}}$	CCN number size distribution of the NPF mode
CCNC	Cloud Condensation Nuclei Counter
$N_{\rm C}$	Coarse mode concentration
СРС	Condensation Particle Counter
CS	Condensation Sink
D _{Crit}	Critical Diameter
D_{50}	Critical Diameter (from sigmoidal fit with size-resolved CCN
D ₅₀	measurements)
S_{Crit}	Critical Saturation ratio
SS _{Crit}	Critical Supersaturation ratio
C _C	Cunningham factor
ρ_{w}	Density of pure water
DMA	Differential Mobility Analyzer
$D_{droplet}$	Droplet diameter
D	Dry Diameter
N_{F}	Fine mode concentration (Nucleation, Aitken, Accumulation)
FT	Free Troposphere
η	Gas viscosity

$\mathrm{D}_{\mathrm{geo}}$	Geometric diameter
GR	Growth Rate
IA	Inorganic Aerosol
IPCC	Intergovernmental Panel on Climate Change
IZO	Izaña Observatory
K _C	Kruskal-Wallis statistical coefficients
MBL	Marine Boundary Layer
D_{max}	Maximum size reached by newly formed particles
D_{m}	Mobility Diameter
M _w	Molecular weight of water
NPF	New Particle Formation
N _{Nucleation}	Nucleation mode concentration
n _e	Number of charged particles
OPC	Optical Particle Counter
OA	Organic Aerosol
е	Particle charge
$ ho_{eff}$	Particle density
PNSD	Particle Number Size Distribution
dN _{NPF} dLogD	Particle Number Size Distribution of the NPF mode
PBAP	Primary Biological Aerosol Particles
V ^{D/ND}	Ratio of the median value of a variable during each dust event compared to non-dusty conditions
RH	Relative humidity
S	Saturation ratio
$P_{\mathrm{H}_2\mathrm{O}}^0$	Saturation water vapor pressure

SMPS	Scanning Mobility Particle Sizer
χ	Shape factor
SNS	Sierra Nevada Station
std	Standard deviation
SPP	Subpollen particles
SS	Supersaturation ratio
σ	Surface tension
σ_{w}	Surface tension of water
t _{start}	Time at which a NPF starts
$t_{ m end}$	Time at which a NPF ends
N	Total Particle number concentration
ρο	Unit density
UTC	Universal Time Coordinated
VOCs	Volatile Organic Compounds
a _w	Water activity
P_{H_2O}	Water vapor pressure

List of figures

Figure 2-1. Scanning electron microscope (SEM) image of intact Olea pollen grain at scale 2 μm (A
and SEM image of <i>Olea</i> subpollen particles at scale 200 nm (B)
Figure 2-2. Scanning electron micrographs individual Saharan dust particles at different scales (A
20 μm and B, 5 μm) (Images taken from Reid et al. 2003)
Figure 2-3. Example of a Köhler curve showing the separate contribution of Kelvin and Raoul
effects. Figure adapted from Zieger (2011)
Figure 3-1. Map showing the location of the AGORA infrastructure: UGR urban site and SNS high
altitude remote site (top panel). The topographic profile between both sites is included (bottom
panel)39
Figure 3-2. Map showing the location of Canary Islands (left panel) and Tenerife Island (right panel
where IZO observatory is located
Figure 3-3. Scheme of the main parts of the Cloud Condensation Nuclei Counter. Figure adapted
from Lance et al. (2006)
Figure 3-4. Illustration of how a constant supersaturation is established along the centerline of the
growth chamber of the CCNC. Figure taken from Roberts and Nenes (2005)4
Figure 3-5. Activation and calibration curves of ammonium sulfate during SS calibration experiment
A) shows the activation curves and B) shows the calibration relationship between temperature
and SS
Figure 3-6. Aerosol and sheath flow calibration curves. 4
Figure 3-7. A) Schematic representation of the TSI 3938 scanning mobility particle sizer and B) cros
section of Long DMA model 3081A. Figures from TSI manual, 20164
Figure 3-8. Schematic representation of the TSI 3772/3771 Model of CPC. Figure from TSI manual
2015

Figure 3-9. A) Results of the sizing calibration of the DMA and B) particle number size distribution
intercomparison between different SMPS available at UGR and SNS stations51
Figure 3-10. A) Total particle number concentration of different CPC models and B) total particle
number concentration measured directly from a CPC and obtained by the integration of the
aerosol concentration at different sizes, determined by different SMPSs during nighttime
intercomparison processes
Figure 3-11. The flow schematic for the TSI model 3321 APS. Figure taken from Aerodynamic
Particle Sizer TSI manual
Figure 4-1. Time alignment of one scan between SMPS and CCNC. A) Aerosol and CCN (at
SS=0.4%) particle number size distributions with different time alignments. B) Activated
fraction curves at SS=0.4% at these time alignments. Solid black line (in A) is referred to
aerosol size distribution. In both subplots, solid clear blue line corresponds to the correct time
alignment at time t (A, CCN size distribution and B, AF curve). In the same way, dashed dark
blue lines correspond to the alignment at time t+2 and t-2 seconds. Dotted red lines are referred
to the curves with the alignment t+5 and t-5 seconds
Figure 4-2. Linear correlations of parameters derived from size-resolved and polydisperse data
throughout the campaign (24^{th} June -12^{th} July) at SS=0.4% with time resolution of 3 hours: A)
Total CCN concentration B) Activation Fraction (AF) C) D_{Crit} - D_{50} and D) κ - κ_{50} 61
Figure 4-3. Scheme of the experimental setup of Pendant Drop Tensiometer at University of Granada
Figure taken from Maldonado-Valderrama et al. (2021)65
Figure 5-1. Critical supersaturations (SS $_{\text{Crit}}$) of the 11 analysed pollen samples at different dry
Figure 5-1. Critical supersaturations (SS_{Crit}) of the 11 analysed pollen samples at different dry diameters (80, 100 and 200 nm). Error bars for each pollen type correspond to the standard
diameters (80, 100 and 200 nm). Error bars for each pollen type correspond to the standard
diameters (80, 100 and 200 nm). Error bars for each pollen type correspond to the standard deviation of SS _{Crit} calculated considering the uncertainties in measured SS (see the text for
diameters (80, 100 and 200 nm). Error bars for each pollen type correspond to the standard deviation of SS _{Crit} calculated considering the uncertainties in measured SS (see the text for further detail in uncertainty calculation). Black line represents the theoretical range of SS _{Crit} for
diameters (80, 100 and 200 nm). Error bars for each pollen type correspond to the standard deviation of SS_{Crit} calculated considering the uncertainties in measured SS (see the text for further detail in uncertainty calculation). Black line represents the theoretical range of SS_{Crit} for ammonium sulfate ((NH ₄) ₂ SO ₄) (Gysel et al., 2002; Topping et al., 2005), black points are SS_{Crit}

Figure 5-2. Bar diagram showing total organic compound concentration (in ng/mg of pollen), protein content (in mg/mL) and mean hygroscopicity parameter κ for each pollen type. The κ error bars represent the standard deviation for the three dry size diameters investigated
Figure 5-3. Relative composition of individual molecular organic compounds (internal ring) and their groups for each pollen type (external ring). Only compounds representing percentages above 10% have been highlighted to appear in pie charts
Figure 5-4. Relative contribution of highly soluble and slightly soluble compounds in SPPs coloured by the hygroscopicity parameter κ for each pollen type
Figure 5-5. Surface tension versus time at different concentrations for <i>Dactylis, Fraxinus, Pinus, Populus deltoides, Populus nigra</i> and <i>Quercus</i> . Dilutions were made in ultrapure water, and measurements were made at room temperature (23 °C)
Figure 5-6. Final values of surface tension after adsorption at constant surface area plotted in Fig. 5-5, as function of concentration for <i>Dactylis, Fraxinus, Pinus, Populus deltoides, Populus nigra</i> and <i>Quercus</i> . Error bars represent the standard deviation of the surface tension measured for pure water during the experiments.
Figure 5-7. κ values obtained using σ_w (noted as $\kappa_{\sigma w}$, color points) and obtained with equilibrium surface tension values at highest concentrations ($\kappa_{\sigma C}$, black points) and concentrations diluted 100 times ($\kappa_{\sigma C/100}$, grey points) for <i>Dactylis, Fraxinus, Pinus, Populus deltoides, Populus nigra</i> and <i>Quercus</i> . The surface tension values at concentrations diluted 100 times are 69.9, 72.5, 70.4, 71.6, 69.2 and 71.4 mN/m, respectively. Horizontal lines represent maxima and minima values obtained for $\kappa_{\sigma w}$ and shaded area the interval between both values
Figure 6-1. Boxplots of A) particle number concentration N, B) N ₁₂₋₂₅ , C) N ₂₅₋₁₀₀ , D) N ₁₀₀₋₁₀₀₀ and E) N _C at SNS and IZO. Black dots and grey lines represent the mean and median values, respectively. Lower and upper limits in the boxplots are the first (Q1) and third (Q3) quartiles respectively. The difference between them is the inter-quartile range (IQR). Lower and upper whiskers show Q1-1.5·IQR and Q3+1.5·IQR, respectively. Diamond markers represent the outliers. The time-resolution of the data is 5 minutes.

concentration, B) $N_{>80}$, C) AF, D) D_{Crit} and E) κ . Black dot and grey line represent the mean

	and median values, respectively. Lower and upper limits in the boxplots are the first (Q1) and third (Q3) quartiles respectively. The difference between them is the inter-quartile range (IQR).
	Lower and upper whiskers show Q1-1.5·IQR and Q3+1.5·IQR, respectively. Diamond markers
	represent the outliers. Time-resolution of the data is 1 hour
Figur	e 6-3. Diurnal patterns of A) N, N_{12-25} , N_{25-100} , $N_{100-1000}$, and N_C , B) $N_{>80}$, C) total CCN
	concentration, D) AF, E) D_{Crit} and E) κ at SS=0.4% at SNS (local time is UTC+2) and IZO
	(local time is UTC+1)99
Figur	e 6-4. Temporal evolution of hourly N_F,N_C and N_C/N during the measurement campaigns at
	SNS (A and B) and IZO (C and D)
Figur	e 6-5. Geopotential height at 700 mb for A)14th June 2021 at 00:00 UTC corresponding with
	dust event 1 at SNS and B) 11th July 2022 at 06:00 UTC corresponding with dust event 2 at
	SNS. Data are from NCEP/NCAR - https://psl.noaa.gov/data/composites/hour/ 102
Figur	e 6-6. Geopotential height at 850 mb for A) 8th May 2022 at 12:00 UTC corresponding with
	dust event 2 at IZO and B) 13th June 2022 at 12:00 UTC corresponding with dust event 5 at
	IZO. Data are from NCEP/NCAR - https://psl.noaa.gov/data/composites/hour/ 104
Figur	e 6-7. Geopotential height at 850 mb for A) 13th May 2022 at 18:00 UTC corresponding with
	dust event 3 at IZO and B) 13th June 2022 at 12:00 UTC corresponding with dust event 4 at
	IZO. Data are from NCEP/NCAR - https://psl.noaa.gov/data/composites/hour/ 105
Figur	e 6-8. Geopotential height at 850 mb for A) 2 nd May 2022 at 12:00 UTC corresponding with
	dust event 1 at IZO Data are from NCEP/NCAR - https://psl.noaa.gov/data/composites/hour/.
Figur	e 6-9. N_{C} (A, B), N_{C} /N (C, D), N_{F} (E, F), N_{12-25} (G, H), N_{25-100} (I, J) and $N_{100-1000}$ (K, L) at SNS
	(left) and IZO (right) during non-dusty conditions and for each dust event identified. Black dot
	and dashed line represent the mean and median values, respectively. Lower and upper limits in
	the boxplots are the first (Q1) and third (Q3) quartiles respectively. The difference between
	them is the inter-quartile range (IQR). Lower and upper whiskers show Q1-1.5·IQR and
	Q3+1.5·IQR, respectively. Outliers are omitted for clarity purposes
Figur	e 6-10. Averaged particle number size distributions during non-dusty conditions and dust events
_	at SNS and IZO

$Figure\ 6\text{-}11.N_{C}\ (A,B),\ N_{C}/N\ (C,D),\ N_{F}\ (E,F),\ N_{12\text{-}25}\ (G,H),\ N_{25\text{-}100}\ (I,J)\ and\ N_{100\text{-}1000}\ (K,L)\ at\ SNS$
during day and nighttime (left) and IZO (right) for non-dusty conditions and for the more
intense dust events identified. Black dot and dashed line represent the mean and median values,
respectively. Lower and upper limits in the boxplots are the first (Q1) and third (Q3) quartiles
respectively. The difference between them is the inter-quartile range (IQR). Lower and upper
whiskers show Q1-1.5·IQR and Q3+1.5·IQR, respectively. Outliers are omitted for clarity
purposes
Figure 6-12. Ratio of the median values of dusty to non-dusty conditions for N_{C} (A, B), N_{C}/N (C, D),
$N_{F}\left(E,F\right),N_{12\text{-}25}\left(G,H\right),N_{25\text{-}100}\left(I,J\right)\text{and}N_{100\text{-}1000}\left(K,L\right)\text{at SNS during day and nighttime (left)}$
and IZO (right) denoted as the variable name with D/ND as a superscript 114
Figure 6-13. CCN (A, B), AF (C, D), D_{Crit} (E, F) and κ (G, H) (SS=0.4%) during day and nighttime
at SNS (left) and IZO (right) during non-dusty conditions and more intense dust events. Black
dot and line represent the mean and median values, respectively. Lower and upper limits in the
boxplots are the first (Q1) and third (Q3) quartiles respectively. The difference between them
is the inter-quartile range (IQR). Lower and upper whiskers show Q1-1.5·IQR and
Q3+1.5·IQR, respectively. Outliers are omitted for clarity purposes
Figure 6-14. Ratio of the median values of dusty to non-dusty conditions for CCN (A, B), AF (C, D),
D_{Crit} (E, F) and κ (G, H) (SS=0.4%) during day and nighttime at SNS (left) and IZO (right),
denoted as the variable name with D/ND as a superscript
Figure 7-1. A) Mean diurnal evolution of aerosol concentration in different modes (12-25 nm, 25-
100 nm and 100-535 nm) during NPF event days and non-NPF event days at SNS and C) IZO.
B) Mean diurnal evolution of total CCN concentration at SS=0.4% and SS=0.8% at SNS and
D) IZO. Local time is UTC+2 at SNS and UTC+1 at IZO
Figure 7-2. A) Diurnal evolution of N_{12-25} (solid black line), N_{25-100} (black dashed line) and $N_{100-535}$
(black dotted line) mode particle number concentration, B) diurnal evolution of total CCN
concentration at different SS conditions and C) Δ CCN concentration between different SS
conditions during NPF 2nd July 2021. Red/black vertical dashed lines at 09:00, and 21:00 UTC
represent tstart, and tend, respectively
Figure 7-3. A) Aerosol size-distribution, B) gradient of aerosol size concentration and C) size-

resolved CCN concentration during 2^{nd} July 2021. Blue, red and green lines correspond to D_{Crit}

at different SS conditions (0.4%, 0.6%, 0.8%, respectively). Grey/black dashed lines
correspond to ceiling size. Vertical white dashed line at 09:00 UTC represents t _{start} . Vertical
dark blue dashed line at 15:00 UTC and 21:00 UTC refer to contribution phase (and t _{end}).
respectively
Figure 7-4. A) Average aerosol (black) and CCN size-distributions during contribution phase period
at different SS values. Orange line corresponds to the bell fit that represents the NPF mode, and
shadow orange area with the error of the fit calculated by propagation. B) -Activated fraction
obtained from size-resolved CCN measurements (solid color lines) and polydisperse
measurements approximated to step functions (dashed color lines). Lighter color lines (light
green, red and blue) correspond to the error of size-resolved activated fraction. C) Size-resolved
CCN concentration that come from NPF in size-resolved (blue, red, green solid lines) and
polydisperse (blue, red, green squares) measurements overlaid on aerosol (black) and NPF
mode size distributions (orange). D) Percent contribution of NPF to CCN concentration at
SS=0.8% and SS=0.6% with size-resolved and polydisperse mode, during the NPF event 2nd
July 2021131
Figure 7-5. A) Boxplots of NPF contribution to CCN concentration and B) NPF-derived CCN
absolute concentrations at different SS values (0.8%, 0.6%, 0.4% and 0.2%) at SNS (blue) and
IZO (pink) using size-resolved and polydisperse variants of the method. Black dots and black
lines represent the mean and median values, respectively. Lower and upper limits of the
boxplots are the first (Q1) and third (Q3) quartiles, respectively. The difference between them
is the inter-quartile range (IQR). Lower and upper whiskers show Q1-1.5·IQR and
Q3+1.5·IQR, respectively. Blank circles represent the outliers
Q3 + 113 1Q1, 10spect 101, Diame choics represent the outhors.
Figure 7-6. A) Relationship of CCN _{NPF} with A) maximum ceiling size reached by newly formed
particles (D_{max}) coloured by critical diameter (D_{Crit}) at SS=0.8%, B) duration of the contribution
phase, C) total particle number concentration, N, D) Aitken mode concentration, N ₂₅₋₁₀₀ , and
CCN _{NPF} at SNS and IZO using the polydisperse variant of the proposed method
Figure 0-1. Geopotential height at 850 mb for A)14th June 2021 at 00:00 UTC corresponding with
dust event 1 at SNS and B) 11th July 2022 at 06:00 UTC corresponding with dust event 2 at
SNS. Data are from NCEP/NCAR - https://psl.noaa.gov/data/composites/hour/166

Figure 0-2. Pie chart of averaged PM10 chemical composition during non-dusty conditions and dust
event 1 at SNS. Only compounds representing percentages above 2% have been highlighted to
appear in the pie charts
Figure 0-3. Pie chart of averaged PM10 chemical composition during non-dusty conditions, dust
event 1, dust event 2 and dust event 3 at IZO. Only compounds representing percentages above
2% have been highlighted to appear in the pie charts
Figure 0-4. Mean particle number size distributions (PNSD) evolution during NPF and non-NPF event days at SNS and IZO stations
Figure 0-5. Graphical representation of the ceiling size calculation method for one D-scan of the
particle number size distribution. Point A represents the minimum value of the gradient, point
B represents the ceiling size (the negative value closest to 0) and point C refers to the first
positive value of the gradient after the minimum value (A)
Figure 0-6. Aerosol size-distribution evolution where black dashed line represents the geometric
diameter. Grey dashed line reference to ceiling size obtained from gradient of concentration
and coloured lines, critical diameters at different SS values (blue for SS=0.4%, red for SS=0.6%)
and green for SS=0.8%)
Figure 0-7. Percentage of contribution of NPF to CCN concentration at different SS values during
the NPF produced 2 nd July 2021 using polydisperse high-time resolution variant
Figure 0-8. Boxplot of maximum ceiling size reached by newly formed particles (left) and critical
diameters (at SS=0.8%) (right) at SNS and IZO during the analysed NPFs. Black dots and black
lines represent the mean and median values, respectively. Lower and upper limits of the
boxplots are the first (Q1) and third (Q3) quartiles, respectively. The difference between them
is the inter-quartile range (IQR). Lower and upper whiskers show Q1-1.5·IQR and
Q3+1.5·IQR, respectively. Blank dots represent the outliers
Figure 0-9. Relationship of CCN _{NPF} with N ₁₀₀₋₅₃₅ at SNS and IZO using the polydisperse variant of
the proposed method

List of tables

Table 4-1. Parameters of the sigmoidal fit applying Eq. 4.4 to the respective activated curves at
different time alignments. Error values for each parameter correspond to errors obtained from
the fit. 60
Table 4-2. SS values selected to study the activation for SPPs of 200, 100 and 80 nm
Table 5-1.Mean hygroscopicity parameter, κ, obtained for each pollen type at 200, 100 and 80 nm
dry diameter (the mean κ does not take into account the results for Acer at 200 nm due to
unstable concentrations during the experiments)
Table 5-2. Percentage surface tension decrease at 300 seconds
Table 6-1. Summary of mean activation parameters at different high-mountain stations at similar SS
conditions. The table is sorted according to the altitude of the station98
Table 6-2. Dust events identified during the campaign at SNS and IZO
Table 6-3:Summary of Mann-Whitney U and Kruskal-Wallis tests for dust events identified at SNS
and IZO. "Yes" indicates that differences are significant with p-values < 0.05 compared to non-
dusty conditions
Table 7-1. Summarised results from 5 NPF events at SNS, including NPF duration and contribution
phase (based on SS=0.8%), as well as the contribution obtained for the size-resolved and
polydisperse variants at 0.8 and 0.6% SS (no contribution was observed for SS≤ 0.4%) 140
Table 7-2. Summarised results from 18 NPF events at IZO, including NPF duration and contribution
phase (based on SS=0.8%), as well as the contribution obtained for polydisperse variant at
different SS. No contribution has been observed at SS≤0.2%
Table 0-1. Water solubility of the analyzed organic compounds between 20-25 ° C. All solubility
values are taken from the National Center for Biotechnology Information (2023). PubChem
Compound Summary for CID 6267. The solubility category is based on Han et al. (2022). 161
Table 0-2. Calculated κ values taking into account different surface tension values for each pollen
type at different sizes. The reduction of κ_{mean} respect to $\kappa_{\sigma w}$ expressed in percentage associated
to the initial solution and the 100 times diluted solution are also showed

Table 0-4. Summary of Kruskal-Wallis tests for concentration at different modes during the mofable 0-3. Summary of Kruskal-Wallis tests for concentration at different modes during the more intense dust events, identified at IZO during dayring dayring time. K _C values represent Kruskar-Wallis dayring dayring time. K _C values represent Kruskar-Wallis dayring dayring time.
indicates Whalliferers efficiently eith inchestes 0 that other ences dure significant with p-values <0.0
conditions. 10
Table 0-5. Enhancements and contributions to CCN of the NPF produced on 2 nd July 2021 at SN
anniving different methodologies

Abstract

This PhD dissertation focuses on improving the existing knowledge of the capacity and influence that different types of aerosol particles exert on the cloud condensation nuclei (CCN) budget and their activation properties. In particular, it focuses on primary aerosol particles, such as pollen and desert dust, and on secondary aerosol particles formed during new particle formation (NPF) events. These aerosol types have been selected due to their significant impact on the global climate (high emission and formation rates) and their potential influence on climate change.

The influence of pollen particles has been investigated through laboratory experiments due to their low number concentration in the atmosphere, as well as the lack of standardized instrumentation capable of discriminating pollen particles in ambient air. In contrast, the influence and impact of dust and NPF events have been studied during experimental field campaigns conducted at two highmountain sites in Spain: one in the southern Iberian Peninsula, in Sierra Nevada National Park (Sierra Nevada Station, SNS, 2500 m a.s.l.), and the other on Tenerife Island, in the Canary Archipelago (Izaña Observatory, IZO, 2367 m a.s.l.). Both sites are frequently influenced by dust events due to their proximity to the Sahara Desert, and both are prone to the occurrence of NPF events at midday.

It has been recently shown that pollen grains can rupture into thousands of smaller particles, known as subpollen particles (SPPs), that may act as CCN. In this thesis we have investigated the ability of SPPs of 10 Mediterranean-climate pollen types to activate as CCN at different sizes (80, 100 and 200 nm) and supersaturations (SS). Results show that all studied SPP samples have critical supersaturations (SS $_{\rm Crit}$) that are atmospherically relevant (0.07%–0.37%, depending on size) and that hygroscopicity values are in the typical range observed for organic compounds (0.1–0.3). We found that the organic chemical speciation and protein content vary substantially among pollen types (with saccharides and fatty acids being the only organic compounds found in all samples). However, a

Abstract

clear relationship between SPP activation and its organic composition was not observed. The analysis of the surface activity using pendant drop tensiometry reveals that all SPPs investigated are surface active at high concentrations, whereas under diluted conditions (such as those of activation as CCN), the surface tension of water serves as a good approximation in Köhler theory. Overall, the analysis points out that all SPPs behave similarly, and pollen emissions might be an important source of CCN in the atmosphere.

Concerning ambient CCN activation properties at SNS and IZO, we found that, despite both observatories being located at a similar altitude, CCN concentration at SNS is approximately four times the value observed at IZO (campaign average values of 645 cm⁻³ and 160 cm⁻³, respectively, at SS=0.4%). The total particle number concentration (N) is also higher at SNS than at IZO, with a mean N value of 2500 cm⁻³ at SNS and 1170 cm⁻³ at IZO. Larger differences in the accumulation mode than in the nucleation and Aitken mode concentrations are observed between the two sites. Although aerosol properties at both sites show the typical diurnal pattern observed at high-mountain locations, with larger particle concentrations around midday, the influence of pollutants transport from the atmospheric boundary layer (ABL) is higher at SNS. In addition to the influence of the ABL on particle concentration and CCN properties, NPF events occurring at midday (at both sites) contribute significantly to total particle number concentration and size distribution, thus modifying CCN activity.

To determine the impact of newly formed particles on CCN concentration we have developed a novel method able to decouple the effect of transport, which mostly influences the accumulation mode, from particle formation and growth (nucleation and Aitken modes). The method distinguishes between NPF-generated particles and background or transported aerosol through the calculation of the NPF mode; and then, knowing the activated fraction curves, activated particles from the NPF events are obtained. Previous methods estimated CCN concentration enhancements by comparing CCN concentration at different times periods (during or after NPF events with those prior the events or with non-event days). Our method overcomes this limitation by focusing on the ceiling size that newly formed

particles can reach, the timing of NPF events, and isolating the NPF mode from the overall aerosol size distribution.

Size-resolved CCN measurements performed at SNS are used to develop the methodology, which is also expanded for application to polydisperse CCN measurements. The new method has been applied to NPF events observed at SNS and IZO, and the results show that NPF events produced at both stations are able to contribute to CCN concentrations under high SS conditions, while for SS<0.4%, this contribution is negligible. NPF events show higher relative contributions to CCN concentration at IZO (campaign average of $24 \pm 25\%$ at SS=0.8%) compared to SNS ($6.2 \pm 4.8\%$ at SS=0.8%). The lower contribution observed at SNS is explained by the higher CCN concentration observed at midday which is not associated with the NPF but with the transport of particles within the ABL. However, in absolute terms, the number of particles produced by the NPF event and activated as CCN is slightly larger at SNS than at IZO (at SS=0.8%, 95 cm⁻³ vs 51 cm⁻³, respectively). Nevertheless, the NPF contributions observed in this thesis are lower than previously determined with other methods, which might impact CCN predictions in the global troposphere.

In addition to NPF events, desert dust events are frequently observed at both high-mountain sites. During the measurement periods, two dust events were identified at SNS and six at IZO. During dust events, the concentration of dust particles is higher at night (at both stations), but their influence on activation properties depends on the intensity, properties and conditions of each particular event. Most dust events show a reduction in submicrometric particles, likely due to the role of dust particles as coagulation sink and a less efficient transport from lower altitudes, which leads to higher activated fraction (AF) values. An analysis of day and nighttime periods has been performed to isolate the effect of desert dust episodes on activation properties from other atmospheric processes that also occur during daytime, such as ABL transport and NPF events. The results show that during the day in dusty conditions, CCN concentrations decrease at SNS and increase at IZO, while an increase is observed at both sites during the night. The decrease observed at SNS during the day might be due to the reduced ABL influence during dust events, while this effect is not as relevant at IZO due to

Abstract

generally lower ABL influence. Conversely, at night, the enhanced CCN concentration observed at both sites suggests that dust particles present in the accumulation mode can activate as CCN. Further analysis with an extended database would be necessary to better understand the role of desert dust transport in the CCN budget and hygroscopic behaviour.

In summary, the results obtained in this thesis evidence that subpollen, dust and newly formed particles can act as CCN and modify activation properties and clouds formation. Further studies expanding on the results obtained in this thesis, applying similar methodologies to an extended dataset, including longer time periods and diverse sites will help to improve the knowledge about CCN properties and their climatic impact in a global scale.

Resumen

Esta tesis doctoral tiene como objetivo ampliar el conocimiento sobre la capacidad de distintos tipos de aerosoles para actuar como núcleos de condensación de nubes (CCN) y su impacto en el clima. La selección de los tipos de partículas estudiadas a lo largo de esta tesis se basa en la relevancia y posible influencia que pueden tener sobre el cambio climático debido a sus elevadas tasas de emisión y formación. De este modo, se ha estudiado el polen y el polvo desértico (partículas primarias), y partículas de aerosol secundarias, formadas durante los eventos de formación de nuevas partículas (NPF).

En el caso del polen, su baja concentración en la atmósfera y la falta de instrumentos estandarizados para detectarlo de forma específica han hecho que su estudio se lleve a cabo mediante experimentos de laboratorio. Por otro lado, la influencia del polvo y de los eventos de formación de nuevas partículas (NPF) se ha analizado a través de campañas de campo en dos estaciones de alta montaña ubicadas en España: una en la Estación de Sierra Nevada (SNS, 2500 m s.n.m.), en el sur de la Península Ibérica, y otra en el Observatorio de Izaña (IZO, 2367 m s.n.m.), en la isla de Tenerife localizada en el Archipiélago Canario. Ambas estaciones están frecuentemente expuestas a intrusiones de polvo sahariano y presentan condiciones propicias para la formación de nuevas partículas.

Estudios recientes han demostrado que los granos de polen pueden fragmentarse en una gran cantidad de partículas más pequeñas, conocidas como subpartículas de polen (SPPs), que podrían actuar como núcleos de condensación de nubes (CCN). Por ello, en esta tesis, hemos investigado la capacidad de activación como CCN de 10 especies diferentes de SPPs, (características de climas mediterráneos), en distintos tamaños (80, 100 y 200 nm) y niveles de supersaturación (SS). Los resultados muestran que todas las SPPs estudiadas presentan supersaturaciones críticas (SS $_{\rm Crit}$) que pueden darse en la atmósfera (0.07% $_{\rm C}$ 0.37%, dependiendo del tamaño) y valores de higroscopicidad ($_{\rm K}$) que se encuentran dentro del rango típico de los compuestos orgánicos (0.1 $_{\rm C}$ 0.3). Se ha

Resumen

observado que los sacáridos y ácidos grasos son los únicos compuestos orgánicos que se encuentran presentes en todas las especies, a pesar de que la composición de química orgánica y el contenido en proteínas varía significativamente de una especie a otra. También cabe mencionar que no se ha observado ninguna relación clara entre la activación de las SPPs y su composición orgánica.

Además del estudio de propiedades de activación y los análisis de composición química de las distintas SPPs, se han realizado experimentos para el análisis de la actividad superficial utilizando la técnica de tensiometría de gota pendiente. Los resultados revelan que todas las SPPs estudiadas tienen la capacidad de actuar como surfactantes y reducir la tensión superficial cuando la concentración de las disoluciones preparadas es elevada. No obstante, si la concentración de dichas disoluciones se encuentra más diluida (concentraciones a las que se produce la activación como CCN), el valor de tensión superficial del agua puede considerarse una buena aproximación en la teoría de Köhler. En general, los resultados indican que todas las SPPs presentan un comportamiento similar, lo que sugiere que las emisiones de polen podrían representar una fuente importante de CCN en la atmósfera.

En cuanto a las propiedades de activación como CCN en condiciones ambientales en SNS e IZO, encontramos que, a pesar de estar a altitudes similares, la concentración de CCN (a SS=0.4%) en SNS es aproximadamente cuatro veces mayor que en IZO, mostrando valores promedio durante las campañas de 645 cm⁻³ en SNS y 160 cm⁻³ en IZO. La concentración total de partículas (N) también es más alta en SNS, con un valor medio de 2500 cm⁻³, frente a 1170 cm⁻³ en IZO, mostrando mayores diferencias en el modo de acumulación que en nucleación y Aitken. Ambas estaciones muestran un patrón diurno típico de zonas de alta montaña, con un aumento de la concentración de partículas a mediodía, debido a la influencia del transporte de contaminantes por el crecimiento de la capa límite atmosférica (ABL) (más pronunciada en SNS) y los eventos de formación de nuevas partículas (NPF), que también se producen en este mismo intervalo horario. Ambos fenómenos atmosféricos contribuyen significativamente a la concentración y modifican las distribuciones de tamaño de las partículas, afectando así la actividad como CCN.

Para evaluar el impacto que tienen las partículas recién formadas (en los eventos de NPF) en la concentración de CCN, hemos desarrollado un nuevo método que permite separar el efecto del transporte (que afecta principalmente al modo de acumulación), de la formación y crecimiento de nuevas partículas (en los modos de nucleación y Aitken). Con este método calculamos el modo de los NPF y separamos las partículas que se han formado en dichos eventos de las partículas de aerosol de fondo o transportado con el crecimiento de la ABL. A partir de ahí, conociendo las curvas de activación, se determina la concentración de CCN de partículas que provienen directamente de los NPF. A diferencia de los métodos utilizados por autores anteriores, que estimaban el incremento en la concentración de CCN comparando con instantes previos al inicio de los NPF o con días en los que no hay producción de NPF, nuestro método se basa en la observación del tamaño máximo que pueden alcanzar las nuevas partículas, el momento exacto en que se producen los eventos de NPF y la obtención del modo de NPF de la distribución de tamaño.

Para desarrollar esta nueva metodología, inicialmente, se han utilizado medidas de CCN en función del tamaño realizadas en SNS. Posteriormente, el método ha sido adaptado para su aplicación con medidas polidispersas de CCN. Este método se ha aplicado tanto a los eventos de NPF observados en SNS e IZO, y los resultados muestran que dichos eventos pueden contribuir a la concentración de CCNs en condiciones de altos valores de SS. Sin embargo, si SS < 0.4%, esta contribución es prácticamente nula. Los valores de contribución relativa de dichos eventos, a la concentración de CCN es mayor en IZO (promedio de campaña de 24 \pm 25% a SS = 0.8%) que en SNS (6.2 \pm 4.8% a SS = 0.8%). La menor contribución en SNS se debe a que las partículas activadas como CCN a mediodía no provienen de los eventos de NPF; si no del transporte de partículas dentro de la capa límite atmosférica. No obstante, en términos absolutos, la cantidad de partículas generadas por eventos de NPF y activadas como CCN es ligeramente mayor en SNS que en IZO (a SS = 0.8%, 95 cm⁻³ frente a 51 cm⁻³, respectivamente). Finalmente, también cabe destacar que las contribuciones de NPF a la concentración de CCN obtenidas en esta tesis, son menores que las estimadas en estudios previos aplicando diversas metodologías, lo que podría afectar a las predicciones de CCN a nivel global.

Resumen

Además de los eventos de NPF, en ambas estaciones de alta montaña se observan con frecuencia episodios de intrusión de polvo Sahariano. Durante los períodos de medición, se identificaron dos eventos de polvo en SNS y seis en IZO. Durante estos eventos, la concentración de partículas de polvo es mayor durante la noche para ambas estaciones, aunque la influencia que tienen sobre las propiedades de activación depende de la intensidad, características y condiciones específicas de cada evento.

La mayoría de los episodios de polvo muestran una reducción en la concentración de partículas submicrométricas, probablemente, debido a la actuación de las partículas de polvo como sumideros de coagulación y a un transporte de partículas menos eficiente desde alturas inferiores. Esta disminución en la concentración de partículas más finas durante los eventos lleva a observar valores más elevados de la fracción activada (AF). No obstante, para aislar la influencia que pueden tener de las intrusiones de polvo sobre las propiedades de activación como CCN de otros procesos atmosféricos que ocurren simultáneamente (transporte y crecimiento de la capa límite atmosférica y los eventos de NPF), se ha realizado un análisis separando periodos diurnos y nocturnos. Los resultados muestran que, durante el día, la concentración de CCN disminuye en SNS y aumenta en IZO, mientras que durante la noche se observa un incremento en ambas estaciones. La disminución en SNS podría deberse a una menor influencia de la ABL durante los eventos de polvo, mientras que este efecto pierde relevancia en IZO, debido a que generalmente se ve menos influenciada por este fenómeno. En cambio, el aumento de la concentración de CCN observado por la noche en ambas estaciones sugiere que las partículas de polvo presentes en el modo de acumulación pueden activarse como CCN. No obstante, para llegar a un mejor entendimiento del papel que juegan y la influencia que tienen las partículas de polvo en las propiedades de los CCN y la higroscopicidad, sería necesario realizar un análisis más detallado con una base de datos que contenga una mayor cantidad de casos de estudio.

Como conclusión de los resultados de esta tesis, podemos decir que tanto las subpartículas de polen, el polvo desértico como las partículas recientemente formadas pueden actuar como CCN, modificando las propiedades de activación y

la formación de nubes. Estudios futuros que amplíen estos resultados, aplicando metodologías similares a conjuntos de datos más extensos, con periodos de medición más largos y en diferentes localizaciones, contribuirán a mejorar el conocimiento sobre las propiedades de los CCN y su impacto climático a escala global.

1. Introduction

Climate change has become one of the most critical topics of our time. The rising frequency and intensity of certain atmospheric events, such as extreme heat, heatwaves, dust events, heavy rainfall, powerful tropical cyclones, and the shrinking of Arctic ice and permafrost, highlight the ongoing global climate change. These changes are driven by disruptions in the Earth's energy balance, leading to shifts in surface temperatures. Improving our knowledge of the mechanisms driving these impactful changes is a crucial scientific challenge.

Radiative forcing is a concept used in climate science to quantify the perturbation in the Earth's energy balance caused by changes in the atmosphere and the Earth's surface. It is a measure of the ability of a specific factor to alter the amount of energy that enters or leaves the Earth's atmosphere, affecting the global climate. Thus, understanding radiative forcing drivers is essential for assessing the potential climate impacts of human activities and natural processes. The Intergovernmental Panel on Climate Change (IPCC) Sixth Assessment Report (AR6) on the physical science basis of climate change states that, among all factors affecting radiative forcing, atmospheric aerosols have the greatest associated uncertainty (IPCC, 2021).

Atmospheric aerosol consists of solid or liquid particles suspended in the atmosphere, excluding clouds (Horvath, 2000). The aerosol sources are many and diverse and they determine the aerosol particles' physical properties (e.g. size, density, shape) and chemical composition. Aerosol sources can directly emit particles (primary particles) into the atmosphere or emit gases that favor the formation of new particles through gas-to-particle conversion processes (secondary particles). Additionally, the origin of these particles can be natural, when they are emitted or generated by the natural environment (such as terrestrial biosphere, volcanoes, oceans or deserts) or anthropogenic when they come from human activities (such as biomass burning, traffic emissions or industries) (Carslaw et al., 2010). These particles can have a significant impact on Earth's energy balance

Introduction

through aerosol-radiation interactions (ARI) and aerosol-cloud interactions (ACI) (Archer-Nicholls et al., 2016). ARI include direct effects, which are related to scattering and absorption of solar and terrestrial radiation by particles as well as semi-direct effects, based on the absorption of radiation that changes the atmospheric stability and circulation and therefore, cloud formation. ACI or indirect effects result from changes in cloud radiative properties due to variations in cloud droplet properties (such as concentration, droplets size or chemical composition, e.g. Seinfeld and Pandis, 1998; Andreae and Rosenfeld, 2008; Zieger et al., 2013). The AR6 reported that atmospheric aerosol presents a net radiative forcing of -1.1 [-1.7 to -0.3] W/m² with moderate confidence, with ACI responsible for 75-80% of the total uncertainty. This high uncertainty is due to the large spatiotemporal variability of aerosol sources and their strength, as well as the atmospheric processes that aerosol particles undergo, which lead to large variations in aerosol physicochemical properties (IPCC, 2021).

The ACI effects are driven by aerosol particles that can act as cloud condensation nuclei (CCN) or ice nucleating particles (INP). Variations in the available amount of CCN or INPs in the atmosphere, or in their properties, can affect cloud radiative properties, cloud lifetime and precipitation, changing the hydrological cycle and therefore, the climate (Kaufman and Tanré, 1994). For instance, in warm clouds with a high concentration of CCN, the cloud droplet number concentration increases when the cloud liquid water content is constant, but the size of the droplets decreases. This leads to a larger total droplet surface area that can interact with radiation, resulting in an increased cloud albedo (Twomey, 1977). Additionally, a decrease in droplet size may slow down and reduce precipitation, potentially extending the cloud's lifetime (Lohmann and Feichter, 2005). All these aerosol-cloud interactions are still not well understood (Seinfeld et al., 2016). Therefore, quantifying CCN concentrations, characterizing the aerosol properties that influence their activation as CCN, and identifying the sources (both natural and anthropogenic) of CCN, along with their temporal and spatial variability, are crucial for improving scientific knowledge and obtaining better predictions of global climate models (e.g. Dusek et al., 2006; Schmale et al., 2018; Legg, 2021).

The ability of aerosol particles to activate as CCN depends on their size, chemical composition, water solubility, hygroscopicity and morphology (Ervens et al., 2010; Bougiatioti et al., 2017; Petters and Kreidenweis, 2008), with size being the most important one (Dusek et al., 2006). Sizes at which particles act as CCN are typically in the range 60 - 115 nm (Hammer et al., 2014), although some observational studies have also shown that particles as small as 50 nm in diameter can form cloud droplets as well (Fan et al., 2018). The effect of chemical composition on activation is associated with their hygroscopic properties (parametrized through the hygroscopicity parameter κ), which reflects the capability of aerosol particles to uptake water. The hygroscopicity parameter, κ , ranges from 0 (insoluble or non-hygroscopic substances) to 1.4 (very soluble or hygroscopic substances such as sodium chloride). For example, inorganic salts are considered hygroscopic particles and present high κ values (Petters and Kreidenweis, 2007; Christiansen et al., 2020). In contrast, aerosol particles such as elemental carbon or dust do not show a clear hygroscopic behavior (Titos et al., 2014b). Depending on the features of aerosol particles, such as their natural or anthropogenic sources, their primary (directly emitted into the atmosphere) or secondary (formed from precursor vapors) origin, transport pathways and atmospheric processes in which they can be involved, particles have different capacities to act as CCN, with varying influence on the CCN budget and overall activation properties (Andreae and Rosenfeld, 2008; Després et al., 2012; Paasonen et al., 2018).

Among primary aerosol particles, increased attention has recently been paid to primary biological aerosol particles (PBAPs) such as pollen (Fröhlich-Nowoisky et al., 2016) due to their impact on human health and climate (Deguillaume et al., 2008; Després et al., 2012; Tanarhte et al., 2018). Global emission rates of pollen particles into the atmosphere are in the range of 47-84 Tg/year (Jacobson and Streets, 2009; Hoose et al., 2010), which might increase in the near future due to climate change (Zhang and Steiner, 2022). Pollen particles tend to have a short lifetime in the atmosphere due to their large size, ranging from 10 to 100 μ m, (Després et al., 2012; Manninen et al., 2014). However, recent studies have shown that under high humidity conditions or mechanical impacts, pollen grains can rupture into thousands of smaller particles (ranging from several nanometers to

1 μm) (Hughes et al., 2020), known as subpollen particles (SPPs) (Grote et al., 2003; Taylor et al., 2004; Mikhailov et al., 2019), thereby increasing their residence time in the atmosphere. Intact pollen grains, SPPs and even pollen-related proteins are the main factors causing seasonal allergic rhinitis in the population as well as the increase in the number of asthma attacks (Cariñanos et al., 2014; Cecchi et al., 2020). Additionally, SPPs are also able to act as CCN and therefore, modify the global CCN budget (Steiner et al., 2015; Mikhailov et al., 2019; Prisle et al., 2019; Mikhailov et al., 2021). SPPs contain many organic biomolecules (Pacini et al., 2006), such as fatty acids (Ischebeck, 2016), amino acids (Gong et al., 2015; Lawson et al., 2021), proteins (Steiner et al., 2015) and saccharides (Pacini et al., 2006; Rathnayake et al., 2017; Mampage et al., 2022). While the activation properties and hygroscopic behavior of inorganic aerosol particles are well defined in the literature (Sorjamaa et al., 2004), these characteristics are still poorly understood for organic aerosols (OA), and especially, for organic aerosol mixtures (such as SPPs) (Prisle et al., 2019). The organic chemical speciation of SPPs differs among pollen species (Axelrod et al., 2021), resulting in different water solubility properties that might influence their hygroscopic behaviour. In addition, many organic compounds are able to act as surfactants and reduce surface tension (σ) , modifying activation properties (Davies et al., 2019).

The importance of surface tension reduction (and its time evolution) in activation as CCN is still not well understood (e.g. Sorjamaa et al., 2004; Varga et al., 2007; Petters and Kreidenweis, 2013; Forestieri et al., 2018; Lin et al., 2020). This is because the presence of surfactants can have opposing effects on aerosol activation related to Kelvin and Raoult effects (described in Köhler Theory) (Köhler, 1936). Surfactants reduce the surface tension, decreasing the critical supersaturation and facilitating particle activation (Kelvin effect). In contrast, the depletion of solute from the droplet bulk (surfactant partitioning effect), in which the surfactant migrates to the surface, might reduce the hygroscopic water uptake and therefore, reduce activation efficiency (Raoult effect). It is an active area of research to determine whether the reduction of surface tension prevails over solute effect increasing activation efficiency (Ovadnevaite et al., 2017) or if, in contrast, the surface partitioning effect is dominant, which limits the activation of particles (Sorjamaa et al., 2004; Forestieri et al., 2018). Thus, further studies on the

characterization of OA hygroscopicity and their behaviour as surfactants are needed to explain these discrepancies and improve the understanding of activation properties and CCN concentration at OA dominated sites, such as high-mountain environments (Rejano et al., 2024).

Another important primary aerosol particle in the atmosphere is dust. Atmospheric dust particles contribute significantly to the global aerosol load, with a global emission rate ranging from 1000-5000 Tg/year (Cakmur et al., 2006; Kok et al., 2021). The main source areas of dust particles are located in the arid regions of the planet, with the Sahara desert and the Arabian Peninsula being the major contributors over the globe (Prospero et al., 2002). In this context, a persistent outflow of Saharan dust is transported westward, toward the Caribbean, and the eastern coasts of North America and South America (Prospero et al., 1981; Prospero, 1999; Prospero and Lamb, 2003). Large quantities of mineral dust are also transported across the Mediterranean Basin to Europe and the Middle East (Moulin et al., 1998; Salvador et al., 2014) in episodic intervals and/or following seasonal patterns (Querol et al., 2009a; Pey et al., 2013).

Mineral dust particles play a crucial role in the global aerosol budget due to their significant contribution, their widespread vertical distribution in the atmosphere, and their potential for long-range transport (e.g. Knippertz and Stuut, 2014; Nenes et al., 2014; Adebiyi et al., 2023; Kok et al., 2023). As climate change is expected to increase the frequency, duration, and intensity of desert dust episodes (Salvador et al., 2022), understanding their impact becomes even more critical. Consequently, extensive research has focused on various aspects of mineral dust, including its emission and transport pathways (e.g. Prospero and Lamb, 2003; Salvador et al., 2008; Zhao et al., 2022), adverse health effects (e.g. Stafoggia et al., 2016; Díaz et al., 2017), direct radiative properties (e.g. Lyamani et al., 2005; Valenzuela et al., 2012; Granados-Muñoz et al., 2019) and its influence on cloud microphysical processes (e.g. Karydis et al., 2011; Nenes et al., 2014; Walser, 2017).

Among these atmospheric effects, dust particles are well recognized as one of the most important ice-nucleating particles (Hoose and Möhler, 2012; Atkinson et al., 2013). However, their role as cloud condensation nuclei (CCN) remains less understood (Karydis et al., 2017; Walser, 2017). Due to their typically large size, often

Introduction

exceeding 1 μ m (Mahowald et al., 2014; Adebiyi et al., 2023), mineral dust particles can act as giant CCN and directly participate in cloud formation. Karydis et al. (2011) estimated that dust particles could contribute 30–40% to CCN concentrations in areas close to dust sources. Nevertheless, other studies suggest that their overall impact on CCN budgets is limited, either due to their low number concentration (Kristensen et al., 2016) or because they act as a coagulation sink for smaller particles, ultimately reducing the availability of aerosols that can serve as CCN (Hussein et al., 2011).

Related to their chemical composition, freshly emitted dust particles may consist of iron oxides (e.g., hematite, goethite), carbonates (e.g., calcite, dolomite), quartz, and clays (e.g., kaolinite, illite, and montmorillonite) (Lafon et al., 2006; Coz et al., 2009). Depending on the chemical composition of these dust particles, their ability to act as CCN can be limited, as some of these compounds exhibit almost non-hygroscopic behaviour (Herich et al., 2009; Kumar et al., 2010). Most models use this simplified assumption attributing a constant κ value around 0.1 for dust particles (Karydis et al., 2017). However, dust particles can become effective CCN after undergoing atmospheric transport and chemical processing, during which they become internally mixed with hygroscopic material (Usher et al., 2002; Hatch et al., 2008; Kakavas et al., 2021). The enhancement of dust hygroscopicity can occur through coagulation and coating with soluble particles, such as sea salt (Denjean et al., 2015), or via heterogeneous condensation of soluble gas species onto the dust particles (Sullivan et al., 2009). Additionally, differences in chemical and mineralogical composition among dust particles from different source regions have been observed (Chiapello et al., 1997). Therefore, depending on the dust source region, transport pathway, and interaction with other atmospheric constituents, their impact on CCN and activation properties might vary (Herich et al., 2009; Pósfai et al., 2013; Karydis et al., 2017).

Aside from primary particles, secondary aerosol particles from new particle formation contribute approximately 50% of the total aerosol particle number concentration (Merikanto et al., 2009). The formation of new atmospheric aerosol particles (also known as nucleation) and their subsequent growth are referred to as new particle formation (NPF) events. Several atmospheric constituents favor the

formation of new particles and have been widely studied. Sulfuric acid has traditionally been considered one of the main precursors of NPF events. However, it alone is insufficient to explain NPF occurrence under various ambient conditions (Kulmala et al., 2004). Additional studies have highlighted the importance of ammonia and amines as vapors that can accelerate the nucleation rate, while lowand extremely low-volatility organic vapors play a role in the growth of the newly formed particles (Kirkby et al., 2011; Ehn et al., 2014). In high-mountain environments, under pristine conditions, biogenic volatile organic compounds (BVOCs) are recognized as important drivers of NPF events (Gordon et al., 2017; Bianchi et al., 2021). However, volatile organic compounds (VOCs) from anthropogenic sources can also drive NPF in polluted areas or be transported from lower-altitude regions to high-mountain sites (Lai et al., 2024). In addition to the role of different atmospheric constituents, meteorological conditions, such as solar radiation or relative humidity, also play a key role in the formation and growth of new particles in the atmosphere (Dada et al., 2017).

Beyond the mechanisms driving new particle formation and growth, the ability of these particles to act as CCN remains highly uncertain (Kerminen et al., 2018). The newly formed particles from NPF events are typically too small to act as CCN; however, they can rapidly grow through further collision and condensation processes or be scavenged by larger pre-existing particles via coagulation (Jorga et al., 2023), eventually reaching CCN relevant sizes and influencing aerosol-cloud interactions (Merikanto et al., 2009; Kerminen et al., 2018; Rejano et al., 2021). Model studies have reported that more than 50% of global CCN are generated by nucleation processes (e.g. Korhonen et al., 2008; Merikanto et al., 2009; Wang et al., 2023). However, the large uncertainty governing NPF-derived CCN estimations arises from the lack of standardized and common methods to disentangle the CCN that comes from NPF events alone (e.g. Dameto de España et al., 2017; Rose et al., 2017; Kalkavouras et al., 2019; Rejano et al., 2021).

Most current methods determine a concentration enhancement factor by comparing the aerosol concentration during or after the NPF event to the concentration prior to the event or to the concentration during non-NPF event days (e.g. Rose et al., 2017; Ren et al., 2021; Sun et al., 2024a). However, these

Introduction

methods do not isolate the contribution of the NPF itself to the measured CCN concentration; rather, they quantify the aerosol concentration enhancement relative to a reference condition. An important limitation of this approach is that the background conditions (i.e., pre-existing particles and precursors) are assumed to be identical during NPF event days and non-event days, or during the NPF event and prior to the NPF event onset. However, this assumption could lead to a significant overestimation of CCN concentration. For example, Rejano et al. (2021) reported an enhancement in CCN concentration during NPF event days of 115% (at SS=0.25%) and 175% (at SS=0.5%), with respect to non-NPF event days at a highmountain site. Park et al. (2023) observed that CCN concentrations increased after the NPF event by 2%-268% at SS=0.4% at a station in the Antarctic Peninsula. Dameto de España et al. (2017) reported that at an urban site, the CCN concentration can increase up to 143% during NPF events respect to CCN concentration before the NPF starts (at SS=0.5%). Kalkavouras et al. (2019) reported NPF days can increase CCN concentrations (from SS=0.10% to SS=1.00%) between 29% and 77% with respect to the time at which the NPF starts. Ren et al. (2021) applied the method developed by Kalkavouras et al. (2019) to eight different stations worldwide with different characteristics and reported greater enhancements factor at sites close to anthropogenic sources (mean factor of 3.6 ± 1.2) within the typical range of supersaturations in clouds (0.1%–1.0%); whereas the mean enhancement factor at remote sites was 1.8 ± 0.6. A different approach was applied by Cai et al. (2021) who calculated the percentage of newly grown particles acting as CCN as the ratio between particles activated as CCN in the size range 3-80 nm and the number concentration of particles around 3-30 nm. In this case, their results show contributions between 8%-38% (at SS=0.8%).

The main challenge when determining the NPF impact on CCN concentrations is disentangling the influence of NPF events from other aerosol sources that might contribute simultaneously to the observed CCN concentration (e.g., Chandra et al., 2016; Cai et al., 2018; Cai et al., 2021). Another difficulty is the exact knowledge of the time at which the NPF-derived particles stop contributing to CCN, as well as tracking the contribution during simultaneous NPF events (i.e. NPF events that last more than a day and overlap with subsequent NPF events) (Dada et al., 2018; Kerminen et al., 2018; Kalkavouras et al., 2019; Su et al., 2022).

Additionally, all observational studies focus on fixed measurement sites; however, particles might grow to CCN sizes at a different location. In contrast to experimental ambient studies, modelling studies are able to track the newly formed particles and provide an estimation of the contribution of the particles produced during NPF events to the CCN concentration (Yu et al., 2020). However, models underestimate the contribution of NPF to CCN due to general underestimation of the amount of newly formed particles and the subsequent growth associated with uncertainties in simulating particle number size distributions (e.g. Williamson et al., 2019). Therefore, due to the potentially large contribution and observed variability of NPF events to the total particle number concentration worldwide, as reported in previous studies (e.g. Merikanto et al., 2009; Spracklen et al., 2010; Kalivitis et al., 2015; Cai et al., 2021), further experimental research is needed to provide more accurate estimates of CCN arising from NPF events and to develop a standardized procedure for performing this quantification.

Objectives and outline

The research activities developed in this thesis have the main objective of advancing in the understanding of CCN activation properties of different types of aerosol particles, with special focus on the knowledge-gaps that are still open and are a source of uncertainty in atmospheric and climate studies. For this purpose, the study was carried out from different experimental points of view, including laboratory and ambient in-situ measurements at highly climatic sensitive environments (i.e., high-mountain natural locations). The thesis dissertation is organized in several chapters, as indicated in the following outline:

Chapter 2 is devoted to the basic concepts behind the aerosol science needed to follow this thesis. The main features affecting aerosol activation as CCN are explained, as well as the physical basis of cloud formation in the atmosphere. Finally, the κ -Köhler theory is presented as the main theory that explains the activation of particles as cloud droplets.

Chapter 3 presents a detailed description of the study areas and the experimental high-mountain stations (Sierra Nevada station in southern Iberian Peninsula and Izaña Observatory in the Tenerife Island, SNS and IZO, respectively) together with a short description of the main instrumentation employed in this thesis.

Chapter 4 deals with the methodological aspects of the thesis. It presents the two main experimental configurations to measure CCN concentrations using in-situ techniques and the retrieval of the activation parameters from each set of measurements. Additionally, the experimental methods used to perform the laboratory experiments of CCN activation of pollen particles are also explained.

Chapter 5 shows the results of activation ability of pollen particles based on laboratory experiments. The main aim consists of studying the activation properties of 10 different pollen types and their relationship with chemical composition, protein content and surface activity.

Chapter 6 focuses on CCN activation properties at two high-mountain sites. Due to the large influence of Saharan dust events at both locations, special

attention is paid to the influence of these atmospheric phenomenon on CCN activation properties.

Chapter 7 focuses on the impact of new particle formation (NPF) events on CCN budget. It presents a novel methodology to obtain the NPF contribution to CCN concentration, that is then applied to measurements performed at SNS and IZO. The results of the NPF contribution to CCN concentration at both sites are extensively analyzed.

Finally, Chapter 8 presents a summary of the main conclusions of this thesis together with an outline of future research.

2. Fundamentals

This chapter describes the main physicochemical properties of atmospheric aerosol particles, focusing on the features of the specific aerosol types studied in the framework of this thesis. The physical basis involved in cloud formation processes in the atmosphere (homogeneous and heterogeneous nucleation), as well as κ -Köhler theory are also explained.

2.1 Atmospheric aerosols

The terrestrial atmosphere is a complex mixture of gases (such as N_2 , O_2 , CO_2 , water vapor or other trace gases) that envelops the Earth. Other components, such as clouds and aerosol particles, are important constituents of the atmosphere. Horvath (2000) defined the atmospheric aerosol as the suspension of solid and/or liquid particles in the atmosphere, excluding cloud components. Clouds consist of water droplets or ice crystals that form over aerosol particles suspended in the atmosphere. Despite atmospheric aerosol particles being a trace component in the atmosphere, they are crucial in defining the climate and might impact human health, ecosystems and cultural heritage (Fröhlich-Nowoisky et al., 2016; Patrón et al., 2017; IPCC, 2023).

Concerning the climatic impact of atmospheric aerosol particles, it is separated into Aerosol-Radiation Interactions (ARI) and Aerosol-Cloud Interactions (ACI). Through ARI, on one hand, atmospheric aerosol particles are able to scatter and absorb short- and long-wave radiation, altering the Earth's energy budget (direct effects). Additionally, due to the absorption of radiation by aerosol particles, changes in atmospheric stability and circulation are produced, and therefore, affecting cloud formation (semi-direct effects). On the other hand, the interaction of aerosol particles with clouds (indirect effect or ACI) is the mechanism by which aerosol particles change cloud properties, potentially affecting

precipitation and the radiative impact of clouds (IPCC, 2023). The ACI is associated with the modifications of cloud properties due to the role of aerosols acting as cloud condensation nuclei (CCN) or ice nucleating particles (INP). Changes in the number concentration of CCN/INP and their physicochemical properties affect cloud properties. An increase in CCN concentrations can lead to the formation of more cloud droplets so that, for fixed cloud liquid water content, the cloud droplet size will decrease. This effect leads to brighter clouds, changing the cloud albedo. Furthermore, aerosol particles may produce an effect on the cloud liquid water content, height and lifetime (IPCC, 2023). These aerosol effects can suppress drizzle and increase the amount of solar radiation reflected from clouds.

Depending on the physicochemical properties of the aerosol particles, their climatic impact can be quite different. The wide range of variability of these properties, such as size, chemical composition or morphology reveals the diversity of different kinds of particles present in the atmosphere. In addition, they can suffer multiple atmospheric processes that modify these properties over time. Due to this high temporal and spatial variability, the study of aerosol particles is very complex and their effects introduce a significant uncertainty in climate models (Lohmann and Feichter, 2005; Myhre et al., 2013).

The particle size and chemical composition are fundamental properties to characterize the aerosol particles. The aerosol size can vary over five orders of magnitude (from a few nanometers to several hundreds of micrometers). According to diameter values, the aerosol size distribution in the atmosphere can be theoretically classified in four modes (Nucleation, Aitken, Accumulation and Coarse) (Seinfeld and Pandis, 1998) which are related to different sources, formation processes and chemical composition. The set of Nucleation, Aitken and Accumulation mode can be grouped in fine mode ($N_{\rm F}$) corresponding to particles smaller than 1 μ m:

 Nucleation mode (N_{Nucleation}): this mode includes the smallest particles ranging in size from 2-3 nm to 25 nm. It constitutes the primary mode of the particle number size distribution, although it contributes the least to overall mass. These particles are created through the nucleation of precursor gases into newly formed particles. They have the shortest atmospheric lifetime (only a few hours) because they tend to grow into larger sizes.

- Aitken mode (N_{Aitken}): it makes the second largest contribution to particle number concentration. Its typical size range spans from 25 to 100 nm and comprises a blend of particles formed through various mechanisms, including the coagulation and growth of nucleation mode particles or direct emission during combustion processes. Primary traffic emissions typically fall within this size range (Li et al., 2018).
- Accumulation mode (N_{Accumulation}): this mode encompasses particles ranging from 100 nm to 1 μm. One of the primary mechanisms for their formation is the growth of Aitken mode particles through the condensation of saturated vapors onto these existing particles in the atmosphere. Additionally, the coagulation of preexisting particles also contributes to the formation of accumulation mode particles. As a result, these particles are often referred to as aged particles, as they have the longest lifetime in the atmosphere due to their low removal efficiency. This mode is particularly significant because of its impact on the concentration of cloud condensation nuclei (CCN) in the atmosphere (Schmale et al., 2018).

Coarse mode (N_C) refers to particles with diameters larger than 1 μ m. These particles are usually directly emitted into the atmosphere by different mechanical processes such as resuspended mineral dust, marine or some biogenic emissions like pollen particles. Due to their large size, they can activate directly as CCN, even at low supersaturations (Tao et al., 2024); although, as they also have higher mass, they are characterized by a short residence time in the atmosphere being removed mainly by gravitational settling.

Depending on their origin, aerosol particles are classified as natural, if they are emitted by natural sources or anthropogenic, when they have been produced by human activities. In addition, if they are directly emitted to the atmosphere in

Atmospheric aerosols

particulate phase, they are defined as primary aerosol particles (such as mineral dust, biological particles like pollen, spores or bacteria, sea salt or elemental carbon from traffic emissions). If particles are formed from precursor gases through different formation and chemical processes that convert those gases into particulate matter, they are classified as secondary aerosol particles.

Among primary aerosol particles, pollen particles are an important source of aerosol particles globally (Andreae and Rosenfeld, 2008; Pöschl et al., 2010), with an emission rate into the atmosphere currently estimated to be higher than 47 Tg/year (Hoose et al., 2010). They are considered as primary biological aerosol particles (PBAP), mostly composed of multiple organic components, that are directly emitted from the vegetation. Its emission rate is expected to increase in the future due to climate change (Zhang and Steiner, 2022) since the increase in temperature has been associated with an increase in the production and emission rate by some species of plants (Ziska et al., 2019; Cariñanos et al., 2022). Pollen grains show a great morphologic variability (e.g., spherical, granulate, reticulate) and they can be transported by insects (entomophilous plants covered by a fatty acid external layer, called pollenkitt) or wind (anemophilous species) (Pacini and Hesse, 2005; Gong et al., 2015). Due to their large size, ranging from 10 to 100 µm, pollen particles tend to have a short lifetime in the atmosphere (Després et al., 2012; Manninen et al., 2014). However, several studies have shown that under high humidity conditions, as well as a consequence of mechanical impacts, pollen grains can rupture into smaller particles (from several nanometers to 1 μm) called subpollen particles (SPPs) (Grote et al., 2003; Taylor et al., 2004; Mikhailov et al., 2019). Fig. 2-1 shows the microscopic image of an intact Olea pollen grain and a smaller Olea subpollen particle. Some estimates suggest that one pollen grain can form up to thousands of SPPs (Hughes et al., 2020; Stone et al., 2021). This leads to increased residence time in the atmosphere and may enhance the direct and indirect influence of pollen on climate. Recent studies have shown that these SPPs can potentially affect climate via aerosol-cloud interaction by acting as CCN (Steiner et al., 2015; Prisle et al., 2019; Mikhailov et al., 2021).

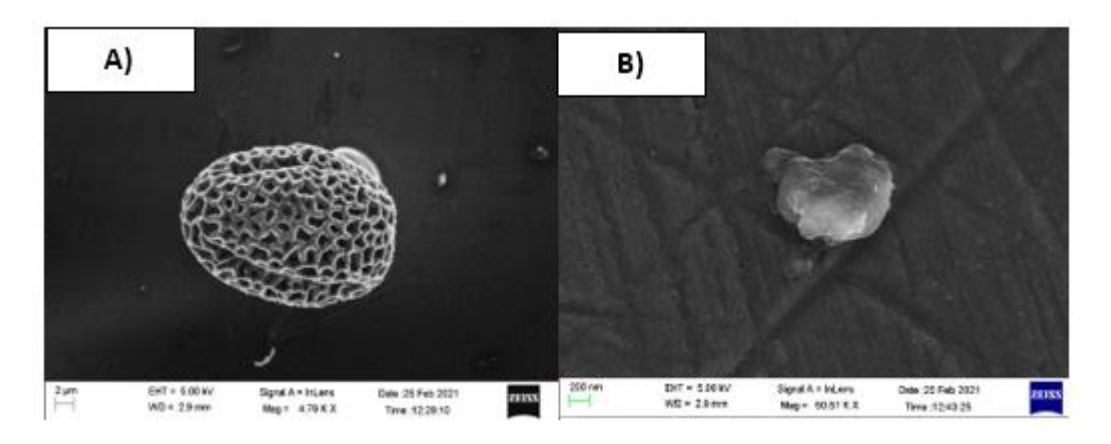


Figure 2-1. Scanning electron microscope (SEM) image of intact *Olea* pollen grain at scale 2 μ m (A) and SEM image of *Olea* subpollen particles at scale 200 nm (B).

Another significant primary aerosol type is mineral dust, which constitutes a major fraction of the global aerosol mass load, with an estimated annual emission rate of 5000 Tg/year (Kok et al., 2023). Mineral dust is mainly produced by wind erosion of soil in arid and semi-arid regions (e.g., Sahara Desert) and is injected into the atmosphere under favorable weather conditions. It is one of the major aerosols of the atmosphere that can be transported over thousands of kilometers and therefore, it has a global climate effect (e.g. Ansmann et al., 2003; Cazorla et al., 2017; Benavent-Oltra et al., 2019). Recent studies point towards an increase in frequency, duration, and intensity of desert dust transport episodes due to climate change (Salvador et al., 2022). Dust particles can be composed of iron oxides such as hematite, carbonates such as calcite, quartz and clays (Lafon et al., 2006; Coz et al., 2009; Karydis et al., 2011). Depending on their origin, emission and transport processes, the composition, size distribution and morphology of dust particles can be very different (Sokolik et al., 2001), as observed in microscope images (Figure 2-2). During transport processes dust particles can also interact with other aerosol particles, such as sea salt or anthropogenic pollutants. These particles can cover the insoluble mineral core with a coating of soluble matter (Kelly et al., 2007) and modify their properties.

Like pollen particles, the presence of dust particles in the atmosphere modifies the surface radiation budget (Lyamani et al., 2005; Valenzuela et al., 2012) as well as affects the CCN/INP properties (Bangert et al., 2012). Hence, they have

Atmospheric aerosols

direct and indirect effects on climate, which is vital to study and understand their behavior.

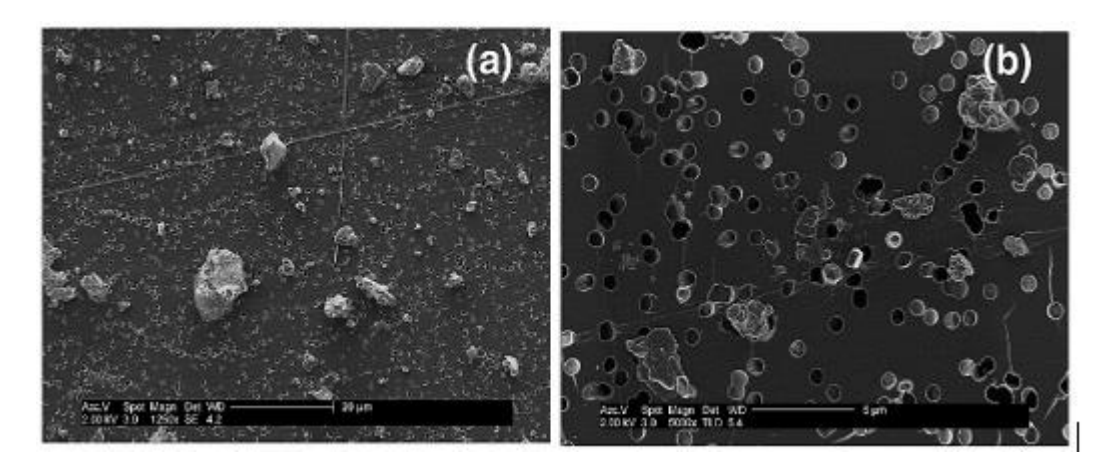


Figure 2-2. Scanning electron micrographs individual Saharan dust particles at different scales (A, $20 \mu m$ and B, $5 \mu m$) (Images taken from Reid et al. 2003).

Besides primary natural particles like pollen or dust, the main sources of secondary natural aerosol in the atmosphere are volcanoes and the biosphere. Volcanoes emit large amount of sulphur dioxide that is considered one of the new particle formation (NPF) precursors through its oxidation to sulfuric acid (e.g. Rose et al., 2019). The biosphere is considered an important source of secondary particles like dimethyl sulfide (DMS) and volatile organic compounds (VOCs) that are able to form new particles by photo-chemical oxidation and the subsequent gas-to-particle conversion of the reaction products (e.g. Ehn et al., 2014). The formation of new particles leads to an increase in the aerosol particle number concentration (particularly in the nucleation mode). These particles subsequently grow in size, first reaching diameters of a few nanometers, then reaching the size of Aitken mode particles (Kulmala et al., 2017).

NPF events have been observed to be important and frequent phenomena that take place in many different environments (Kulmala et al., 2004). The nucleation process consists of the formation of a molecular cluster that grows instead of evaporating. Then, the cluster continues growing by condensation or coagulation of more nucleated or pre-existent particles. Simultaneously, chemical

reactions such as oxidation or interactions with additional vapors take place allowing the continuous growth of particles.

There is still no consensus in scientific community about molecules and mechanisms involved in the process to form stable clusters (e.g. Yao et al., 2018; Zhao et al., 2024). Sulfuric acid (H₂SO₄) is considered as one of the main precursors for aerosol nucleation and growth, however, it needs some others compounds such as ammonia and amines as well as the oxidation of VOCs that produces oxidized organic species, called HOMs (highly oxidized organic molecules) (Bianchi et al., 2016, 2017). Additionally, the role of ions is important for NPF events to occur. The presence of ions strongly enhance pure sulfuric acid nucleation (Duplissy et al., 2015) and sulfuric acid—ammonia nucleation (Kirkby et al., 2011). Kirkby et al. (2016) showed that ions can strongly enhance the nucleation of pure organic particles in absence of sulfuric acid.

It should also be mentioned that atmospheric and meteorological conditions, such as temperature, solar radiation or lower pre-existing aerosol particles benefit the clusters formation (Dada et al., 2017; Kerminen et al., 2018). Due to the collisions between particles, the smallest ones have a very short lifetime. Therefore, when environmental conditions are favorable to produce the nucleation, a competition between particle formation and growth, and scavenging by pre-existing aerosol particles is produced (Kulmala et al., 2017). This competition is regulated by the ratio between the growth rate (GR, which defines how fast particles grow to larger sizes) and the condensation sink (CS, loss rate due to scavenging) (Du et al., 2022). High CS might influence NPF inhibiting the process or limiting the grow. However, if particles are able to reach larger size, they could be able to activate as CCN. When newly formed particles grow to sizes larger than 70 nm approximately, they might contribute to the CCN concentration (Wiedensohler et al., 2009; Rejano et al., 2021).

2.2 Cloud formation and Köhler Theory

The formation of cloud droplets (phase transition of the water vapor contained in an air parcel to form liquid water droplets) occurs due to homogeneous and heterogeneous nucleation processes. It depends on the saturation; that is described as the point at which if you try to pack too much water vapor into a particular volume, the excess will condense to form liquid droplets (Chilson, 2009). A volume that contains less water vapor than that found at saturation is called subsaturated; and liquid water may evaporate until saturation is reached. In contrast, if there is more, it is supersaturated and usually, condensation will quickly occur to reduce the vapor content. The vapor saturation ratio (S) depends on temperature (T) (Eq. 2-1) and is defined as the ratio between water vapor pressure in the air parcel ($P_{\rm H_2O}$) and the saturation water vapor pressure ($P_{\rm H_2O}^0$ (T)), which increases with temperature (T) according to the equation of Clausius-Clapeyron (Eq. 2-2) (Seinfeld and Pandis, 1998). The saturation ratio can also be expressed in terms of relative humidity (RH).

$$S = \frac{P_{H_2O}}{P_{H_2O}^0(T)} = \frac{RH(\%)}{100}$$
 Eq. (2-1)

$$P_{H_2O}^0(T) = P_{H_2O}^0(T_0)e^{\left[\frac{L}{R}\left(\frac{1}{T_0} - \frac{1}{T}\right)\right]}$$
 Eq. (2-2)

where $P^0_{H_2O}(T_0)$ is the saturation vapor pressure at temperature T_0 , R is the universal gas constant and L the latent heat of vaporization (assumed to be constant during the phase change from liquid to vapor when pressure and temperature are held constant). To obtain Eq. (2-2), it is also assumed that water vapor behaves as an ideal gas.

2.2.1 Homogeneous nucleation

Homogeneous nucleation is responsible for the formation of droplets from the vapor phase. Vapor molecules are transformed into liquid particles in supersaturated conditions (which means RH values higher than 100%) and are defined as SS (%) = $(S-1) \cdot 100$ without the presence of a foreign phase. Classical homogeneous nucleation theory describes the formation of nuclei when the degree of supersaturation of the vapor phase is driving force. Small clusters are produced, although most of them are thermodynamically unstable and disappear in a short time. Only a small fraction of these clusters will grow to a size large enough (critical size) to produce nuclei. In a cluster of critical size, molecules condense and evaporate at the same rate. Clusters with a size smaller than critical size will evaporate, while clusters larger than critical size will probably continue to grow and become droplets. The saturation values required to produce homogeneous nucleation are between $2 \le S \le 5$ and corresponding to RH conditions between 200% - 500%. These values are too high to be observed in the atmosphere. The typical maximum supersaturation observed in convective updrafts is 1-2% (Chilson, 2009). Therefore, this process is not atmospherically relevant.

2.2.2 Heterogeneous nucleation

Heterogeneous nucleation is the formation of water droplets by condensation of water vapor on pre-existing aerosol particles. It requires smaller saturations than homogeneous nucleation and therefore, it is the dominant cloud-droplet formation mechanism in the atmosphere. The pre-existing aerosol particle is referred as cloud condensation nuclei (CCN). The Köhler theory (Köhler, 1936) explains how water vapor pressure over a droplet is affected by considering an aqueous solution instead of pure water (solute effect or Raoult effect) and considering a curved surface (curvature effect or Kelvin effect).

Raoult effect consists of the decrease of the saturation ratio when some solute particles are present in an aqueous solution. Due to the presence of solute

particles in the surface of the solution, the water molecules concentration is reduced (Raoult, 1887) and water vapor pressure over the solution decreases. The effect is quantified by the water activity (a_w) which is defined as the ratio between the number of moles of water (n_w) and solute (n_s) in the solution:

$$a_w = \frac{n_w}{n_w + n_s}$$
 Eq. (2-3)

Kelvin effect describes the increase of vapor pressure over a curved surface because molecules on the surface can escape to the gas phase more easily if the surface is curved because the considered molecule has fewer adjacent molecules close to it. Therefore, the vapor pressure over curved surface is higher than over a flat surface.

Combining both effects, the saturation value necessary for the nucleation process to occur is defined by Köhler equation:

$$\ln S = \frac{4 M_w \sigma_w}{RT \rho_w D_{droplet}} - \frac{6 n_s M_w}{\pi \rho_w D_{droplet}^3}$$
 Eq. (2-4)

where M_w , σ_w and ρ_w are the molecular weight, surface tension and density of pure water, respectively. It should be noted that σ_w is a good approximation for diluted droplets not composed of > 80% surface-active material (Ruehl et al., 2012). R is the universal gas constant and $D_{droplet}$ is the solution droplet diameter. It can be rewritten more simply by grouping the constant terms as:

$$\ln S = \frac{A}{D_{droplet}} - \frac{B}{D_{droplet}^3}$$
 Eq. (2-5)

The first term $(A/D_{droplet})$ represents the Kelvin effect which tends to increase S, while the second term $(B/D_{droplet}^3)$ represents the Raoult effect which decreases S. Due to the dependence on the diameter of each of the terms we can

deduce that for large diameters the Kelvin effect dominates over the Raoult effect, whereas for small diameters it is the Raoult effect which dominates over the Kelvin effect. Figure 2-3 shows the behavior of both effects and the resultant Köhler curve.

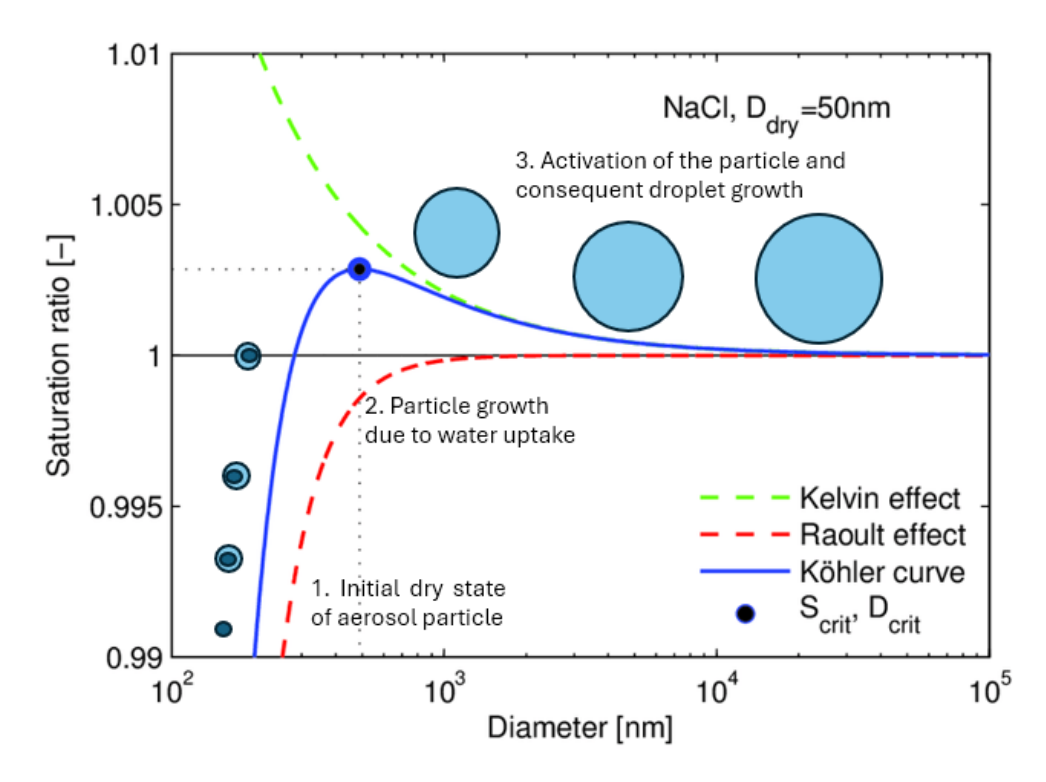


Figure 2-3. Example of a Köhler curve showing the separate contribution of Kelvin and Raoult effects. Figure adapted from Zieger (2011).

Between the two regimes, the Köhler curves exhibit a maximum defined as critical saturation (S_{Crit}), which depends on the properties of dry aerosol particle. This maximum occurs at a specific diameter value, known as critical diameter (D_{Crit}). The S_{crit} value of an arbitrary particle will determine if the particle can form a cloud droplet under a certain ambient S. The S of the droplet will tend to equalize with the ambient S to achieve an equilibrium state. If $S < S_{crit}$, the Köhler curves exhibit two equilibrium states (a stable equilibrium at smaller diameters and an unstable equilibrium at larger diameters); and the one with the lower diameter is the stable equilibrium state that the droplet will reach. Aqueous solution droplets must overcome a high energy barrier to transition from the stable to the unstable

Cloud formation and Köhler Theory

equilibrium state and although the aerosol particle can grow to a certain size and form a droplet, if the diameter is smaller than D_{Crit} it is not considered a cloud droplet. Thus, this particle cannot activate as CCN at this S. However, if $S > S_{Crit}$ the droplet keeps growing without limit (Figure 2-3). Therefore, the particle is considered activated as CCN at S and forms a cloud droplet.

2.2.3 κ-Köhler Theory

Petters and Kreidenweis (2007) introduced a simplification of the classical Köhler theory by expressing the water activity through the hygroscopicity parameter (κ). This parameter depends on the chemical composition of the aerosol particles and the influence of the water activity of an aqueous solution:

$$\frac{1}{a_w} = 1 + \kappa \frac{V_s}{V_w}$$
 Eq. (2-6)

where V_s is the volume of the dry aerosol particle and V_w is the volume of the water in the droplet. Particles composed of a mixture of substances with individual hygroscopicity parameter, κ_j , exhibit a collective κ given by their volume weighted average:

$$\kappa = \sum_{j} \frac{V_{s,j}}{V_s} \kappa_j$$
 Eq. (2-7)

In this sense, the hygroscopicity of a multi-component arbitrary particle can be estimated by knowing its internal chemical composition and characterizing the hygroscopicity of each component. The hygroscopicity parameter takes values from 0 for non-hygroscopic particles like black carbon particles, to 1.4, for most hygroscopic inorganic salts like sodium chloride (Petters and Kreidenweis, 2007).

Finally, if water activity is substituted by the hygroscopicity parameter and it is introduced in the Köhler equation the new expression results:

$$S\left(D_{droplet}\right) = \frac{D_{droplet}^{3} - D^{3}}{D_{droplet}^{3} - D^{3}\left(1 - \kappa\right)} \exp\left(\frac{4M_{w}\sigma_{w}}{RT\rho_{w}D_{droplet}}\right)$$
 Eq. (2-8)

where D is the dry diameter of the aerosol particle. Eq. (2-8) describes a curve analogous to that described by Eq. (2-4) and Eq. (2-5), with its corresponding S_{Crit} and D_{Crit} . In addition, this equation can also be expressed in terms of the supersaturation (SS), which is commonly defined as $(S-1) \cdot 100$. The maximum of the curve, SS $(D_{droplet})$, is called critical supersaturation (SS_{Crit}). This value establishes the activation threshold for a particle with a determined diameter. Thus, Eq. (2-8) is the mathematical expression of the κ -Köhler theory, which is the main theory describing the ability of an individual aerosol particle to activate as CCN depending on its size and hygroscopicity; and hence, its chemical composition. It should be noted that κ can depend on solution concentration for a given particle composition, therefore, these κ values are representative of dilute solutions around the point of CCN activation, i.e. representing CCN-derived hygroscopicity. In addition, the size dependence of particle composition leads to SS dependence of CCN-derived κ ; and as previously mentioned, the surface tension value (σ) is usually assumed to be σ_w that corresponds to surface tension of pure water at temperature T=298.15 K ($\sigma_{\rm w}$ =0.072 J/m²).

3. Experimental sites and instrumentation

This chapter describes the experimental sites and the measurement stations where the campaigns and experiments presented in this thesis took place. Ambient measurements were performed at two atmospheric observatories: Sierra Nevada Station (SNS), located in the Southern Iberian Peninsula and Izaña observatory (IZO), located in the Canary Archipelago. Controlled experiments described in section 4.4 took place at the facilities of the Andalusian Institute for Earth System Research (IISTA). Additionally, this section also shows the main features of the instruments used to obtain the results of this thesis.

3.1 Experimental sites

3.1.1 Sierra Nevada Station: SNS

The Andalusian Global Observatory of the Atmosphere (AGORA, https://atmosphere.ugr.es/en/about/presentation/agora) is located in the southeast of Spain, in the Granada area. It is managed by the Atmospheric Physics Group (GFAT) of the University of Granada, and it consists of an infrastructure designed for the multi-instrumental study of atmospheric processes, with a special focus on (i) atmospheric aerosol and its impact on climate and air quality, (ii) aerosol-cloud interaction processes, and (iii) trace gases in the lower layers of the atmosphere. AGORA comprises two experimental stations that represent distinct atmospheric conditions: an urban background station located in the southern part of the city of Granada (UGR, 37.16° N, 3.61° W, 680 m a.s.l.) and a high-mountain station (SNS, 37.10° N, 3.39° W, 2500 m a.s.l.) located in the Sierra Nevada National Park. Fig. 3-1 shows the map with the location (upper panel) and topographic profile (lower panel) of UGR and SNS. Part of the ambient aerosol measurements presented in Chapters 6 and 7 were performed at the SNS observatory during an experimental measurement campaign. Sierra Nevada mountain range has an alpine climate influenced by the Mediterranean Sea. It presents big thermal

Experimental sites

oscillations due to the complex orography and altitudinal breadth. The station is surrounded by a wide variety of plants species and communities commonly found in mountainous ecosystems and endemic species from this area such as pine forests (Pinus sylvestris, P. nigra), oak forests (Quercus spp.) and junipers (Juniperus spp.) (Algarra et al., 2019; Cariñanos et al., 2021). As a high-mountain station, SNS shows frequently free tropospheric conditions during nighttime, especially in winter. Due to its proximity to the African continent, SNS is frequently influenced by long-range transported aerosol particles such as dust particles from Sahara Desert (Jaén et al., 2023). During summer, transported particles from the Granada area reach the station due to atmospheric boundary layer (ABL) height increase and mountain-valley breeze phenomenon. Therefore, the sources of aerosol particles in Granada can be relevant for the measurements performed at SNS (Rejano et al., 2021). Road traffic is the main local source in Granada; as well as domestic heating and biomass burning (these last ones, especially in winter) (Lyamani et al., 2012; Titos et al., 2017). However, primary and secondary local sources from SNS related to human activities have a small impact on the aerosol population (Jaén et al., 2023). The surrounding vegetation emissions contribute to the local aerosol load, such as pollen emissions from different plant communities or biogenic volatile organic compounds (BVOCs) (Cariñanos et al., 2025). Additionally, Casquero-Vera et al. (2020) observed that NPF events can significantly contribute to the aerosol number concentration during summer and observed frequent NPF events occurring simultaneously at SNS and UGR.



Figure 3-1. Map showing the location of the AGORA infrastructure: UGR urban site and SNS high-altitude remote site (top panel). The topographic profile between both sites is included (bottom panel).

3.1.2 Izaña Observatory: IZO

Results shown in Chapter 6 and Chapter 7 were also obtained during an experimental campaign performed at the Izaña Observatory (IZO, 28.3° N, 16.5° W, 2367 m a.s.l.), which is which is a Global Atmospheric Watch (GAW) station located in the Tenerife Island, Spain (Fig. 3-2) managed by Agencia Estatal de Meteorología (AEMET). Tenerife has a central volcanic caldera that serves as a base for the Teide volcano (3718 m a.s.l.); and the island is divided into two main slopes (northern and southern). IZO station is located on the northern slope, in a high-mountain remote site to the east of this caldera. It is surrounded by forests of endemic species of pine (*Pinus canariensis*) located between 600 and 2000 m a.s.l whose biogenic emissions of particles and gases can be transported to the station. Above

Experimental sites

this altitude the terrain is arid, and few local species of plants can be found (Rodríguez et al., 2009).

The region is influenced by two distinct air mass regimes. The marine boundary layer (MBL), where the trade winds prevail, and the free troposphere (FT), which is typically dominated by descending dry airflows throughout the year. During summer, this pattern is frequently disrupted by the arrival of dust-laden airmasses from the Sahara Desert (Rodríguez et al., 2015). The MBL and the FT are clearly separated by a stable temperature inversion layer (TIL) (Rodríguez et al., 2009). IZO is situated above this TIL, and representative of FT conditions during nighttime (when catabatic winds prevail), whereas during daytime, orographic upward flows transport water vapor and trace gases from the MBL (Rodríguez et al., 2009). The transport of particles and gaseous precursors from the boundary layer are associated with the new particle formation (NPF) events observed at the observatory (García et al., 2014). The top of the MBL is characterized by a layer of stratocumulus and the station usually remains above this layer. The stratocumulus layer creates a foggy and rainy regime at altitudes between 800 and 2000 m a.s.l.



Figure 3-2. Map showing the location of Canary Islands (left panel) and Tenerife Island (right panel) where IZO observatory is located.

3.2 Instrumentation and experimental data

3.2.1 Cloud Condensation Nuclei Counter

A Continuous-Flow Streamwise Thermal-Gradient CCN Chamber (CFSTGC), manufactured by Droplet Measurements Technologies (DMT), was employed for in-situ measurements of CCN concentrations (Roberts and Nenes 2005). It operates by establishing a constant supersaturation (SS) across a cylindrical column (inner diameter 2.3 cm and length 50 cm). A vertical gradient of temperature is applied along the column while the inner surface is wetted with liquid water. The temperature gradient is regulated by three thermal electric coolers (TECs) positioned at different heights (at the beginning, T1, in the middle, T2 and at the end of the column, T3). The total flow is 500 cm³/min; and it is divided into aerosol and sheath flow. In this study, the instrument is operated with a sheath to aerosol flow ratio around 10. Figure 3-3 shows a scheme of the main parts of CCNC. The constant SS established at the centerline of the column depends on the temperature gradient, flow rate and pressure.

This constant SS is achieved as follows. Laminar aerosol flow traverses the column in the up-down direction at the central part of the cylinder. Simultaneously, heat and water vapor are diffused from the inner surface toward the tube's center. Since water molecules diffuse more rapidly than heat, a uniform water vapor supersaturation is achieved along the central axis of the column. Particles with a critical supersaturation lower than the central supersaturation become activated as CCN. During the residence time in the column, activated particles are able to grow into droplets (larger than 1 µm) to be detected and separated from non-activated particles. At the bottom of the column, the CCNC is equipped with an optical particle counter (OPC), which determines the concentration and size distribution of the droplets in the size range 0.75-10 µm. Depending on the supersaturation value (especially at low SS), the residence time in the column might not be enough to enable particles to grow to the required sizes to be detected. Therefore, the temperature gradient along the column is not perfectly linear (the bottom corresponds to the warmest area) (Rose et al., 2008). T2 is slightly higher than it should be to obtain a slightly higher gradient in the first half of the column to restrict the CCN activation to this part and increase the residence time in the second half of the column, ensuring the droplet growth.

CFSTGC (CCN Counter)

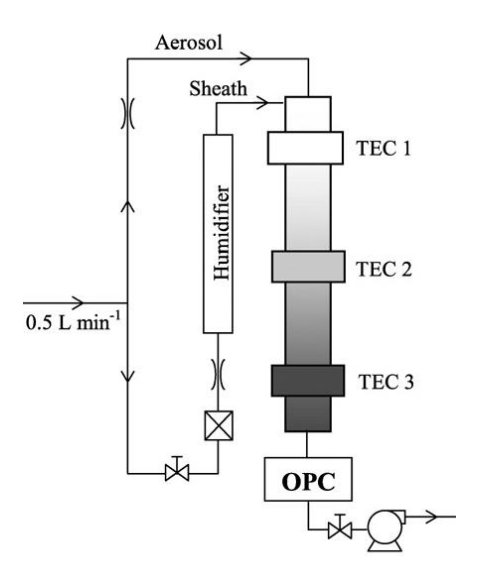


Figure 3-3. Scheme of the main parts of the Cloud Condensation Nuclei Counter. Figure adapted from Lance et al. (2006).

Concerning the physical principles under which CCNC operates generating different supersaturation conditions, they are based on the difference between heat and mass diffusion. Water molecules diffuse more quickly than heat in air since they are lighter than O_2 and N_2 (main air components) whereas heat diffusion depends on air molecules collisions. Heat and water vapor diffuse from the walls of the column in the axial direction to the centerline. However, due to the differences in propagation, the same properties of the walls are reached at the centerline in different points of the axial direction, defined as x_T and x_C for the heat flux and water vapor flux, respectively; and being $x_C < x_T$ because water vapor diffuses faster than heat (Figure 3-4). Hence, temperature and water vapor pressure at the point (0,z) are $T\left(0,z\right)\approx T\left(R,z-x_T\right)$ and $P_{H_2O}\left(0,z\right)\approx P_{H_2O}\left(R,z-x_C\right)$, respectively. In addition, since water vapor is saturated at the walls, $P_{H_2O}\left(R,z-x_C\right)=P_{H_2O}^0\left(R,z-x_C\right)$ where $P_{H_2O}^0$ denotes the saturation

water vapor pressure which increases with temperature. Therefore, the saturation ratio at any point of the centerline of the column, S(0, z), is:

$$S(0,z) = \frac{P_{H_2O}(0,z)}{P_{H_2O}^0(T(0,z))} \approx \frac{P_{H_2O}^0(R,z-x_C)}{P_{H_2O}^0(R,z-x_T)}$$
 Eq. (3-1)

To achieve the last version of Eq. (3-1) we must consider that two points with the same temperature have the same saturated water vapor pressure and remember that water vapor pressure at the wet walls is in fact the saturated water vapor. It should be noted that S(0,z) is greater than 1 (supersaturated condition) because temperature at $(R,z-x_C)$ is higher than $(R,z-x_T)$ due to the vertical temperature gradient. So, this technique allows us to obtain a constant SS value at the centerline of the column.

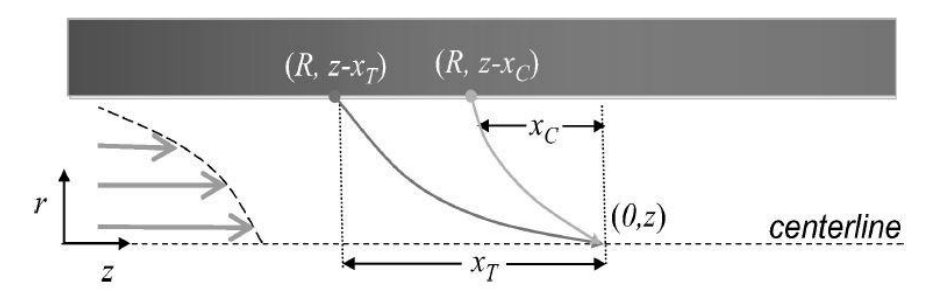


Figure 3-4. Illustration of how a constant supersaturation is established along the centerline of the growth chamber of the CCNC. Figure taken from Roberts and Nenes (2005).

To measure at determined SS values in the column, it is necessary to establish different temperature gradients (controlled, as we mentioned, by TECS) and obtain the correlation between both variables. It implies performing the instrument calibration procedures periodically. To perform the SS calibration, in this thesis we followed the **ACTRIS** standard protocol (available in http://actris.nilu.no/Content/SOP) using size-selected particles of ammonium sulfate. This aerosol flow has been generated by nebulization of an ammonium sulfate solution (0.1 g L⁻¹) using an aerosol generator system (model TSI 3076). The aerosol flow passes through a differential mobility analyzer (DMA) to select specific sizes (40, 60, 80 and 100 nm) maintaining particle number concentrations lower than 3000 cm⁻³ to minimize water vapor depletion effects (Lathem and Nenes, 2011). After this selection, the flow is split into a condensation particle counter (CPC) and the CCNC. The activated fraction (AF) is obtained as the ratio between CCN number concentration (measured with the CCNC) and total particle number concentration (measured with the CPC). For each specific size we performed various SS-scans covering the range between 0.08%-1.0% and obtained the activation curves from the temperature gradients (Figure 3-5 A, between the top and the center of the activation column) defined as $\Delta T = 2(T_2 - T_1)$. To obtain the critical temperature gradient (ΔT_{Crit}) at which half particles activate (AF=0.5) the calibration curves are fit to a sigmoidal function (Moore et al., 2010; Cai et al., 2018) (Eq. 3-2):

$$AF(SS) = \frac{E(SS)}{1 + \left(\frac{\Delta T}{\Delta T_{Crit}(SS)}\right)^{C(SS)}}$$
Eq. (3-2)

where ΔT is the temperature gradient, and E, C and ΔT_{Crit} are fitting coefficients that represent the asymptote (whose maximum value must be 1), the slope and the inflection point of the sigmoid, respectively. The calibration curve is established between the supersaturation and the temperature gradient; therefore, it is necessary to calculate the temperature in the activation column where the growing particles cross the critical activation threshold for each size, defined as activation temperature $\left(T_{act} = \frac{T_1 + T_2}{2}\right)$. Then, theoretical critical supersaturation values of ammonium sulfate for each size and activation temperatures are calculated based on Köhler theory and have been obtained from a lookup-table (Gysel et al., 2002; Topping et al., 2005). A linear correlation between these critical supersaturation and critical temperature values is established, which represent the calibration curve. Figure 3-5 shows the results during a calibration experiment with ammonium sulphate. Figure 3-5 A is referred to activation curves at 40, 60, 80 and 100 nm and Figure 3-5 B shows the correlation between SS and temperature gradients. This calibration curve is introduced into the CCNC software and applied to the data to obtain the correlated SS values.

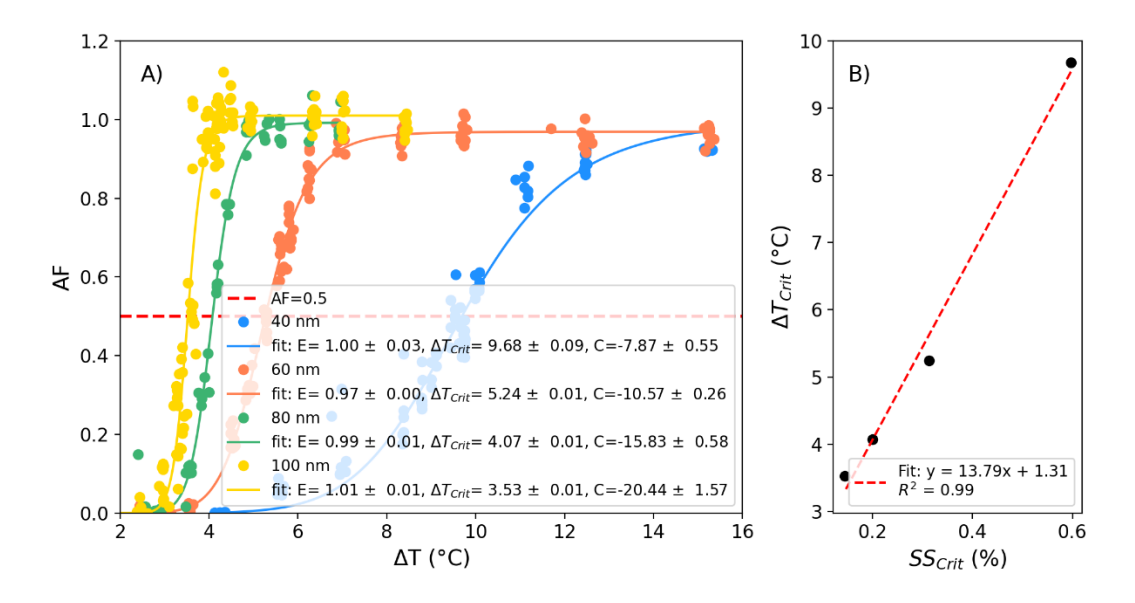


Figure 3-5. Activation and calibration curves of ammonium sulfate during SS calibration experiment. A) shows the activation curves and B) shows the calibration relationship between temperature and SS.

It should be mentioned that the DMT CCNC exhibits kinetic limitations under low SS conditions (<0.1%) that could affect CCN measurements leading to increased uncertainties in SS_{Crit} estimations at low SS (Lance et al., 2006; Yang et al., 2012; Wang et al., 2019). The accuracy in supersaturation is $\pm 10\%$ (relative) when SS are higher than 0.2% and \pm 0.03% (absolute) when SS are lower than 0.2% (http://actris.nilu.no/Content/SOP).

Since the flow rate also affects the SS values inside the column (Rose et al., 2008) a flow rate calibration is also necessary. Aerosol and sheath flows were calibrated using an external volumetric displacement flow meter (Gillibrator-2, Sensidyne) and following the guideline available in the operator manual of the CCNC from Droplet Measurement Technologies. Firstly, aerosol flow is calibrated with sheath flow valve completely closed and adjusting the valve voltage until aerosol flow as measured on the external flow meter is in the range 20-75 cm³/min. A linear correlation between the aerosol flow value observed in the instrument and the aerosol flow measured with the external flow meter is established. Then, sheath flow is calibrated with sheath flow valve completely opened. Valve voltage is adjusted and modified to obtain total flow values measured with the external flow meter from 200-600 cm³/min and real sheath flow is calculated as the

difference between total and aerosol flow. Finally, the linear correlation between the sheath flow given by the instrument and real sheath flow is obtained and introduced in CCNC software. Figure 3-6 shows the calibration curves of sheath and aerosol flow.

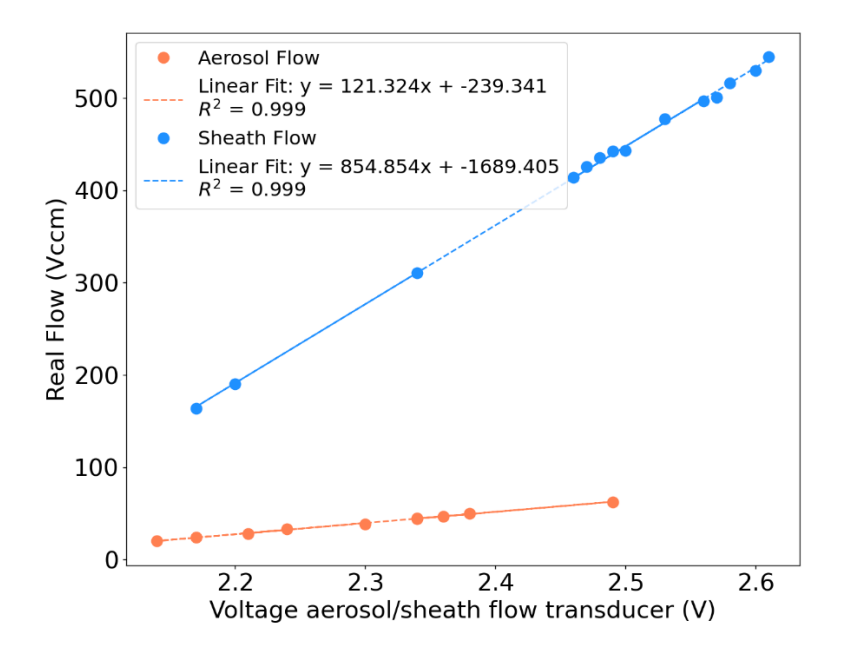


Figure 3-6. Aerosol and sheath flow calibration curves.

Despite obtaining good results during SS and flow calibrations, it is important to highlight that the actual SS measured in the CCNC column might differ from the SS set point configured in the instrument SS schedule. This is due to oscillations in the air sample pressure, air temperature or the signal in temperature controllers that establish the temperature gradients. Also, the CCNC needs some time to stabilize when the SS is changed in the configuration, especially when going from the highest to the lowest SS value. To account for this unstable SS values, we have filtered the data (following ACTRIS guidelines procedures) when the difference between the SS setpoint value and the actual SS in the CCNC column is more than 20%. Additionally, when the total flow deviates more than 5% from the target flow, the data are flagged as invalid, and it is not further used.

Finally, it should be mentioned that two different CCNC models have been used in the framework of this thesis (CCNC-100 and CCNC-200). Both models are based on the same physical principles as explained before, the only difference is

the number of activation columns. Model CCNC-200 has two activation columns (dual-column CCNC) and it has been used during the campaigns at SNS and IZO while the CCNC-100, single-column instrument, has been used for laboratory experiments. For the CCNC-200 calibration procedures must be performed for both columns independently.

3.2.2 Scanning Mobility Particle Sizer

The Scanning Mobility Particle Sizer (SMPS) spectrometer is an instrument that determines the particle number size distribution (PNSD) of submicrometer aerosol particle population. The size classification of aerosol particles is based on their electrical mobility, which is converted to PNSD by a numerical inversion procedure. Most mobility particle size spectrometers consist of a sequential setup of a bipolar diffusion charger (or neutralizer), a Differential Mobility Analyzer (DMA) and a Condensation Particle Counter (CPC). Firstly, the ambient aerosol particles are charged by the neutralizer, producing positive and negative ions by a radioactive or X-ray source. Secondly, the charged aerosol flow passes through the DMA, which selects specific particle size depending on their electrical mobility. A DMA consists of an electrical capacitor with a pair of concentric cylindrical electrodes across which a differential voltage is established. Charged particles are separated according to their electrical particle mobility (Z_p , Eq. 3.3) that depends proportionally on the number of charged particles (n_e), particle charge (e) and the Cunningham factor (C_C) that accounts for non-continuum effects when calculating the drag on small particles, and inversely proportional on particle diameter (D) and gas viscosity (η):

$$Z_{p} = n_{e}e \frac{C_{C}}{3 \pi \eta D}$$
 Eq. (3-3)

Adjusting the voltage between both electrodes in function of DMA's geometry, as well as the sheath and aerosol flow, particles with certain electrical mobility are selected. In addition, varying this differential voltage cyclically, the electrical mobility values can be scanned continuously (Figure 3-7 A shows a scheme of a

SMPS and Figure 3-7 B the cross section of the DMA). Finally, the monodisperse particle number concentration is measured optically by the CPC. In the CPC, the vapor of certain substances such as butanol or water condenses onto particles to grow the nanometer-sized particles to around 10 μ m and be individually counted by a laser optic (particles smaller than 100 nm are not detectable for the laser counter). Figure 3-8 shows a schematic representation of a CPC. It should be mentioned that particles can be multiply charged perturbing their electrical mobility. In this sense, the knowledge of the bipolar size distribution is essential to perform the multiple charge correction and obtain the particle number size distribution (Fuchs, 1963).

Due to the working principles of this instrument that measures the charged particles in an electric field, it determines the PNSD in terms of mobility particle diameter ($D_{\rm m}$). Due to the relevance of this instrument in the framework of this thesis, the term dry particle diameter (D) refers to the mobility diameter, $D_{\rm m}$.

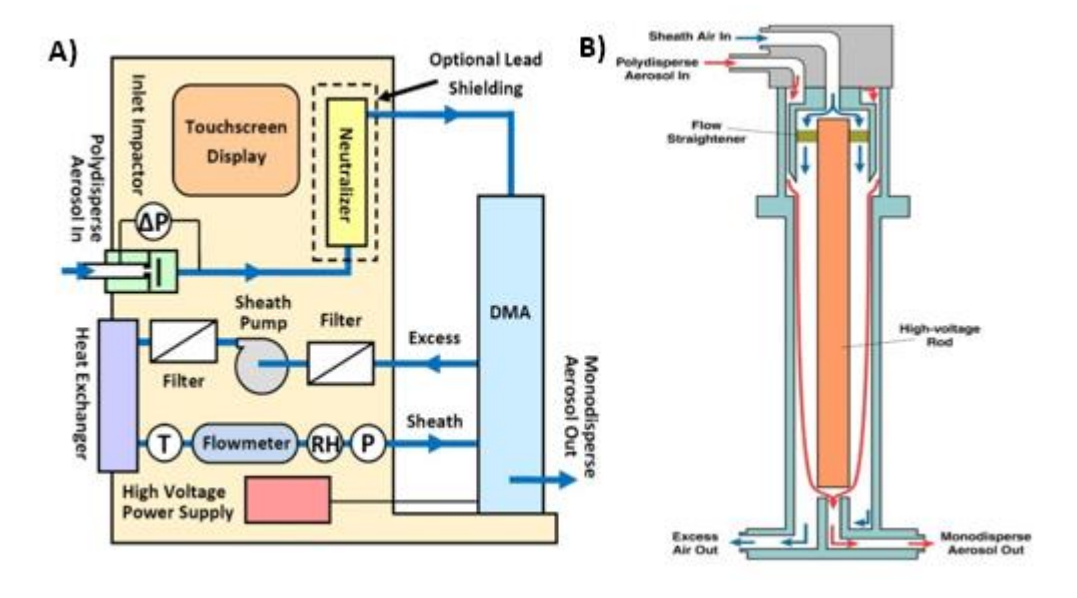


Figure 3-7. A) Schematic representation of the TSI 3938 scanning mobility particle sizer and B) cross section of Long DMA model 3081A. Figures from TSI manual, 2016.

Along this thesis, different SMPS and CPC models have been used. At SNS, the SMPS was equipped with long-DMAs (TSI model 3081), neutralizers (TSI, 3088) and CPCs (TSI model 3750 and 3772) while at IZO, the DMA model was also TSI model 3081, neutralizer 3077A and CPC TSI 3772. The diameter range of aerosol size distribution measurements depends on the combination of the DMA and CPC models used. The minimum particle size detection (defined as the diameter at which 50% of particles are detectable) is established by the CPC model, while the total size selection range is limited by the DMA model and aerosol/sheath flow configuration. At both measurement sites, the PNSD covers the size range 12-535 nm and was obtained by performing scans of 5 minutes length. The SMPSs data have been processed using the AIM software (version 10.3.0, TSI, Inc) provided by the manufacturer. This software applies data corrections derived from multiply charged particles and internal diffusion losses due to the particle's Brownian movement along the instrument tubing. In addition, to achieve the highest accuracy in the measurements of the instrument, the performance of calibration procedures and instrument intercomparisons are performed frequently. During these calibrations and intercomparison procedures additional models of CPC and DMA available in our laboratory have been used (CPC TSI model 3775 and 3776; and DMA TSI model 3083).

The quality assurance procedures are based on 1) calibration of counting efficiency curves related to size-dependence of the CPCs; 2) calibration of the sizing of the DMA using certified polystyrene latex (PSL) particle size standard at 203 nm; and 3) intercomparison between particle number size distributions and particle number concentrations among different units of SMPSs and CPCs. These procedures have been performed periodically at our laboratory, except for the calibration of the counting efficiency curves which are performed by the manufacturers.

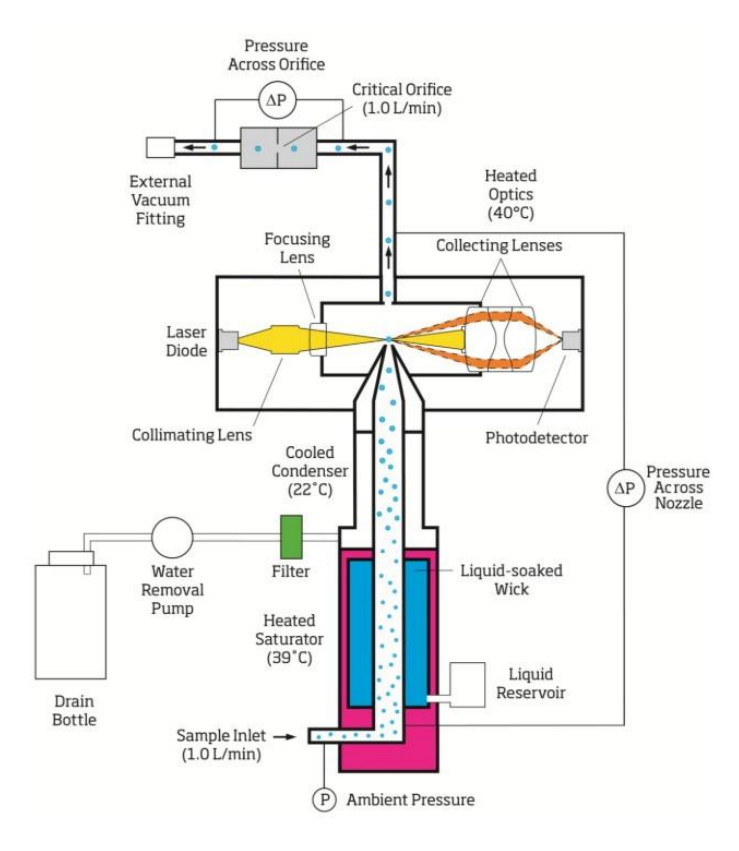


Figure 3-8. Schematic representation of the TSI 3772/3771 Model of CPC. Figure from TSI manual, 2015.

For the sizing calibration of the DMA, we scan the particle size range of a PSL solution from 100 to 400 nm. The geometric mean of the main peak (μ) must be recorded at 203 nm (within 3% of deviation, 197-209 nm). After checking sizing calibration is correct, particle number size distribution intercomparisons between different SMPSs are performed and differences in the size range 20-200 nm must be within 10%. If these differences are larger, possible malfunctions of the DMA could occur due to internal aerosol particle deposition, flow or electric field disturbances (Wiedensohler et al., 2018). In those cases, additional cleaning or replacement of spare parts is performed until a good agreement is achieved. Figure 3-9 shows PSL calibration of the SMPS (1) equipped with DMA 3081 and CPC model 3772 (A) and an intercomparison between three SMPS (B) (1 and 2 with DMAs 3081 and CPC models 3772 and 3775, respectively). The third one (measuring in the size range 10-800 nm) is considered as reference (DMA 3083 and CPC 3750) because it

was acquired and compared just when we received it directly from the manufacturer.

Finally, to keep the instruments in good shape, cleaning and replacements procedures explained in operational manuals from manufacturers have also been performed periodically as well as relative humidity (RH) and flow checks.

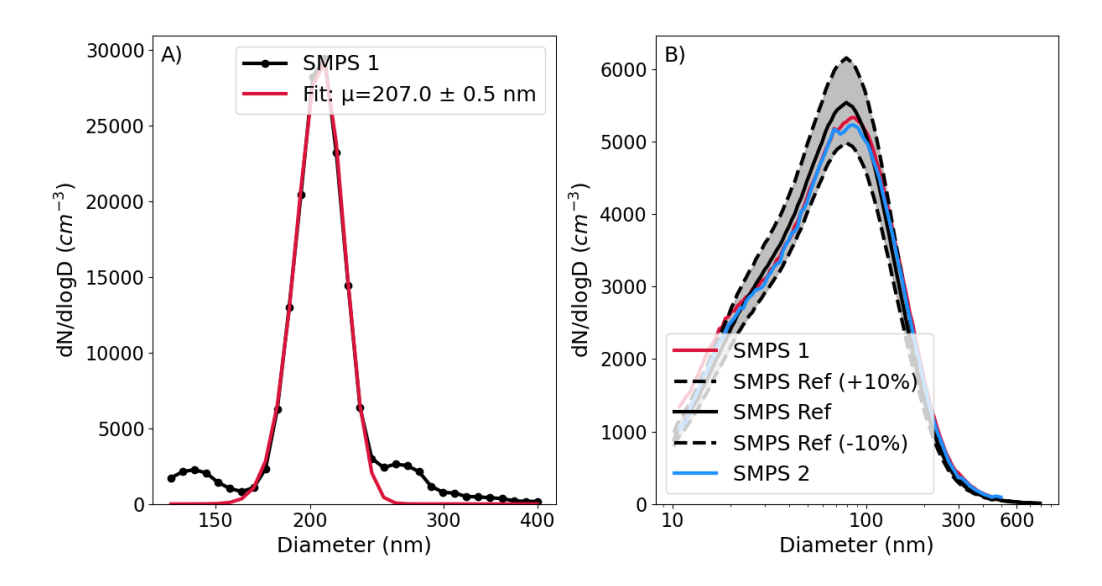


Figure 3-9. A) Results of the sizing calibration of the DMA and B) particle number size distribution intercomparison between different SMPS available at UGR and SNS stations.

Concerning the CPCs, flow checks, cleaning and maintenance procedures available at the operational manuals for users have been performed routinely as well as intercomparison exercises among different units. Different CPC models have different minimum particle size detection. For this reason, the intercomparison exercises have been performed during nighttime (when the concentration of smaller particles in the range of nucleation and fine Aitken mode is lower).

As a final quality check, the total concentration, integrated by the SMPS is compared with the total concentration measured by the stand-alone CPC, and differences must be within 10% (Wiedensohler et al., 2018). Figure 3-10 shows total concentration measured by different CPC models (Fig. 3-10 A) and integrated size-resolved concentration from two different SMPSs and total concentration

from the stand-alone CPC (B). It should be mentioned that the integration range of the SMPSs is from 10 nm to 500 nm, while the lower detection size limit in the CPC model 3776 is <10 nm (therefore, higher concentrations are expected in the CPC than in the SMPSs). In this example, the CPC 3750 and 3776 were considered as reference measurements because the intercomparison exercises were performed just when they arrived at our station after calibration by the manufacturer.

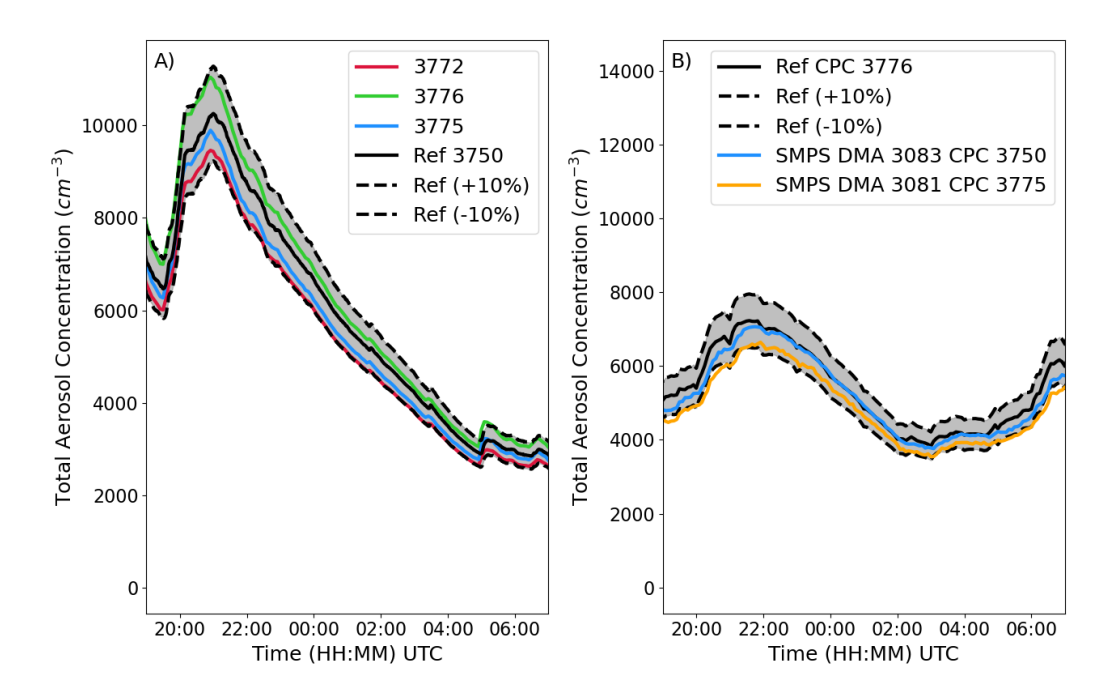


Figure 3-10. A) Total particle number concentration of different CPC models and B) total particle number concentration measured directly from a CPC and obtained by the integration of the aerosol concentration at different sizes, determined by different SMPSs during nighttime intercomparison processes.

3.2.3 Aerodynamic Particle Sizer

The Aerodynamic Particle Sizer (APS) spectrometers are instruments designed to measure particle number size distributions of coarse mode particles (in the size range 600 nm to 20 μ m). Therefore, combining SMPS and APS measurements most of the atmospherically relevant particle size range is covered.

The physical principle of this instrument is based on measuring the particle time of flight between two laser beams. Particles are accelerated through an expansion nozzle and the particle time of flight (dependent on velocity) is converted to an aerodynamic diameter. Then, particles concentration is measured in an optical particle counter. Figure 3-11 shows a schematic representation of the APS (TSI model 3321, which is the model used in this thesis).

This instrument operates at a flowrate of 5 lpm (aerosol flow of 1 lpm and sheath flow of 4 lpm). It should be noted that the uncertainty of particle number size distribution in the range 900 nm up to 3 μ m is within 10%-20%, which is acceptable for atmospheric particles (Pfeifer et al., 2016). However, outside of this size range, the variation and uncertainties could increase, and the particle number size distribution data must be used carefully.

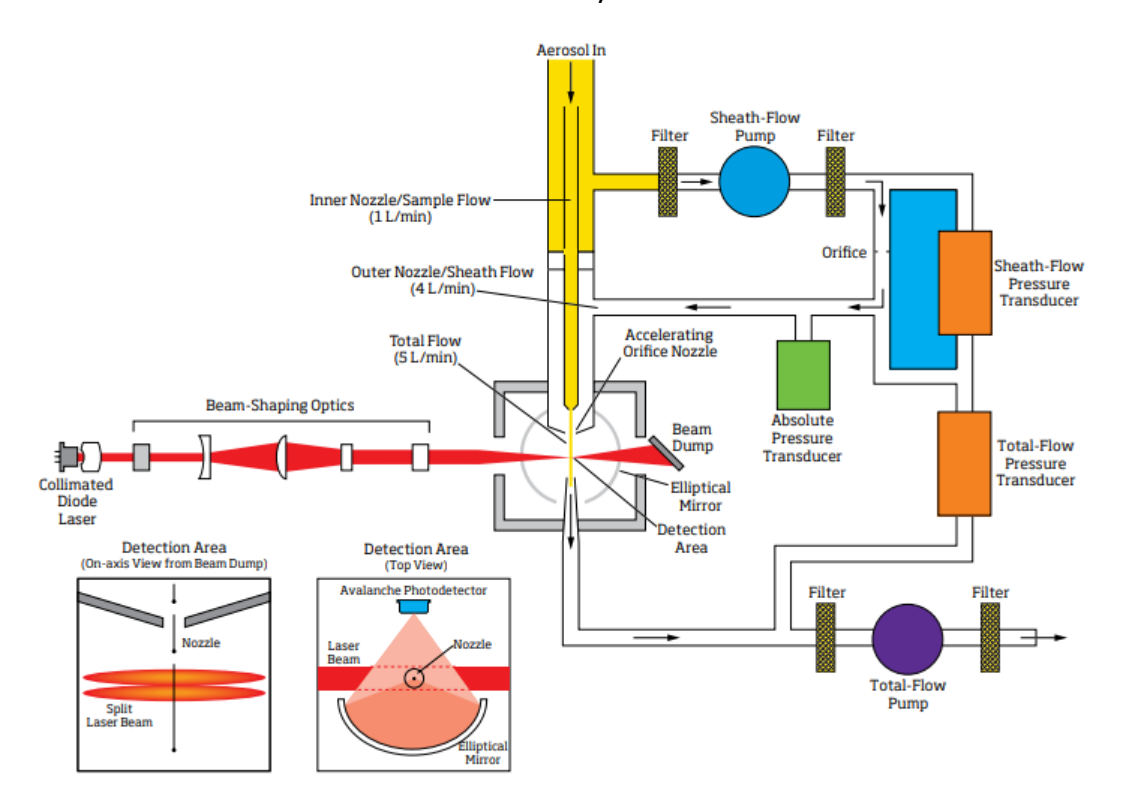


Figure 3-11. The flow schematic for the TSI model 3321 APS. Figure taken from Aerodynamic Particle Sizer TSI manual.

Instrumentation and experimental data

As it has been mentioned in Section 3.2.2 particle diameter is referred to mobility diameter. Therefore, diameters of the particle number size distributions measured with the APS need to be converted from aerodynamic diameter (D_a) to mobility diameters (D_m). The relationship between both types of diameters is dependent on particle density (ρ_{eff}) and shape factor (χ), which are assumed to be independent of particle size. Equation 3-4 shows the relationship between D_a and D_m , where ρ_0 corresponds to the unit density, 1 g/cm³ (Kaaden et al., 2009; Sorribas et al., 2015):

$$D_{\rm m} = \frac{D_{\rm a}}{\sqrt{\frac{\rho_{\rm eff}}{\rho_0 \chi^3}}}$$
 Eq. (3-4)

Depending on the aerosol particles, ρ_{eff} and χ take different values. In this thesis, to convert aerodynamic diameters from the APS to mobility diameters, we have distinguished between dust and non-dust dominated periods. During non-dusty conditions spheric and homogeneous aerosol particles with $\chi=1$ and $\rho_{eff}=1.4$ g/cm³ have been considered (Rissler et al., 2006; Sorribas et al., 2015). In contrast, during dust episodes, χ and ρ_{eff} have been approximated to 1.5 and 2.6 g/cm³, respectively (Hess et al., 1998; Wagner et al., 2009; Sorribas et al., 2015).

4. Methodology

This chapter explains in detail all methods and data analysis tools used in this thesis to achieve the results obtained. First, subsection 4.1 focuses on polydisperse CCN measurements that is the most common approach to measure CCN properties. Subsection 4.2 continues with CCN properties but focuses on size-resolved measurements. Subsection 4.3 shows the comparison between both methods, size-resolved and polydisperse configurations, on CCN concentrations and activation properties. Finally, subsection 4.4 is devoted to the characterization of pollen particles with different laboratory techniques.

4.1 CCN-derived activation properties from polydisperse CCN measurements

Ambient CCN measurements in polydisperse mode (i.e. with no a priori size selection) were performed by doing SS-scans at pre-defined SS values (0.2%, 0.4%, 0.6% and 0.8%). The activated fraction at each SS, is expressed as the ratio between total CCN and total aerosol concentration, N.

$$AF (SS) = \frac{CCN (SS)}{N}$$
 Eq. (4-1)

The effective critical diameter (D_{Crit}) for an aerosol population can be defined as the dry diameter above which all aerosol particles are activated (Kammermann et al., 2010). At a certain SS the effective D_{Crit} can be derived from PNSD and CCN (SS) measurements:

$$CCN (SS) = \int_{D_{Crit}(SS)}^{D_{upper}} \frac{dN}{dlogD} dlogD$$
Eq. (4-2)

where D is the particle diameter and D_{upper} is the upper limit of the PNSD. In this way, the PNSD is integrated from the D_{upper} value to a certain diameter at which the integral value equals the simultaneously measured polydisperse CCN (SS) concentration. This diameter corresponds to $D_{Crit}(SS)$ and is defined as the stepfunction activation cut-off diameter, assuming perfectly internally mixed aerosol population with identical chemical composition (e.g., Jurányi et al., 2011; Paramonov et al., 2015; Schmale et al., 2018). Thus, all particles with $D > D_{crit}(SS)$ will activate at SS, while particles with $D < D_{Crit}(SS)$ will remain unactive.

The hygroscopicity parameter κ , characterizes the hygroscopicity of a specific aerosol particle and is related to its chemical composition. However, an effective hygroscopicity parameter can be defined for the whole aerosol population from PNSD and polydisperse CCN measurements using κ -Köhler theory. This effective κ , also known as CCN-derived κ , quantifies the effective hygroscopicity of the activated particles in the CCNC and as it was mentioned, shows a dependence with SS. Thus, the effective κ gives information about the hygroscopicity in a certain size range depending on the SS value. Eq. 2-8 is solved numerically to calculate κ values, considering the effective $D_{Crit}(SS)$ as the dry diameter (D) of the Köhler curve. κ and the droplet diameter, $D_{droplet}$ are varied until the supersaturation is equal to the SS prescribed in the CCNC and corresponding to the maximum value of the Köhler curve of CCN activation (Rose et al., 2010). This effective CCN-derived κ in polydisperse mode and calculated from D_{Crit} will be referred in this thesis as κ .

4.2 CCN-derived activation properties from sizeresolved CCN measurements

Size-resolved CCN measurements allow to know the specific size at which particles are activated as CCN. The experimental configuration to obtain the CCN size distributions consists in the size-selection of aerosol particles in a DMA (TSI model 3081, in our experimental configuration used in Chapter 7). Then, the monodisperse flow is split to feed into a CPC (in our case a TSI model 3750, 1 L min⁻¹) and one of the CCNC columns (0.5 L min⁻¹). The SMPS-CPC provides the size-resolved particle number concentration and the CCNC provides the number of particles activated as CCN at each specific size.

The results presented in Chapter 7 were obtained based on diameter scans (D-scans) that were performed from 12-535 nm every 5 minutes; and in the CCNC, the SS was held constant during 2 D-scans (10 minutes) for each SS (SS =0.2%, SS=0.4%, SS=0.6% and SS=0.8%). Both CCNC columns (mono- and polydisperse) were measuring simultaneously at the same SS (0.2%, 0.4%, 0.6% and 0.8%). It should be mentioned that occasionally, only one out of the two diameter scans provided valid data with constant SS during the complete scan due to imperfect time synchronization between the SMPS and the CCNC.

The activated fraction for each scan at a fixed SS is calculated as the ratio between CCN and aerosol concentration (N) at each size diameter (Eq. 4-3):

$$AF (D,SS) = \frac{\frac{dCCN (D,SS)}{dlogD}}{\frac{dN(D)}{dlogD}} = \frac{dCCN(D,SS)}{dN (D)}$$
Eq. (4-3)

These activation curves are fitted to a sigmoidal function similar to Eq. 3-2, but in this case, the independent variable is the dry particle diameter (D) (Eq. 4-4) (Moore et al., 2010; Cai et al., 2018):

AF (D, SS) =
$$\frac{E \text{ (SS)}}{1 + \left(\frac{D}{D_{50}\text{ (SS)}}\right)^{C(SS)}}$$
 Eq. (4-4)

The inflection point of the sigmoid corresponds to the critical diameter, defined in this case as the diameter at which 50% of particles are activated as CCN (D_{50}), at a certain SS. The coefficients E and C represent the asymptote (maximum value of activation that must be 1) and the slope of the sigmoid, respectively. D_{50} is used (as previous D_{Crit} values obtained from polydisperse measurements) in Eq. 2-8 to obtain the CCN-derived hygroscopicity parameter, denoted in this case as κ_{50} (from size-resolved CCN measurements), as it has been explained in previous section 4.1. It should be noted that the time-resolution of D_{50} and κ_{50} retrievals is 3 hours because the sigmoidal fits have been performed over averaged AF to reduce noise (higher time resolution resulted in noisy AF curves).

An important aspect of size-resolved CCN measurements is the time-alignment between data from both instruments (CCNC and SMPS). This was done following Moore et al. (2010) method (matching the minimum in counts that occurs during the transition between diameter up-scan and down-scan). Only those D-scans performed at constant SS in the CCNC were further consider for analysis of the size-resolved CCN spectra. Figure 4-1 A shows an example of one D-scan (at SS=0.4%) of particle number concentration and size-resolved CCN concentration with different time alignments, and the corresponding activated fraction curves, AF (D) (Figure 4-1 B).

For verifying the correct time alignment, different time shifts (t ± 2 s and t ± 5 s) were considered. The optimal alignment is obtained based on the coincidence in the peak (observed at around 4 minutes in Figure 4-1A) and the behaviour of the AF (D). Figure 4-1B shows the activation curves obtained for each time alignment. The correct alignment is observed at time, t within an error range of ± 2 seconds. At t $\pm > 2$ seconds, the activation curves suffer deviations, and sigmoidal fits cannot be performed correctly.

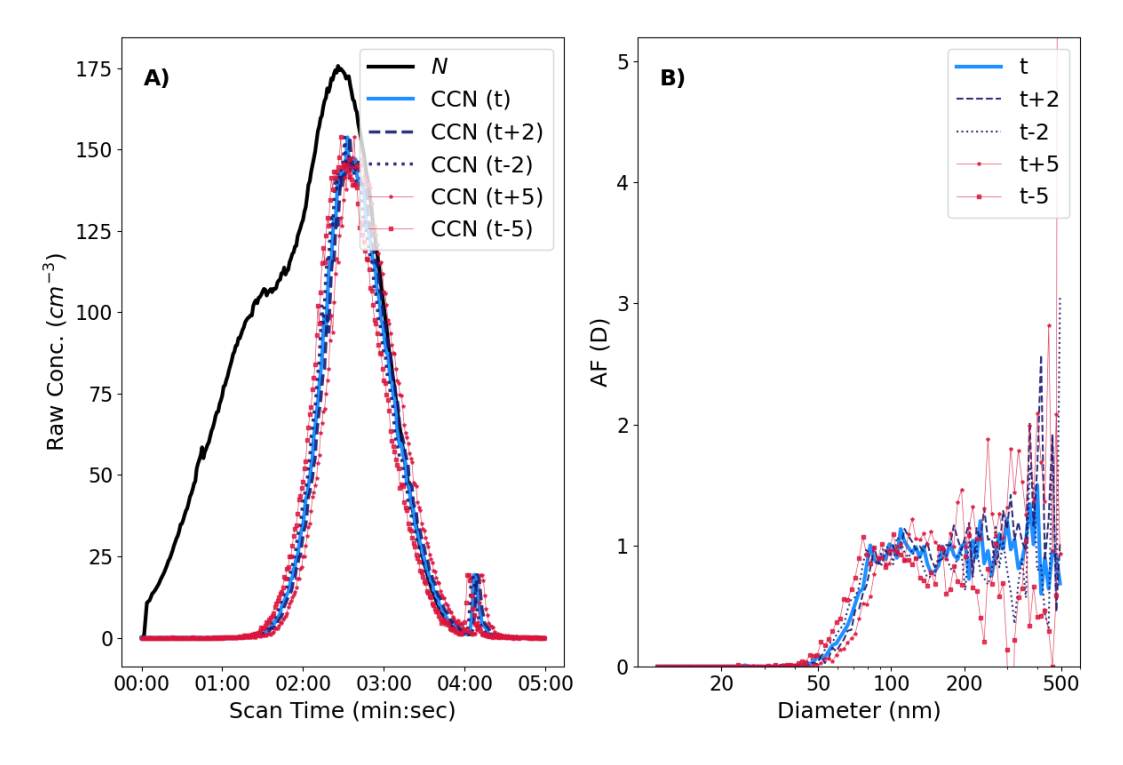


Figure 4-1. Time alignment of one scan between SMPS and CCNC. A) Aerosol and CCN (at SS=0.4%) particle number size distributions with different time alignments. B) Activated fraction curves at SS=0.4% at these time alignments. Solid black line (in A) is referred to aerosol size distribution. In both subplots, solid clear blue line corresponds to the correct time alignment at time t (A, CCN size distribution and B, AF curve). In the same way, dashed dark blue lines correspond to the alignment at time t+2 and t-2 seconds. Dotted red lines are referred to the curves with the alignment t+5 and t-5 seconds.

Table 4-1 shows the parameters obtained from the sigmoidal fits at each time alignment. It should be noted that it was not possible to obtain a good sigmoidal fit for the alignment t-5 s due to the deviation in activation curve. At t+5 seconds, activated fraction curve does not reach a stable plateau close to 1 (E > 1) which is expected at diameters sufficiently large of wettable particles. On the other hand, D50 differs from the value obtained from the correct alignment ~35%. In contrast, we observe similar values of the parameters at t and t \pm 2 seconds. The errors obtained from the sigmoidal fits are within the deviations obtained from the timealignment.

the fit.			
Time alignment (s)	$E \pm \Delta E$	$D_{50}\pm\Delta D_{50}$ (nm)	$C \pm \Delta C$
t	0.953 ± 0.016	68.8 ± 1.2	-10.6 ± 1.7
t+2	1.13 ± 0.04	72 ± 4	-9.8 ± 1.8
t-2	0.92 ± 0.04	65 ± 4	-11 ± 5
t+5	1.53 ± 0.07	103 ± 6	-2.9 ± 0.4
t-5	-	-	-

Table 4-1. Parameters of the sigmoidal fit applying Eq. 4.4 to the respective activated curves at different time alignments. Error values for each parameter correspond to errors obtained from the fit.

After time-alignment of the raw datasets from both instruments, data inversion was performed following the scheme of Petters et al. (2009) to obtain the aerosol particle number size distribution and CCN size distribution. Data inversion does not require any a priori knowledge related to chemical composition, and it accounts for the presence of multiple charged particles, DMA transfer probability, and CPC efficiency. Finally, raw and inverted data (from PNSD and CCN size-distributions) are correlated through the inversion matrix which correct these measurements. The integration of these distributions results in total aerosol number concentration (N) and total CCN number concentration in the diameter range 12-535 nm (approximately fine mode concentration). Thus, the total CCN concentration obtained in this way should be similar to total CCN concentration measured using polydisperse mode if the contribution of coarse particles acting as CCN is negligible.

4.3 Comparison of size-resolved and polydisperse CCN approaches

As explained in sections 4.1 (polydisperse CCN measurements) and 4.2 (size-resolved CCN measurements), different activation properties are obtained from both approaches. In principle, both methods should provide similar results especially under the assumption of a homogenous and internally mixed aerosol population (Jurányi et al., 2013). In this section we show a comparison between both methods for total CCN concentration and activation properties (AF, D_{Crit} - D_{50}

and κ - κ 50) at SS=0.4% (Figure 4-2). The measurements were performed during a summer field campaign at SNS from 24th June to 12th July 2021.

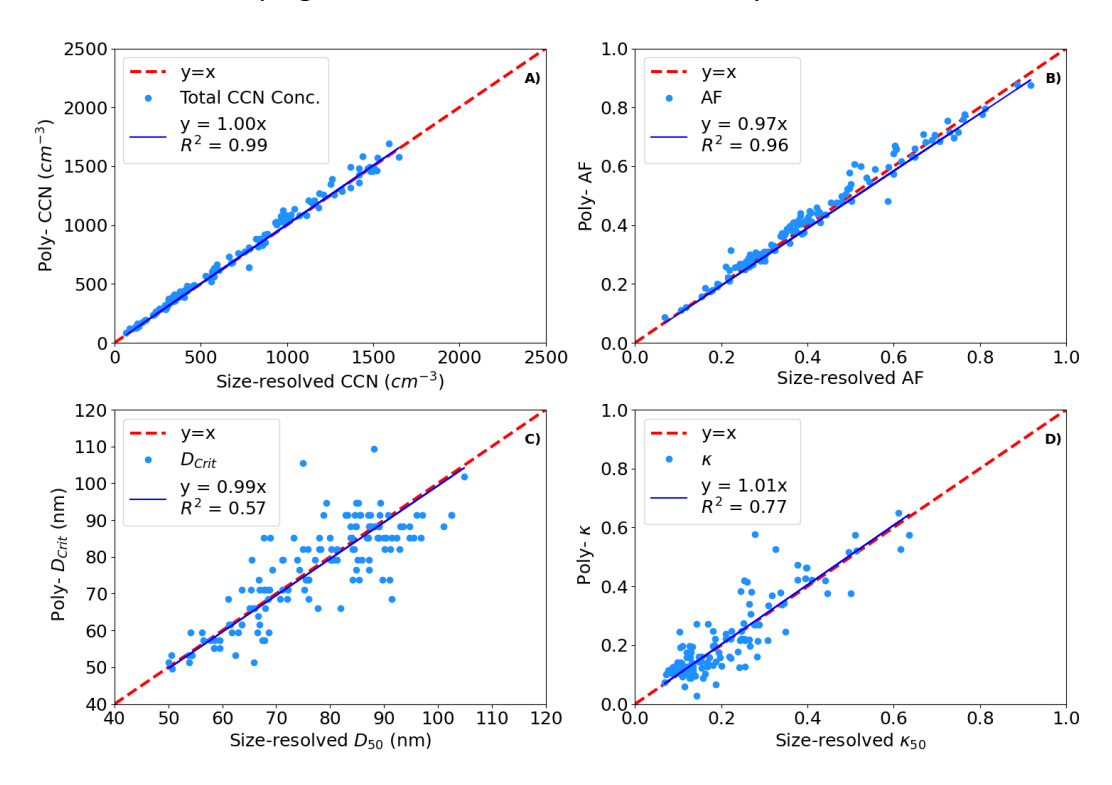


Figure 4-2. Linear correlations of parameters derived from size-resolved and polydisperse data throughout the campaign (24^{th} June -12^{th} July) at SS=0.4% with time resolution of 3 hours: A) Total CCN concentration B) Activation Fraction (AF) C) D_{Crit} - D_{50} and D) κ - κ_{50} .

Figure 4-2 shows the relationships between total CCN concentration and activated fraction from size-resolved and polydisperse modes and the relationships between D_{Crit} - D_{50} and κ - κ_{50} . Better correlations are reported for CCN and AF (slopes and R^2 show values very close to 1) because they are direct measurements but performed with two different experimental approaches. The integration of size-resolved CCN measurements in the size range 12-535 is expected to be similar to total CCN concentration measured in polydisperse mode if the number particle concentration larger than 535 nm active as CCN is negligible. Previous studies (e.g. Moore et al., 2010; Jurányi et al., 2013) also reported similar slope and R^2 values in the correlation of total CCN concentration. In the case of D_{Crit} and D_{50} and therefore, κ - κ_{50} , R^2 values are slightly lower (0.57 and 0.77, respectively) since they actually represent different aspects of activation (Kuwata et al., 2008).

4.4 Pollen Characterization

4.4.1 Pollen sampling and SPP generation

Fresh pollen samples of common plant species characteristic of Mediterranean climate were collected directly from trees in the Granada area. It should also be noted that some of these pollen species has been found in Canary Islands; probably transported from Mediterranean areas (Izquierdo et al., 2011; de Nascimento et al., 2015). In this thesis, we focus on 10 pollen types collected during the flowering season in 2021, one sample collected in the flowering season in 2019 and store in the refrigerator, as well as one commercial pollen sample (Reference product P7395-1G, Merck). For the fresh pollen samples, after collection, samples were stored for two days at room temperature to dry them out. Later, they were sifted to separate pollen from flowers and spurious particles. Finally, each pollen sample was stored in a refrigerator at 4 °C. Organic pollen solutions were prepared by adding 0.5 g of pollen to 300 mL of ultrapure water (Milli-Q, 0.054 μS) and shaking mechanically for 15 seconds to allow pollen grains to break into subpollen particles (SPP) (Steiner et al., 2015). Rupture of pollen grains was confirmed by Scanning Electron Microscopy (SEM; ZEISS operating at 5 kV accelerating voltage and 2.9 mm working distance). SPP dispersions were left in the refrigerator at 3 °C for 1 hour and then filtered three consecutive times using 47 mm diameter quartz microfibers filters with 0.45 µm pore size (Pall Corporation, New York, USA) to remove any large pollen particles. These solutions were then used for the analysis described below.

4.4.2 Cloud condensation activity of size-selected SPPs

The filtered solutions of each pollen sample were aerosolized using an Aerosol Generator (TSI 3076) and passed through a diffusion dryer connected to a small dilution chamber to stabilize the generated particle number concentrations. In this case, we used the scanning mobility particle sizer (SMPS, TSI 3938), with the neutralizer (TSI 3088) and DMA, model TSI 3081A. Subpollen particles (SPPs) with electric mobility diameter sizes of 80, 100 and 200 nm were selected. Then, the aerosol flow was split between the CPC (TSI 3372, 1 L min⁻¹) to provide the total particle number concentration (N) for each selected size (a concentration of

around 2000-4000 particles cm⁻³ was maintained) and the CCNC (DMT model CCN-100 with one activation column, 0.5 L min⁻¹) to provide the number of particles that are activated (CCN) at each selected size.

For each selected diameter (80, 100 and 200 nm), the SS was scanned over 10 different SS values (Table 4.2 shows the SS used for each particle size), taking 5 min at each SS. Despite the larger uncertainties and limitations mentioned before at SS<0.1%, the SS table for 200 nm particles includes SS values below this limit. This was necessary to determine the SS_{Crit} for large SPPs that was expected to be between 0.05 and 0.12%.

Size (nm)	SS (%)									
200	0.01	0.02	0.04	0.06	0.08	0.1	0.2	0.4	0.6	0.8
100	0.1	0.15	0.2	0.22	0.25	0.28	0.3	0.4	0.6	0.8
80	0.1	0.15	0.2	0.24	0.28	0.3	0.34	0.38	0.5	0.8

Table 4-2. SS values selected to study the activation for SPPs of 200, 100 and 80 nm.

To obtain the critical supersaturation, SS_{Crit} , it is necessary to know the activated fraction (AF, ratio between CCN and N concentration) at different SS values; and the obtained activation spectra at each size is fitted to a cumulative Gaussian distribution as function of supersaturation (Rose et al., 2008; Mei et al., 2013; Thalman et al., 2017); similarly to sigmoidal fit performed during the calibration procedure of the CCNC described in section 3.2.1.

$$AF(SS) = a \left(1 + erf\left(\frac{SS - SS_{Crit}}{\beta\sqrt{2}}\right) \right)$$
 Eq. (4-5)

where a is half the maximum value of AF (ideally 0.5), erf is the error function, β is the standard deviation of the cumulative Gaussian distribution and SS_{Crit} is the value of supersaturation when AF is 0.5. We retrieved the experimental values of SS_{Crit} from this fit and then, the hygroscopicity parameter, CCN-derived κ value (also referred as κ) for each pollen type was determined following κ -Köhler theory and Eq. (2-8). In this case, D values correspond to dry diameters (80, 100 and 200

nm) and κ and $D_{droplet}$ values were varied until reach the maximum value of the Köhler curve at experimental SS_{Crit} values obtained from Eq. 4-5.

4.4.3 Surface tension analysis

As it has been mentioned in section 2.2.3, water surface tension value is a good approximation in κ-Köhler theory if droplets are diluted enough and do not contain surface-active compounds. However, it is known that pollen particles are mostly composed by organic matter that is able to reduce surface tension, σ (Axelrod et al., 2021). Therefore, to study this behaviour and its implications on the CCN activation, the surface tension of pollen solutions was measured using a Pendant Drop Tensiometer developed at the University of Granada (Cabrerizo-Vílchez et al., 1999). Sample preparation was performed following the procedure explained in Sect. 4.4.1. Due to variation in filtration efficiency of the different pollen types, the actual concentration in the solutions differs among pollen species. These actual concentrations were calculated by placing 100 μL of the solutions on aluminium foil surfaces, evaporating the water in a furnace (at 60 °C for 1 hour) and weighing the resulting sample. The initial concentrations (prior to the filtration process) of the solutions species were 5 g/L and 50 g/L, depending on the filtration efficiency of each pollen type. These solutions were then diluted 10, 100 and 1000 times in ultrapure water.

Once solutions were prepared, the experimental setup was used to measure surface tension values of each sample. Additionally, to ensure that there were no contaminant substances, the surface tension of pure water (σ_w) was measured between each pollen solution yielding the expected value of 72.5 \pm 1.5 mN/m at room temperature (23 °C) (Maldonado-Valderrama et al., 2004). The pendant drop technique consists in acquiring the silhouette of an axisymmetric fluid droplet and takes multiple images of the pendant drop at different instants in time, capturing the variations of the droplet shape as the surface tension changes.

The system is based on a CCD (Charge-Coupled Device) video camera (Pixelink) connected to an optical microscope (Edmund Optics), a diffused light source to avoid aberrations and spurious reflections and a microinjector (Hamilton PSD3 Half-Height Syringe Pump) connected to a Teflon capillary where the pendant

drop of solution is formed. The whole experimental setup is computer controlled by the software DINATEN© (University of Granada) which processes the digitized images of pendant drops. A schematic of the experimental setup is shown in Figure 4-3.

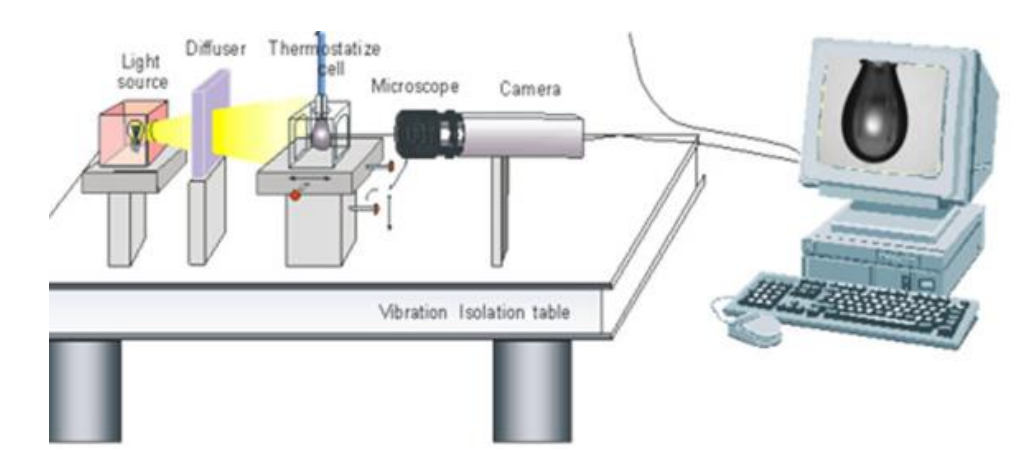


Figure 4-3. Scheme of the experimental setup of Pendant Drop Tensiometer at University of Granada. Figure taken from Maldonado-Valderrama et al. (2021).

4.4.4 Organic chemical analysis

Due to the organic nature of the different pollen types (Axelrod et al., 2021; Bahdanovich et al., 2024), the organic chemical composition of different pollen species was analysed for their saccharide and organic acid content at the Institute of Environmental Assessment and Water Research (IDAEA-CSIC). Twenty five μL of surrogate standards levoglucosan-d7 (Cambridge Isotopic Laboratories, UK) and succinic acid-d4 (Sigma Aldrich) were added to a vial (Merck, Darmstadt, Germany) to which between 0.1–20 mg of pollen in 0.5 mL of methanol was added (Medeiros and Simoneit, 2007). Extraction was done in an ultrasonic bath for 15 minutes.

After extraction, the sample was transferred to a vial and evaporated to dryness under a N₂-gas stream. Then, 25 μ L of bis (trimethylsilyl)trifluoroacetamide (BSFTA)+trimethylchlorosilane (99:1) (Supelco) and 10 μ L of pyridine (Merck) were added for derivatization of the polar compounds to their trimethylsilyl esters at 70 °C during 1 h. Before analysis, 100 μ L of isooctane was added to the vial. Sample extracts were injected into a gas chromatograph coupled to a mass spectrometer

(Thermo Trace GC Ultra – DSQ II) equipped with a 60 m fused capillary column (HP-5MS 0.25 mm \times 25 μm film thickness). The oven temperature program started at 60 °C held for 1 min, and then heated at 12 °C/min to 120 °C and to 320 °C at 4 °C/min, where it was held for 15 min. The temperatures of the injector, ion source, quadrupole and transfer line were 280 °C, 200 °C, 150 °C and 280 °C, respectively. Helium was used as a carrier gas at 0.9 mL/s. The MS selective detector was operated in full scan (m/z 50–650) and electron impact (70 eV) ionization modes. Compounds were identified with authentic standards and the corresponding retention times in the chromatograms (Fontal et al., 2015). The recoveries of the surrogate standards were higher than 70% in all samples. Analytical blank levels were lower than 1% of the sample levels. Limits of quantification (LOQ) were calculated by dividing the lowest measured levels in the standard calibration curves by the mass of the analysed sample fraction. These were 0.4 ng/mg for the saccharides and 0.06 ng/mg for the acids.

Additionally, the protein content of these different pollen samples was also analysed at Research Support Central Service of the University of Córdoba (Spain). Each pollen type was dissolved as explained in Sect. 4.4.1 with the same concentration, matching that used to generate SPPs. Protein content in the solutions was determined using the "Bradford assay" method (Bradford, 1976). It consists of a protein quantification technique based on variation in absorbance produced by the colour change of Coomassie Brilliant Blue G-250 (Bio-Rad Protein Assay). The maximum absorbance of the dye changes from 465 nm to 595 nm, when it is linked to the protein. The absorbance at 595 nm is directly proportional to the protein concentration in the sample. Therefore, the calibration curve was obtained using Bradford reactive (Bio-Rad Protein Assay Dye Reagent concentrate, 450 mL, #5000006) and known concentrations of a standard protein. Then, the protein content in each sample was determined by measuring the absorbance of each solution at 595 nm using this calibration curve.

5. Cloud condensation nuclei activation properties of Mediterranean pollen types: a laboratory study

This chapter has been adapted from "Cloud condensation nuclei activation properties of Mediterranean pollen types considering organic chemical composition and surface tension effects" by A. Casans, F. Rejano, J. Maldonado-Valderrama, J.A. Casquero-Vera, S. Ruiz-Peñuela, B.L. van Drooge, H. Lyamani, A. Cazorla, E. Andrews, Jack J. Lin, F. Mirza-Montoro, D. Pérez-Ramírez, F.J. Olmo, L. Alados-Arboledas, P. Cariñanos and G. Titos. Published in Atmospheric Environment, Volume 310, 1 October 2023, 119961.

This chapter analyses the activation properties of different pollen types, characteristic of the Mediterranean region and some of them, of the Canary Archipelago (Cupressus sempervirens, Dactilys glomerata, Olea europaea, Pinus spp., Platanus hispanica, Acer negundo, Fraxinus angustifolia, Populus nigra and Quercus rotundifolia). Ambient pollen samples were collected and analyzed following the methodology explained in subsection 4.4. Here, we first present the results of the calculated SS_{Crit} and κ values for all types of subpollen particles (SPPs) at different sizes (80, 100 and 200 nm in diameter); and link the activation properties to their organic chemical composition and solubility. Then, the capability of SPPs to reduce surface tension (σ) and act as surfactant have also been explored to determine if the use of the surface tension of water (σ_w) in κ -Köhler theory is suitable for organic aerosol particles such as pollen. This study is approached from laboratory experiments due to the difficulty of performing ambient measurements of pollen and SPPs in the atmosphere, isolated from other aerosol particles. This is due to their low number concentration compared to other atmospheric aerosol particles, the lack of standardized measurement techniques to distinguish pollen from other particles, and the seasonal nature of tree species that release pollen into the atmosphere.

5.1 Activation properties: Critical supersaturation and hygroscopicity

Figure 5-1 shows the measured CCN activity (i.e., critical supersaturations) of SPPs of 11 pollen samples of different dry size (80, 100 and 200 nm diameter) together with the calibration points of ammonium sulphate and the theoretical range of SS_{Crit} for this substance as a reference for hygroscopic particles according to Gysel et al. (2002) and Topping et al. (2005). As well as the pollen types mentioned above, that were collected during flowering season 2021, we also analysed pollen samples of *Olea europaea* collected in 2019 and commercial samples of *Populus* (tree pollen *Populus deltoides*, Reference product P7395-1G, Merck). All SPPs studied exhibited similar activation ability, with slight differences among different species. The SS_{Crit} values obtained for all pollen types correspond to supersaturations values that can be found in the atmosphere, which evidence that the SPPs analysed here can act as cloud condensation nuclei at atmospherically relevant conditions.

The obtained SS_{Crit} range between (0.07 - 0.12)%, (0.17 - 0.28)% and (0.25 -0.37)% for 200 nm, 100 nm and 80 nm particle diameters, respectively (Fig. 5-1). SS_{Crit} uncertainties have been calculated as the standard deviation of the SS_{Crit} values obtained by varying the measured SS within its range of uncertainty (±10% relative for SS>0.2% and ± 0.03% absolute for SS<0.2%) (Schmale et al., 2017). SScrit values obtained in this study are in the lower range of previously reported values by Steiner et al. (2015) and Mikhailov et al. (2019). The studies mentioned before investigated a lower number of common pollen types from United States and Central Europe, respectively, while here we explore the activation ability of 10 different species characteristics of the Mediterranean area. Our results show that SS_{Crit} values depend mainly on the SPP size, however, differences are observed among species for each size indicating different CCN activity for each pollen type. Quercus is the pollen type with the highest SScrit values for all sizes, denoting its lower activation ability. The highest activation ability is found for those pollen types with the lowest SScrit: Populus nigra for 80 nm, Populus deltoides for 100 nm and Cupressus for 200 nm.

Cloud condensation nuclei activation properties of Mediterranean pollen types: a laboratory study

Figure 5-1 also shows that the two *Olea* pollen samples investigated exhibit different activation behaviours, especially at 100 nm (SS_{Crit} values are 0.23% for *Olea* 2021 and 0.19% in *Olea* 2019) and 80 nm (0.33%, *Olea* 2021 and 0.28%, *Olea* 2019). This could indicate that *Olea* collected in 2019 might have experienced some chemical degradation, in some of its organic components, over time affecting its CCN activity. On the other hand, *Populus nigra* and *Populus deltoides* have almost indistinguishable SS_{Crit} values for all sizes. SS_{Crit} values for *Populus nigra* (noncommercial) are 0.25%, 0.17% and 0.07% for 80, 100 and 200 nm, respectively. *Populus deltoides* (commercial) yields SS_{Crit} values at 80, 100 and 200 nm of 0.26%, 0.17% and 0.07%. *Populus deltoides* properties might differ from natural ambient pollens due to the commercial sample preparation, however, the analogous SS_{Crit} values obtained for both indicate that using commercial pollen types to investigate CCN activation properties provides similar results as the natural samples, at least for these species.

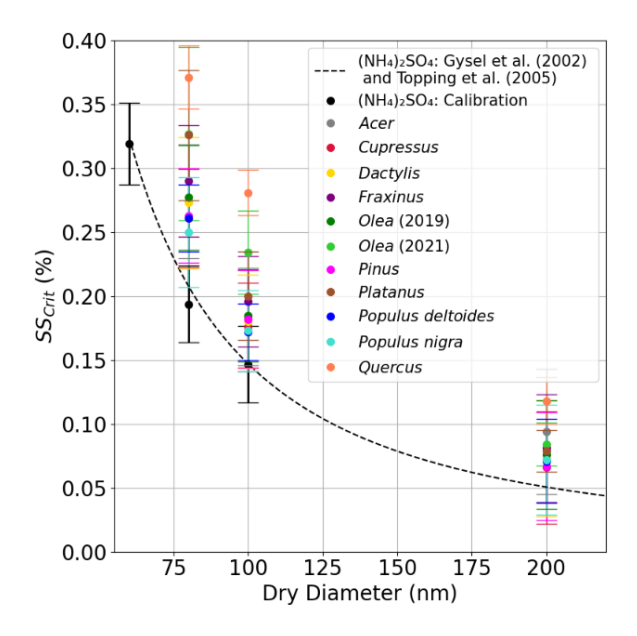


Figure 5-1. Critical supersaturations (SScrit) of the 11 analysed pollen samples at different dry diameters (80, 100 and 200 nm). Error bars for each pollen type correspond to the standard deviation of SScrit calculated considering the uncertainties in measured SS (see the text for further detail in uncertainty calculation). Black line represents the theoretical range of SScrit for ammonium sulfate ((NH₄)₂SO₄) (Gysel et al., 2002; Topping et al., 2005), black points are SScrit values of (NH₄)₂SO₄ obtained during CCNC calibration at 60, 80 and 100 nm and their respective error bars that have been calculated considering SS uncertainties (\pm 10% for 60 nm and \pm 0.03% absolute SS for 80 and 100 nm).

Low SS values should be analysed with caution due to potential constraints of the CCNC at these SS conditions. As we have mentioned above (Section 3.2.1), the CCNC exhibits kinetic limitations related to droplet growth. In the CCNC measurements, the CCN identification criteria is based on a threshold diameter (0.75 µm) from which all particles are considered activated (https://dropletmeasure.wpenginepowered.com/wp-

content/uploads/2020/02/DOC-0086-Rev-N-CCN-Manual.pdf). However, unactivated particles may also grow to such a diameter due to hygroscopic growth. Using this default cut off diameter can lead to 30% overestimation of the bulk CCN number concentration measurements for SS lower than 0.1% (Yang et al., 2012; Tao et al., 2023). Furthermore, there are higher uncertainties in the CCNC column temperature gradient at low SS (<0.05%). The accuracy in supersaturation is ±10% (relative) when SS are higher than 0.2% and ΔSS≤0.03% (absolute) when SS are lower than this value (http://actris.nilu.no/Content/SOP). In this study, SS<0.05% have been used to determine SScrit (see SS table, Table 4.2) and results for 200 nm particles show SScrit values are within the range 0.07-0.12%. To check for deviations in the estimated SScrit at this size due to potential CCNC overcounting issues, we have re-calculated the SS_{Crit} assuming an overestimation of 30% at SS<0.1% and the analysis determined that the SScrit values were within the estimated uncertainty. This 30% overestimation is expected to be lower for organic particles (Ruehl et al., 2008; Shantz et al., 2012; Yang et al., 2012), such as SPPs. Therefore, the SS_{Crit} values reported in this study are not substantially affected by CCNC limitations at low SS, and the associated uncertainties have been estimated so they take into account the lower accuracy of the instrument at low SS. Further studies investigating how to correct for kinetic limitations are still required to improve CCN activation properties accuracy at low SS (Tao et al., 2024).

To describe the SPP hygroscopicity, κ values have been calculated for each pollen type at each size using Eq. (2-8) and the results are given in Table 5.1. All pollen types show similar κ values with size (except *Acer*), indicating that κ is mostly independent from the particle size. Prisle et al. (2019) and Mikhailov et al. (2021) also found a weak dependency of κ with size. The differences observed here are in the range 0-20% for all pollen types, except *Acer*, which shows differences higher than 50% (53.6%). This could be due to unstable and higher SPP concentration at 200 nm during the experiments with *Acer*. As explained in Sect. 4.4.2, total

Cloud condensation nuclei activation properties of Mediterranean pollen types: a laboratory study

concentration of particles was kept in the range 2000-4000 particles/cm³. However, during the experiments with *Acer* at 200 nm, concentrations were unstable. Not taking into account the results for Acer at 200 nm, the average κ values for 80, 100 and 200 nm SPPs are 0.29, 0.29 and 0.28, respectively. Hygroscopicity κ values are within the range 0.137 \pm 0.018 (*Quercus*) and 0.328 \pm 0.019 (*Cupressus*), characteristic of moderately hygroscopic organic aerosols (Petters and Kreidenweis, 2007). Previous studies showed that organic aerosol particles exhibit a wide range of κ values ranging from 0 to 0.3 (e.g., Dusek et al., 2010; Pöhlker et al., 2016; Thalman et al., 2017). In this work, the κ for most pollen types is approximately 0.3, suggesting pollen could be considered a good surrogate for more hygroscopic organic species (Ruehl et al., 2016).

It should be noted that *Quercus* is the least hygroscopic specie (Fig. 5-1 and Table 5.1) exhibiting the highest SS_{Crit} . κ values are arranged from 0.11 to 0.15 and they are very similar to the SPP κ values obtained by Thalman et al. (2017), Mikhailov et al. (2019; 2021) and Prisle et al. (2019). The differences found between fresh *Olea* (2021) (κ ~ 0.24) and *Olea* (2019) (κ ~0.30) should also be highlighted. This could be due to aging of *Olea* collected in 2019, leading to an increase in κ .

Table 5-1.Mean hygroscopicity parameter, κ , obtained for each pollen type at 200, 100 and 80 nm dry diameter (the mean κ does not take into account the results for Acer at 200 nm due to unstable concentrations during the experiments).

Dollon Types	Dr	14 /m a m l			
Pollen Types	200	100	80	к (mean)	
Acer	0.17 ± 0.03	0.30 ± 0.10	0.27 ± 0.08	0.287 ±	
Acei	0.17 ± 0.03	0.30 ± 0.10	0.27 ± 0.00	0.022	
Cupressus	0.34 ± 0.05	0.31 ± 0.06	0.34 ± 0.06	0.328 ±	
сиргеззиз	0.54 ± 0.05	0.51 ± 0.00	0.54 ± 0.00	0.019	
Dactylis	0.30 ± 0.03	0.31 ± 0.06	0.31 ± 0.05	0.307 ±	
2 4.007.110		0.01 = 0.00		0.005	
Fraxinus	0.256 ± 0.30 ± 0.05		0.28 ± 0.04	0.280 ±	
				0.023	
Olea 2019	0.28 ± 0.03	0.32 ± 0.06	0.30 ± 0.05	0.301 ±	
0/64 2013	0.20 2 0.03		0.50 = 0.05	0.017	
Olea 2021	0.236 ±	0.236 ±	0.243 ±	0.238 ±	
0/64 2021	0.011	0.019	0.015	0.004	
Pinus	0.33 ± 0.04	0.32 ± 0.06	0.32 ± 0.07	0.325 ±	
7 1103	0.00 = 0.01	0.02 = 0.00	0.02 2 0.07	0.010	
Platanus	0.266 ±	0.29 ± 0.05	0.239 ±	0.28 ± 0.03	
	0.019	0.20 2 0.00	0.015	0.20 _ 0.00	
Populus nigra (non-	0.31 ± 0.04	0.30 ± 0.06	0.32 ± 0.05	0.311 ±	
commercial)	0.51 = 0.01	0.31 1 0.04		0.012	
Populus deltoides	0.32 ± 0.04	0.31 ± 0.06	0.33 ± 0.06	0.321 ±	
(commercial)	0.02 _ 0.04	0.01 _ 0.00		0.015	
Quercus	0.117 ±	0.146 ±	0.150 ±	0.137 ±	
Que, 643	0.008	0.024	0.022	0.018	
κ (mean) for all pollen types	0.28 ± 0.07	0.29 ± 0.05	0.29 ± 0.06	0.283 ±	
(can, for an ponen types	5.25 ± 6.67	5.23 ± 6.63	5.25 ± 6.66	0.006	

5.2 Organic composition

Hygroscopic properties of inorganic compounds are well defined, however large uncertainties are associated with the effect of organic compounds on cloud droplet activation (Sorjamaa et al., 2004; Dawson et al., 2020). Previous studies have demonstrated the negative relationship between aerosol hygroscopicity at subsaturated conditions and organic content (Quinn et al., 2005; Titos et al., 2014a; Chen et al., 2018; Burgos et al., 2020), but the role of different organic components is still unclear especially in complex organic aerosol mixtures (Petters and Petters, 2016; Axelrod et al., 2021). Therefore, in this section, we explore the relationship between organic concentration, organic speciation, protein content and aerosol hygroscopicity (κ parameter calculated at supersaturated conditions).

Figure 5-2 shows the total concentration of organic compounds and protein content for each pollen type and the κ values (results of organic concentration for Platanus are not shown due to unavailability of this pollen type for GC-MS analysis). The protein and organic contents are highly variable among pollen types. *Pinus* and Olea 2021 are the pollen types with the highest concentration of organics (Olea 2021 has 90800 ng/mg and Pinus 88000 ng/mg). However, other species (Acer, Populus deltoides and Quercus) are the pollen types with the highest protein content. The lowest organic concentrations are found for Olea 2019 (6000 ng/mg), Cupressus (4416 ng/mg) and Acer (4411 ng/mg). Dactylis, Fraxinus, and Populus deltoides have organic concentrations ranging from 36600 ng/mg to 44100 ng/mg; and finally, Quercus and Populus nigra have an organic content of 13400 ng/mg and 20700 ng/mg, respectively. Cupressus has the lowest proteins concentration (0.41 mg/mL), and the rest of pollen types show values in the range 1.10-1.60 mg/mL. Two results should be highlighted: (1) Populus deltoides has higher concentrations of organics and proteins than *Populus nigra* but almost identical κ values and (2) the composition of Olea 2019 and Olea 2021 are quite different which may explain differences in SS_{Crit} and κ for the two samples.

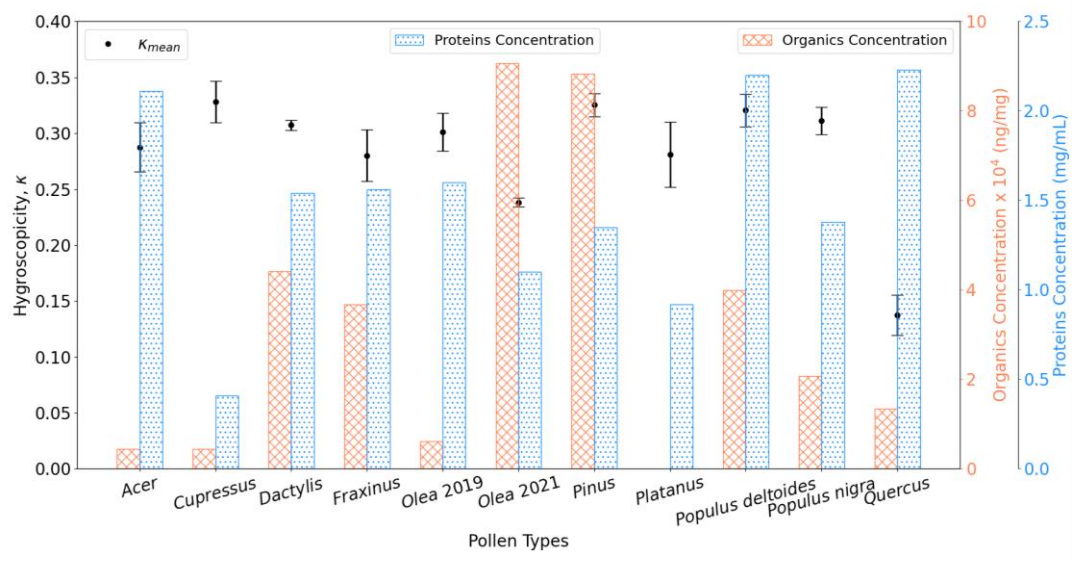


Figure 5-2. Bar diagram showing total organic compound concentration (in ng/mg of pollen), protein content (in mg/mL) and mean hygroscopicity parameter κ for each pollen type. The κ error bars represent the standard deviation for the three dry size diameters investigated.

In general, the hygroscopicity parameter does not show a significant relationship with the organic or proteins content. *Quercus* has the lowest κ value and the lowest organic concentration, but the highest protein content. *Acer* shows similar organic and protein content to *Quercus*, but it exhibits a higher κ value. Steiner et al. (2015) pointed out that the protein content might play a role in determining SPP hygroscopicity. These authors observed that, from the 6 pollen types they investigated, *Ambrosia* (not studied here) showed the highest SS_{Crit} and the highest protein content; but they also did not find a clear trend with κ . Similarly, Mikaihlov et al. (2021) did not observe a direct relationship between organic concentration and pollen hygroscopicity.

To relate SPP hygroscopicity to its organic content, we have to take into account that organic compounds cover hundreds of different chemical components (Oros and Simoneit, 2001; Rissanen et al., 2006) that can exist in the atmosphere affecting the ability of aerosol particles to act as CCN (Raymond and Pandis, 2002). Studies investigating the ability of individual organic components (such as oleic acid, stearic acid, levoglucosan, glucose, glutamic acid or palmitic acid) have clearly shown their different hygroscopic and activation properties (Abbatt et al., 2005; Rosenørn et al., 2006; Kristensson et al., 2010; Nguyen et al., 2017; Dawson et al., 2020). Many of these organic compounds have been identified in pollen samples (Axelrod et al., 2021). Figure 5-3 shows the relative contribution

Cloud condensation nuclei activation properties of Mediterranean pollen types: a laboratory study

of different organic compounds for each pollen type grouped by chemical families: saccharides (α -glucose, θ -glucose and sucrose), fatty acids (alpha-linoleic acid, linoleic acid, oleic acid, palmitic acid and stearic acid), amino acids (aspargine, glutamine, histidine and proline), diacids (azealic, glutaric, malic, succinic and terephthalic), ciclitols (pinitol, shikimic), anhydro-sugars (levoglucosan), plants compounds (oleanolic acid and sitosterol) and sugar-alcohols (mannitol and sorbitol).

The results show that the contribution of organic compounds among pollen types is highly variable (Fig. 5-3), which is consistent with recent studies (Axelrod et al., 2021; Mampage et al., 2022). Saccharides (α -glucose, θ -glucose and sucrose) are the most prominent organic component in most of the pollen types, contributing over 80% in *Dactylis* (84.50%), *Fraxinus* (86.32%), and *Quercus* (87.57%). Among saccharides, *Fraxinus* and *Quercus* mainly contain α -glucose and θ -glucose and their chemical compositions are quite similar, while sucrose dominates in *Dactylis*.

Amino acids are quite abundant organic components of *Populus nigra* (69.84%) and *Olea* 2021 (79.03%). *Populus deltoides* and *Acer* also show percentages of amino acids higher than 25%, but the contribution of amino acids to the rest of pollen types is lower than 10%. One of the most abundant amino acids in pollen grains is proline. We observe that its concentration is quite different between fresh *Olea* (55.33% of total measured organic compounds) and *Olea* 2019 (less than 7%). Proline is thought to have a protective role against environmental stress in addition to preserving pollen fertility (Trovato et al., 2019), however, it is a component that degrades as pollen ages (Mattioli et al., 2020) which might explain the degradation of *Olea* over time.

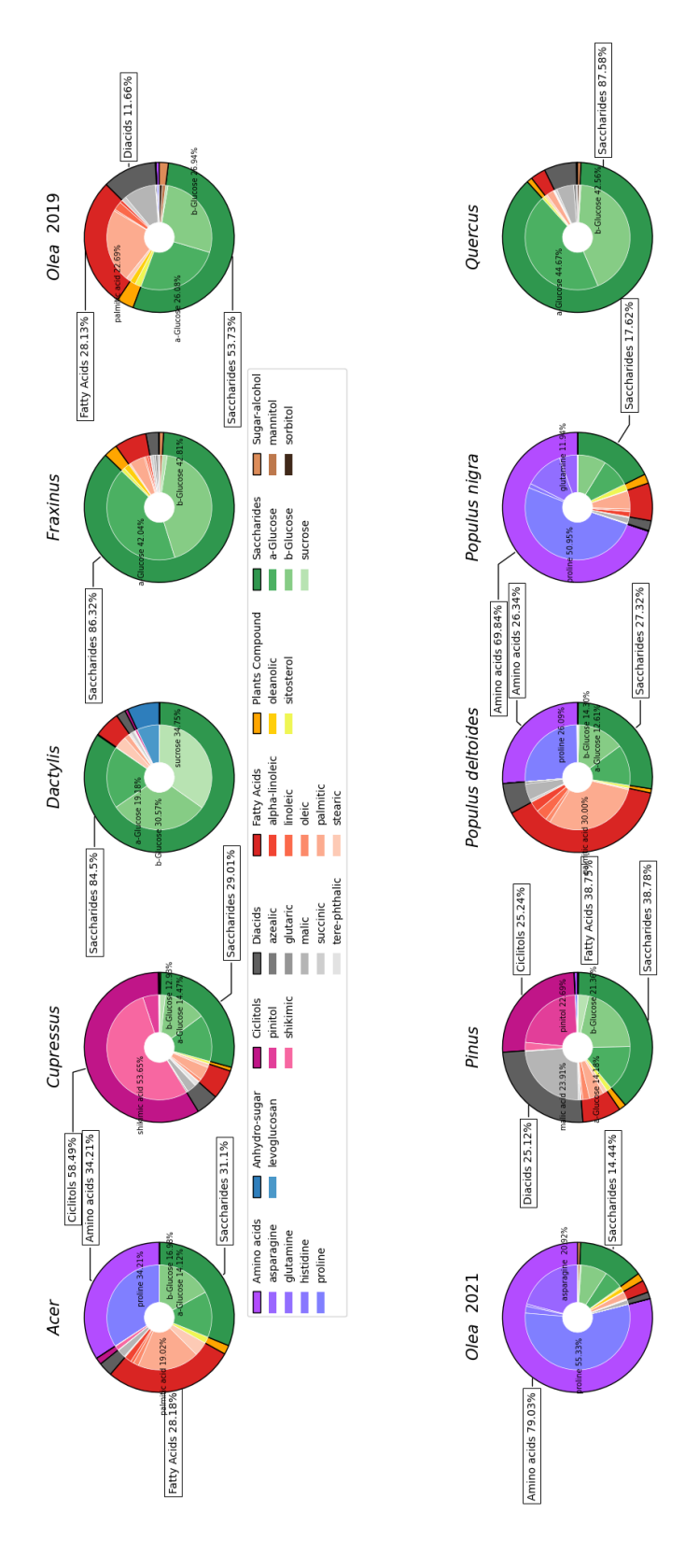


Figure 5-3. Relative composition of individual molecular organic compounds (internal ring) and their groups for each pollen type (external ring). Only compounds representing percentages above 10% have been highlighted to appear in pie charts.

Cloud condensation nuclei activation properties of Mediterranean pollen types: a laboratory study

The results also show that fatty acids and diacids are also present in all pollen types but with varying contributions across types. Palmitic acid is the most abundant fatty acid in all pollen types, except for Dactylis where stearic acid is dominant. The overall low concentration of fatty acids in most pollen types could be attributed to absence of pollenkitt. Pollenkitt is the outermost layer of pollen (also called pollen coat) (Gong et al., 2015) and is composed mainly of lipids (as well as proteins and saccharides) (Ischebeck, 2016). It also has a sticky character which makes it more common in entomophilous plants (pollinated by insects) (Pacini and Hesse, 2005; Gong et al., 2015). However, it is not very common to find pollenkitt in anemophilous species (wind pollinated) which are the pollen types studied in this work. Acer, Populus deltoides and Olea 2019 show higher contribution of fatty acids compared with the rest of pollen types investigated. In contrast, Quercus has the lowest concentration. Previous studies concluded that fatty acids are generally hydrophobic (Kumar et al., 2003; Broekhuizen et al., 2004) and they are characterised by low water activity (Haynes, et al., 2016) therefore, they do not contribute significantly to water uptake (Nguyen et al., 2017), and are not likely to lead to CCN activity (Kumar et al., 2003; Petters and Petters, 2016). Although we were not able to find any connection with the retrieved κ values, fatty acids have the ability to reduce surface tension at lower concentrations than other compounds (Petters and Petters, 2016), therefore, they could have a role in surface activity as will be discussed in Sect. 5.3.

Dactylis, Fraxinus and Quercus, have a similar relative concentration of saccharides, but Dactylis shows a slightly higher κ value. This could be due to the presence of levoglucosan, which is not present in Fraxinus or Quercus. Rosenørn et al. (2006) found that the potential of disaccharides (such as sucrose) to nucleate cloud droplets is lower than the potential of monosaccharides (such as glucose) and levoglucosan (anhydro-sugar). Dawson et al. (2020) also obtained κ values of sucrose (0.10-0.15) lower than levoglucosan (0.20-0.30). However, Dactilys exhibits a higher contribution of sucrose, making it difficult to draw absolute conclusions on hygroscopicity based on the amount of these saccharides in the pollen samples.

Mikaihlov et al. (2021) suggested that the difficulty in finding a relationship between κ and organic concentration is related to the different solubility values of

the organic compounds. SPPs are composed of both water-soluble components (such as sugars, proteins and inorganic ions) responsible for water uptake, and water-insoluble compounds (such as hydrosols or colloids) able to suppress hygroscopic growth and CCN activity. Our results have shown that SPPs consist of multiple organic compounds and their solubility values might be very different. The water solubility of each of these compounds (at 20 °C - 25 °C) is shown in Table 0-1 (in Appendix) and they have been classified as: (A) highly soluble (>700 mg/mL), (B) slightly soluble (0.5 mg/mL < solubility < 700 mg/mL) and (C) non-soluble compounds (<0.5 mg/mL) according to Han et al. (2022). Following this criteria, we obtained the percentage of these categories with respect to the considered organic compounds as Petters and Kreidenweis (2008) suggested. The relation between the mean values of SPP hygroscopicity and the relative contribution of the organic compounds in terms of water-solubility is shown in Figure 5-4.

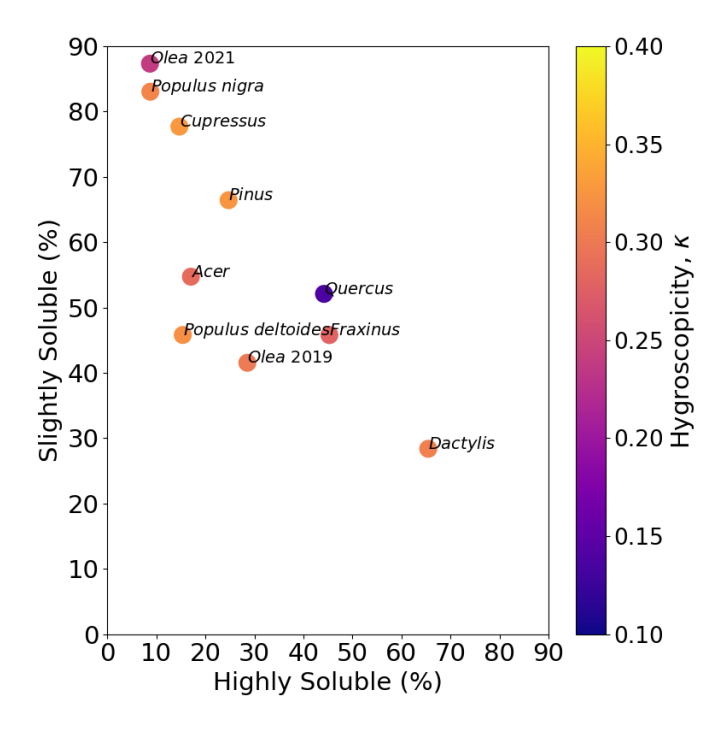


Figure 5-4. Relative contribution of highly soluble and slightly soluble compounds in SPPs coloured by the hygroscopicity parameter κ for each pollen type.

Figure 5-4 shows all κ values are in the same range (except *Quercus*) and there is not a clear relationship between hygroscopicity and chemical composition in terms of its solubility. Despite variations in the contribution of highly- and non-

soluble constituents among species, the hygroscopicity parameter is similar. The slightly and highly soluble compounds exhibit a wide range for all pollen types, between 30%-90% and from 8% to 66%, respectively. Therefore, non-soluble compounds make up less than 40%. Figure 5-4 shows that SPPs composed of highly soluble constituents, such as Dactylis, exhibit similar hygroscopicity values as those found for SPPs with higher contribution of non-soluble compounds such as *Populus* deltoides or Olea 2019. Establishing a general relationship with the amount or contribution of soluble and non-soluble organic constituents in the pollen types analysed here requires further investigation. In contrast, studies based on single compounds (e.g., Kumar et al., 2003) found clear relationships between solubility and κ, consistent with highly soluble organic particles being CCN active while the same size particle composed of an insoluble species would have low CCN activity. Riipinen et al. (2015) studied activation properties of multicomponent organic particles, and they concluded that hygroscopicity is related to water solubility in the range of slightly soluble species. However, Kuwata et al. (2013) showed molecular weight is the property that controls activation properties instead of solubility for highly soluble compounds. Wang et al. (2019) also concluded that the activation of most secondary organic aerosol (SOA) particles is related to molecular weight. We also explored the relationship between κ and molecular weight (not shown here), but the results were not conclusive since most pollen types exhibit similar hygroscopicity while estimated molecular weights had higher variability. Nevertheless, it should be mentioned that the results on the relationship between aerosol hygroscopicity, solubility and molecular weight are based on a selection of organic compounds and the bulk chemical composition is not fully recovered, which hampers the comparison. Further studies providing a more detail chemical speciation of SPPs could shed light on the relationship between solubility, molecular weight and hygroscopicity of primary organic aerosol mixtures.

5.3 Surface activity

Previous studies have evaluated the effect that surface tension (σ) might have on the CCN activation of organic aerosols (Ruehl et al., 2010; Prisle et al., 2019). To investigate the role of surface activity in cloud droplet activation we

Surface activity

measured the surface tension of different SPPs solutions (at different concentrations) for 6 pollen types (*Dactylis, Fraxinus, Pinus, Populus deltoides, Populus nigra* and *Quercus*) using Pendant Drop Tensiometry (see Sect. 4.4.3). The rest of the pollen types analysed in previous sections have not been considered in this analysis due to limited sample availability. As explained in Sect. 4.4.3, the filtration efficiency for each pollen type is different, thus, the initial concentrations calculated after filtration process were: 1.87 g/L, 1.43 g/L, 2.23 g/L, 1.83 g/L, 5.23 g/L and 1.05 g/L for *Populus deltoides, Populus nigra, Dactylis, Quercus, Pinus* and *Fraxinus*, respectively.

Figure 5-5 shows the time evolution of surface tension at the initial concentration and at 1/10, 1/100 and 1/1000 of the initial concentration. The plots for *Dactylis, Fraxinus* and *Pinus* do not show the most diluted solutions because the other pollen types analysed demonstrate that if the measured surface tension remains close to that of water (σ_w ~72.5 mN/m) over time, the more diluted solutions also exhibit σ_w values and do not change with time. All pollen types are surface active because the surface tension decreases in time for at least some solution concentrations. A lack of surface activity is indicated by surface tension values that are constant and similar to σ_w . However, the decreasing trend varies among species depending on pollen type and initial concentration. In general, the surface activity decreases as the initial solutions are diluted, consistent with recent results by Prisle et al. (2019).

Cloud condensation nuclei activation properties of Mediterranean pollen types: a laboratory study

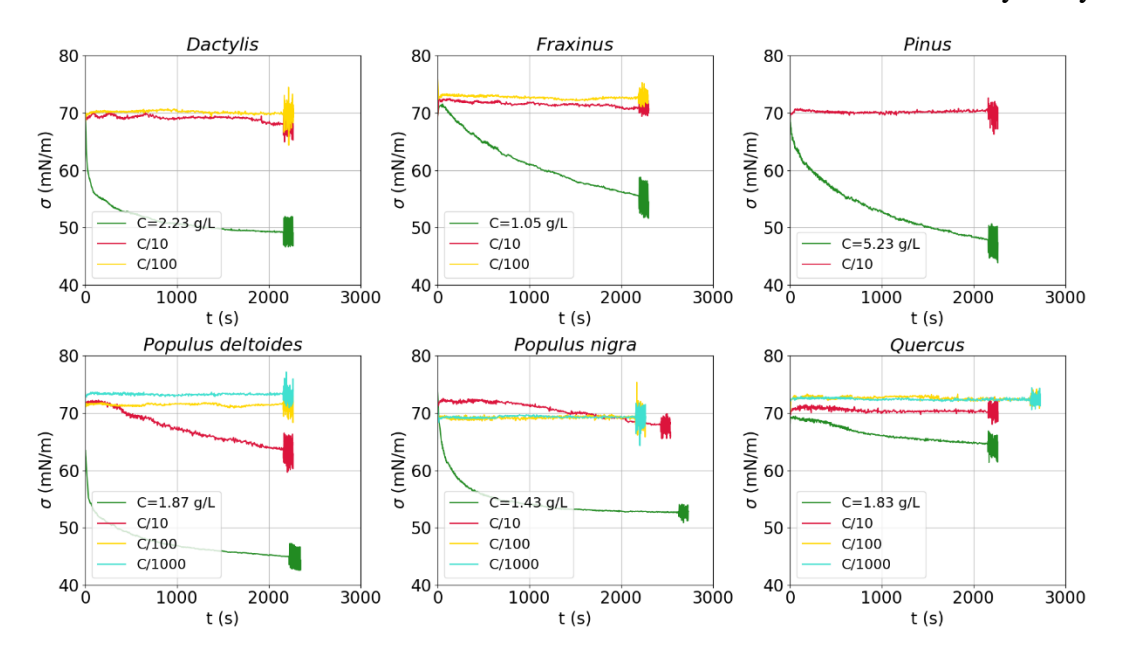


Figure 5-5. Surface tension versus time at different concentrations for *Dactylis*, *Fraxinus*, *Pinus*, *Populus deltoides*, *Populus nigra* and *Quercus*. Dilutions were made in ultrapure water, and measurements were made at room temperature (23 °C).

Table 5-2. Percentage surface tension decrease at 300 seconds.

Pollen Type	Concentration (g/L)	% decrease in surface tension		
Dactylis	C=2.2 ± 0.4	22.0%		
Fraxinus	C=1.05 ± 0.08	6.6%		
Pinus	C=5.23 ± 0.06	14.9%		
Populus deltoides	C=1.9 ± 0.8	20.6%		
r opulus delloides	C/10	1.9%		
Populus nigra	C=1.4 ± 0.4	17.4%		
	C/10	0%		
Quercus	C=1.8 ± 0.7	3.8%		

At the initial concentrations, all pollen types analysed significantly reduce the surface tension over the course of the surface tension measurement. Interestingly, *Populus deltoides* is the only pollen type that reduces the surface tension at

concentrations diluted 10 times. Finally, none of the pollen types are surface active at concentrations diluted 100 or 1000 times regardless of the initial concentration (Fig. 5-5). The reduction of surface tension is due to the adsorption of surface-active compounds present in different pollen types and proceeds in two steps. A first period (<300 s) characterised by a rapid reduction of the surface tension and second phase in which the surface tension reaches a pseudo plateau (Nozière et al., 2014). For diluted solutions, the first period of the adsorption process is diffusion controlled, and the rate of the surface tension reduction provides information on the diffusion of surface-active compounds to the air-water surface. Conversely, highly concentrated solutions and/or highly surface active compounds begin with initial values of surface tension already low, indicating that the surface is already occupied by surface active compounds and the adsorption of new molecules encounters an energy barrier (Eastoe and Dalton, 2000). This is the case for the initial solution of *Populus deltoides* which shows surface tension values of $63.5 \pm 1.5 \, \text{mN/m}$, which is significantly lower than σ_{w} .

The decreasing rate of surface tension varies among species. Some pollen types, such as *Quercus* shows a decay curve of surface tension which is more linear with time than *Populus deltoides* or *Populus nigra* with similar initial concentrations. Table 5-2 shows the percentage of surface tension reduction during the first 300 seconds (time at which fast phase of decay is measurable and comparable between pollen species with fast and slow dynamical phases) for each SPP species for the concentrations at which they have been shown to be surface active. Comparison of the rate of surface tension reduction recorded for similar concentrations of approximately 1 g/L (Table 5-2) follows the order: *Populus deltoides > Populus nigra > Fraxinus > Quercus*, with *Populus deltoides* having the highest fatty acids concentration and *Quercus*, the lowest (Fig. 5-3). This could suggest that the surface-active compounds may come principally from the free fatty acids.

After the initial rapid decay, the rate of surface tension reduction decreases until reaching a pseudo plateau indicative of saturation of the surface layer. However, not all pollen types reach a clear plateau during the experiment time (Fig. 5-5). At initial concentrations, *Dactylis, Quercus, Populus deltoides* and *Populus nigra* seem to be able to achieve this state, forming a surface layer characterised

Cloud condensation nuclei activation properties of Mediterranean pollen types: a laboratory study

by surface tension values of 49.2 ± 1.5 , 64.4 ± 1.5 , 45.0 ± 1.5 and 52.7 ± 1.5 mN/m, respectively. However, *Fraxinus* (initial concentration), *Pinus* (initial concentration) and *Populus deltoides* (diluted 10 times) need more than ~2500 seconds to achieve it.

The last 200 seconds of the processes shown in Fig. 5-5 corresponds to dilatational rheology of adsorbed layers. It consists of inducing sinusoidal perturbations by injecting and extracting liquid into the droplet (Maldonado-Valderrama et al., 2005). This analysis provides information about the interfacial elasticity or viscosity, related to the response of the surface tension to area deformation (Seidl, 2000; Decesari et al., 2003) and is related to particle growth, kinetics and relaxation processes (not addressed in this thesis).

As it has been mentioned before, at the end of the adsorption kinetics curves, the surface tension reaches pseudo stable values indicative of the saturation of the surface layer (Fig. 5-5). The final values of surface tension are plotted in Fig. 5-6 versus SPP concentration in the solution and error bars correspond to standard deviations of σ_w values obtained between each experiment. It should be mentioned that Fig. 5-6 only shows initial concentrations and concentrations diluted 10 and 100 times because Fig. 5-5 demonstrated that more diluted concentrations correspond to σ_w values. In the case of *Pinus*, the point representing the concentration diluted 100 times (open pink circle) is not an experimental value. It has been assumed to have the same surface tension value as the C/10 sample and has only been plotted to guide the eye and visualize the pattern easier.

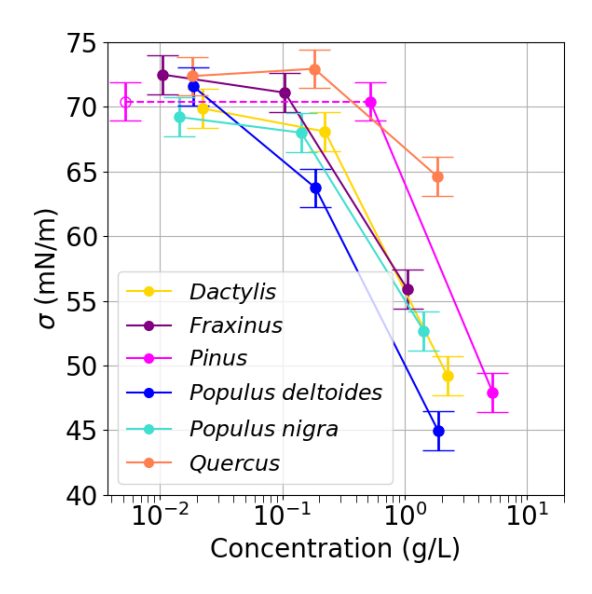


Figure 5-6. Final values of surface tension after adsorption at constant surface area plotted in Fig. 5-5, as function of concentration for *Dactylis, Fraxinus, Pinus, Populus deltoides, Populus nigra* and *Quercus*. Error bars represent the standard deviation of the surface tension measured for pure water during the experiments.

The experimental results (Fig. 5-6) show again that the surface tension decreases for more concentrated solutions, while the surface tension approaches the value of water for more diluted solutions. However, as noted above, not all pollen types exhibit the same behaviour. Figure 5-6 shows that the surface activity of all types of pollen analysed lie between the most surface active Populus deltoides and the least surface-active Quercus. This is consistent with the amount of fatty acids found in these pollen types (Fig. 5-3). Also, the shape of the surface tension curves plotted in Figure 5-6 can provide additional information on the development of the surface layer by looking at both, the bulk concentration needed to reduce significantly the surface tension and, the lowest surface tension achieved by each of the pollen species. For concentrations between 1 g/L - 10 g/L, Dactylis, Pinus and Populus deltoides show surface tension values from 45 mN/m to 50 mN/m. Populus nigra, Fraxinus and Quercus reached 52.68 mN/m, 55.96 mN/m and 64.64 mN/m, respectively. For the range of concentrations between 0.1 g/L - 1 g/L, SPPs show surface tension values ranging from 60 mN/m to 72 mN/m. Finally, for concentrations lower than 0.1 g/L, surface tension values are found between 69 mN/m-72 mN/m, which are similar to σ_w . It should be highlighted that Populus deltoides requires the lowest bulk concentration to significantly reduce the Cloud condensation nuclei activation properties of Mediterranean pollen types: a laboratory study

surface tension and reaches the lowest value, hence it is the most surface active SPP type. In contrast, *Quercus* requires high bulk concentration to decrease σ , and still the final σ value reached remains high, indicative of a very diluted surface layer, and hence arises as the less surface active SPP type.

Petters and Petters (2016) showed that different surfactants groups do not have the same ability to reduce surface tension. Saccharides are not good surface tension reducers; they may even increase surface tension. This may be the reason for the low surface activity observed for *Quercus* (which has a chemical composition dominated by glucose). The surface activity of amino acids depends on their hydrophobicity/hydrophilicity (Kristensson et al., 2010; Raza et al., 2019); and the amino acids present in pollen are mostly hydrophilic. While *Fraxinus*, *Populus nigra*, *Pinus* and *Dactylis* contain similar amounts of fatty acids, the rest of their components are mostly non surface active, hence we cannot fully account for the surface activity shown in Fig. 5-6. Due to the limited number of pollen types investigated (6 in this case) and the similar behaviour and predominant organic composition of most of them, it is not possible to establish a clear relationship between composition and surface activity, although our findings suggest the presence of fatty acids could be related to the observed surface activity.

Our results have shown all types of SPPs act as surfactants, able to reduce surface tension. Nevertheless, this behaviour is strongly dependent on concentration, that is, pollen types tend to decrease surface tension when solutions are sufficiently concentrated but their impact on activation properties needs to be evaluated.

5.4 Impact of surface tension on hygroscopicity

To determine the impact of lowering the surface tension of SPP solutions on their hygroscopic properties, in this section we study how the hygroscopic parameter κ varies with decreasing surface tension. SPPs clearly contain surface active compounds (likely related to fatty acids) because there is a reduction on surface tension, which might affect the derived hygroscopicity using Köhler theory. The experimental SScrit derived in Sect. 5.1 and the lowest surface tension values

obtained in Section 5.3 (instead of the water surface tension) have been used in Eq. 2-8 to recalculate the hygroscopicity parameter and to determine whether surface activity involves a significant impact on the ability of particles to activate as CCN, as previous studies suggest (Ruehl et al., 2016; Ovadnevaite et al., 2017).

According to Prisle et al. (2019) the concentration of SPP in cloud droplets is in the range of $10^{-5}-2\cdot 10^{-1}$ g/L and concentrations diluted C/100 fall within this range. The final surface tension values of these solutions are quite similar to $\sigma_{\rm W}$ (within the measurement uncertainties). Here we determine if slight variations in σ could be relevant for the retrieved κ values. Results are shown in Figure 5-7 and Table 0-2 (Appendix), indicating that κ values for the most concentrated solutions ($\kappa_{\sigma c}$) and at concentrations diluted 100 times ($\kappa_{\sigma c/100}$) are lower than the κ value obtained using water surface tension ($\kappa_{\sigma w}$) for all pollen types. Table 0-2 also shows the reduction percentage in the κ mean value ($\kappa_{\rm mean}$).

All $\kappa_{\sigma C}$ are in the range 0.10 – 0.17 (for all particle dry diameters investigated 80, 100 and 200 nm) and the reduction in κ , relative to assuming the surface tension of water, is around 50 – 68%, except for *Quercus* (17.2%) and *Fraxinus* (39.3%). *Quercus* is the least surface-active pollen type, with an equilibrium surface tension of 64.6 ± 1.5 mN/m (similar to σ_{w}). In contrast, *Populus deltoides* reached the lowest equilibrium surface tension (45.0 mN/m), and exhibited a strong reduction in κ .

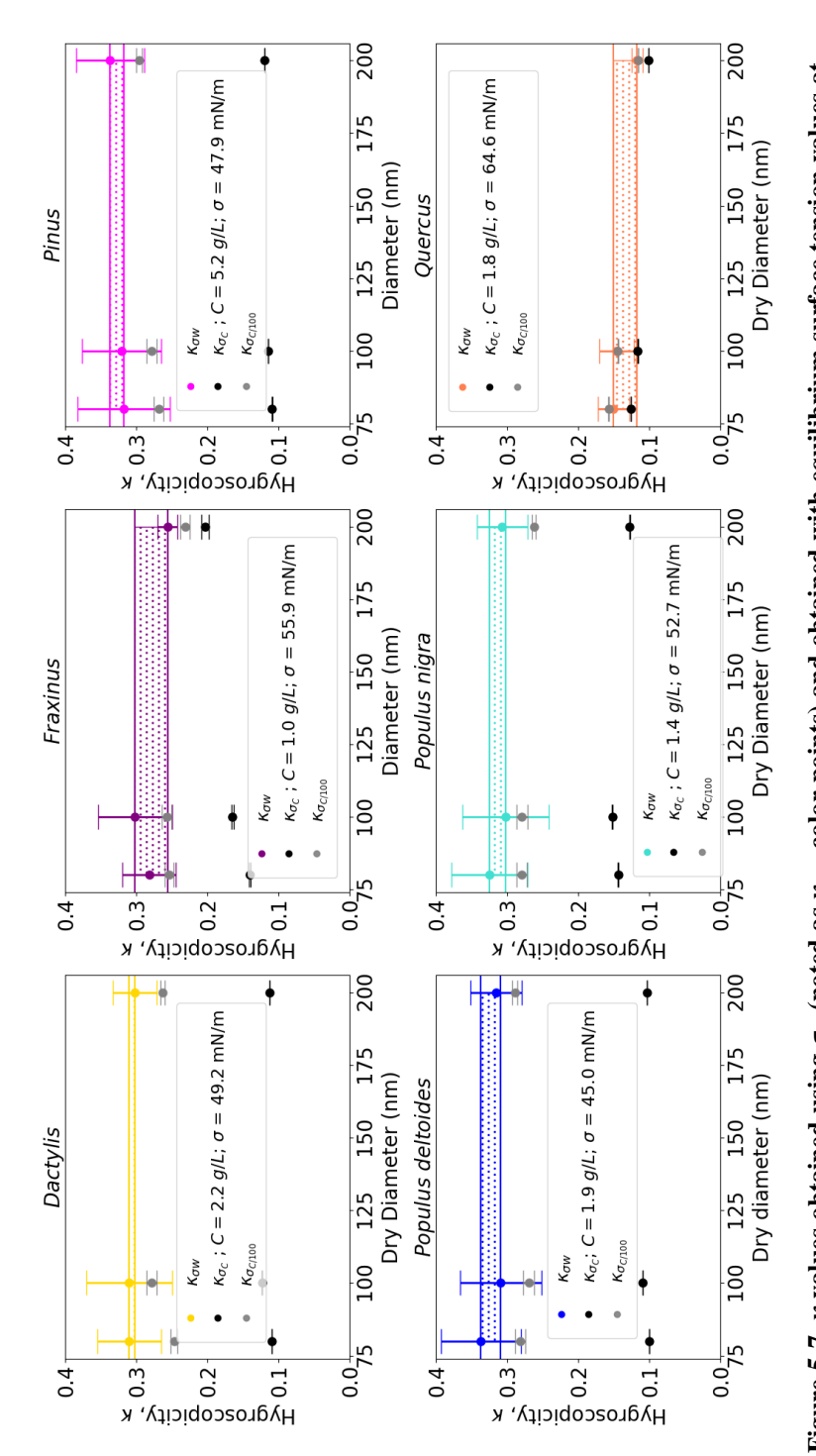
Surfactant substances lead to reduced surface tension, decreasing the energetic barrier to equilibrium droplet growth, thus decreasing critical supersaturation (Davies et al., 2019) and leading to an overestimation of activation potential (Sorjamaa et al., 2004; Prisle et al., 2008). However, because the surfactant partitioning effect occurs, surfactants can migrate from the bulk to the surface, limiting the amount of dissolved solute in the droplet and thereby reducing water uptake capacity and κ (Sorjamaa et al., 2004; Fuentes et al., 2011).

For the κ values obtained using the modified surface tension values, in all cases there is a pronounced decrease in aerosol hygroscopicity for the most concentrated solutions (C). For solutions diluted 100 times from the initial concentration (C/100) the final σ values are similar to σ_w , resulting in a lesser impact on the κ values ($\kappa_{\sigma c/100}$ in Figure 5-7). The percentage of reduction of mean

Cloud condensation nuclei activation properties of Mediterranean pollen types: a laboratory study

 $\kappa_{\sigma c/100}$ values is in the range 11.7 – 13.9% for all pollen types except for *Quercus* (1.5%) and all $\kappa_{\sigma c/100}$ values are within the error range of $\kappa_{\sigma w}$ values obtained.

We focused on macroscopic droplets and concentrations that could be observed in atmospheric cloud droplets. Diluted concentrations reached surface tension values similar to σ_w . However, in microscopic droplets with high surface area to volume ratios, the partitioning of surface active compounds will deplete the bulk concentration as well as depress the surface tension of the droplet (Prisle et al., 2010). For a model system of Nordic Aquatic Fulvic Acid (NAFA) and NaCl, Lin et al. (2020) found that the surface tension depression and bulk depletion effects on cloud activation largely cancelled each other out. However, the extent to which that conclusion can be applied to other mixtures of atmospheric interest is unknown. Specifically, our results suggest that the minimal reduction in surface tension observed at low solute concentrations will not have a significant impact on whether SPPs activate as cloud condensation nuclei. However, more studies considering additional multicomponent organic aerosol particles (such as these different pollen types) where surface tension behaviour can be quite relevant would be essential for further progress. Recent studies (Davies et al., 2019; Lin et al., 2020) point to the relevance of considering surface tension time-evolution in CCN activation suggesting further evaluation is necessary to draw more accurate conclusions.



Pinus, Populus deltoides, Populus nigra and Quercus. The surface tension values at concentrations diluted 100 times are 69.9, Figure 5-7. κ values obtained using σw (noted as κσw, color points) and obtained with equilibrium surface tension values at highest concentrations (KGC, black points) and concentrations diluted 100 times (KGC/100, grey points) for Dactylis, Fraxinus, 72.5, 70.4, 71.6, 69.2 and 71.4 mN/m, respectively. Horizontal lines represent maxima and minima values obtained for $\kappa_{\sigma w}$ and shaded area the interval between both values.

5.5 Conclusions

In this chapter we have analysed the activation properties (critical supersaturation and hygroscopicity parameters), surface tension effects and organic composition of SPPs from 10 different Mediterranean pollen types. Our results demonstrated that subpollen particles (SPPs) of the most important Mediterranean species are able to activate at atmospherically relevant supersaturations (0.07%-0.37%, depending on size). Hygroscopicity parameters, κ , obtained for each pollen type show that SPPs are classified as a moderately hygroscopic organic aerosol varying in the range between 0.23-0.33, except *Quercus* that showed very low hygroscopicity (0.14). This suggests that SPPs might be an important natural contribution to the CCN budget. However, further studies are needed to determine more accurately how kinetic limitation in the CCN counter could affect the obtained activation properties of SPPs, although our results suggest they are within the range of SS measurements uncertainties.

Regarding chemical composition, our analysis shows that total organic concentration and especially protein content is quite different among species. Saccharides are present in all analysed pollen types (α -glucose and θ -glucose are the most abundant) although they show different relative contributions. The results also show a large variation of the composition of fatty acids among species, comprising nearly 40% of *Populus deltoides* and less than 5% in *Quercus*. Other chemicals such as amino acids and individual organic components also exhibit a great variability among species. The relative concentration of highly, slightly and non-soluble organic compounds is also quite similar for all pollen types, which could be one of the reasons why the hygroscopic behaviour is not so different for the pollens studied here.

Surface tension experiments reveal surface activity of all pollen types at high concentrations. *Populus deltoides* is the most surface active and *Quercus* is the least surface active. However, all SPPs from different pollen types are surface active at concentrations higher than 1 g/L. The surface activity reduces κ values by around 50%-60%, except for *Quercus* which only reduces κ values by 17.7%. The capacity to reduce surface tension decreases as SPP solution concentration decreases. If the SPP concentrations are lower than 0.03 g/L, surface tension values

Conclusions

are similar to the surface tension of water (σ_w) and κ values are barely modified. Therefore, we can assume that for low solution concentration (which is expected during SPP activation in real cloud droplets), σ_w is a good approximation in the Köhler equation.

However, it is difficult to identify any clear relationships among κ , chemical composition and the surface activity of SPPs, at least for the pollen types investigated in this study. Our results suggest an increase in fatty acids contribution leads to higher surface activity when concentrations exceed 1 g/L. However, at low concentrations (suitable for cloud droplets) all SPPs are practically non-surface active, independently of chemical composition.

Previous research with single organic components provides insightful results on the CCN activation properties of different organic compounds such as fatty acids, amino acids or saccharides, however our analysis is focused on atmospheric pollen samples, composed of multiple different chemical compounds, which makes it very difficult to draw conclusive results. We have seen that all these pollen types, except *Quercus*, exhibit similar activation properties, suggesting that their behaviour is quite similar in terms of activation and cloud droplet formation. Comprehensive additional studies including new SPPs types, typical in different regions and chemical analysis should be performed in order to improve the understanding of activation and hygroscopic properties of SPPs. Due to the forecasted increase in pollen release with climate change, and the large SPP generation potential of each pollen grain, further research and additional physical and chemical properties should be studied to better understand the factors controlling SPPs activation properties.

6. Ambient measurements of cloud condensation nuclei activation properties during Saharan dust events

High-mountain areas provide unique opportunities to study aerosol-cloud interactions in near-pristine conditions, similar to pre-industrial times. Despite their climatic importance, there are few studies on CCN properties in these regions. These studies are crucial for understanding the impact of long-range transported particles, such as desert dust, on aerosol properties and climate.

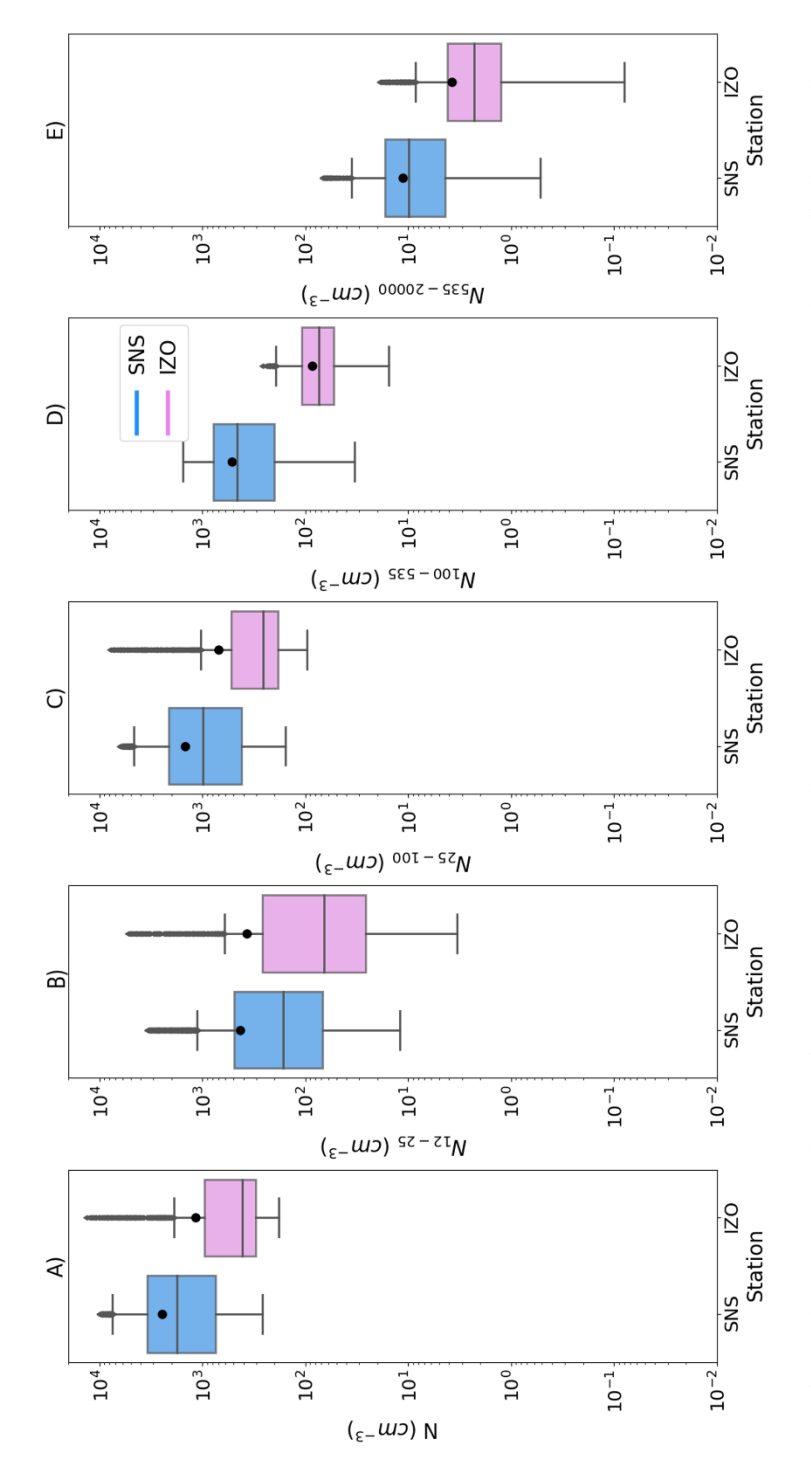
This chapter examines the impact of transported desert dust on CCN activation properties at two high-altitude remote stations, SNS and IZO, which frequently experience dust events. Section 6.1 characterizes CCN concentrations and activation properties at these sites, providing insights into CCN behavior in high-mountain and remote environments. Several dust events were identified, allowing for the characterization of CCN properties during these events. Section 6.2 discusses the synoptic conditions driving desert dust transport to SNS and IZO, while section 6.3 explores how these dust events influence aerosol particle activation as CCN.

The measurement campaign at SNS was conducted from 8th June to 12th July 2021, while at the IZO station the measurement period took place from 27th April to 27th June 2022. During both campaigns, one column of the CCNC-200 was operated in polydisperse mode to measure CCN concentration at varying SS (0.2%, 0.4%, 0.6% and 0.8%), holding each SS constant for 10 minutes at SNS and 6 minutes at IZO. The second column of the CCNC-200 at IZO measured also in polydisperse mode at constant SS (SS=0.4%) and in size-resolved mode at varying SS (0.2%, 0.4%, 0.6% and 0.8% for 10 minutes) at SNS (only available from 24th June to 12th July 2021). Only results of the first CCNC column (polydisperse CCN measurements at scanning SS) are presented in this chapter.

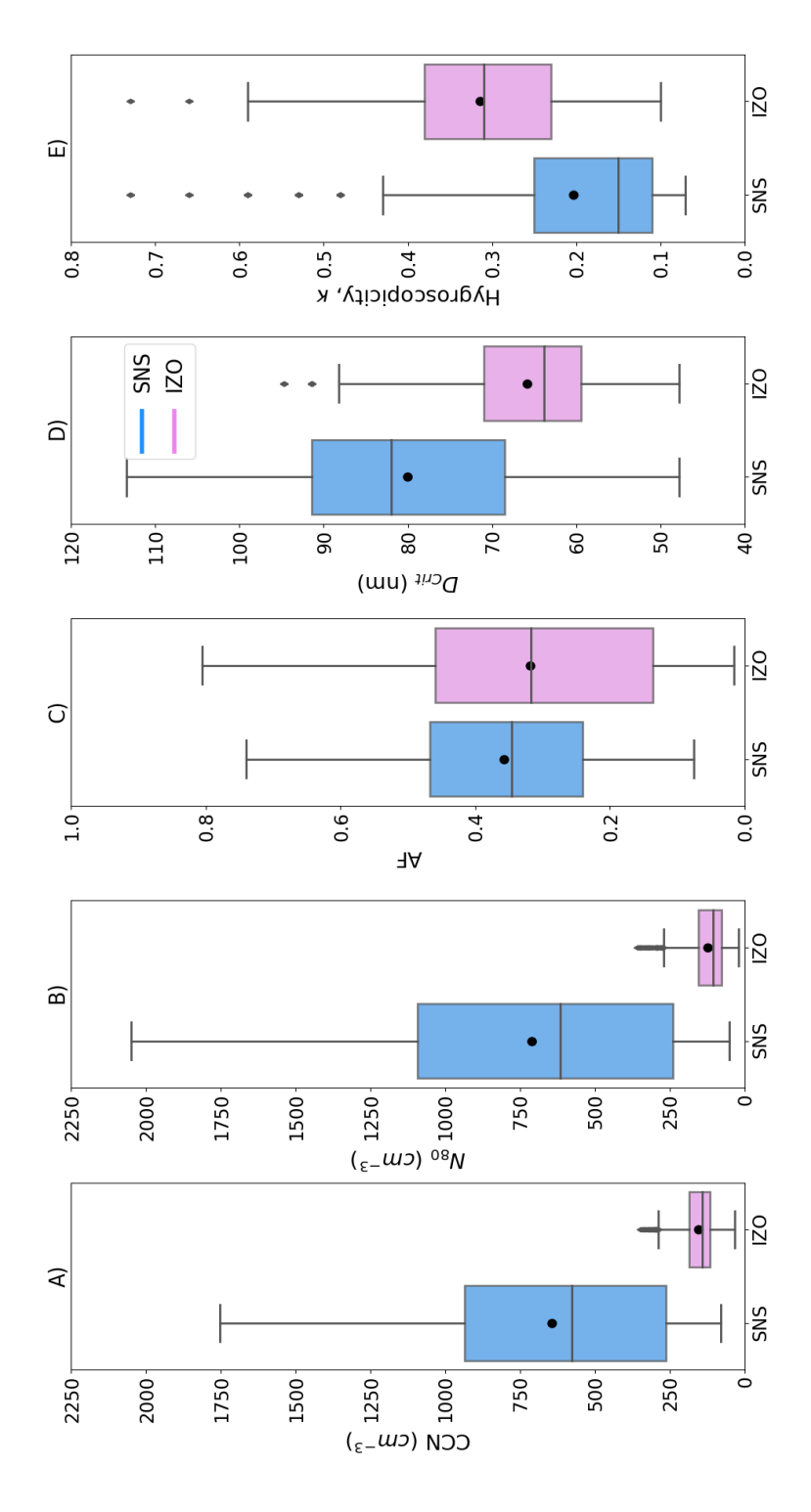
6.1 Overview of CCN activation properties at SNS and IZO

A statistical overview of total particle number concentration, the mode-segregated particle number concentrations and the main activation properties of aerosol particles at SNS and IZO over the measurement periods are shown in Figure 6-1 and Figure 6-2, respectively. The mean diurnal patterns of these properties are shown in Figure 6-3. Activation properties shown in this section refer only to a single supersaturation, SS=0.4%, for clarity purposes. Similar behavior and diurnal variability have been observed for all SS conditions (CCN measurements are also available at SS=0.2%, 0.6% and 0.8%). Table 5-3 shows a literature review of CCN concentration and activation properties at similar SS values at high-mountain sites.

SNS is characterized by higher total particle number concentration (N) than IZO with median value of 1800 cm^{-3} and 411 cm^{-3} at SNS and IZO, respectively (Fig. 6-1). This higher concentration at SNS is observed in all size ranges, especially in the size range 25-100 nm ($N_{25\text{-}100}$) and 100-1000 nm ($N_{100\text{-}1000}$), while lower differences are observed in the nucleation mode ($N_{12\text{-}25}$). In fact, similar mean particle number concentration is observed for the nucleation mode at both sites (428 cm^{-3} and 367 cm^{-3} at SNS and IZO, respectively). There is a strong variability in terms of particle number concentration in all size ranges, highlighting the large number of outliers (especially at IZO), associated with sporadic events of high particle number concentrations. Based on previous studies performed at both locations, the highest $N_{12\text{-}25}$ concentrations are likely associated with new particle formation events while highest coarse mode concentrations, N_C , might be related with dust events (García et al., 2014; Casquero-Vera et al., 2020; Casquero-Vera et al., 2023). The potential impact of both phenomena (new particle formation and dust events) on CCN concentrations and activation properties will be addressed in more detail in the following sections.



Black dots and grey lines represent the mean and median values, respectively. Lower and upper limits in the boxplots are the first (Q1) and third (Q3) quartiles respectively. The difference between them is the inter-quartile range (IQR). Figure 6-1. Boxplots of A) particle number concentration N, B) N12-25, C) N25-100, D) N100-1000 and E) NC at SNS and IZO. Lower and upper whiskers show Q1-1.5 IQR and Q3+1.5 IQR, respectively. Diamond markers represent the outliers. The time-resolution of the data is 5 minutes.



D_{Crit} and E) K. Black dot and grey line represent the mean and median values, respectively. Lower and upper limits in the boxplots are the first (Q1) and third (Q3) quartiles respectively. The difference between them is the inter-quartile range (IQR). Lower and upper whiskers show Q1-1.5-IQR and Q3+1.5-IQR, respectively. Diamond markers represent the Figure 6-2. Boxplot of activation properties at SS=0.4% at SNS and IZO. A) Total CCN concentration, B) N>80, C) AF, D) outliers. Time-resolution of the data is 1 hour.

The particle number concentration observed at SNS and IZO during the measurement period are in the range of values observed in the literature for highmountain environments. The values reported in the literature (Table 6-1) show large variability, with concentration decreasing as the altitude of the station and the distance to anthropogenic sources increases. In particular, the observed particle number concentration at SNS is similar to the one observed at Schneefernerhaus station at Zugspitze (2650 m a.s.l., in the German Alps) during the summer period (Birmili et al., 2009), while IZO shows concentrations in the range of those observed at Jungfraujoch (3580 m a.s.l., in the central Swiss Alps) that showed median values of 600 cm⁻³ (in the size-range 16-570 nm during summer) (Jurányi et al., 2011). It should be mentioned that summer is the period when SNS station is more influenced by transport of pollutants from the nearby metropolitan area of Granada due to mixing layer height growth and mountain-valley breeze regime (Casquero-Vera et al., 2020). In contrast, IZO is frequently under free troposphere (FT) conditions (Rodríguez et al., 2009), even during summer, and shows lower aerosol concentration compared to stations located at similar altitude.

Concerning the CCN concentration, lower concentrations are also observed at IZO than at SNS (Figure 6-2), as expected based on the particle number concentration in the different size ranges observed at each site (Figure 6-1). The median CCN concentration (at SS=0.4%) at SNS is 577 cm⁻³ compared to 142 cm⁻³ at IZO. As is the case for the total particle number concentration, CCN concentration at SNS is in the upper range of values observed at other mountain sites, while the opposite occurs at IZO (Table 6-1). In this sense, CCN concentrations at Jungfraujoch (at SS=0.47%) show mean value of 289 cm⁻³ (Jurányi et al., 2011); while Asmi et al. (2012) reported at Puy de Dôme, CCN concentrations in the range from 200-2000 cm⁻³ at SS=0.51%. Aryabhatta observatory also shows high CCN concentration (mean value of 1064 cm⁻³ at SS=0.46%) due to the strong influence of the ABL in the afternoon and anthropogenic activities during summer (Gogoi et al., 2015). Lower CCN concentration (at SS=0.42%) was observed at Storm Peak Laboratory (mean 250 cm⁻³) that is characterized by FT conditions at night and during the day is under the influence of the local boundary layer. However, it is probably less influenced by human activities (Friedman et al., 2013).

Despite the differences observed between SNS and IZO in terms of N and CCN concentrations, similar AF median values are observed at both sites (0.34 and 0.32 at SNS and IZO, respectively); but lower minima values are reached at IZO. D_{Crit} shows significantly larger values at SNS (median D_{Crit} = 82.0 nm) than at IZO (median D_{Crit} = 63.7 nm), denoting that smaller particles can activate at IZO compared to SNS. This results in larger hygroscopicity values at IZO than at SNS (the median κ value at SNS is 0.15 and 0.31 at IZO), probably due to the influence of marine aerosol and less presence of organics (Alastuey et al., 2005; García et al., 2017; Jaén et al., 2023; Rejano et al., 2024). Similar κ values to SNS are observed at others continental highmountain stations, such as Jungfraujoch or Storm Peak Laboratory (Table 6-1) which are also not influenced by marine aerosol particles.

It should also be noted that particle number concentration and activation properties show large variability (IQR in Figures 6-1 and 6-2). This variability is related with the strong diurnal changes observed at both sites (Fig. 6-3), which is typical of mountain environments (e.g. Rodríguez et al., 2009; Andrews et al., 2011; Collaud Coen et al., 2018). During nighttime, N shows almost constant values around 1000 cm⁻³ at SNS and significantly lower (around 400 cm⁻³) at IZO. At midday, both stations show an increase in N, N₁₂₋₂₅, N₂₅₋₁₀₀, and N₁₀₀₋₁₀₀₀. The great peak in nucleation mode N_{12-25} at both stations (Fig. 6-3 A) is associated with the high frequency of NPF events that occur at midday during summer (Rodríguez et al., 2009; Casquero-Vera et al., 2020). The peak in Aitken mode is observed one hour after nucleation due to the time that newly formed particles need to grow to larger sizes (Rejano et al., 2021). $N_{100-1000}$ is also higher at noon due to the increase in height of the ABL and winds that favor the transport of particles from lower altitudes (García et al., 2014; Casquero-Vera et al., 2020). This mode ($N_{100-1000}$) is the most sensitive to CCN activation because particles are large enough to act as CCN (Rejano et al., 2021). However, the D_{Crit} at IZO is in the range ~62 nm during nighttime and ~75 nm at midday, denoting that particles in the Aitken mode (N₂₅₋₁₀₀) are also activated. At SNS, the D_{Crit} ranges from ~72 nm during the night up to ~90 nm at noon. Concerning the AF, it shows the opposite diurnal pattern (minima values at midday at both stations, especially at IZO) (Fig. 6-3 D) due to the increase of nucleation mode particles (especially at IZO) that are too small to act as CCN. Differences in AF pattern between both stations are higher at midday with lower values at IZO because at this time the contribution of particles in nucleation mode is higher than at SNS (34% at IZO and 26% Ambient measurements of cloud condensation nuclei activation properties during Saharan dust events

at SNS). N_C also shows higher values at SNS (around 10 cm⁻³ and 3 cm⁻³ at SNS and IZO, respectively); however, no clear diurnal pattern is observed (Fig. 6-3 A).

The diurnal pattern of D_{Crit} (Fig. 6-3 E) with larger values at noon is related to less hygroscopic particles and therefore, smaller values of κ parameter (Schmale et al., 2018), especially at SNS (Fig. 6-3 F). The differences between both stations are associated with the influence of different aerosol sources and transformation processes. SNS is a continental high-mountain station with FT conditions during nigh-time but a strong prevalence of ABL influence and up-slope winds during daytime that promotes the transport of pollutants from lower altitudes (Rejano et al., 2021; Jaén et al., 2023; Rejano et al., 2024). On the other hand, IZO is a high-mountain station located in an island where the marine boundary layer (MBL) and trade winds prevail, except during nighttime when the station is mostly in the FT (Barreto et al., 2022). Therefore, higher anthropogenic influence is expected at SNS, where organic aerosols dominate the fine mode mass concentration (García et al., 2017; Rejano et al., 2024), leading to lower κ values; whereas at IZO, less anthropogenic influence is expected and the prevalence of particles from marine origin may led to higher κ values.

Table 6-1. Summary of mean activation parameters at different high-mountain stations at similar SS conditions. The table is sorted according to the altitude of the station.

Site location	Altitude	Period	PNSD Size-	N (cm ⁻³)	(%) SS	CCN (cm ⁻³)	AF	Dcrit	2	Reference
	(m a.s.l.)		range (nm)					(nm)		
Qilian Shan Station, China	4180	Summer	10.9-478.3	~ 1500	0.4	340	0.32	1	0.48	Xu et al. (2024)
Waliguan Baseline Observatory, China	3816	Summer	1	1	0.4	860		1		Xu et al. (2024)
Jungfraujoch Station, Switzerland	3580	Summer	16-570	596	0.47	289	0.5	89	0.17	Jurányi et al. (2011)
Storm Peak Laboratory, Colorado, USA	3210	Spring	20-800	~ 1000	0.42	250	0.25	1	0.2	Friedman et al. (2013)
Sierra Nevada Station, Spain	2500	Summer	12-20000	2500	0.4	645	0.36	80	0.2	This study
Izaña Observatory, Canary Islands, Spain	2367	Spring /Summer	12-20000	1170	0.4	160	0.32	99	0.32	This study
Aryabhatta Research Institute Observatory, India	2000	Summer	>10	1937	0.46	1064	0.46	1		Gogoi et al. (2015)
Puy de Dôme Station, France	1465	Summer	10-400	~ 3500	0.51	~800	1	65	0.22	Asmi et al. (2012)

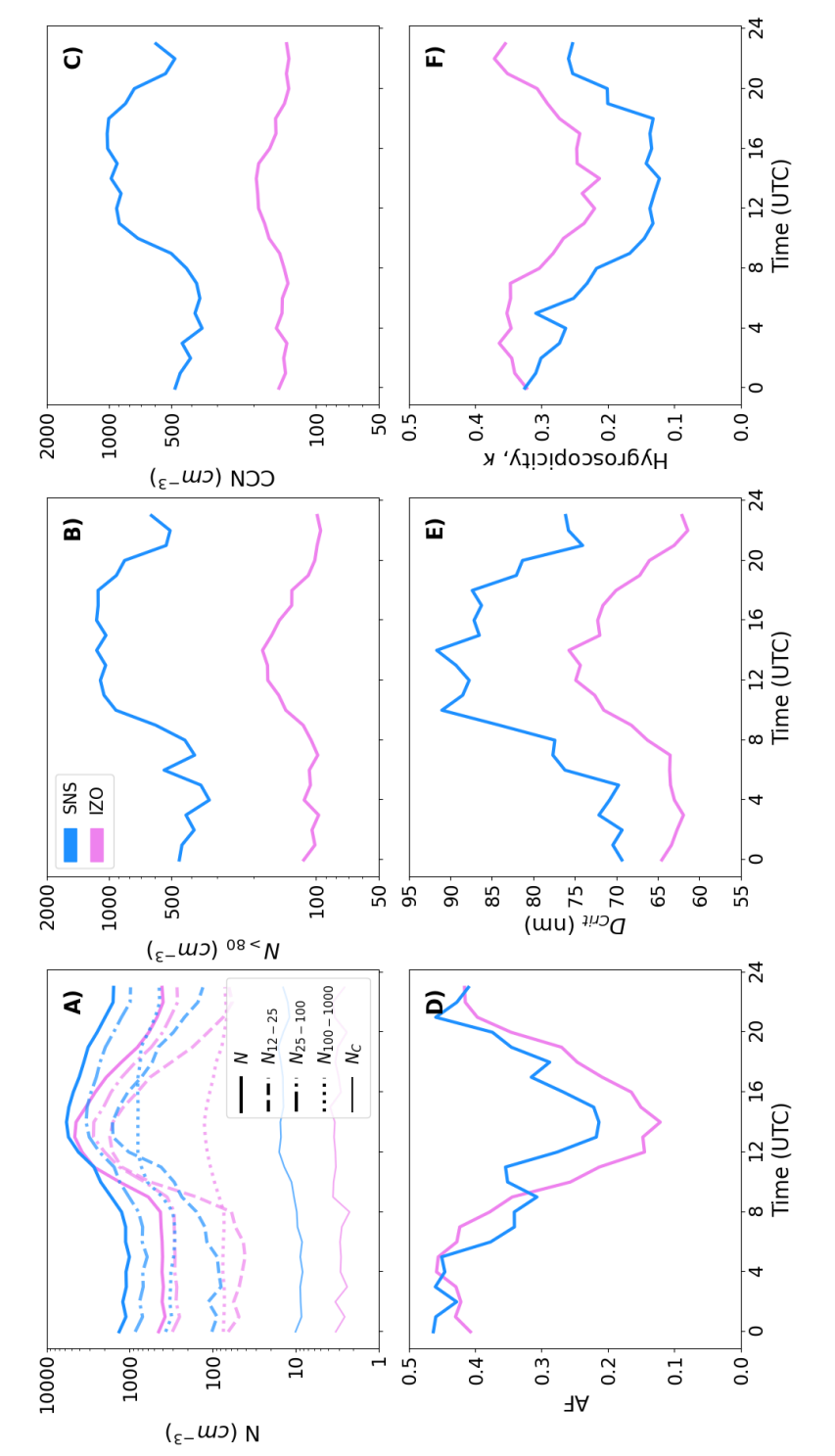


Figure 6-3. Diurnal patterns of A) N, N12-25, N25-100, N100-1000, and Nc, B) N>80, C) total CCN concentration, D) AF, E) D_{Crit} and E) κ at SS=0.4% at SNS (local time is UTC+2) and IZO (local time is UTC+1).

6.2 Identification of dust events at SNS and IZO

In order to identify the periods affected by transport of dust particles from the Sahara Desert at SNS and IZO, several tools have been used. Since dust particles are predominantly found in the coarse mode (particles larger than $1 \mu m$), an increase in coarse mode concentration or coarse mode contribution is expected during these events (Valenzuela et al., 2012; Mahowald et al., 2014). Figure 6-4 shows the temporal evolution of particle number concentration of fine (N_F, particles smaller than 1 μ m) and coarse (N_C, particles larger than 1 μ m) mode as well as the ratio between coarse mode and total aerosol concentration (N_c/N) at SNS (Fig. 6-4 A and B) and IZO (Fig. 6-4 C and D). Based on the increase in N_{C} and N_C/N, two potential dust events were identified at SNS and six at IZO during the measurement periods (Table 6-2). For this first identification of potential dust events, short periods (~hours) were not considered and only complete days in which there is a clear increase in N_C and N_C/N have been classified as potential dust events. It should be noted that due to low data availability of CCN measurements during dust event 6 at IZO (Fig. 6-4), this dusty period has not been considered for further analysis in the following sections.

Table 6-2. Dust events identified during the campaign at SNS and IZO.

Station	Dust Event Period				
SNS	1	11 th June-17 th June 2021			
	2 9 th July-12 th July 202				
	1	1 st May-3 rd May 2022			
IZO	2	8 th May-11 th May 2022			
	3	13 th May-15 th May 2022			
	4	7 th June-8 th June 2022			
	5	10 th June-13 th June 2022			
	6	19 th June-22 nd June 2022			

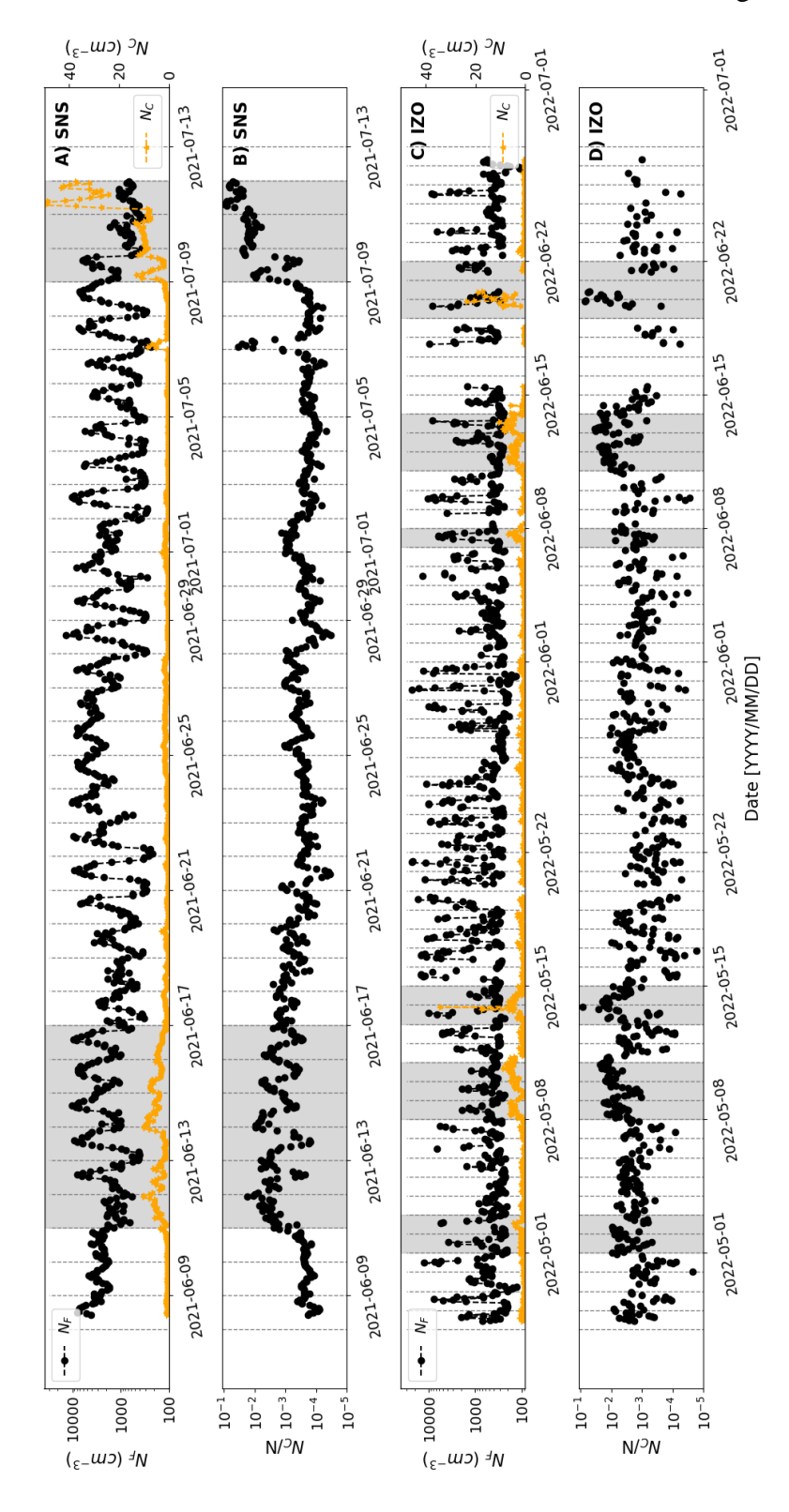


Figure 6-4. Temporal evolution of hourly N_F, N_C and N_C/N during the measurement campaigns at SNS (A and B) and IZO (C and D).

To confirm the influence of dust during the periods listed in Table 6-2, the synoptic conditions have been analyzed in detail for each dust period. Dust events might be characterized by different synoptic conditions that favor the advection of dust at the source region and the transport towards the southern Iberian Peninsula and the Canary Islands (Escudero et al., 2005). The geopotential maps (Figures 6-5 to 6-8) are an example corresponding with the synoptic condition during the most intense period of the dust event according to the $N_{\rm C}$ and $N_{\rm C}/N$ temporal variation at SNS and IZO.

During dust events identified at SNS, the synoptic pattern was characterized by a high-geopotential dipole with centers over Azores and North-Africa region, and a lower geopotential system over west of Portugal, and another low geopotential system northwest of Ireland. The interaction between the circulations of high and low centers favored dust advection towards the Iberian Peninsula in both cases (Figure 6-5).

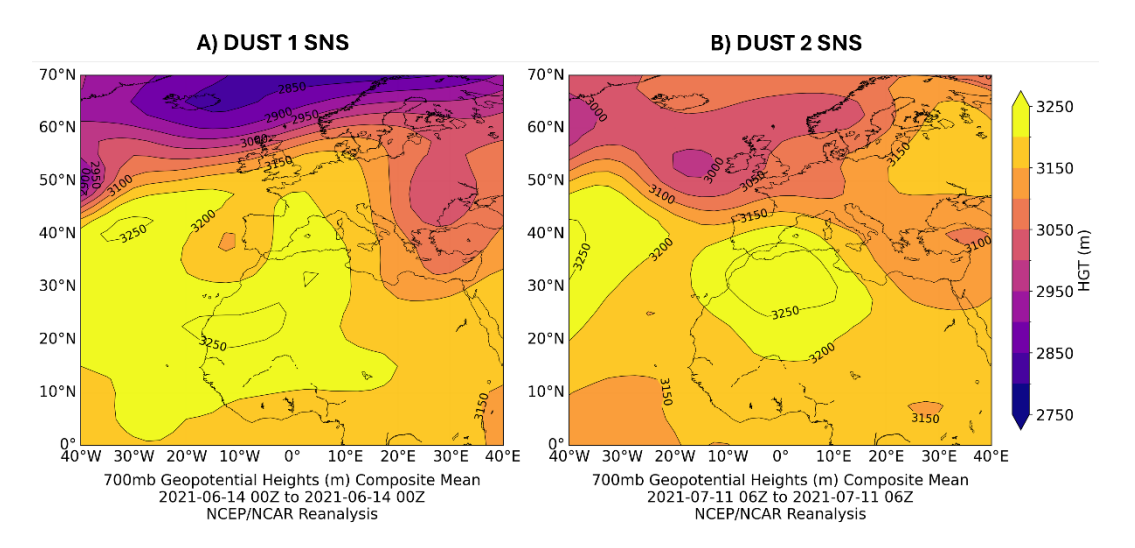


Figure 6-5. Geopotential height at 700 mb for A)14th June 2021 at 00:00 UTC corresponding with dust event 1 at SNS and B) 11th July 2022 at 06:00 UTC corresponding with dust event 2 at SNS. Data are from NCEP/NCAR - https://psl.noaa.gov/data/composites/hour/.

Specifically, for the first dust event at SNS, Figure 6-5 A shows the geopotential height maps at 700 mb. In this case, an area of high geopotential values is observed over the African continent, which slightly interacts with a low geopotential center located to the west of Lisbon. This interaction generates a southerly flow at low levels over Spain from northern Africa. This situation favors

Ambient measurements of cloud condensation nuclei activation properties during Saharan dust events

the advection of dry air with potentially high dust content from the Sahara northward, extending into the Iberian Peninsula. In the geopotential image for 11th July 2021 (Fig. 6-5 B), during the second dust event at SNS, a low-pressure center is observed at the surface over western Ireland, represented by a low geopotential height center at 700 mb and at upper levels (it has also been observed at 850 mb, Fig. 0-1 B in Appendix). From this low geopotential center, a trough extends to 40°N. Over northwest Africa, an area of high pressure, represented by a high geopotential height center in the lower and middle troposphere, extends its ridge to the Iberian Peninsula. The interaction between the circulation of this anticyclone and the ascending branch of the aforementioned trough is evident at the periphery of both systems. This generates strong southwesterly winds, which could potentially transport high dust concentrations towards the peninsula and, consequently, to SNS station.

It should be noted that the main difference between both events lies in the intensity and structure of the systems. In the second dust event, both the low-pressure system and the anticyclone are well-defined in height, and the interaction between the anticyclone and the ascending branch of the trough generated a strong low-level jet, potentially resulting in more intense dust transport to the region. In contrast, during the first event, the low and high geopotential centers were well-defined up to 700 mb, but the structure weakened near the surface (this behavior is not observed at 850 mb, Fig. 0-1 A in Appendix). Additionally, the isohypses were more spaced apart, resulting in weaker winds.

The synoptic conditions during the dust events at IZO favored dust advection over the Canary Islands. The most intense event (in terms of $N_{\rm C}$ and $N_{\rm C}/N$ increase) was dust event 5, in which the synoptic conditions for dust transport from Africa to the islands were more favorable than for the rest of events. Dust event 2 and dust event 5 were characterized by the influence of a low geopotential center embedded between two high geopotential centers, with the Canary Islands located to the north (during the second event) and to the south (during the fifth one) of the low geopotential center (Figure 6-6).

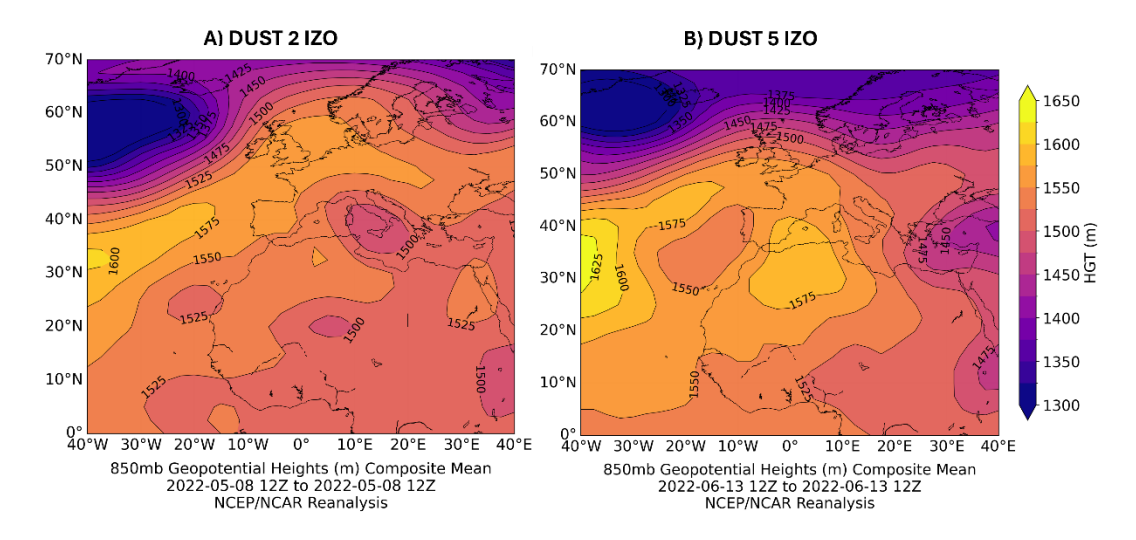


Figure 6-6. Geopotential height at 850 mb for A) 8th May 2022 at 12:00 UTC corresponding with dust event 2 at IZO and B) 13th June 2022 at 12:00 UTC corresponding with dust event 5 at IZO. Data are from NCEP/NCAR - https://psl.noaa.gov/data/composites/hour/.

During the second dust event at IZO (Fig. 6-6 A), the low geopotential center is observed at low, mid, and upper tropospheric levels. It was located south of the Canary Islands and moved northwestward as altitude increased. This center, combined with a weak high geopotential center located over northwest Africa and represented only at low levels, generated a southeasterly flow that transported dry air towards the islands. The expansive Azores-Bermuda anticyclone extended its ridge northeastward across the eastern Atlantic, reaching western Europe. The winds associated with the low geopotential center were strengthened by the interaction between this center and the two high geopotential centers.

During dust event 5 at IZO, Fig. 6-6 B shows a low geopotential center over the Madeira Islands, which shifted northwestward with altitude. The circulation of this system extended from the Canary Islands to the vicinity of Portugal. This low geopotential center separated two high geopotential systems: one over the central Atlantic and the other over northwest Africa and the Iberian Peninsula. The southerly flow associated with the high geopotential center over Africa brought dry, dust-laden air towards the Canary Islands. In this case, the systems were better defined than in the second event, extending throughout the tropospheric column, which caused the winds generated by the circulation between them to be more intense.

Ambient measurements of cloud condensation nuclei activation properties during Saharan dust events

Dust events 3 and 4 were characterized by the influence of the anticyclonic ridge of the Azores-Bermuda anticyclone over the Canary Islands. In both cases, the anticyclone exhibited secondary centers, one of which extended over northwest Africa, generating easterly winds towards the islands and thereby facilitating the advection of dry, dust-laden air.

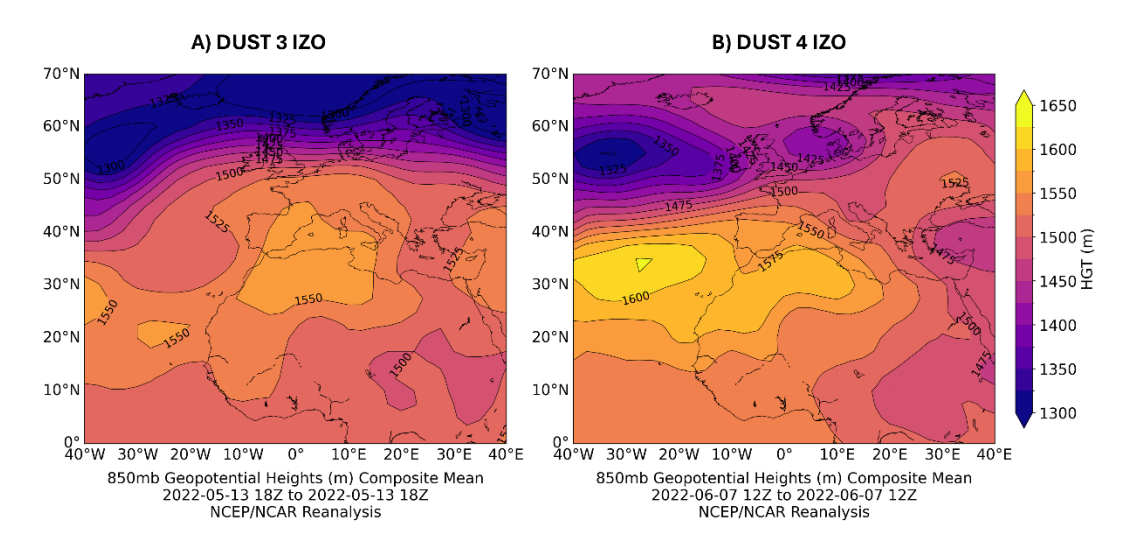


Figure 6-7. Geopotential height at 850 mb for A) 13th May 2022 at 18:00 UTC corresponding with dust event 3 at IZO and B) 13th June 2022 at 12:00 UTC corresponding with dust event 4 at IZO. Data are from NCEP/NCAR - https://psl.noaa.gov/data/composites/hour/.

During event 3 at IZO (Fig. 6-7 A), a broad high geopotential cell at 850 mb was located over northwest Africa, the western Mediterranean, and southeastern Spain. In contrast, during event 4 (Fig. 6-7 B), the extensive area of high geopotential was situated over the Atlantic and northwest Africa, with embedded centers descending in latitude as altitude increased. In both cases, the Canary Islands were within this broad circulation, promoting the advection of a mixture of moist air from the Atlantic and drier air from the desert, with dryness prevailing in the region.

Finally, during dust event 1 at IZO, the synoptic conditions were the least favorable for the advection of dust-laden air from Africa to the Canary Islands compared to the other events. In this case, the circulation of the outer ridge of the Azores-Bermuda anticyclone interacted with easterly winds over the western coast of Africa (Fig. 6-8). These easterly winds caused a decrease in humidity in the air

coming from the Atlantic, which is advected by the anticyclone. As a result, a mixture of moist and dry air, together with dust from the Sahara, was present over the Canary Islands.

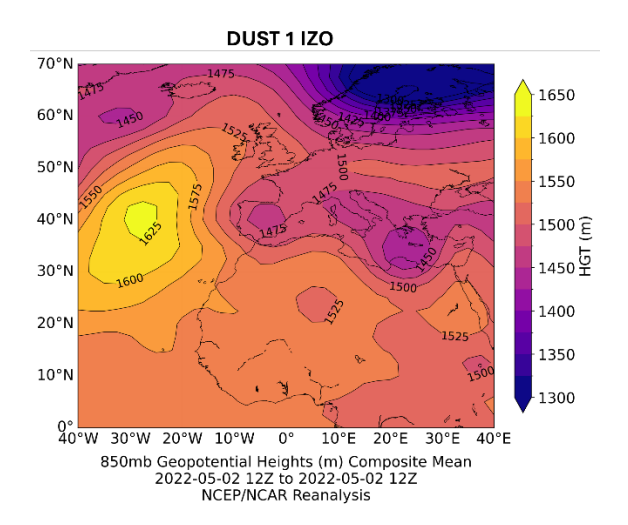


Figure 6-8. Geopotential height at 850 mb for A) 2nd May 2022 at 12:00 UTC corresponding with dust event 1 at IZO Data are from NCEP/NCAR - https://psl.noaa.gov/data/composites/hour/.

In addition to the increase in N_C and N_C/N , and the favoring atmospheric scenario for dust transport, we have confirmed the increase in mineral matter concentration during dust events (when available). During both campaigns at SNS and IZO, atmospheric particulate matter with aerodynamic diameters smaller than $10~\mu m$ (PM10) was collected in filters using high volume samplers. Filters were treated and weighted pre- and post-sampling, and a complete chemical analysis was performed over all filters sampled following the methodology of Querol et al. (2009b). At SNS day- and nighttime samples were collected (day filters from 10:00-18:00 UTC and night filters from 18:00-10:00 UTC) whereas at IZO, only day samples are available (from 8:00 to 16:00 UTC). Samples are available for dust event 1 at SNS, and dust events 1, 2 and 3 at IZO. For non-dusty periods we have considered all the filters available not included in the dust periods (44 samples at SNS and 34 samples at IZO).

Figure 0-2 and Figure 0-3 (Appendix) show the averaged percentages of contribution and absolute concentrations of the major components grouped as mineral (ΣAl_2O_3 , SiO_2 , CO_3 , $CO_$

Ambient measurements of cloud condensation nuclei activation properties during Saharan dust events

non-marine, NO₃-, NH₄+), sea spray (ΣNa, Cl, SO₄²-marine), organic carbon (OC) and elemental carbon (EC) (Titos et al., 2012) at SNS and IZO during non-dusty conditions and for each dust event identified, respectively. As it was expected, there is an increase in total PM10 concentration during dust events, also showing a higher contribution and absolute concentration of the mineral fraction during dust events than during non-dusty conditions. SIA absolute concentration is also higher during dusty conditions at both sites, which is associated with the high correlation with SO₄²⁻ transported in dust particle surface (Cipoli et al., 2023) and the aging of aerosols during atmospheric transport (Jaén et al., 2023). It has been observed, during dust event 1 at SNS, SO₄²⁻ (non-marine) concentration increased from 0.6 µg/m³ during non-dusty conditions to 1.1 µg/m³. At IZO, it raised from 0.3 μg/m³ during non-dust to 0.6, 0.7 and 0.4 μg/m³ during dust event 1, 2 and 3, respectively. On the other hand, sea spray has a negligible contribution at SNS (lower than 3% during dusty and non-dusty conditions), while at IZO it accounts for up to 16.5% of PM10 during non-dusty conditions and between 6.4%-10.1% during dust events. OC and EC are minor contributors to PM10 at IZO, while at SNS, OC concentration is >2 µg/m³ accounting for up to 22% of PM10 during non-dust conditions. As previous studies reported, it should also be noted that minerals are the most abundant compounds (at both stations), even during non-dusty conditions (García et al., 2017; Jaén et al., 2023). The chemical speciation of the mineral fraction shows SiO₂ as the most abundant component at SNS and IZO during dusty and non-dusty conditions. In addition, both sites present similar SiO₂ absolute concentration during non-dusty conditions (2.9 µg/m³ at SNS and 2.6 μg/m³ at IZO). However, during dust events as well as the increase in SiO₂ concentration (with enhancements between 100%-400%, depending on the intensity of each dust event, with respect to non-dusty conditions), CO₃²⁻ and Al₂O₃ also show a great increase (160% and 250%, respectively, at SNS and between 160%-760% for CO_3^{2-} and 100%-315% for Al_2O_3 at IZO). The increase of these compounds is associated with the transport of desert dust particles and it has also been previously observed during desert dust episodes in Spain (Nicolás et al., 2008; Galindo et al., 2017).

6.3 Influence of dust events on CCN concentration and activation properties

After identifying desert dust events, this section deals with the analysis of their influence on CCN activation properties. Figure 6-9 presents boxplots of N_{C} , N_{C}/N , N_{F} (particles ranging from 12 nm to 1 μ m), $N_{12\text{-}25}$, $N_{25\text{-}100}$ and $N_{100\text{-}1000}$ (nucleation, Aitken and accumulation modes, respectively) during the identified desert dust events and for non-dusty conditions at both sites. Additionally, Figure 6-10 shows the averaged aerosol size distributions for each period, while Table 6-3 summarizes statistical tests (Mann-Whitney U and Kruskal-Wallis non-parametric tests; Kruskal and Wallis, 1952; McKnight and Najab, 2010) to assess the significance of the observed differences with respect to non-dusty conditions for each dusty identified period.

As expected, dust events significantly enhance coarse mode concentration and their relative contribution to the total particle number concentration, $N_{\rm C}/N$, compared to non-dusty conditions at both stations. The second dust event at SNS and the second and fifth dust events at IZO show the highest increases in $N_{\rm C}$ and $N_{\rm C}/N$ at their respective sites. During the first dust event at SNS, the concentration of coarse particles is comparable to those observed during the second and fifth dust events at IZO, while the second event at SNS is the most intense. During dust event 2 at SNS (the most intense event analyzed), $N_{\rm C}$ values peaked below 60 cm⁻³, with a median value during the event of 10 cm⁻³, while at IZO, the maximum $N_{\rm C}$ value was 11 cm⁻³, recorded during dust event 5. It is also important to mention that although the increase in coarse mode particle number concentration is usually relatively modest (Walser, 2017), these particles contribute significantly to aerosol mass or volume due to their large size.

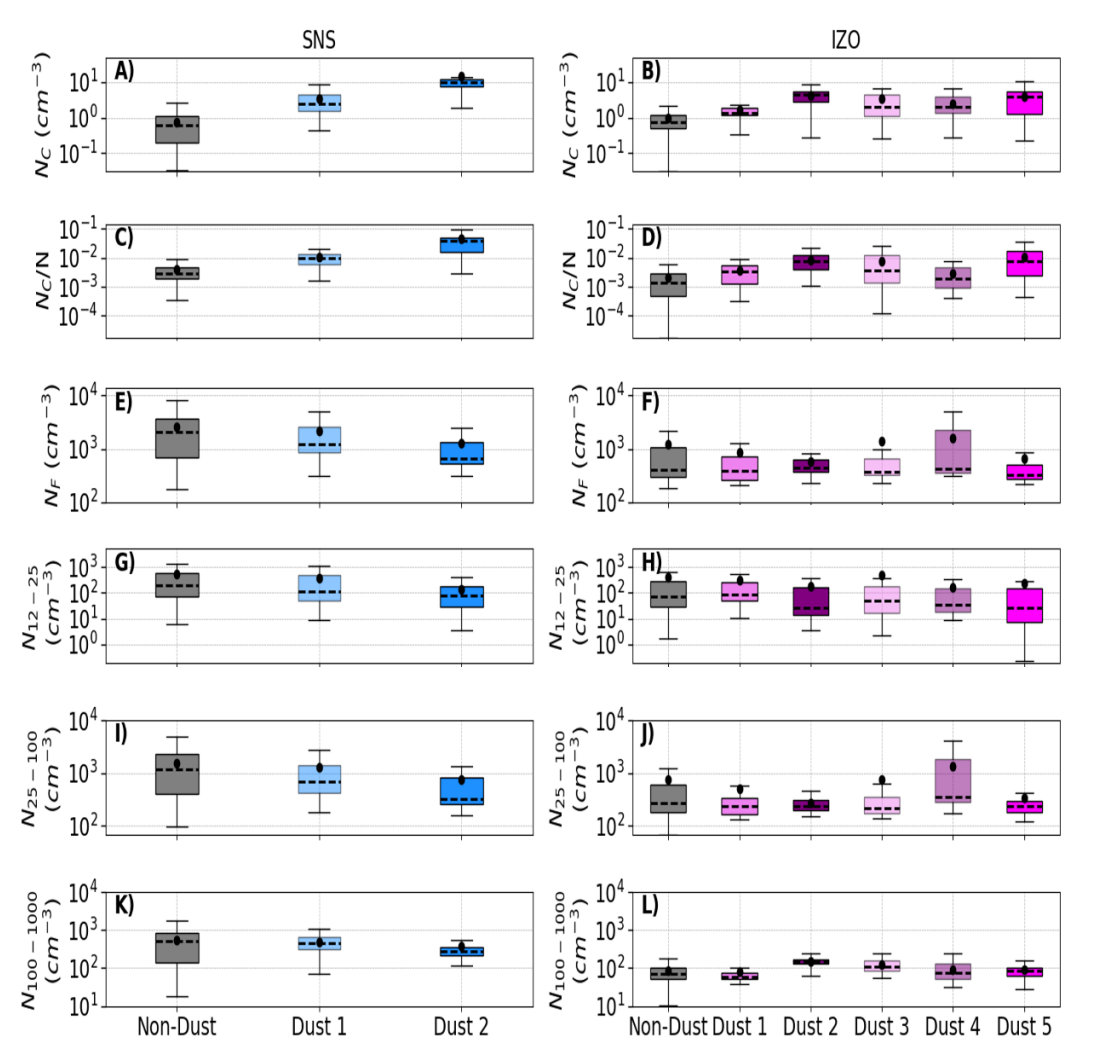


Figure 6-9. N_C (A, B), N_C/N (C, D), N_F (E, F), $N_{12\cdot25}$ (G, H), $N_{25\cdot100}$ (I, J) and $N_{100\cdot1000}$ (K, L) at SNS (left) and IZO (right) during non-dusty conditions and for each dust event identified. Black dot and dashed line represent the mean and median values, respectively. Lower and upper limits in the boxplots are the first (Q1) and third (Q3) quartiles respectively. The difference between them is the inter-quartile range (IQR). Lower and upper whiskers show Q1-1.5·IQR and Q3+1.5·IQR, respectively. Outliers are omitted for clarity purposes.

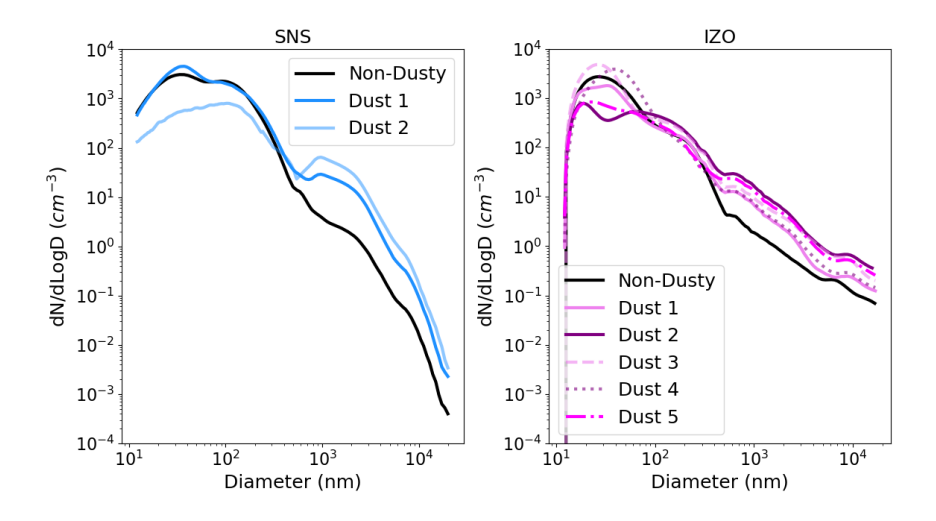


Figure 6-10. Averaged particle number size distributions during non-dusty conditions and dust events at SNS and IZO.

Table 6-3:Summary of Mann-Whitney U and Kruskal-Wallis tests for dust events identified at SNS and IZO. "Yes" indicates that differences are significant with p-values < 0.05 compared to non-dusty conditions

Variable	SNS		IZO					
variable	Dust 1	Dust 2	Dust 1	Dust 2	Dust 3	Dust 4	Dust 5	
Nc	Yes							
Nc/N	Yes							
NF	No	Yes	No	Yes	No	Yes	Yes	
N ₁₂₋₂₅	Yes	Yes	No	Yes	No	Yes	Yes	
N ₂₅₋₁₀₀	Yes							
N ₁₀₀₋₁₀₀₀	No	Yes	No	Yes	Yes	No	Yes	
Size-distribution (12-535 nm)	Yes	Yes	No	Yes	No	Yes	Yes	

In addition to the anticipated effects of dust events on the coarse aerosol mode, notable changes were also observed in the fine aerosol mode size distribution during these events, as shown in Figures 6-9 and 6-10, and in Table 6-3. The observed reduction in fine mode particle number concentrations during dust events primarily stems from decreases in N_{12-25} (except for dust event 1 at IZO) and N_{25-100} (except during dust event 4 at IZO). This reduction is statistically significant

Ambient measurements of cloud condensation nuclei activation properties during Saharan dust events

for dust event 2 at SNS and dust events 2, 4, and 5 at IZO. The observed decrease may be linked to the role of larger desert dust particles acting as a coagulation sink, which could inhibit particle formation and growth (Manktelow et al., 2010; Hussein et al., 2011; Casquero-Vera et al., 2023). However, reduced efficiency in transporting aerosols from lower altitudes during dust events, likely due to changes in the atmospheric boundary layer (ABL) dynamics, may also contribute to this effect (Adame et al., 2015).

Despite the decrease in fine particle number concentration, mean values of N_F , N_{12-25} , and N_{25-100} remain at the upper limit of the interquartile range (IQR) or within the upper whisker. This phenomenon is likely driven by outliers (not shown in Fig. 6-9 for clarity purposes), associated with high nucleation mode concentrations during NPF events at midday (as discussed in Sect. 6.1), which can still occur even during dust episodes (Casquero-Vera et al., 2023).

Throughout the day, various atmospheric processes, including NPF events and the transport of aerosols and precursors from the ABL, occur at both SNS and IZO. These concurrent phenomena, combined with the atmospheric conditions that facilitate dust transport, may influence cloud condensation nuclei (CCN) activity. To isolate the impact of dust from other processes occurring throughout the day, data have been divided into two-time frames: daytime (10:00 to 20:00 UTC) and nighttime (20:00 to 10:00 UTC). This analysis focuses on the more intense dust events, characterized by higher $N_{\rm C}$ and $N_{\rm C}/N$ ratios, which show statistically significant differences from non-dusty conditions. Specifically, dust events 1 and 2 at SNS and dust events 2 and 5 at IZO are examined.

Figure 6-11 presents boxplots of Nc, Nc/N, NF, N₁₂₋₂₅, N₂₅₋₁₀₀, and N₁₀₀₋₁₀₀₀ for both daytime and nighttime at SNS and IZO. We conducted Kruskal-Wallis tests to determine whether the differences between dust events and non-dusty conditions are significant. To observe if these differences are more pronounced during the day or night, the Kruskal-Wallis coefficient (Kc) was used, with higher Kc values indicating greater differences (see Tables 0-3 and 0-4 in Appendix). Additionally, Figure 6-12 illustrates the ratio of the median values of dusty to non-dusty conditions for each variable, denoted as the variable name with D/ND as a superscript (e.g., $N_{\rm F}^{\rm D/ND}$ represents the ratio of median fine particle number concentrations during each dust event compared to non-dusty conditions). It

should be noted that to clarify the figure, grey bars refer to the ratio of non-dusty to non-dusty conditions during day- and nighttime. Thus, the values of all of them are 1.

As previously noted, N_C and N_C/N increase during dusty conditions with respect to non-dusty at both SNS and IZO, regardless of the time of day (refer to Fig. 6-11 A, B, C, and D). However, this enhancement is more pronounced and statistically significant at night, as indicated by higher K_C values (Table 0-3 and 0-4 in Appendix), especially at SNS, which also reflects higher $N_C^{D/ND}$ during nighttime (8.6 and 30.6 for dust event 1 and dust event 2, respectively at night with respect to 3.1 and 13.7, respectively during daytime) (Fig. 6-12 A). In contrast, fine particle number concentrations decrease with respect to non-dusty conditions during the day ($N_F^{D/ND}$ <1) for all dust events at both stations, although this difference is not statistically significant during dust event 1 at SNS (Table 0-3). These day-night differences suggest that, beyond a reduced contribution of transported particles during the day, coagulation of fine particles due to desert dust presence may also play a role. This reduction is particularly notable during dust event 2 at SNS and dust event 5 at IZO.

Regarding nucleation, Aitken, and accumulation mode particles, the accumulation mode is the only size range where particle concentrations consistently increase during nighttime dust events at both sites ($N_{100-1000}^{D/ND} > 1$) (Fig. 6-12). This enhancement likely reflects the presence of dust particles within this size range, as reported by Hussein et al. (2018). However, during the day, accumulation mode particle concentration at SNS shows a different trend, showing lower median values during dusty conditions ($N_{100-1000}^{D/ND} < 1$). This behavior is attributed to the large influence of particles in this size range at SNS (i.e., Casquero-Vera et al., 2020; Rejano et al., 2021), which is associated with atmospheric transport within the ABL. Since this dynamic is disrupted during dust events, the conditions favoring the transport of pollutants from Granada to SNS may also change.

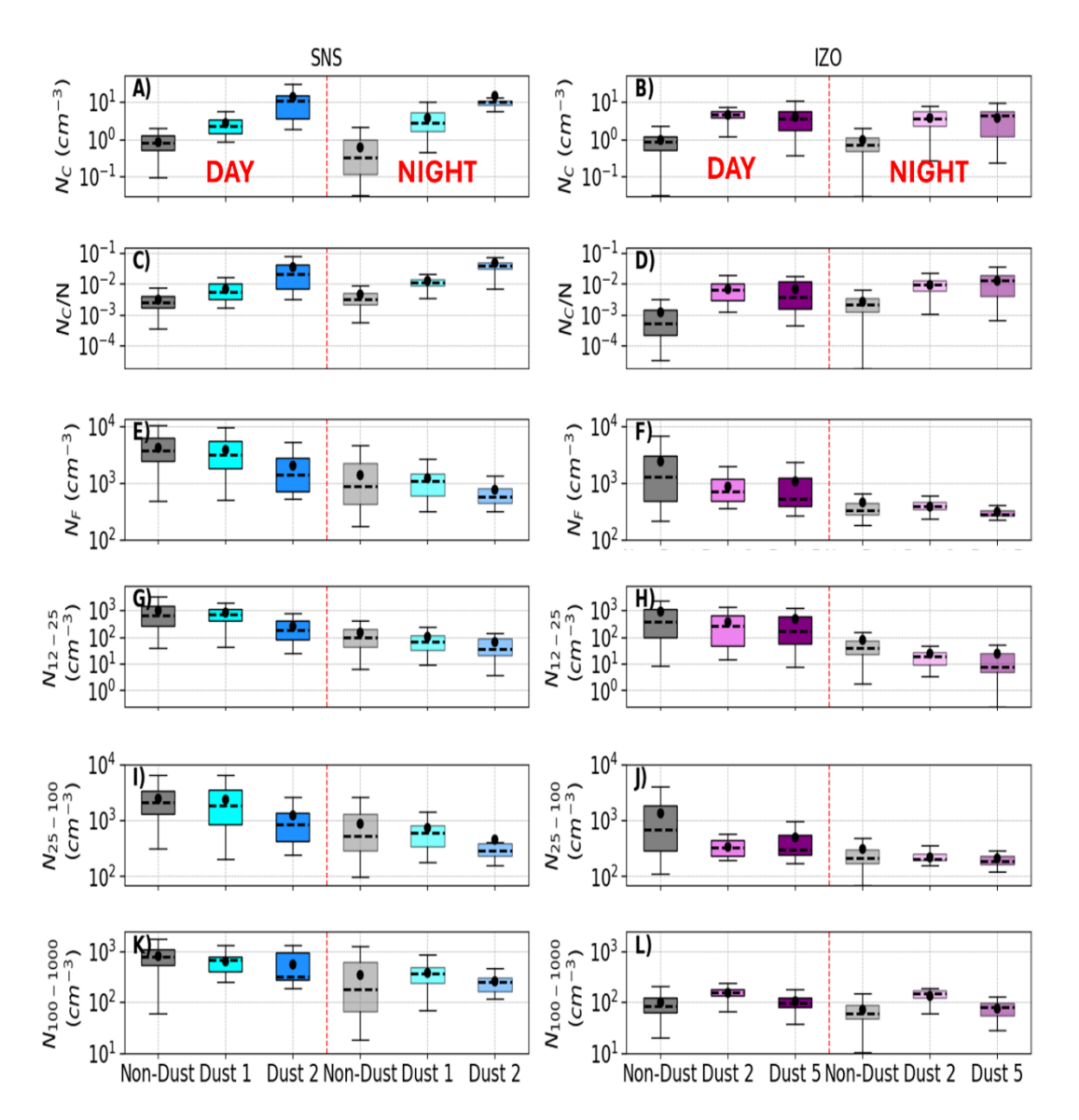


Figure 6-11.Nc (A,B), Nc/N (C,D), N_F (E,F), N₁₂₋₂₅ (G,H), N₂₅₋₁₀₀ (I,J) and N₁₀₀₋₁₀₀₀ (K,L) at SNS during day and nighttime (left) and IZO (right) for non-dusty conditions and for the more intense dust events identified. Black dot and dashed line represent the mean and median values, respectively. Lower and upper limits in the boxplots are the first (Q1) and third (Q3) quartiles respectively. The difference between them is the inter-quartile range (IQR). Lower and upper whiskers show Q1-1.5·IQR and Q3+1.5·IQR, respectively. Outliers are omitted for clarity purposes.

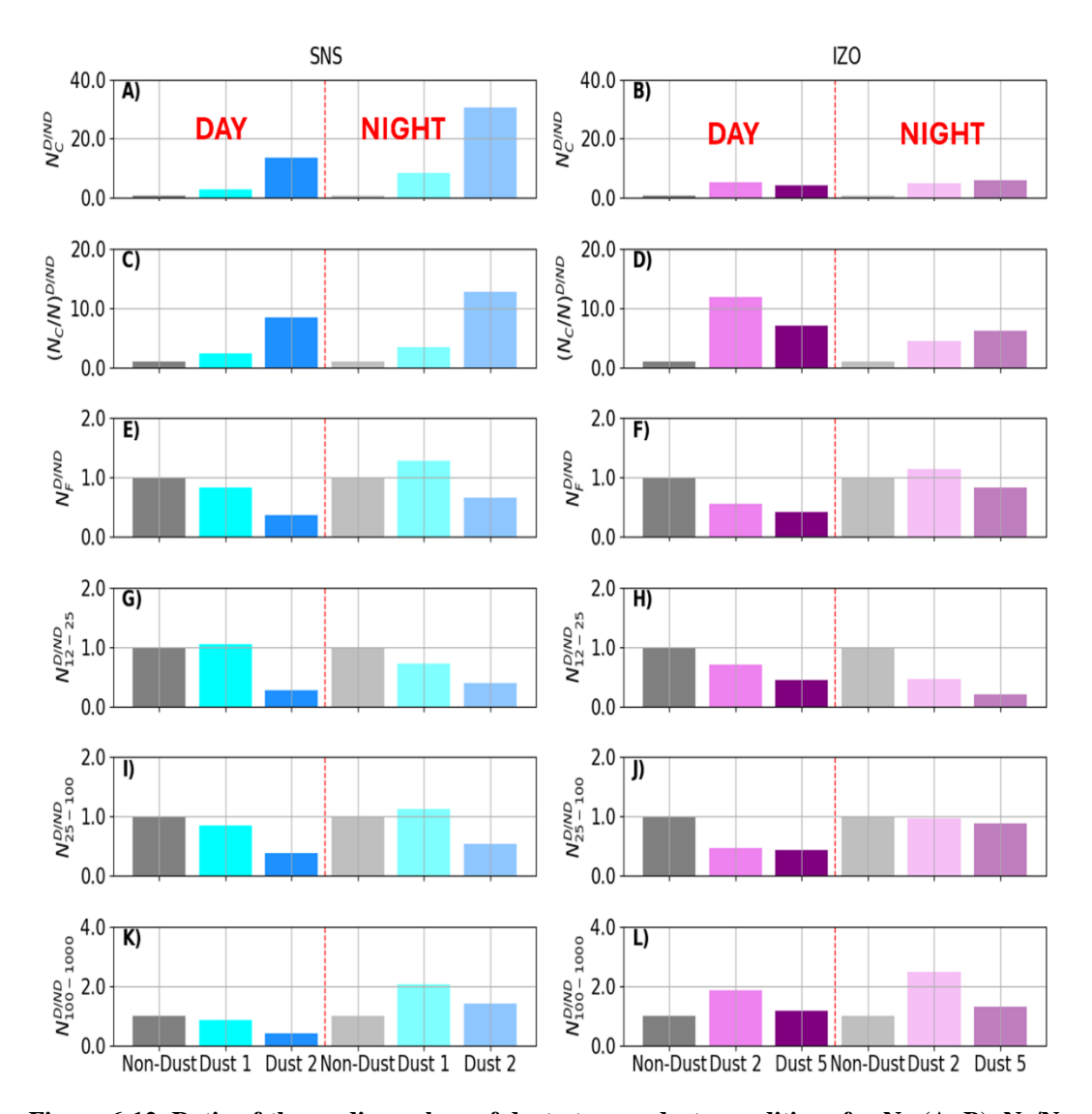


Figure 6-12. Ratio of the median values of dusty to non-dusty conditions for $N_{\rm C}$ (A, B), $N_{\rm C}/N$ (C, D), $N_{\rm F}$ (E, F), $N_{12\text{-}25}$ (G, H), $N_{25\text{-}100}$ (I, J) and $N_{100\text{-}1000}$ (K, L) at SNS during day and nighttime (left) and IZO (right) denoted as the variable name with D/ND as a superscript.

Due to the differences observed in particle number concentrations and size distributions, the influence of dust events on CCN activation properties may also vary between day- and nighttime. Figure 6-13 shows the activation properties at SS=0.4% for dust events 1 and 2 at SNS and dust events 2 and 5 at IZO, during day- and nighttime. Additionally, Figure 6-14 illustrates the ratio of dusty to non-dusty conditions for the CCN activation properties, denoted as the variable name with $\rm D/ND$ as a superscript (e.g., $\rm CCN^{D/ND}$ represents the ratio of median CCN

Ambient measurements of cloud condensation nuclei activation properties during Saharan dust events

concentrations during each dust event compared to non-dusty conditions). Similarly to Figure 6-12, grey bars are represented for clarity purposes, and they refer to the ratio of non-dusty/non-dusty conditions, therefore, they reach 1 value.

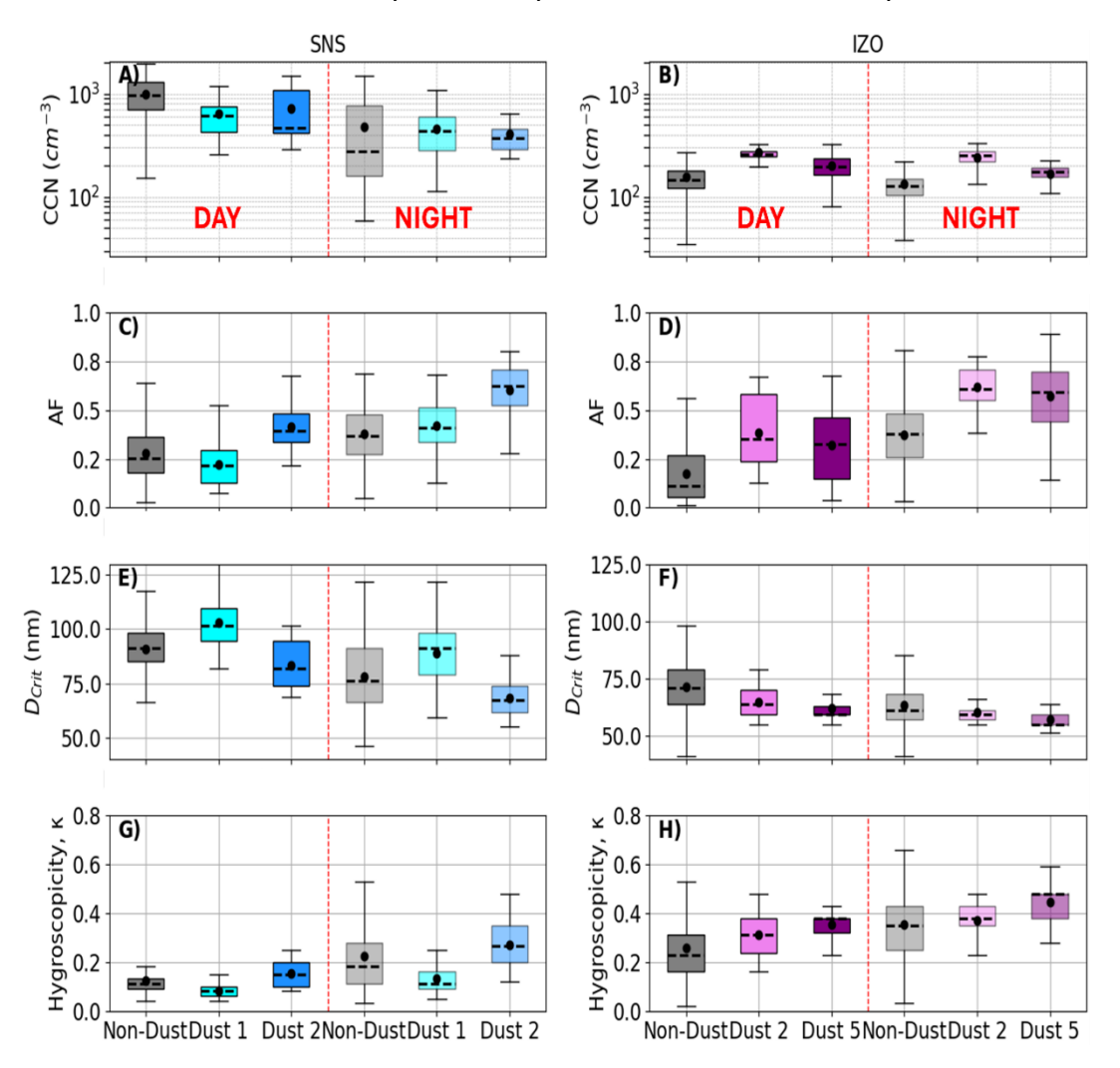


Figure 6-13. CCN (A, B), AF (C, D), D_{Crit} (E, F) and κ (G, H) (SS=0.4%) during day and nighttime at SNS (left) and IZO (right) during non-dusty conditions and more intense dust events. Black dot and line represent the mean and median values, respectively. Lower and upper limits in the boxplots are the first (Q1) and third (Q3) quartiles respectively. The difference between them is the inter-quartile range (IQR). Lower and upper whiskers show Q1-1.5·IQR and Q3+1.5·IQR, respectively. Outliers are omitted for clarity purposes.

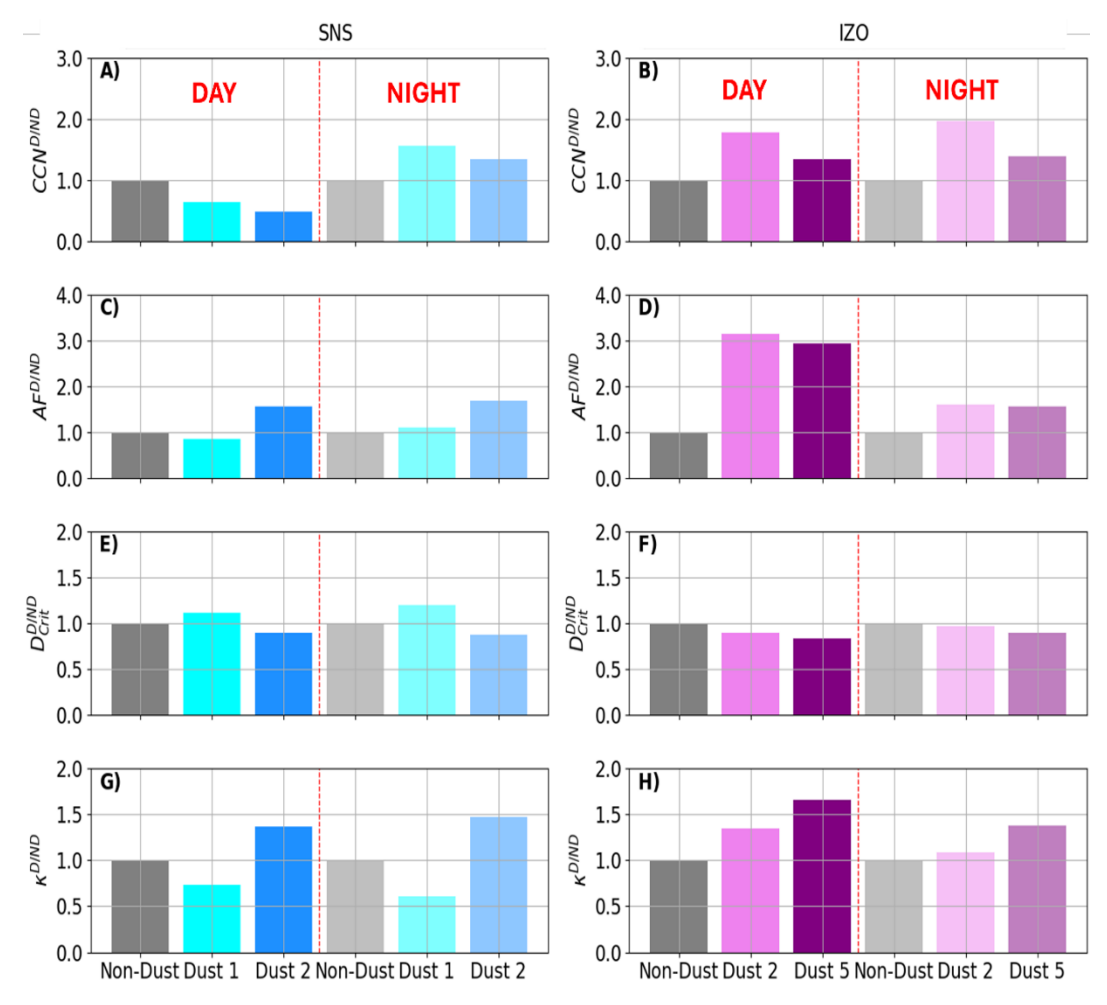


Figure 6-14. Ratio of the median values of dusty to non-dusty conditions for CCN (A, B), AF (C, D), D_{Crit} (E, F) and κ (G, H) (SS=0.4%) during day and nighttime at SNS (left) and IZO (right), denoted as the variable name with D/ND as a superscript.

The trend in CCN concentration during dust events closely mirrors that of accumulation mode particle number concentration, as particles in this size range are highly likely to activate as CCN. Contrasting trends with respect to non-dusty conditions are observed during the day at SNS (CCN $^{\rm D/ND}<1$) and IZO (CCN $^{\rm D/ND}>1$), with CCN concentrations decreasing at SNS and increasing at IZO. The decrease observed at SNS during daytime may be attributed to the reduced influence of the ABL during dust events, whereas this effect is less significant at IZO. Conversely, at night, CCN concentrations increase at both sites, that might be related to presence of dust particles in the accumulation mode that can activate as CCN.

Ambient measurements of cloud condensation nuclei activation properties during Saharan dust events

Activated fraction (AF) exhibits higher values during dusty conditions, reaching values around 0.6 during dust event 2 at SNS, and during both dust events at IZO at night. For dust event 1 at SNS, AF shows a slight increase at night but decreases during the day, due to a higher contribution of nucleation mode particles contributing to the total particle number concentration (N) (22% during dust event 1 and 13% during dust event 2) but these smaller particles are less likely activating as CCN due to their lower size. At IZO, Figure 6-14 D shows that the increase in AF values with respect to non-dusty conditions is more relevant during the day due to the greater reduction of concentration of particles confined in Aitken mode (which they can also be too small to act as CCN) than during nighttime (the median values of Aitken mode concentration during dust events are reduced 50% and 10% during daytime and nighttime, respectively).

In contrast to AF, D_{Crit} decreases during dust event 2 at SNS and dust events 2 and 5 at IZO compared to non-dusty conditions (Fig. 6-13 E and F), resulting in higher κ values (D_{Crit}^{D/ND} < 1 and $\kappa^{D/ND}$ > 1 for all events except for dust event 1 at SNS, Fig. 6-14). The different behaviour observed during dust event 1 at SNS could be explained by a higher presence of pollutants with non-hygroscopic properties (e.g. Titos et al., 2014b; Rejano et al., 2024) during this event. However, this hypothesis cannot be confirmed without additional measurements of pollution tracers, such as NOx or speciated chemical composition. Shen et al. (2023) also observed an increase of hydrophobic particles during a dust storm, reducing κ values; probably due to a large contribution of components such as Al- and Si-, which are non-hygroscopic; (Kelly et al., 2007) that could present hydrophobic behavior (Coz et al., 2009; Karydis et al., 2011). However, there are also studies (e.g. Zhang et al., 2019; Sun et al., 2024b) that reported opposite results in which enhancements of sulfates during dust outbreaks raise κ (Perry et al., 2004). Other studies (e.g. Gibson et al., 2006; Sullivan et al., 2009) revealed that both freshly emitted (Gibson et al., 2006) and aged or processed mineral dust (Ro et al., 2005) turn out to be hygroscopic (Vlasenko et al., 2006; Kostenidou et al., 2015). In addition, strong dust events with a reduction of fine particles concentration, imply the presence of larger particles that tend to be more effective at attracting water vapor because their radius of curvature is smaller than that of smaller particles (Kelvin effect). Therefore, it could also result in more hygroscopic behavior.

Conclusions

The results discussed in this section refer to SS=0.4%. In agreement with Lee et al. (2009) that reported that CCN properties during dust events have similar behavior at SS>0.2%, we have also observed similar patterns at all SS (SS=0.2%, 0.4%, 0.6% and 0.8%) (not shown). At SS>0.4%, dust events have a more pronounced impact on CCN concentrations and AFs during nighttime compared to non-dusty conditions. However, similarly to SS=0.4%, the influence of dust events on $D_{\rm Crit}$ and κ continues to differ between day- and nighttime. Therefore, further long-term observational studies are necessary to fully understand the influence of dust events on CCN concentration and activation properties.

6.4 Conclusions

In this chapter we have analysed the CCN activation properties at two highmountain stations SNS and IZO, which are frequently influenced by Saharan dust intrusions. The CCN and activation properties phenomenology have been studied and the impact of different dust events that took place during measurement periods have also been studied.

Our results show that total particle number concentration and the concentration of all modes are higher at SNS than at IZO; being Aitken mode ($N_{25\text{-}100}$) the most relevant at both sites. Consequently, CCN concentration is also higher at SNS. AF show similar maxima values at both sites but lower minima values at IZO due to the higher contribution of newly formed particles in the size range of nucleation mode at midday. At noon, there is an increase in Aitken and accumulation mode particles concentration produced by transported particles from lower altitudes when the ABL height increases. This effect is more pronounced at SNS than at IZO, leading to higher CCN concentrations. Concerning activation parameters such as D_{Crit} , the observed values are higher at SNS than at IZO; therefore, κ parameter is lower at SNS due to the potential greater influence of organic particles at SNS and sea salt aerosol particles at IZO.

The impact of dust events is linked to observed increase in coarse mode concentration. Two dust outbreaks were observed at SNS; whereas at IZO, six dust intrusions have been identified. Synoptic situations also confirm the transport of

Ambient measurements of cloud condensation nuclei activation properties during Saharan dust events

dust particles from Sahara Desert. All dust events showed different properties and intensity (being the strongest one with the highest increase of coarse mode concentration and highly favourable synoptic situation, dust event 2 at SNS). In general, dust events do not represent a large contribution to particle number concentration; however, changes in activation properties as CCN have been found. To isolate the effect of dust and additional atmospheric processes that can occur during the day at both stations, the influence of dust events has been studied separating day- and nighttime periods.

Our results suggest that dust particles can reduce submicron particle concentration if N_C is large enough so that the larger particles are able to act as coagulation sink of smaller particles. Additionally, the results point out to a less efficient transport from lower altitudes during dust events during daytime that can also contribute to reduce particle number concentration and CCN concentration (especially at SNS). At night, an enhancement in $N_{100-1000}$ concentration has been observed during dust events with respect to non-dusty conditions denoting presence of dust particles in accumulation mode. Linked to this increase in accumulation mode, CCN concentration during dust events, at night, is also higher compared to non-dusty conditions at both stations denoting dust particles are able to activate as CCN. The reduction of small particles concentration in nucleation and Aitken mode and the increase in accumulation mode during dust events is associated with higher AF values; except for dust event 1 at SNS. This dust episode at SNS may have been produced under more polluted conditions because there was not a clear reduction in fine mode concentration. In addition, the presence of non-hygroscopic particles would tend to increase D_{Crit} and reduce κ values. The rest of dust events show lower D_{Crit} and consequently, higher κ values with respect to non-dusty conditions.

There are not many observational studies about the influence of dust events on CCN activation properties. This work is focused on experimental and direct CCN measurements, and we have observed that depending on the intensity of dust events, their impact on activation properties can be different. To obtain more conclusive results, long-term measurements over stations frequently influenced by dust events are necessary, which will help to provide a more robust statistics and

Conclusions

improve the understanding of the influence of dust events on CCN concentrations and activation properties under a variety of atmospheric conditions.

7. Impact of new particle formation on the cloud condensation nuclei budget

This chapter has been adapted from "Determining the impact of new particle formation events on cloud condensation nuclei (CCN) concentrations "by A. Casans, J.A. Casquero-Vera, F. Rejano, H. Lyamani, A. Cazorla, I. Zabala, W. Huang, M. Agro', A. Barreto, S. Rodríguez, Y. González, F. Bianchi, T. Petäjä, F.J. Olmo, L. Alados-Arboledas, P. Cariñanos, M. Gysel-Beer and G. Titos. Published in *Science of the Total Environment*, Volume 972, 1 April 2025, 179094

This chapter introduces a novel methodology to estimate the direct contribution of NPF events to CCN concentrations, distinguishing between NPF-generated particles and background or transported aerosols. Developed using size-resolved CCN measurements at the high-altitude remote observatory SNS, the method is also suitable for polydisperse CCN measurements, showing good agreement between both types of estimates. The method was also applied to polydisperse data during NPF events at IZO, comparing NPF contributions at both sites. Despite frequent NPF events at SNS and IZO, their differing environmental and aerosol characteristics provide insights into the method's limitations and advantages (also explained in this section).

The data used in this chapter was gathered during the same measurement campaigns as in Chapter 6. SNS: 8th June to 12th July 2021 with size-resolved CCN data available from 24th June to 12th July 2021; and IZO: 27th April to 27th June 2022. During both campaigns, the CCNC-200 was used. At SNS, one column measured in polydisperse mode at varying SS (0.2%, 0.4%, 0.6%, and 0.8%), holding each SS constant for 10 minutes, while the other column measured in size-resolved mode under the same SS conditions and time scan configuration. At IZO, one column measured in polydisperse mode with the same SS conditions (0.2%, 0.4%, 0.6%, and 0.8%), but holding each SS constant for 6 minutes. The other column of the CCNC-200 also measured in polydisperse mode at a constant SS (SS=0.4%).

7.1 NPF events at SNS and IZO stations

New particle formation (NPF) events are frequently produced at both sites (García et al., 2014; Casquero-Vera et al., 2020). Therefore, using the guidelines in Dal Maso et al. (2005), we classified the measurement days at both sites into the following categories: (i) NPF event, (ii) non-event, (iii) undefined and (iv) bad-data days by visual inspection of the daily PNSD temporal evolution. We classified NPF event days as those when sub-25 nm particle formation was observed, followed by particle growth. Days on which neither new growing modes nor the production of sub-25 nm particles were observed, were classified as non-event days. The remaining days were classified as undefined or bad-data days.

As has already been observed, SNS and IZO stations are frequently affected by Saharan dust outbreaks, which might influence the occurrence of NPF events and aerosol characteristics (e.g. Casquero-Vera et al., 2023). Hence, we excluded the days influenced by Saharan dust from our analysis. At SNS, we focused on NPF events with concurrent size-resolved and polydisperse CCN data. Following these criteria, we compiled a high-quality database of 5 NPF event and 5 non-event days at SNS and 18 NPF event days and 3 non-event days at IZO.

The mean diurnal evolution of particle number concentration in different size modes (N_{12-25} , from 12 nm to 25 nm, N_{25-100} from 25 nm to 100 nm and $N_{100-535}$ from 100 nm to 535 nm) during NPF event and non-event days at SNS and IZO is shown in Figure 7-1 (A and C) while the mean PNSD diurnal evolution for both sites is shown in Figure 0-4 (Appendix). In general, particle number concentrations at SNS are higher than at IZO across all size ranges investigated. However, during NPF events, N_{12-25} and N_{25-100} exhibit more similar values at both sites. Among the three size ranges, N_{25-100} (Aitken mode) shows the highest concentrations throughout the day at both sites, for both NPF and non-NPF days, contributing the most to total particle number concentration. During NPF events, particle number concentration in the three aerosol modes display a clear diurnal cycle. This cycle is characterized by an increase in concentration from around 09:00 UTC, peaking at noon and decreasing during night-time at both sites. The time at which N_{12-25} begins to increase is typically considered the onset of NPF events (Kalkavouras et al., 2019). As observed in previous studies at these sites (e.g. Rodríguez et al., 2009;

García et al., 2014; Casquero-Vera et al., 2020), the noon-time aerosol concentration increase is likely associated with the diurnal growth of the boundary layer, which transports gases and aerosol particles from lower altitudes. In addition, the more pronounced increase in the concentration of smaller particles during NPF event days suggests that these events contribute significantly to the total particle number concentrations at both sites, especially in the nucleation and Aitken modes.

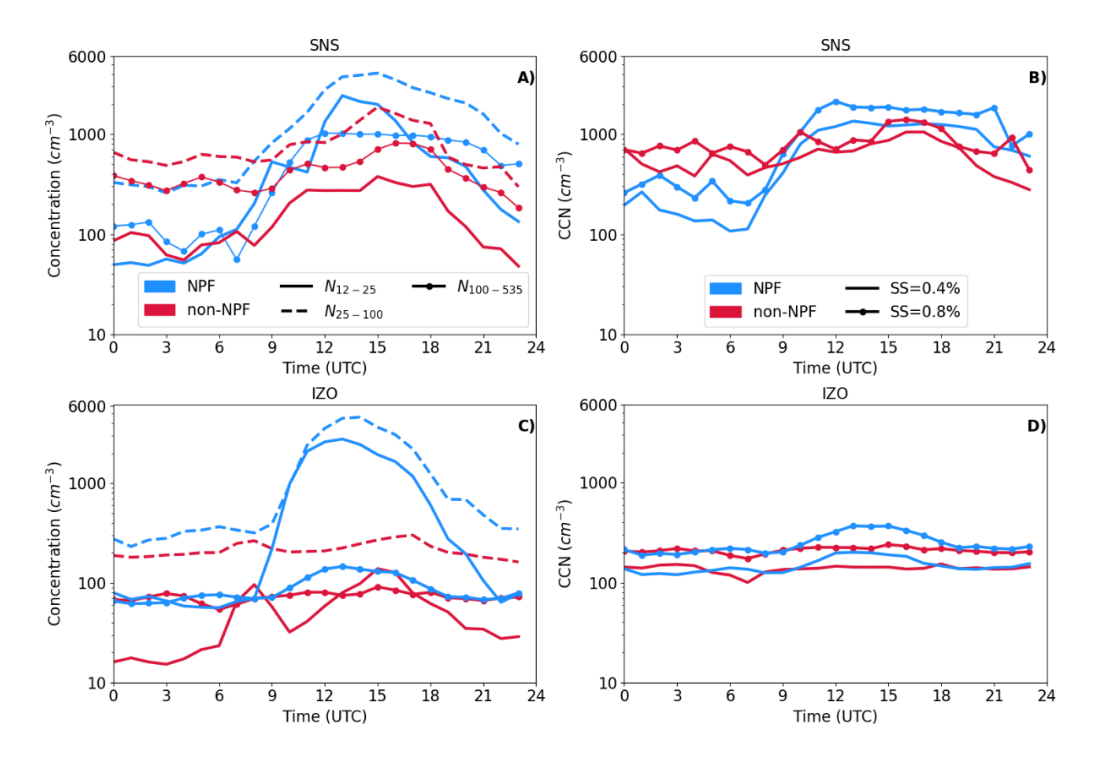


Figure 7-1. A) Mean diurnal evolution of aerosol concentration in different modes (12-25 nm, 25-100 nm and 100-535 nm) during NPF event days and non-NPF event days at SNS and C) IZO. B) Mean diurnal evolution of total CCN concentration at SS=0.4% and SS=0.8% at SNS and D) IZO. Local time is UTC+2 at SNS and UTC+1 at IZO.

Figure 7-1 (B and D) shows the mean diurnal evolution of total CCN concentration at SS=0.4% and SS=0.8% at SNS and IZO during NPF event and non-event days. Consistent with the particle concentration results, where SNS exhibited higher concentrations (especially for larger particles, which are expected to activate as CCN), CCN concentrations were also higher at SNS than at IZO. The diurnal patterns of CCN concentrations reveal a pronounced increase at noon during NPF days, whereas a flatter behaviour is observed during non-NPF event

days at both sites. When comparing NPF and non-NPF event days, SNS shows an enhancement of 51% and 60% in total CCN concentration at SS=0.4% and SS=0.8%, respectively, between 9:00-21:00 UTC during NPF event days with respect to non-NPF event days. At IZO, CCN enhancement during NPF days is 11% and 35% at SS=0.4% and 0.8%, respectively. This rough estimation highlights the potential significant impact that NPF events may have on CCN concentration, assuming that differences in emission sources, transport, transformation processes or atmospheric conditions between NPF and non-NPF event days are negligible. In this context, Figure 7-1 shows clear differences during NPF and non-NPF event days, as well as before and after NPF events, in terms of pre-existing particles, aerosol size-distribution and the diurnal evolution of the particle concentration across different size ranges. However, to more accurately determine the contribution of newly formed particles to CCN concentrations cannot rely solely on comparisons with a baseline period (commonly defined as non-event days or time preceding the onset of the NPF event). This is because the conditions that favour NPF events may differ significantly from those during the baseline period. Current existing methods based on comparison approaches (e.g. Dameto de España et al., 2017; Rose et al., 2017; Kalkavouras et al., 2019; Jiang et al., 2021; Rejano et al., 2021; Park et al., 2023) might yield erroneous results at IZO and especially, at SNS. At these sites, the environmental conditions that favour NPF events not only trigger their occurrence but also alter the background aerosol properties and precursor characteristics, potentially impacting CCN concentrations. As a result, the NPF enhancement factor derived using such methods may not accurately reflect the true impact of NPF on CCN concentrations due to the differences in the aerosol background conditions and aerosol sources between NPF event and nonevent days.

7.2 New method to estimate the NPF contribution to CCN concentrations

To address some of the limitations observed in previous methods which estimated CCN concentration enhancements by comparing CCN concentration at

different times periods (during or after NPF events with those prior the events or with non-event days), in the following we present a new methodology based on size-resolved CCN measurements. This approach enables the estimation of the direct contribution of NPF events to CCN concentrations by distinguishing particles originating from NPF events that can grow to CCN sizes from those arising from other sources (e.g., background, pre-existing, or transported aerosol particles) that also contribute to the total CCN concentration. With appropriate adjustments, the method has also been applied to polydisperse CCN measurements, which are more commonly available at measurement stations worldwide (Schmale et al., 2018; Andrews et al., 2025). The main feature of this new method lies in calculating the NPF mode by fitting the PNSD during NPF events and identifying CCN particles from that mode using activation fraction curves.

The method is divided in two steps: first, the duration of the NPF event and the contribution time of the NPF event to CCN concentration are determined based on the time when the size of newly formed particles reaches the critical diameter, D_{Crit} or D_{50} (depending on whether polydisperse or size-resolved measurements are used). This diameter is assumed to represent the minimum activation particle size. Secondly, the percentage of CCN associated with the NPF event is calculated based on the NPF mode from the PNSD and the activation curves. It should be noted that the first step is necessary due to the lower time resolution of the size-resolved CCN measurements in this study compared to the polydisperse data. However, if high-time resolution data are available, the first step could be skipped. Data from 2^{nd} July 2021 measured at SNS are used as an example to guide the presentation of the methodology:

1) Contribution time:

We first determine the start and end times of the NPF event. To do so, we follow a methodology similar to that proposed by Kalkavouras et al. (2019). This consists in analysing the evolution of the aerosol size distribution and changes in CCN concentration at various SS levels (Δ CCN) over time to estimate the time at which each NPF event starts (t_{start}) and ends (t_{end}). The t_{start} is defined as the time at which nucleation mode particles begin to rapidly increase, while t_{end} corresponds to the time when the Δ CCN at the highest SS returns to initial values. It should also be clarified that t_{end} is identified on the day when the NPF event

occurs. Figure 7-2 shows the duration time (from 9:00 to 21:00 UTC) of the NPF event on the 2^{nd} of July 2021.

Once the t_{start} and t_{end} are calculated, we define the contribution phase as the timeframe in which the NPF contributes to CCN concentration (i.e., the period in which newly formed particles might act as CCN at a specific SS value) during the time window t_{start} - t_{end} . This contribution phase is estimated as the timeframe when the ceiling size (the maximum size that newly formed particles can reach, shown as a grey and black dashed line in Fig. 7-3) exceeds the critical diameter.

To calculate the ceiling size, we analyse the gradient of the PNSD for each D-scan (Fig. 7-3 B). Figure 0-5, in Appendix, provides an example of the gradient, and the corresponding ceiling size obtained for one D-scan. This ceiling size is defined as the diameter at which the gradient of each scan reaches the negative value closest to 0 (Fig. 0-5, point B) after hitting its minimum value (Fig. 0-5, point A) and before transitioning to positive gradients (Fig. 0-5, point C). Using this approach, we determine the ceiling size for each D-scan. The temporal evolution of the ceiling size is then constructed from the diameters determined for each D-scan (i.e. for each size distribution over time). In Figure 7-3 B, the temporal evolution of the ceiling size during the NPF event observed on 2nd July 2021 is shown. The ceiling size increases throughout the event, reaching its maximum value of 79 nm around 18:00 UTC.

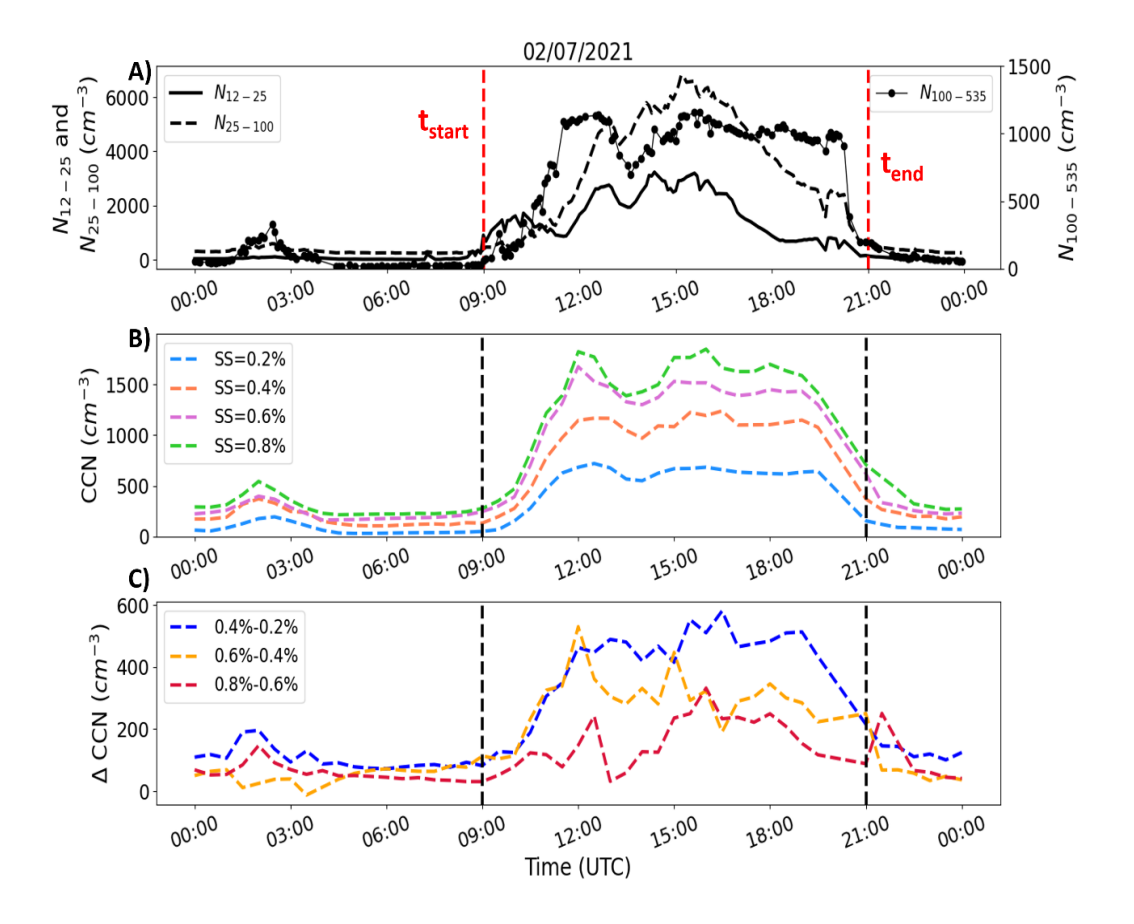


Figure 7-2. A) Diurnal evolution of N_{12-25} (solid black line), N_{25-100} (black dashed line) and $N_{100-535}$ (black dotted line) mode particle number concentration, B) diurnal evolution of total CCN concentration at different SS conditions and C) Δ CCN concentration between different SS conditions during NPF 2nd July 2021. Red/black vertical dashed lines at 09:00, and 21:00 UTC represent tstart, and tend, respectively.

Ceiling size values remain below the critical diameters at SS=0.4% (and consequently at SS<0.4%) throughout the entire NPF event (Fig. 7-3). Therefore, there is no contribution of newly formed particles to CCN concentration for SS≤0.4%. In contrast, at SS=0.8% the ceiling size is larger than the critical diameter from 15:00-21:00 UTC (Fig. 7-3), marking this period as the contribution phase of the event for SS=0.8%. At SS=0.6%, the critical diameter and ceiling size have very similar values from 15:00-21:00 UTC (Fig. 7-3), suggesting the contribution phase time period for SS=0.8% and SS=0.6% is the same. It is important to note that the contribution phase may vary depending on the SS conditions, potentially resulting in different periods of contribution for different SS.

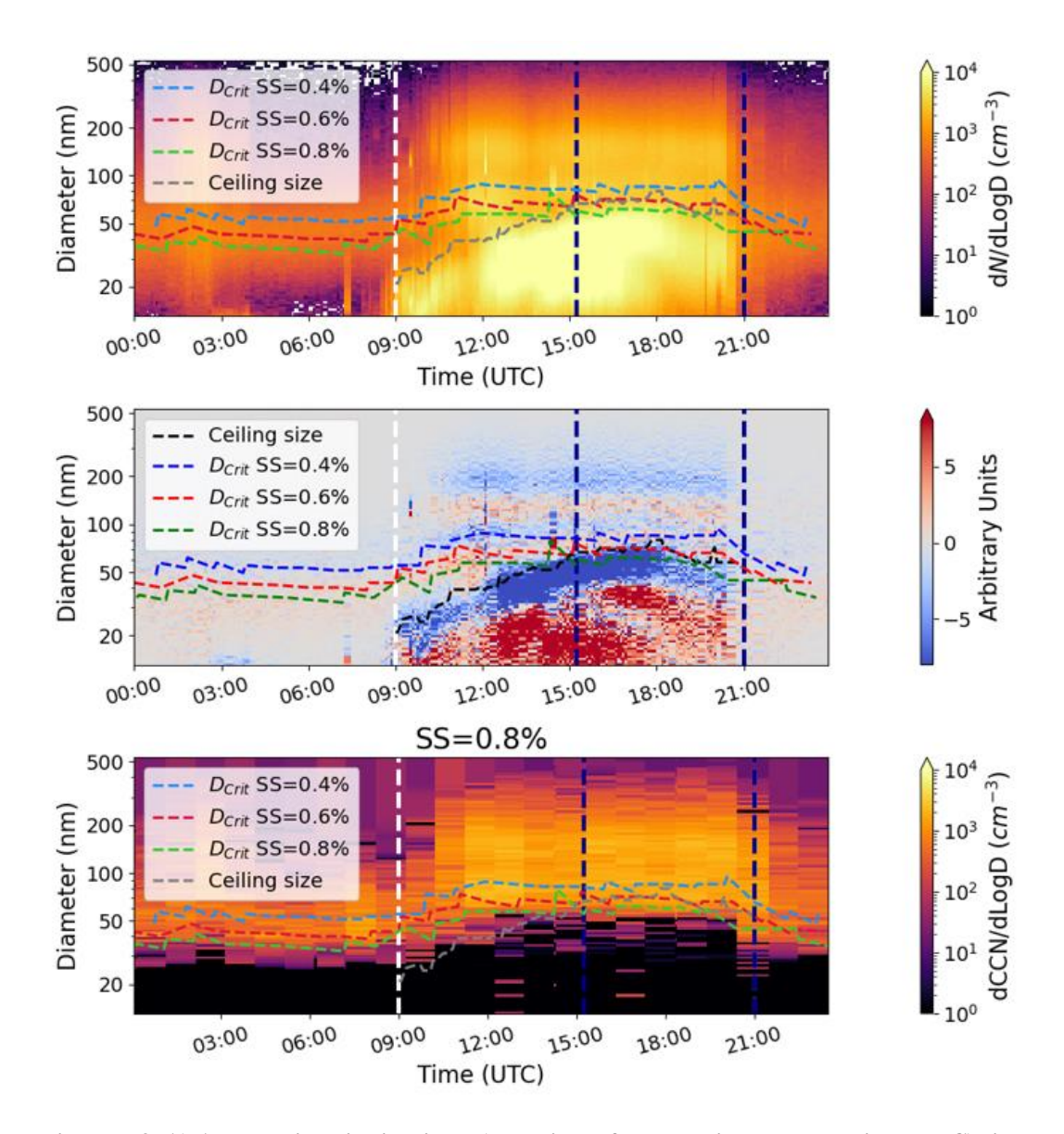


Figure 7-3. A) Aerosol size-distribution, B) gradient of aerosol size concentration and C) size-resolved CCN concentration during 2^{nd} July 2021. Blue, red and green lines correspond to D_{Crit} at different SS conditions (0.4%, 0.6%, 0.8%, respectively). Grey/black dashed lines correspond to ceiling size. Vertical white dashed line at 09:00 UTC represents t_{start} . Vertical dark blue dashed line at 15:00 UTC and 21:00 UTC refer to contribution phase (and t_{end}), respectively.

2) Calculating NPF-derived CCN contribution

Once the contribution phase period is determined, the next step is to estimate the concentration of particles acting as CCN that are associated with the NPF event, CCN_{NPF} . This is calculated as the integral of equation 7-1:

$$\frac{\text{dCCN}_{\text{NPF}}(\text{SS})}{\text{dLogD}} = \frac{\text{dN}_{\text{NPF}}}{\text{dLogD}} \times \text{AF}_{\text{NPF}}(\text{SS}, D)$$
 Eq. (7-1)

where $\frac{dN_{NPF}}{dLogD}$ represents the average aerosol size distribution of the NPF mode (Eq. 7-2) and $AF_{NPF}(SS,D)$ is the average size-resolved activated fraction during the contribution phase, associated with the NPF mode. Here, we assume that $AF_{NPF}(SS,D) = AF(SS,D)$ (Fig. 7-4 B), which is equivalent to assuming the particles have similar chemical composition across each size bin of the size distribution.

The application of this equation is crucial in the method because it directly allows us to use the NPF mode to separate activated newly formed particles during NPF events from activated pre-existing aerosol particles, $\frac{dN_{NPF}}{dLogD}$ corresponds to the particle number size distribution of the NPF mode. This mode is obtained by fitting the nucleation mode (assuming that particles in this mode are exclusively newly formed and do not originate from other sources) to the following equation (orange dashed line in Figure 7-4 A):

$$\frac{dN_{NPF}}{dLogD} = \alpha e^{\frac{-(D-\gamma)^2}{2\delta^2}}$$
 Eq. (7-2)

where α is the height of the curve's peak, γ is the position of the centre of the peak and δ controls the width of the curve.

Once Eq. 7-1 is applied, we obtain the CCN concentration of particles that directly originate from the NPF event. Figure 7-4 C shows the size distribution of

particles acting as CCN originating from the event $\left(\frac{dCCN_{NPF}(SS)}{dLogD}\right)$ with the solid green, red and blue lines indicating the contribution for each SS.

Finally, the direct NPF contribution to CCN concentration can be estimated as the ratio between CCN_{NPF} concentration (integral of $\frac{dCCN_{NPF}(SS)}{dLogD}$) and the total CCN concentration (which includes both activated particles originating from the NPF and activated background or pre-existing aerosol particles acting as CCN) at each SS during the contribution time-period:

Contribution (%) =
$$\frac{\int_{\text{dLogD}}^{\text{dCCN}_{\text{NPF}}(SS)}}{\text{CCN (SS)}} x \ 100$$
 Eq. (7-3)

Fig. 7-4 D shows that the contribution of the NPF to CCN concentration at SS=0.8% is 15.5% and 4.9% at SS=0.6%. The contribution at lower SS values is around 0 and can be neglected (newly formed particles were not able to reach D_{50} values at those SS).

Although the method has been developed using size-resolved CCN measurements, which allows us to obtain the size-resolved activated fraction, the method can be used for polydisperse measurements under the assumption of a sharp activated fraction curve (step function at D_{Crit}):

$$AF_{NPF}(SS,D) \approx \begin{cases} 0 & D < D_{Crit} \\ 1 & D \ge D_{Crit} \end{cases}$$
 Eq. (7-4)

where D_{Crit} is derived from the total particle number size distribution and polydisperse CCN measurements using Eq. 4-2. The result of Eq. 7-1 using this polydisperse variant of the method at different SS values is shown in Fig. 7-4 C (coloured squares markers).

Using this step function approximation in Eq. (7-4) to the polydisperse data, the resulting NPF contributions applying Eq. 7-3 are 11.6% and 3.1%, at 0.8% and

0.6% SS respectively. These are slightly lower than the NPF contributions obtained using size-resolved data (the percent difference between the size-resolved and polydisperse NPF contribution is 3.9% at SS=0.8% and 1.8% at SS=0.6%) (Fig. 7-4 D).

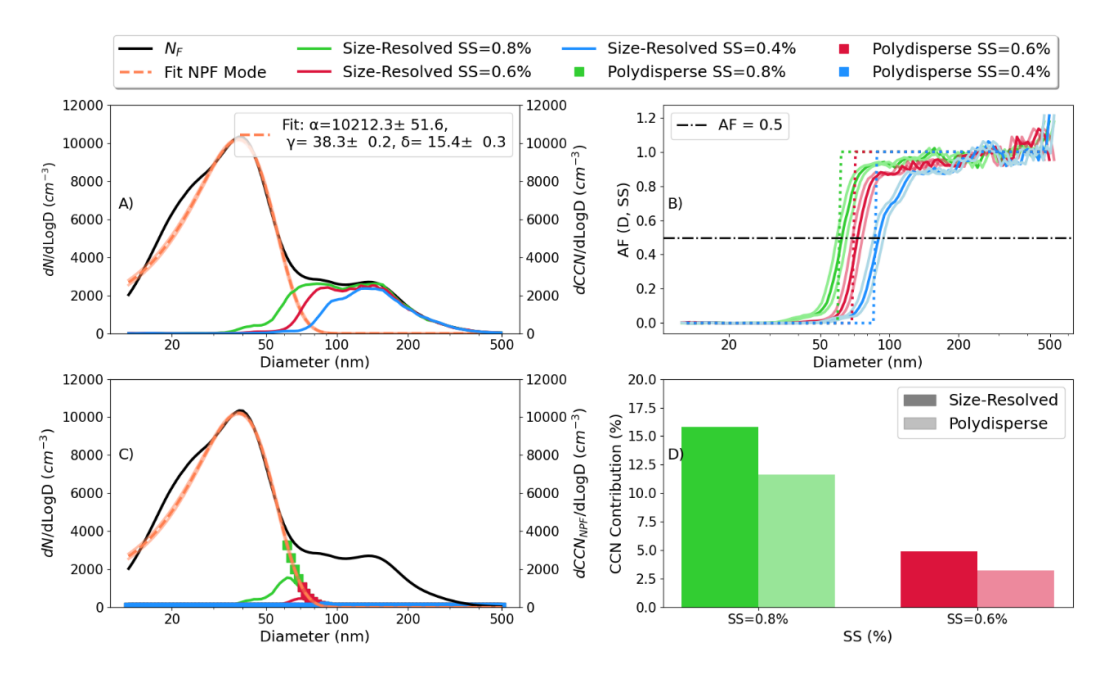


Figure 7-4. A) Average aerosol (black) and CCN size-distributions during contribution phase period at different SS values. Orange line corresponds to the bell fit that represents the NPF mode, and shadow orange area with the error of the fit calculated by propagation. B) - Activated fraction obtained from size-resolved CCN measurements (solid color lines) and polydisperse measurements approximated to step functions (dashed color lines). Lighter color lines (light green, red and blue) correspond to the error of size-resolved activated fraction. C) Size-resolved CCN concentration that come from NPF in size-resolved (blue, red, green solid lines) and polydisperse (blue, red, green squares) measurements overlaid on aerosol (black) and NPF mode size distributions (orange). D) Percent contribution of NPF to CCN concentration at SS=0.8% and SS=0.6% with size-resolved and polydisperse mode, during the NPF event 2nd July 2021.

7.3 Assumptions, limitations and sources of uncertainty of the new method

The main advantage of this novel method is that it allows a direct estimation of the contribution of NPF mode particles to CCN concentrations. In this subsection, a summary of the assumptions, limitations, and sources of uncertainty associated with the new method is presented.

The three main assumptions on which the method relies are summarized below:

- 1. This method assumes that the size range in the fitted mode is exclusively composed of newly formed particles (NPF mode) (Eq. 7-2). This is a valid assumption at remote sites (Boulon et al., 2011; Casquero-Vera et al., 2020), where no other sources of nucleation mode particles are present.
- 2. Another assumption of the method is that the activation fraction curve of the NPF particles is approximated by the measured AF for the whole aerosol population, $AF_{NPF}(SS,D) = AF(SS,D)$. This implies that particles have similar chemical composition across each size bin of the size distribution, which, in turn, means that the critical diameter of particles that come from the NPF events is similar to critical diameter obtained for the whole aerosol population. This assumption is considered reasonable because newly formed particles activate once they reach relevant sizes, and in terms of activation, size is more important than chemical composition (Dusek et al., 2006), and critical diameters are not strongly dependent on chemical composition (except for low hygroscopic particles). Moreover, it has been observed that NPF events contribute to CCN concentrations at high SS values, and under these conditions, composition effects are less important (McFiggans et al., 2006).
- 3. In the polydisperse variant of the method, activated fraction curves are approximated as step functions at these critical diameters (Eq. 7-4) which assumes that aerosol particles are internally mixed and have the same chemical composition.

The aforementioned assumptions lead to the following limitations:

- 1. The method as it is presented here might not be suitable for polluted environments. In those environments, the nucleation and Aitken modes could be influenced by particles from different sources (i.e., traffic emissions) (Laborde et al., 2013), as well as by NPF events. A possible option to overcome this limitation and isolate the NPF mode from the particle number size distribution is to apply clustering (Rejano et al., 2023) or source apportionment tools (Garcia-Marlès et al., 2024) to accurately separate the NPF mode from other sources influencing the nucleation mode. Furthermore, it is important to take into account that an accurately identifying which CCN-active particles come from the NPF event, versus those which have been transported or come from other sources/processes and activate as CCN is not feasible with the available measurements at most atmospheric observatories. This challenge can likely only be addressed using model simulations. However, it is possible to determine whether the different environments are influenced by fresh anthropogenic emissions or transported particles, and whether the NPF mode is affected by additional sources (beyond newly formed particles), by considering black carbon measurements or the concentrations of gases such as NOx, CO, SO2, which can be used as tracers of anthropogenic pollution (Querol et al., 2014; Dameto de España et al., 2017; Casquero-Vera et al., 2019; Rejano et al., 2024).
- 2. In the case of low hygroscopicity particles, the assumption of $AF_{NPF}(SS, D) = AF(SS, D)$ limits the applicability of the method due to a stronger dependence of D_{Crit} on chemical composition (Dusek et al., 2006; Quinn et al., 2008). In addition, for highly polluted urban environments with fresh emissions of non-hygroscopic particles, activated fraction curves may not reach the maximum value of 1 and, therefore, the approximation used in the polydisperse variant (activated fraction curves as step functions) would not be correct.
- 3. Due to the low temporal resolution of size-resolved CCN measurements, it is necessary to determine the contribution phase using the end time and ceiling size of the NPF events. This introduces some limitations related to both the ceiling size and the end time:

- * In terms of ceiling size, there might be some NPF contribution from the newly formed particles that are not captured by the ceiling size. Also, the method used to calculate the ceiling size might influence the results. For example, Zhu et al. (2014) determined the ceiling size by considering that particles originating from the NPF event have their maximum size in the geometric diameter ($D_{\rm geo}$) of the NPF mode. Applying Zhu et al. (2014) method to the case study presented here ($2^{\rm nd}$ July 2021; Fig. 0-6 in Appendix), the ceiling size shows lower values than the critical diameters throughout the entire NPF event, indicating that the NPF event would not contribute to CCN concentration at any SS value.
- * In terms of end time, the determination of tend can be affected by activated particles in the accumulation mode that are transported from lower altitudes (as it is the case for SNS) rather than originating from NPF events. In situations when transport processes occur on a similar timescale as NPF events, leading to an increase in accumulation mode particles, it is recommended to focus on Δ CCN at the highest SS values when calculating tend, as NPF particles have a greater influence under these SS conditions. However, the calculation of tend is not crucial for the methodology because if high-time resolution data are available, this step of the method can be skipped and instead step#2 of the method can be directly applied to calculate the contribution. Applying directly step#2 of the method is likely more suitable when using polydisperse measurements because sizeresolved measurements require longer averaging periods to reduce noise, making this approach difficult to implement. Figure 0-7 (Appendix) shows the contribution at high-time resolution for the NPF event 2nd July 2021 with polydisperse data. At SS=0.8%, the NPF contribution to CCN concentration lasts from 14:00-20:30 UTC, which is very similar to the contribution phase obtained using the ceiling size approach (15:00-21:00 UTC). In terms of contribution, the mean estimated values are 17.5% at SS=0.8% and 6% at SS=0.6%, which are similar, but slightly higher (values differ by 2 to 6 percentage points at SS=0.8% and 1-3 percentage points at SS=0.6%) than the results obtained using averaged conditions during the contribution time. The NPF contribution determined using the averaged contribution phase appears to be more conservative.

4. It should also be noted that our method quantifies the contribution of the event on the same day and at the measurement site. The overall contribution of NPF events could be larger as coagulation and repeated condensational growth could occur over multiple days, increasing the fraction of NPF particles that reach the CCN activation threshold. This potential contribution on consecutive days as well as at different locations other than the measurement sites cannot be accounted for with this method, nor with the already existing ones.

Despite the shortcomings discussed above, the method overcomes the main limitation of previous existing methods by providing a direct estimation of the NPF contribution to CCN concentration, rather than a CCN concentration enhancement relative to a reference condition. Table 0-5 in Appendix shows a comparison of the contribution of the NPF event produced on the 2nd July 2021 at SNS to CCN concentration, applying different methodologies (Rose et al., 2017; Kalkavouras et al., 2019; Cai et al., 2021). While Rose et al. (2017) and Kalkavouras et al. (2019) estimate concentration enhancements with respect to reference conditions, Cai et al. (2021) provides the event specific contribution to CCN. Table 0-5 shows high CCN enhancements at all SS (>200% with Rose et al. (2017) method and >400% with Kalkavouras et al. (2019) method at 0.8% SS). In addition, both methods show the highest enhancements at the lowest SS. These results suggest that larger particles, transported from lower altitudes when the height of the ABL increases at the same time at which the NPF event occurred, are activated as CCN at low SS values, contributing to CCN concentration. Results for our method agree more closely with those of Cai et al. (2021), which makes sense as the methods are comparable. Both methods provide negligible contributions at SS=0.2% and SS=0.4%, and similar contributions are obtained at SS=0.8% (differences of 1.5% and 5.4% with size-resolved and polydisperse variant, respectively) and SS=0.6% (differences of 2.6% with size-resolved variant and 4.4% with polydisperse variant). It should be noted that the Cai et al. (2021) method assumes that the newly formed particles activate as CCN at diameters between 3-80 nm and that the NPF mode is confined between 3-30 nm. In contrast, this new methodology avoids these assumptions by providing a way to calculate the NPF mode and the ceiling size. Further studies dealing with the evaluation of existing methods using a larger and more diverse dataset are necessary.

Concerning the range of uncertainty in the estimated NPF contribution to CCN concentrations, we have considered the errors associated with the NPF mode fits and the AF curves (the two terms involved in Eq. 7-1). The error of the NPF mode fit has been calculated by propagation of each fit parameter (α , γ and δ in Eq. 7-2). The error of the AF curve has been retrieved for the size-resolved data from the time-alignment (between SMPS and CCN measurements) t ± 2 seconds (see section 4.2), resulting in a minimum and maximum AF curve for that time window. It should be noted that during the campaign, the error in D_{50} obtained from different time alignments (at t and t ± 2 seconds) between CCNC and SMPS was estimated to be 5%, which is in the upper limit of uncertainty reported by Rose et al. (2013). These authors obtained a statistical uncertainty in the determination of critical diameters with size-resolved CCN measurements (from cumulative Gaussian fits) in the range of \sim 1-5%. Due to the agreement between D_{50} and D_{Crit} values obtained with size-resolved and polydisperse CCN measurements, respectively (Fig. 4-2 and Fig. 7-4 B), it has also been assumed a deviation of $\pm 5\%$ in the determination of D_{Crit} obtained from polydisperse measurements. Finally, the error range of NPF contributions to CCN concentration goes from the lowest to the highest contributions obtained from the product of minimum and maximum PNSD errors and activation fraction curves. The results of this uncertainty calculation are shown in the following section when providing the NPF contribution to CCN concentration at the measurement sites.

7.4 Contribution of NPF events to CCN concentrations at SNS and IZO

The proposed methodology has been applied to the NPF events observed during the SNS and IZO campaigns. As described in Sect. 7.1, a total of 5 and 18 NPF events have been analysed at SNS and IZO, respectively. Table 7-1 (SNS) and Table 7-2 (IZO) present the results, including the duration and contribution phase period of the NPF events as well as the averaged NPF contribution to CCN at each SS value. The associated uncertainty, calculated as described in Sect. 7.3, is also included. Additionally, Figure 7-5 provides a statistical overview of the contribution of NPF

events to CCN concentration, as well as the absolute concentration of CCN associated with the NPF event (CCN_{NPF}) at SNS (for both, size-resolved and polydisperse variants) and IZO (where only polydisperse data are available).

The results show significant variability in the characteristics of NPF events at both sites, including 1) starting time, 2) duration of contribution phase and 3) NPF contribution to CCN concentration. In general, the estimations from size-resolved and polydisperse variants are consistent. The application of the polydisperse variant consistently provides lower estimates (except on 7th July 2021 at SNS) compared to size-resolved data. However, the contribution obtained from the polydisperse variant generally falls within the uncertainty range of the sizeresolved variant (Table 7-1). Differences between the size-resolved and polydisperse variants are higher in terms of contribution (Fig. 7-5 A) than in absolute values (Fig. 7-5 B) at SNS. At SS=0.8%, the median contribution with sizeresolved variant is around 35% higher than the median value with the polydisperse variant (the median contributions are 6.4% with the size-resolved variant and 4.7% with polydisperse variant); whereas the median value with size-resolved variant of CCN_{NPF} concentration is 15.5% higher than with the polydisperse variant. The median CCN_{NPF} values at SNS are 110 cm⁻³ with the size-resolved variant and 95 cm⁻³ with the polydisperse variant. At IZO, at SS=0.8% with polydisperse variant, the median contribution is 15.7% (218% higher than at SNS). The median CCN_{NPF} concentration is reduced by 46.3% relative to SNS (51 cm⁻³ at IZO and 95 cm⁻³ at SNS). Therefore, the differences of the NPF impact on CCN concentration between SNS and IZO are greater than the bias between the size-resolved and polydisperse variants.

In general, the results show that the contributions of NPF events to CCN concentrations at all SS are higher at IZO than at SNS during the respective measurement periods. As mentioned, Figure 7-5 A indicated that the median contributions in polydisperse variant at SNS are 4.7% and 1.0% at SS=0.8% and 0.6%, respectively; whereas at IZO, the contributions are 15.7% (SS=0.8%) and 6.3% (SS=0.6%). The mean and median contribution values at SS=0.4% and SS=0.2% are also higher at IZO, however, the contributions of NPF events to CCN concentrations at SS \leq 0.4% can be considered neglegible at both high mountain stations (especially at SNS, where no contribution phase was identified). In addition, Table

7-1 and 7-2 show that some NPF events do not contribute to CCN concentrations (the contribution is 0%), even at the highest SS (SS=0.8%) such as on 29^{th} June 2021 at SNS and 25^{th} June 2022 and 7^{th} July 2022 at IZO. During these NPF events, growing particles are not able to reach the appropriate size (i.e., $> D_{Crit}$ (SS)) for CCN activation at the measurement location. The differences observed in the contribution of NPF events to CCN concentrations between IZO and SNS could be related to air mass transport when the height of the ABL increases. Air mass transport effects are more pronounced at SNS (Figure 0-4 in Appendix, and Figure 7-1) (García et al., 2017; Jaén et al., 2023). This greater influence at SNS is reflected in higher particle number concentrations and higher total CCN concentrations but lower relative contributions of NPF events to total CCN concentration. In contrast, at IZO, NPF events occur under cleaner or more pristine conditions, so that most activated particles originate from NPF events. Thus, applying Eq. 7-3 we obtain a higher relative contribution of NPF events to total CCN concentration at IZO than at SNS.

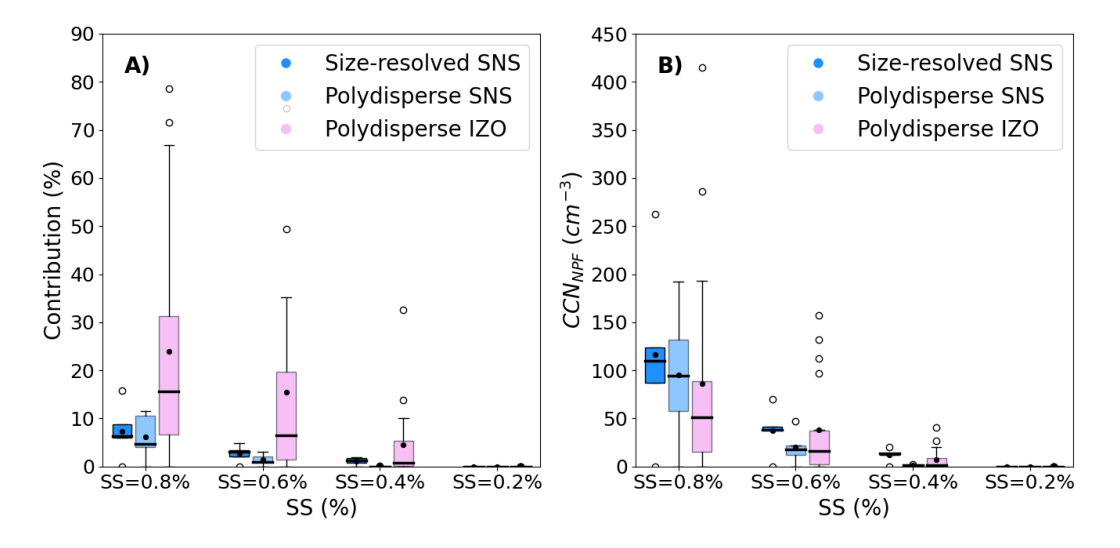


Figure 7-5. A) Boxplots of NPF contribution to CCN concentration and B) NPF-derived CCN absolute concentrations at different SS values (0.8%, 0.6%, 0.4% and 0.2%) at SNS (blue) and IZO (pink) using size-resolved and polydisperse variants of the method. Black dots and black lines represent the mean and median values, respectively. Lower and upper limits of the boxplots are the first (Q1) and third (Q3) quartiles, respectively. The difference between them is the inter-quartile range (IQR). Lower and upper whiskers show Q1-1.5·IQR and Q3+1.5·IQR, respectively. Blank circles represent the outliers.

In contrast, in absolute terms, the CCN_{NPF} concentration (Figure 7-5 B) is somewhat more similar than the relative contribution at both sites (median CCN_{NPF} concentration values at SS=0.8% of 95 cm⁻³ and 51 cm⁻³ and 18 cm⁻³ and 16 cm⁻³ at SS=0.6% at SNS and IZO, respectively, for the polydisperse variant). The slightly higher concentration of CCN_{NPF} at SNS compared to IZO might be related to the higher particles concentration (Fig. 7-1) and slightly higher formation and growth rates at SNS (Casquero-Vera et al., 2023), which is associated with the presence of anthropogenic precursor gases that promote the condensational growth of the new particles (Kulmala, 2003; Hamed et al., 2010).

Table 7-1. Summarised results from 5 NPF events at SNS, including NPF duration and contribution phase (based on SS=0.8%), as well as the contribution obtained for the size-resolved and polydisperse variants at 0.8 and 0.6% SS (no contribution was observed for $SS \le 0.4\%$).

			SNS			
NPF DAYS	Time Duration (UTC)	Contribution phase (hours)	Size-resolved contribution (%) at SS=0.8% (minmax. contribution)	Polydisperse contribution (%) at SS=0.8% (minmax. contribution)	Size-resolved contribution (%) at SS=0.6% (minmax. contribution)	Polydisperse contribution (%) at SS=0.6% (minmax. contribution)
29 th June 2021	12:00-17:00	1	0	0	0	0
30 th June 2021	12:30-01:30 (1/07/2021)	10	5.9 (5.5-6.5)	4.1 (3.1-6.8)	3.1 (2.8-3.3)	1 (0.6-2)
2 nd July 2021	09:00-21:00	9	15.5 (15-16)	11.6 (9-15)	4.9 (4-5.2)	3 (2-7)
7 th July 2021	12:45-22:00	7	8.8 (8-9.3)	10.5 (8.3-13.2)	3.4 (3.1-3.7)	2 (1.3-2.7)
8 th July 2021	12:15-00:00 (9/07/2021)	8	6.2 (6-6.6)	4.7 (3.4-6.2)	2 (1.8-2.5)	1 (0.6-1.5)
Mean ± std		7.8 ± 1.7	7.3 ± 5.6	6.2 ± 4.8	2.7 ± 1.8	1.4±1.1

Table 7-2. Summarised results from 18 NPF events at IZO, including NPF duration and contribution phase (based on SS=0.8%), as well as the contribution obtained for polydisperse variant at different SS. No contribution has been observed at SS < 0.2%.

			021		
NPF DAYS	Duration time (UTC)	Contribution phase (hours)	Polydisperse contribution (%) at SS=0.8% (minmax. contribution)	Polydisperse contribution (%) at SS=0.6% (minmax. contribution)	Polydisperse contribution (%) at SS=0.4% (minmax. contribution)
28 th April 2022	11:00-19:00	2	8 (5-19)	1 (0.8-2)	1
30 th April 2022	10:00-17:00	2	26 (21-31)	13 (7-16)	1.5 (1-2)
7 th May 2022	10:00-17:00	1	0	0	ı
12 th May 2022	09:20-20:00	6	21 (22-24)	14 (11-14)	4 (3-5)
15 th May 2022	09:30-21:00	10	10 (5-11)	4 (2-5)	1
16 th May 2022	09:40-01:00 (17/05/2024)	12	14 (6-19)	2 (1-5)	ı

phase (based on SS=0.8%), as well as the contribution obtained for polydisperse variant at different SS. No contribution has been observed at SS≤0.2%. Table 7-2 (continued). Summarised results from 18 NPF events at IZO, including NPF duration and contribution

			OZI		
NPF DAYS	Duration time (UTC)	Contribution phase (hours)	Polydisperse contribution (%) at SS=0.8% (minmax. contribution)	Polydisperse contribution (%) at SS=0.6% (minmax. contribution)	Polydisperse contribution (%) at SS=0.4% (minmax. contribution)
17 th May 2022	10:30-19:00	8	36 (28-61)	35 (27-62)	7 (3-10)
19 th May 2022	09:40-20:00	8	79 (76-80)	34 (32-35)	10 (9-10)
22 nd May 2022	10:00-23:00	10	67 (46-77)	49 (41-74)	33 (18-41)
23 rd May 2022	09:00-21:00	7	0.9 (0.2-1.6)	0	1
24 th May 2022	09:00-50:00	8	18 (9-24)	8 (3-5)	2 (0-5)
25 th May 2022	10:00-20:00	2	32 (25-52)	16 (8-21)	3 (2-7)

contribution phase (based on SS=0.8%), as well as the contribution obtained for polydisperse variant at different SS. No contribution has been observed at $SS\le0.2\%$. Table 7-2 (continued). Summarised results from 18 NPF events at IZO, including NPF duration and

			OZI		
NPF DAYS	Duration time (UTC)	Contribution phase (hours)	Polydisperse contribution (%) at SS=0.8% (minmax. contribution)	Polydisperse contribution (%) at SS=0.6% (minmax. contribution)	Polydisperse contribution (%) at SS=0.4% (minmax. contribution)
29 th May 2022	09:30-20:30	8.5	1.7 (0.5-2.6)	0.2 (0.1-0.3)	1
31 st May 2022	09:30-21:00	8	6 (4-5)	1.4 (0.6-1.7)	ı
5 th June 2022	09:30-18:00	2	28 (24-40)	21 (17-33)	6 (4-10)
9 th June 2022	10:00-19:00	9	72 (60-100)	75 (42-91)	14 (6-18)
23 rd June 2022	11:15-17:00	4.5	11 (4-16)	5 (3-13)	ı
25 th June 2022	12:00-18:00	ı	0	0	ı
Mean ± std	ı	7.3 ± 2.4	24 ± 25	16 ± 21	4±8

To determine the potential factors driving the CCN_{NPF} concentration at both locations (using the polydisperse variant), Figure 7-6 explores the relationship of CCN_{NPF} with several factors: (i) the size that the newly formed particles are able to reach (i.e., D_{max}) and the size at which particles activate as CCN, D_{Crit} (Fig. 7-6 A), (ii) the duration of the contribution phase (Fig. 7-6 B), (iii) total particle number concentration (N) (Fig. 7-6 C) and (iv) the particle number concentration in Aitken mode (N_{25-100}) (Fig. 7-6 D). Figure 7-6 A reveals a slight positive trend between D_{max} and CCN_{NPF} concentration at SS=0.8% at SNS and IZO, with larger D_{max} values implying higher concentration of particles acting as CCN that come from the NPF events. However, on average (Fig. 0-8 in Appendix), the NPF events observed at IZO show larger D_{max} (78 nm) than at SNS (68 nm), while the CCN_{NPF} concentrations are slightly higher at SNS (95 cm⁻³) than at IZO (86 cm⁻³). No clear relationship is observed between CCN_{NPF} concentration and the critical diameter during the events (Fig. 7-6 A). Regarding the duration of the contribution phase, the results are not conclusive; however, at SNS, there appears to be a slight trend in which longer contribution phase periods are associated with lower CCN_{NPF} concentrations (Fig. 7-6 B). Regarding total particle number concentration, there is a slight increasing trend of CCN_{NPF} concentration as the total particle number concentration increases (Fig. 7-6 C). Looking at different size ranges, the trend is consistent with higher concentration of Aitken mode particles (N₂₅₋₁₀₀) (Fig. 7-6 D). In contrast, no correlation is observed with $N_{100-535}$ (Figure 0-9 in Appendix), suggesting that particles activated in this larger size range do not originate from the growth of newly formed particles. Ren et al. (2021) also found inconclusive results in terms of relationships between CCN enhancements and other variables. These authors only observed higher CCN enhancements during NPF events associated with higher aerosol concentration (PM1 in their study), suggesting that more polluted sites characterized by higher PM1 concentration have higher CCN enhancements. That trend is not observed in our study, since SNS is more impacted by the advection of anthropogenic pollution than IZO, but it shows lower NPF contribution to CCN concentration. A larger and more diverse database is necessary to obtain conclusive results on the relationship between CCN_{NPF} concentration and NPF characteristics. Future studies applying this method to longterm datasets and multiple sites with distinct characteristics will likely provide more insight into the factors driving the NPF contribution to the CCN budget.

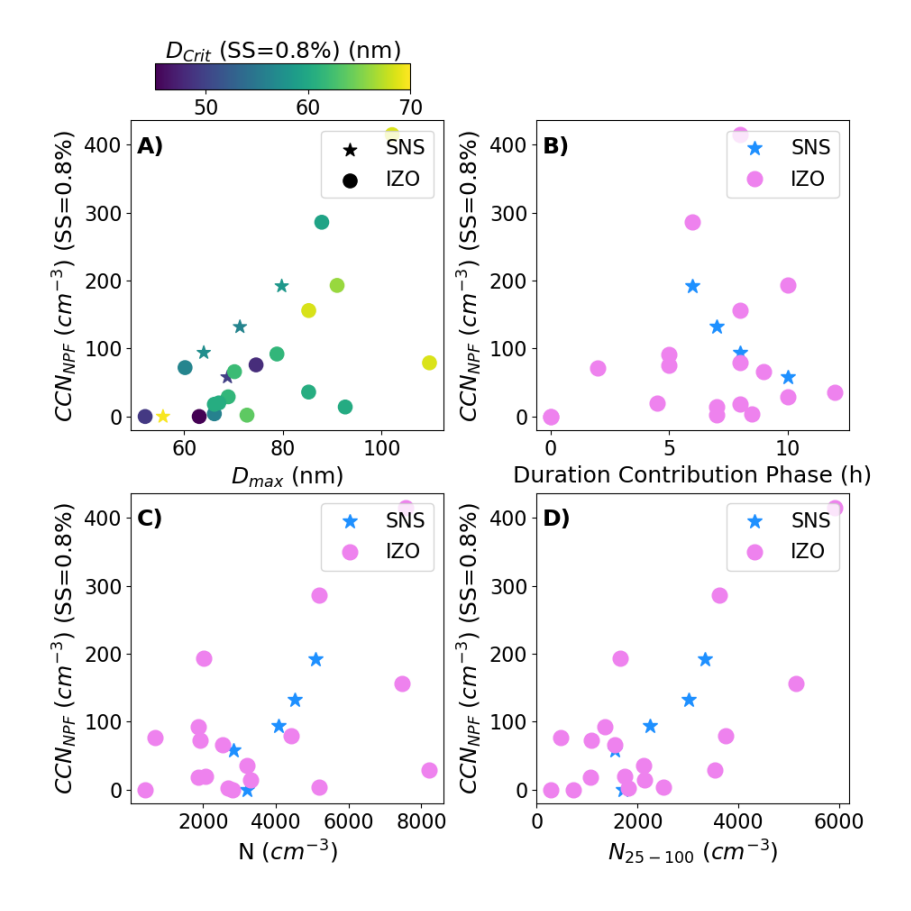


Figure 7-6. A) Relationship of CCN_{NPF} with A) maximum ceiling size reached by newly formed particles (D_{max}) coloured by critical diameter (D_{Crit}) at SS=0.8%, B) duration of the contribution phase, C) total particle number concentration, N, D) Aitken mode concentration, N_{25-100} , and CCN_{NPF} at SNS and IZO using the polydisperse variant of the proposed method.

7.5 Conclusions

Collocated CCN and aerosol size distribution data from two high mountain sites (SNS in the southern Iberian Peninsula and IZO in the Canary Islands) have been utilized to investigate the contribution of NPF to CCN concentrations. The two column CCNC at SNS was operated such that one column sampled in polydisperse mode and the other in size-resolved mode, while the CCNC at IZO was only operated in polydisperse mode. Using SNS data set a new methodology using the size-resolved CCN measurements has been developed to directly quantify the

contribution of NPF events to CCN concentration. Through some theoretical approximations, the methodology was adapted for use with polydisperse data, which are more commonly available worldwide and demonstrated a strong agreement between both variants. The polydisperse variant consistently yields lower estimates of NPF contribution relative to the size-resolved one. This suggests that the size-resolved measurement provides a more conservative estimate of the NPF contribution to CCN concentration (at SS=0.8% the polydisperse variant percent contribution (6.2%) is 15% lower than the size-resolved variant percent contribution (7.3%) and at SS=0.6% the percent contribution is reduced by 48% (1.4% polydisperse variant and 2.7% size-resolved variant)). However, results using both variants are within the uncertainty range of the method. The new method has been applied to data collected during field campaigns at both IZO and SNS. These measurements offer valuable insights into the potential contribution of NPF events to the CCN budget in semi-pristine environments.

The new methodology enables the direct calculation of the contribution of NPF events to CCN concentrations, distinguishing between NPF modes and background or transported aerosol particles. Unlike previous methods, which estimate enhancements by comparing different conditions or assuming that particles are activated as CCN within a specific size range, this approach addresses these limitations by focusing on the size that newly formed particles can reach, the timing of NPF events, and isolating the NPF mode from the overall aerosol size distribution. The results show that NPF events produced at both stations are able to contribute to CCN concentrations under high SS conditions while for SS<0.4% this contribution can be neglected. NPF events show higher contributions to CCN concentration at IZO (campaign averages of 24% at SS=0.8% and 16% at SS=0.6%), compared to SNS (6.2% at SS=0.8% and 1.4% at SS=0.6%). However, in absolute terms, the number of particles produced by the NPF event and activated as CCN is slightly higher at SNS than at IZO (at SS=0.8%, 95 cm⁻³ vs 51 cm⁻³ and at SS=0.6%, 18 cm⁻³ vs 16 cm⁻³ at SNS and IZO, respectively). The differences in the impact of NPF events on CCN concentration between the two high-mountain sites are closely related to the NPF phenomena. While both sites experience NPF events under atmospheric boundary layer transport conditions, SNS is more influenced by transported particles from lower altitudes, resulting in lower relative contribution of NPFs to CCN concentration. No clear relationship between the CCN_{NPF} concentration and the critical diameter is observed, but a slight positive trend has been obtained for $D_{\rm max}$, N and $N_{25\text{-}100}$ at both sites. Additional drivers, such as aerosol hygroscopicity or the duration of the event do not show a clear relationship with the NPF event contribution.

Although some open questions remain unresolved, such as the contribution of grown particles over consecutive days or at different locations, the newly proposed method demonstrates promising potential to provide more accurate and realistic determination of the impact of NPF events on the CCN budget. The differences observed between both high-mountain sites, along with the high variability, highlight the importance of conducting long-term studies across multiple environments. Such studies are crucial for improving our understanding and better characterizing the effects of NPF events on CCN concentrations in the global atmosphere.

8. General conclusions and perspectives

This chapter summarizes the main conclusions obtained in the framework of this thesis based on the conclusions presented at the end of each chapter. The research of this thesis is focused on the study of the influence of different primary aerosol particles (subpollen particles, SPPs, and dust particles) and newly formed particles, on CCN activation properties and their contribution to the CCN budget. The focus is kept in these three aerosol types due to their expected impact at the global scale and the lack of studies addressing their influence in the aerosol-cloud interaction mechanisms. They have been investigated from two different points of view. The capability of SPPs to activate as CCN has been addressed from laboratory experiments due to the difficulties to measure ambient SPPs with current techniques. The influence of dust events and new particle formation (NPF) events on activation properties and CCN concentration has been studied through two field campaigns at two high-mountain sites frequently influenced by dust episodes due to their proximity to Sahara Desert and with a high occurrence of NPF events. It should also be mentioned that the pollen species investigated are characteristics of the Mediterranean climate and can be found at both high-mountain locations.

Results demonstrated that both types of primary aerosol particles investigated, i.e. SPPs and dust, are able to activate as CCN at atmospherically relevant supersaturations. Experiments performed in the laboratory with SPPs show that they can activate at SS within the range 0.07%-0.37%, (depending on size), showing κ parameters, for most pollen types, in the range of 0.23-0.33 (moderately hygroscopic organic aerosol). This suggests that all SPP types might be an important natural contribution to the CCN budget, independently of the pollen specie. Concerning dust particles, we found that desert dust events can modify CCN activation properties. Despite the low contribution of dust particles in terms of aerosol number concentration, dust particles in accumulation and coarse mode are able to activate at SS \geq 0.2%. However, the results show a general reduction of submicron particle concentration during dust events, suggesting that large dust particles act as coagulation sink. Another factor contributing to this decrease in fine particles is a less efficient transport from lower altitudes due to changes in the

dynamic of the ABL during dust episodes, leading to an enhanced in AF values during dust events.

The analysis of chemical composition of SPPs shows similar contributions of highly, slightly and non-soluble organic compounds for all samples, which could explain their similar hygroscopic behaviour. No clear relationship between organic speciation and protein content was clearly found. During the dust events, the hygroscopic behaviour was different from event to event and no clear conclusions could be obtained from our results. Chemical analysis was not available for all dust events, limiting the scope of the study. Therefore, additional studies with long-term measurements at different stations influenced by dust episodes are needed to better understand the role of dust events in the global scale.

The study of surface activity using pendant drop tensiometry showed that κ values can be reduced by around 50%-60% for all pollen types (except for *Quercus*). The capacity to reduce surface tension decreases as SPP solution is more diluted. For SPP concentrations lower than 0.03 g/L surface tension values are similar to the surface tension of water (σ_w) and κ values do not change significantly. Therefore, our results demonstrate that at low solution concentration (which is expected during SPP activation in real cloud droplets), σ_w is a good approximation in the Köhler equation.

Concerning the influence of NPF events on CCN concentrations, in the frame of this thesis we have developed a new methodology that allows a better estimation of the CCN particles originating from the NPF events. Existing methods determine a concentration enhancement referred to a baseline period, so they do not determine the contribution of the NPF itself to the measured CCN concentration, but rather the concentration enhancement with respect to a reference condition. This new method has been developed using size-resolved CCN measurements at SNS, and it has been applied to polydisperse measurements at IZO and SNS under some theoretical approximations. The results show that NPF events produced at both stations are able to contribute to CCN concentrations at high SS conditions while for SS<0.4% their contribution is negligible. NPF events show higher contributions to CCN at IZO (campaign average of 24% at SS=0.8% and 16% at SS=0.6%) compared to SNS (6.2% at SS=0.8% and 1.4% at SS=0.6%). However, in absolute terms, the number of particles produced by the NPF event

and activated as CCN is slightly larger at SNS than at IZO. Concerning absolute CCN_{NPF} concentration, no clear relationship has been observed with the critical diameter, while a slight positive trend was obtained between CCN_{NPF} concentration and D_{max} , N and N_{25-100} at both sites. The NPF to CCN contributions obtained in this thesis are in average terms lower than previous estimates at highmountain sites based on enhancement calculations, which might lead to reconsider their climatic impact worldwide.

Differences in the impact of NPF events to CCN concentrations between both stations are related to the phenomenology of NPF occurrence at each site. Aerosol phenomenology at SNS and IZO are quite different despite their similar altitude. Total aerosol concentration as well as the concentration of the different size modes (nucleation, Aitken, accumulation and coarse) are higher at SNS than at IZO due to higher influence of pollutants transported at midday at SNS from the Granada metropolitan area. IZO is mostly in the free troposphere and is less affected by anthropogenic pollution. Aerosol concentration at both sites shows the typical diurnal pattern observed at high-mountain areas. This pattern is characterized by an increase in total particle number concentration at midday related to the occurrence of NPF events at this time and enhanced transport of aerosol particles from lower altitudes due to atmospheric boundary layer height increase. CCN concentrations are also higher at SNS (645 cm⁻³ at SS=0.4%) than at IZO (160 cm⁻³ at SS=0.4%) whereas AF mean values are very similar (0.36 at SNS compared to 0.32 at IZO). Aerosol particles are found to be less hygroscopic at SNS than at IZO, which might be due to the high influence of organics at SNS and the higher contribution of marine aerosol particles at IZO, as suggested by previous studies at both sites.

Although some open questions about the influence and impact of primary and secondary aerosol particles on CCN concentration and activation properties remain unsolved, the studies performed in the framework of this thesis provide new insights and constitute a solid starting point for future studies. Concerning pollen activation properties, previous research mostly focused on single organic components, and very few is known about organic complex mixtures such as ambient SPPs. Our results on the activation properties of 10 pollen types that are very common in the Mediterranean area can be used to improve estimates of

natural aerosol impact on climate. Concerning what happens during dust events in terms of CCN activation properties, this is the first study addressing this topic using in-situ ambient measurements during several Saharan dust intrusions and the results demonstrate the ability to modify the activation as CCN depending on the event characteristics. Finally, the newly proposed method developed in this thesis to estimate the NPF contribution to CCN concentration provide more accurate and realistic determination of the impact of NPF events in the CCN budget than previous methods.

In spite of the aforementioned scientific advancement, further research will be essential to advance beyond the aspects addressed in this thesis with a specific focus on certain topics:

- Additional studies including new SPPs types, in addition to other PBAPs such as fungi, bacteria, viruses, etc., with complementary analysis, such as chemical composition, will help to improve the understanding of natural primary aerosols activation and hygroscopic properties.
- Due to the forecasted increase of dust events with climate change, a long-term analysis at multiple sites influenced by dust events is needed to obtain a robust statistic that allows to improve our knowledge of the influence of dust particles on CCN concentration and activation properties.
- As well as the capability of dust and pollen particles to activate as CCN influencing the climate, it would also be interesting to study the ability of these particles to activate as ice nucleating particles (INP).
- The new methodology developed to estimate the contribution of newly formed particles on CCN concentration could be applied to long-term data at multiple and different environments to improve and better determine the NPF events impact in the global atmosphere. The use of open-access databases such as those developed in ACTRIS are a promising future study. Additionally, measurements of size-resolved chemical composition would help to overcome some limitations of the method.

 Applying the new method to modelled data will allow additional tunning of the method and the models to improve NPF-CCN estimations.

Conclusiones generales y perspectivas

En este capítulo podemos encontrar un resumen de las principales conclusiones obtenidas en esta tesis, basándose en las conclusiones presentadas al final de cada uno de los capítulos anteriores. Como hemos visto, la investigación de esta tesis se basa en el estudio de la influencia de diferentes tipos de partículas de aerosol primario (partículas subpolínicas, SPPs, y partículas de polvo) y partículas secundarias, que provienen de los eventos de formación de nuevas partículas (NPF), en la concentración y las propiedades de activación como CCN. El enfoque se centra en estos tres tipos de aerosol debido a su impacto esperado a escala global y a la influencia sobre los mecanismos de interacción aerosol-nube. El estudio se ha realizado desde dos puntos de vista diferentes. La capacidad de las SPPs para activarse como CCN ha sido abordada mediante experimentos de laboratorio debido a las dificultades para medir las SPPs ambientales con las técnicas actuales; y la influencia de los eventos de polvo y los eventos NPF sobre las propiedades de activación y la concentración de CCN se ha llevado a cabo a través de dos campañas de campo en dos estaciones de alta montaña. Dichas estaciones se ven frecuentemente influenciadas por intrusiones de polvo, debido a su proximidad al desierto del Sahara; y pueden observarse múltiples eventos de NPF. También cabe destacar que las especies de polen investigadas son características del clima mediterráneo y pueden encontrarse en ambas estaciones.

Los resultados demuestran que ambos tipos de partículas de aerosol primario, es decir, las SPPs y el polvo, son capaces de activarse como CCN a supersaturaciones que pueden darse en la atmósfera. Las SPPs pueden activarse a supersaturaciones dentro del rango 0.07%-0.37% (dependiendo del tamaño) y presentan parámetros de higroscopicidad, κ típicos de aerosol orgánico moderadamente higroscópico (0.23-0.33). Esto sugiere que todos los tipos de SPPs pueden ser una fuente natural importante de CCN. En cuanto al estudio del polvo, encontramos dichos episodios tienen la capacidad de modificar las propiedades de activación como CCN. A pesar de su baja contribución en términos de concentración numérica, las partículas de polvo en modo grueso y de acumulación pueden activarse a SS ≥ 0.2%. Sin embargo, los resultados también muestran que

durante los eventos de polvo se produce una reducción en la concentración de partículas submicrométricas y, por tanto, un aumento en los valores de la fracción de activación. Esto sugiere que las partículas grandes de polvo pueden actuar como sumideros de coagulación. Otro factor que puede contribuir a esta disminución de concentración es que haya un transporte menos eficiente desde altitudes más bajas debido a los cambios que puedan darse en la dinámica de la capa límite atmosférica (ABL).

El análisis de la composición química de las SPPs muestra que todas las muestras tienen contribuciones similares de compuestos orgánicos altamente solubles, ligeramente solubles y no solubles; lo que podría explicar su comportamiento higroscópico similar. Sin embargo, no se observó una relación clara con la especiación orgánica y el contenido proteico. En cuanto a los eventos de polvo, el comportamiento higroscópico varió de un evento a otro y no se pudieron obtener conclusiones definitivas a partir de nuestros resultados. Además, no se cuenta con el análisis químico de todos los eventos de polvo, lo que limita el alcance del estudio. Por tanto, para comprender mejor la influencia del polvo sobre las propiedades de activación a escala global, sabemos que es necesario realizar más estudios con medidas a largo plazo en estaciones con diferentes características frecuentemente afectadas por intrusiones de polvo.

El estudio de la actividad superficial mediante tensiometría de gota pendiente mostró que los valores de κ pueden reducirse en un 50%-60% para todos los tipos de polen analizados (excepto para el *Quercus*). La capacidad de reducir la tensión superficial disminuye a medida que la concentración de SPPs se diluye. Para concentraciones de SPP inferiores a 0.03 g/L, los valores de tensión superficial son similares a los valores de tensión superficial del agua (σ_w) y los valores de κ no cambian significativamente. Por lo tanto, nuestros resultados demuestran que, a bajas concentraciones (las esperadas durante la activación de SPPs), σ_w es una buena aproximación en la ecuación de Köhler.

Para estudiar el impacto que tienen los eventos de formación de nuevas partículas (NPF) en las concentraciones de CCN, se ha desarrollado una nueva metodología que permite obtener una mejor estimación de la concentración de partículas activadas como CCN que provienen directamente de los eventos de NPF. Los métodos existentes estiman dicha contribución respecto a un periodo

determinado, por lo que no determinan la contribución directa del propio NPF; sino más bien un incremento de la concentración con respecto a una condición de referencia. Esta nueva metodología se ha desarrollado utilizando medidas de CCN con resolución por tamaño tomadas en SNS y se ha aplicado a medidas de CCN polidispersas tomadas en IZO y SNS; asumiendo determinadas suposiciones teóricas.

Los resultados de aplicar esta metodología muestran que los eventos de NPF son capaces de contribuir a las concentraciones de CCN a altas SS en ambas estaciones; mientras que para SS<0.4% su contribución puede ser despreciable. Los eventos de NPF muestran una mayor contribución a la concentración de CCN en IZO (promedio de la campaña de 24% a SS=0.8% y 16% a SS=0.6%) que en SNS (6.2% a SS=0.8% y 1.4% a SS=0.6%). Sin embargo, en términos absolutos, el número de partículas producidas por los eventos de NPF y activadas como CCN (CCN_{NPF}) es ligeramente mayor en SNS que en IZO. En cuanto a la concentración absoluta de CCN que provienen de los eventos de NPF (CCN_{NPF}), no se ha observado una relación clara con el diámetro crítico; pero sí se obtuvo una ligera tendencia positiva con D_{max}, N y N₂₅₋₁₀₀ en ambos lugares. También cabe destacar que las contribuciones relativas de NPF a los CCN obtenidas en esta tesis son, en términos promedio, más bajas que las estimaciones previas observadas en lugares de alta montaña aplicando métodos previos que se basan en el cálculo de incrementos comparando con situaciones de referencia; lo que podría llevar a reconsiderar su impacto climático a nivel global.

Las diferencias en el impacto de los eventos de NPF sobre las concentraciones de CCN, en ambas estaciones, están relacionadas con la fenomenología de los NPF de cada lugar; que difiere bastante a pesar de ser estaciones que se encuentran a altitudes similares. La concentración total de aerosoles, así como de los distintos modos (nucleación, Aitken, acumulación y grueso) son mayores en SNS que en IZO debido a que SNS, se ve más influenciada por los contaminantes transportados a mediodía desde el área metropolitana de Granada. En cambio, IZO, suele encontrarse en condiciones de troposfera libre y se ve menos afectada por la contaminación de actividades antropogénicas que se dan en niveles de altitud inferiores. No obstante, ambas estaciones muestran patrones diurnos típicos de lugares de alta montaña. Este patrón se caracteriza por un

aumento en la concentración total de partículas a mediodía, relacionado con la producción de eventos de NPF y el transporte de partículas de aerosol desde altitudes más bajas, debido al aumento de la altura de la capa límite atmosférica. Las concentraciones de CCN también son más altas en SNS (645 cm⁻³ a SS=0.4%) que en IZO (160 cm⁻³ a SS=0.4%), mientras que los valores medios de AF son muy similares (0.36 en SNS frente a 0.32 en IZO). También se ha visto que las partículas de aerosol son menos higroscópicas en SNS que en IZO, lo que podría deberse a la alta influencia de compuestos orgánicos en SNS y una mayor contribución de partículas de aerosol marino en IZO, como sugieren estudios previos realizados en ambos lugares.

Aunque aún quedan algunas preguntas sin resolver sobre la influencia e impacto de las partículas de aerosol primarias y secundarias en la concentración de CCN y sus propiedades de activación, los estudios realizados en esta tesis aportan nuevos conocimientos y ofrecen un sólido punto de partida para futuras investigaciones. En cuanto a las propiedades de activación del polen, la mayoría de las investigaciones previas se han centrado en componentes orgánicos individuales, y se sabe poco sobre las mezclas orgánicas complejas como las SPPs. Nuestros resultados sobre las propiedades de activación de 10 tipos polínicos característicos del área mediterránea pueden ayudar a mejorar las estimaciones del impacto de los aerosoles naturales en el clima. Respecto a la influencia de los eventos de polvo, este es el primer estudio con medidas in-situ durante varias intrusiones; y los resultados muestran cómo dependiendo de las características de los eventos, se pueden modificar las propiedades de activación como CCN. Finalmente, el nuevo método propuesto en esta tesis para estimar la contribución de los eventos de NPF a la concentración de CCN, permite una estimación más precisa y realista del impacto de dichos eventos en comparación con los métodos anteriormente utilizados.

Finalmente, aunque se han logrado avances científicos importantes, sabemos que es fundamental continuar con más investigaciones que profundicen en los aspectos tratados en esta tesis, probablemente enfocándose en los siguientes puntos:

 Se necesitan estudios adicionales que incluyan nuevos tipos de SPPs, además de otros aerosoles biológicos primarios (PBAPs), como hongos, bacterias, virus, etc., con análisis complementarios, como la composición química, para mejorar la comprensión de las propiedades de activación y la higroscopicidad de los aerosoles naturales primarios.

- Dado el pronóstico de aumento de los eventos de polvo debido al cambio climático, es necesario un análisis a largo plazo en múltiples sitios afectados por dichas intrusiones para obtener una estadística robusta que permita mejorar nuestro conocimiento sobre la influencia de las partículas de polvo en la concentración de CCN y las propiedades de activación.
- Además de la capacidad de las partículas de polvo y polen para activarse como CCN e influir en el clima, también sería interesante estudiar la habilidad de estas partículas para activarse como partículas de nucleación de hielo (INP).
- La nueva metodología desarrollada para estimar la contribución de las partículas recién formadas a la concentración de CCN podría aplicarse a bases de datos mucho más extensas y en estaciones con características atmosféricas diferentes para determinar con mayor precisión el impacto de que tienen los eventos de NPF. El uso de bases de datos de acceso abierto, como las desarrolladas en ACTRIS, es una vía prometedora para futuros estudios. Además, las medidas de composición química con resolución de tamaño ayudarían a superar algunas limitaciones del método.
- Aplicar esta nueva metodología a datos modelados, también permitiría implementar mejoras en los modelos, en la propia metodología y en los resultados de su aplicación.

Appendix

Supplementary Tables

Table 0-1. Water solubility of the analyzed organic compounds between 20-25 ° C. All solubility values are taken from the National Center for Biotechnology Information (2023). PubChem Compound Summary for CID 6267. The solubility category is based on Han et al. (2022).

Compound Summary f	or CID 6267. The solubi	lity category is based on H	an et al. (2022).
Compound	Chemical	Water Solublity 20-25	Category of
	Classification	°C (mg/mL)	Solubility
β-Glucose	Saccharides	1200.0	Highly Soluble
Sorbitol	Sugar-alcohol	2750.0	Highly Soluble
Sucrose	Saccharides	2100.0	Highly Soluble
Asparagine	Amino acids	29.4	Slightly Soluble
Glutamine	Amino acids	41.3	Slightly Soluble
Histidine	Amino acids	45.6	Slightly Soluble
Proline	Amino acids	162.0	Slightly Soluble
Levoglucosan	Anhydro-sugar	62.3	Slightly Soluble
Shikimic	Ciclitols	180	Slightly Soluble
Azealic	Diacids	2.4	Slightly Soluble
Glutaric	Diacids	>100	Slightly Soluble
Malic	Diacids	0.592	Slightly Soluble
Succinic	Diacids	83.2	Slightly Soluble
Sitosterol	Plants Compound	10	Slightly Soluble
α-Glucose	Saccharides	500	Slightly Soluble
Mannitol	Sugar-alcohol	216	Slightly Soluble
Tere-phthalic	Diacids	0.015	Non-Soluble
Alpha-linoleic	Fatty Acids	0.000124	Non-Soluble
Linoleic	Fatty Acids	-	Non-Soluble
Oleic	Fatty Acids	-	Non-Soluble
Palmitic	Fatty Acids	0.0004	Non-Soluble
Stearic	Fatty Acids	0.000597	Non-Soluble
Oleanolic	Plants Compound	0.000001748	Non-Soluble

Table 0-2. Calculated κ values taking into account different surface tension values for each pollen type at different sizes. The reduction of κ_{mean} respect to $\kappa_{\sigma w}$ expressed in percentage associated to the initial solution and the 100 times diluted solution are also showed.

Pollen Types	σ (mN/m)	к (200 nm)	κ (100 nm)	<i>κ (</i> 80 nm)	<i>K</i> mean	% reduction K _{mean} (initial concentration)	% reduction Kmean (diluted 100 times)
	σ_{w}	0.302	0.310	0.310	0.307 ± 0.005		
Dactylis	$\sigma_{C/100} = 69.9$	0.262	0.286	0.246	0.265 ± 0.020	62.7%	13.9%
	$\sigma_{\rm C}$ = 49.2	0.112	0.123	0.109	0.115 ± 0.007		
	σ_{w}	0.256	0.302	0.282	0.280 ± 0.023		
Fraxinus	$\sigma_{C/100} = 72.5$	0.231	0.257	0.253	0.247 ± 0.014	39.3%	11.7%
	$\sigma_{\rm C}$ = 55.9	0.203	0.164	0.140	0.17 ± 0.03		
	σ_{w}	0.337	0.321	0.318	0.325 ± 0.010		
Pinus	$\sigma_{C/100} = 70.4$	0.302	0.283	0.264	0.283 ± 0.019	64.9%	13.0%
	$\sigma_{\rm C}$ = 47.9	0.119	0.115	0.109	0.114 ± 0.005		
	σ_{w}	0.316	0.309	0.337	0.321 ± 0.015		
Populus deltoides	σ _{C/100} =71.6	0.292	0.267	0.282	0.280 ± 0.013	67.6%	12.6%
	$\sigma_{\rm C}$ = 45.0	0.103	0.109	0.100	0.104 ±0.004		
	σ_{w}	0.307	0.302	0.325	0.311 ± 0.012		
Populus nigra	$\sigma_{C/100} = 69.2$	0.263	0.289	0.283	0.273 ± 0.014	54.8%	12.3%
	$\sigma_{\rm C} = 52.7$	0.127	0.152	0.143	0.140 ± 0.013		
	σ_{w}	0.117	0.146	0.150	0.138 ± 0.018		
Quercus	σ _{C/100} = 71.4	0.112	0.140	0.155	0.136 ± 0.022	17.2%	1.5%
	$\sigma_{\rm C} = 64.6$	0.101	0.116	0.125	0.114 ± 0.012		

Table 0-3. Summary of Kruskal-Wallis tests for concentration at different modes during the more intense dust events identified at SNS. $K_{\rm C}$ values represent Kruskal-Wallis coefficients. "Yes" indicates that differences are significant with p-values < 0.05 compared to non-dusty conditions.

			SNS	SNS (DAY)					SNS (F	SNS (NIGHT)		
Variable		Dust 1			Dust 2			Dust 1			Dust 2	
	ر لا	p-value	Signif. Diff.	K	p-value	Signif. Diff.	کّر	p-value	Signif. Diff.	K	p-value	Signif. Diff.
Nc	72	2 · 10-17	Yes	98	$1 \cdot 10^{-20}$	Yes	117	3 · 10-27	Yes	113	$2 \cdot 10^{-27}$	Yes
N _C /N	38	7 · 10-10	Yes	29	$3 \cdot 10^{-16}$	Yes	112	$3 \cdot 10^{-26}$	Yes	115	$6 \cdot 10^{-27}$	Yes
N	ı	ı	No	29	7 · 10-8	Yes	ı	ı	No	9	0.01	Yes
N ₁₂₋₂₅			No	29	$6\cdot 10^{-8}$	Yes	8	$4 \cdot 10^{-3}$	Yes	56	$4\cdot 10^{-7}$	Yes
N25-100	ı	1	No	26	4 · 10-7	Yes	1	ı	No	18	$2 \cdot 10^{-5}$	Yes
N ₁₀₀₋₁₀₀₀	8	4 · 10-3	Yes	11	$6\cdot 10^{-8}$	Yes	7	7 · 10-3	Yes	ı	ı	No

Table 0-4. Summary of Kruskal-Wallis tests for concentration at different modes during the more intense dust events identified at IZO during day and nighttime. Kc values represent Kruskal-Wallis coefficients. "Yes" indicates that differences are significant with p-values < 0.05 compared to non-dusty conditions.

			ZI	IZO (DAY)	,				ı) OZI	IZO (NIGHT)		
Variable		Dust 2			Dust 5			Dust 2			Dust 5	
	Κ _C	p-value	Signif. Diff.	Κ _C	p-value	Signif. Diff.	Κ̈́c	p-value	Signif. Diff.	κ _c	p-value	Signif. Diff.
$N_{\rm C}$	72	$2 \cdot 10^{-17}$	Yes	62	$3\cdot 10^{\text{-}15}$	Yes	91	$1\cdot 10^{-21}$	Yes	69	$9\cdot 10^{\text{-}17}$	Yes
N _C /N	29	$3\cdot 10^{-16}$	Yes	61	$6 \cdot 10^{-15}$	Yes	90	$2 \cdot 10^{-21}$	Yes	75	$4 \cdot 10^{-18}$	Yes
$ m N_F$	2	0.05	Yes	11	0.0004	Yes	2	0.03	Yes	15	0.0001	Yes
N ₁₂₋₂₅	ı	ı	No	7	900.0	Yes	30	$4 \cdot 10^{-8}$	Yes	59	$2 \cdot 10^{-14}$	Yes
N25-100	14	0.0002	Yes	14	0.0002	Yes		1	No	5	0.02	Yes
N100-1000	33	$8 \cdot 10^{-9}$	Yes	ı	ı	No	29	$3\cdot 10^{\text{-}16}$	Yes	7	200'0	Yes

Table 0-5. Enhancements and contributions to CCN of the NPF produced on 2^{nd} July 2021 at SNS applying different methodologies.

Methodology	SS=0.8%	SS=0.6%	SS=0.4%	SS=0.2%
Rose et al.	262%	247%	184%	380%
(2017)				
Kalkavouras et	436%	459%	656%	1049%
al. (2019)				
Cai et al.	17%	7.5%	2.8%	-
(2021)				
Size-Resolved	15.5%	4.9%	2%	-
variant (this				
study)				
Polydisperse	11.6%	3.1%	-	-
variant (this				
study)				

Supplementary Figures

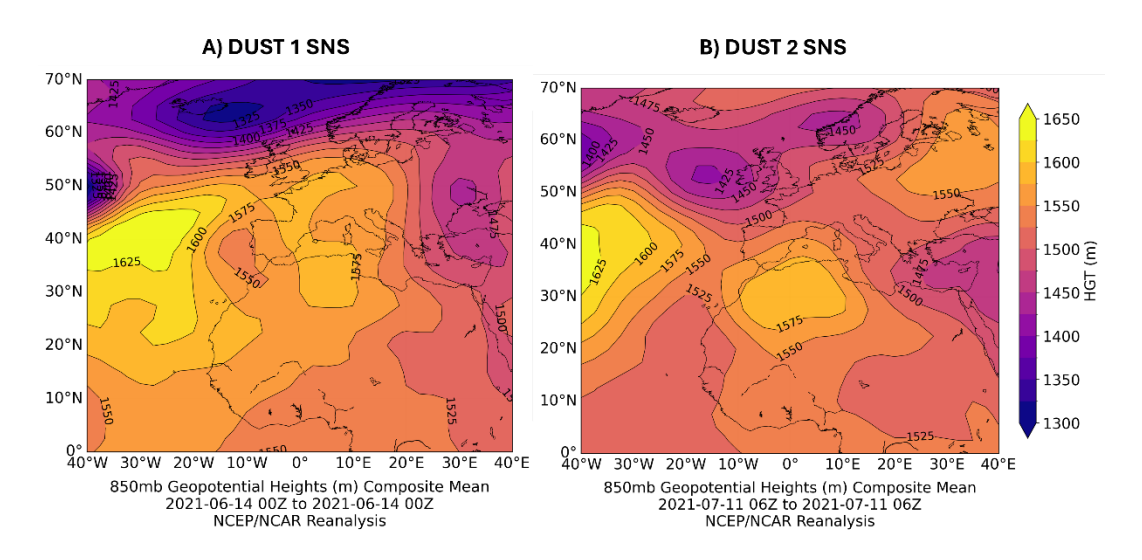


Figure 0-1. Geopotential height at 850 mb for A)14th June 2021 at 00:00 UTC corresponding with dust event 1 at SNS and B) 11th July 2022 at 06:00 UTC corresponding with dust event 2 at SNS. Data are from NCEP/NCAR - https://psl.noaa.gov/data/composites/hour/.

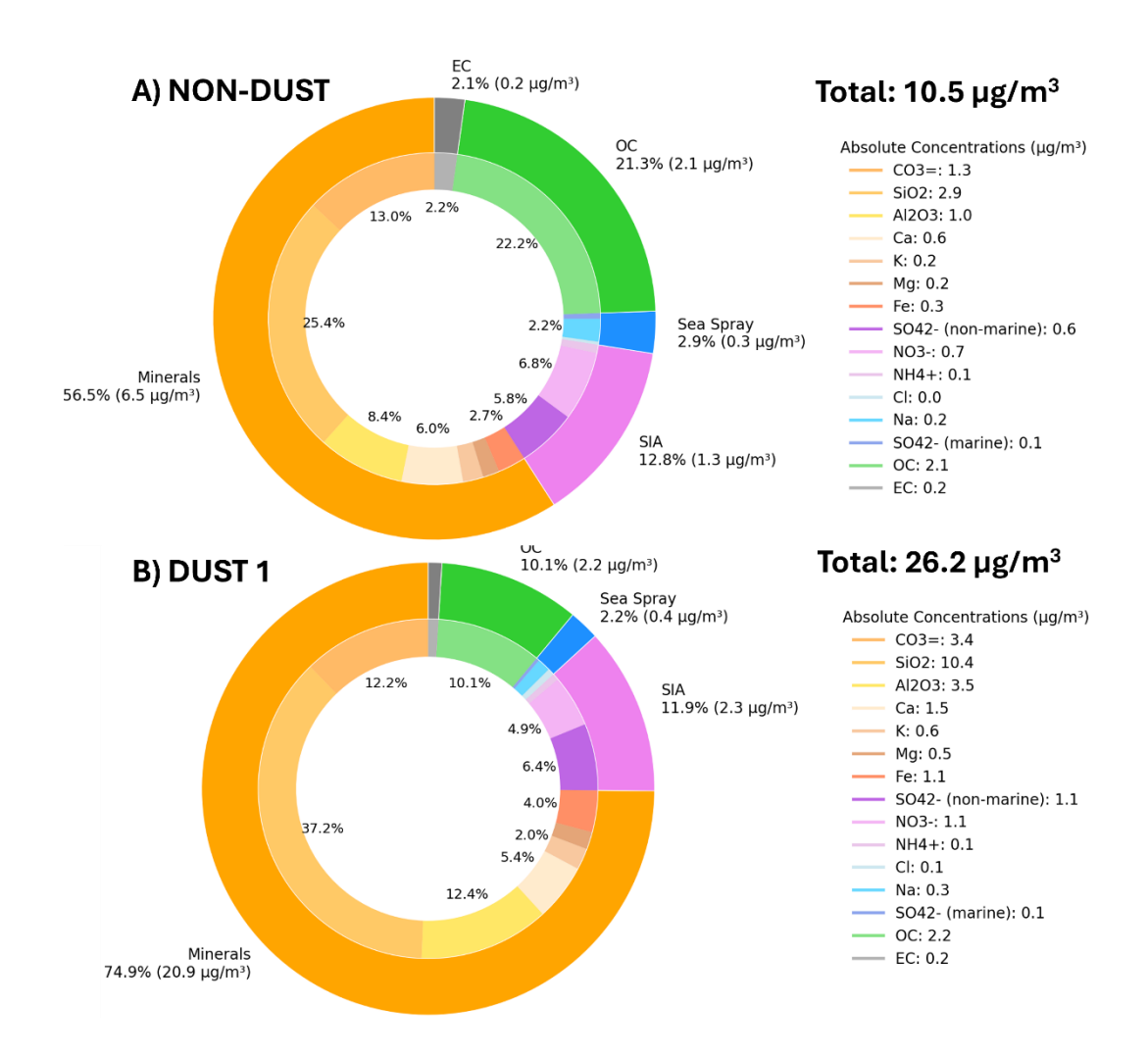


Figure 0-2. Pie chart of averaged PM10 chemical composition during non-dusty conditions and dust event 1 at SNS. Only compounds representing percentages above 2% have been highlighted to appear in the pie charts.

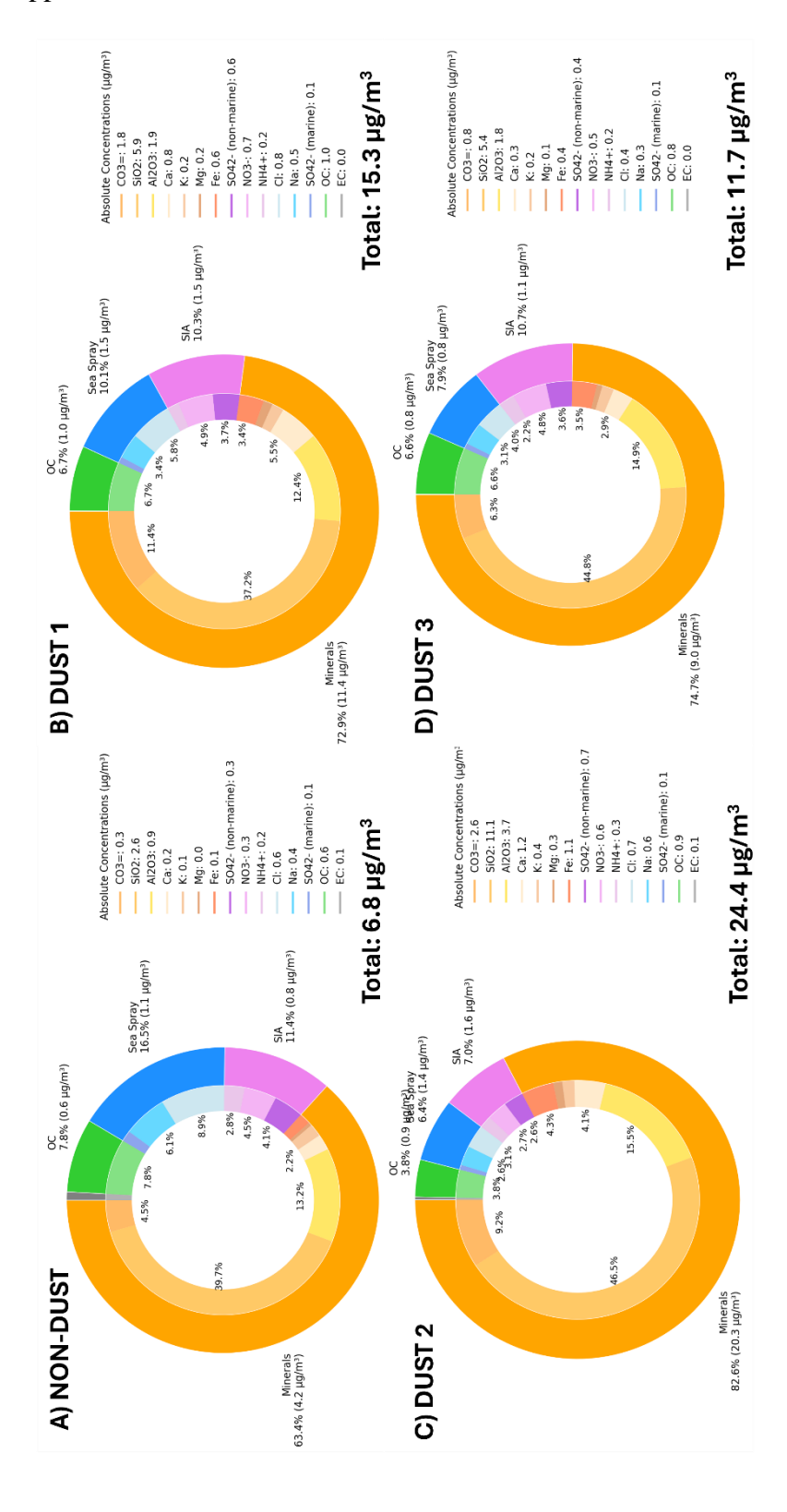


Figure 0-3. Pie chart of averaged PM10 chemical composition during non-dusty conditions, dust event 1, dust event 2 and dust event 3 at IZO. Only compounds representing percentages above 2% have been highlighted to appear in the pie charts.

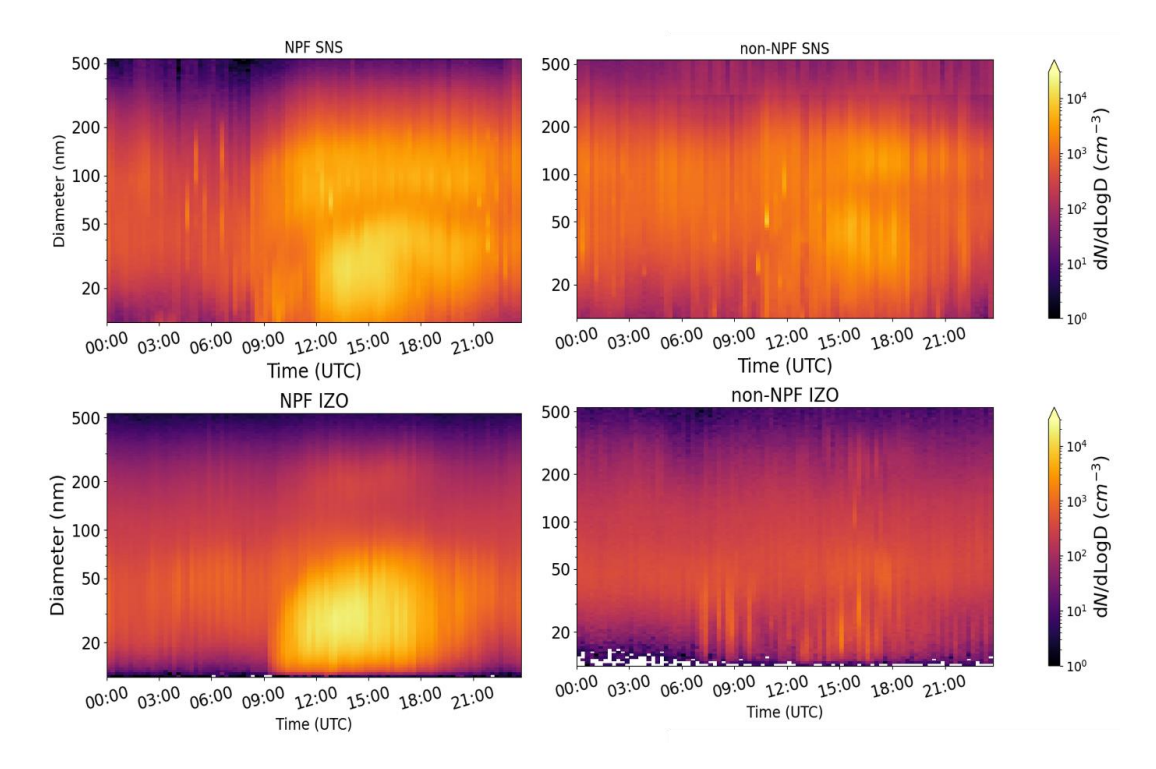


Figure 0-4. Mean particle number size distributions (PNSD) evolution during NPF and non-NPF event days at SNS and IZO stations.

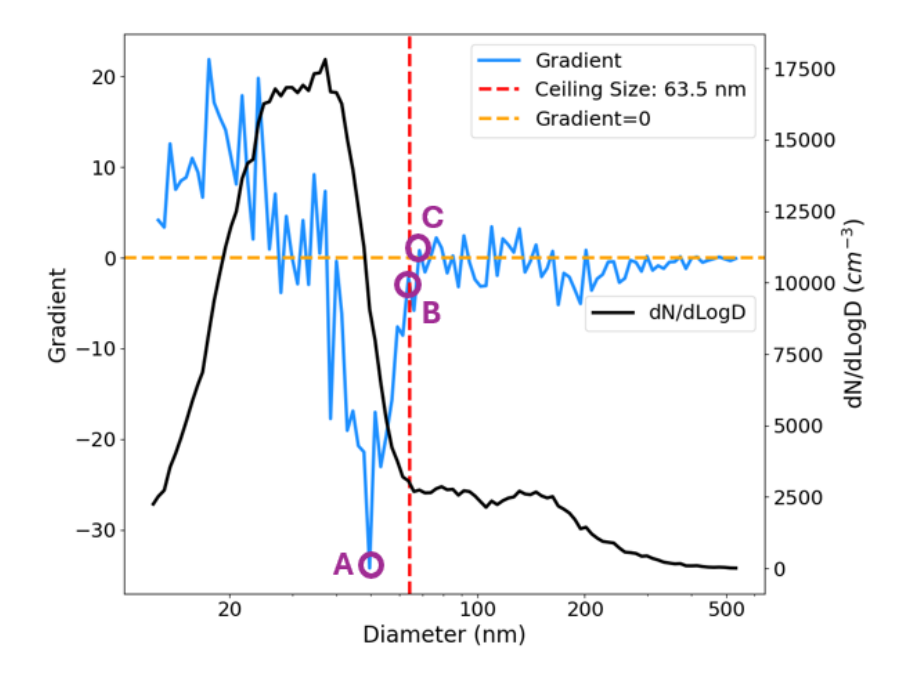


Figure 0-5. Graphical representation of the ceiling size calculation method for one D-scan of the particle number size distribution. Point A represents the minimum value of the gradient, point B represents the ceiling size (the negative value closest to 0) and point C refers to the first positive value of the gradient after the minimum value (A).

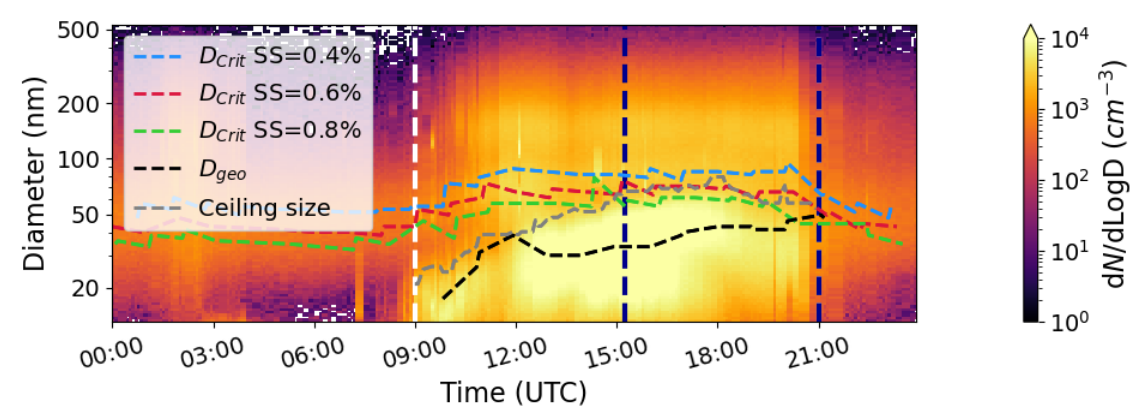


Figure 0-6. Aerosol size-distribution evolution where black dashed line represents the geometric diameter. Grey dashed line reference to ceiling size obtained from gradient of concentration and coloured lines, critical diameters at different SS values (blue for SS=0.4%, red for SS=0.6% and green for SS=0.8%).

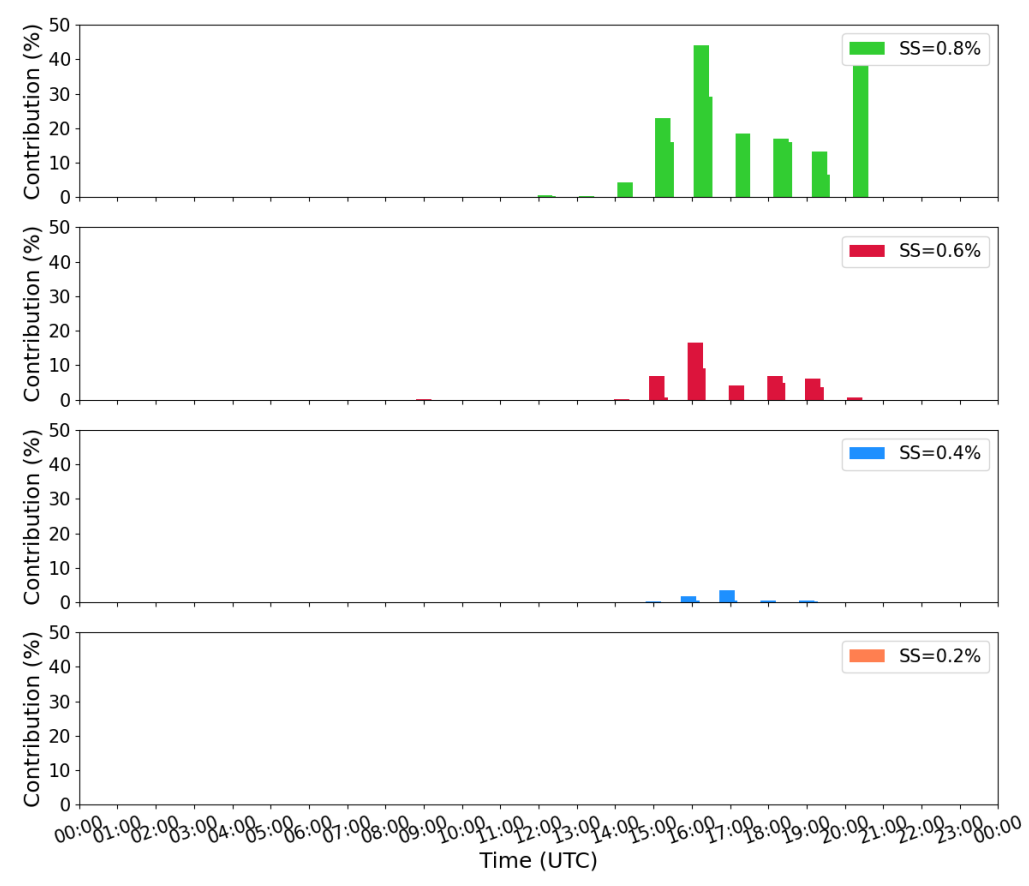


Figure 0-7. Percentage of contribution of NPF to CCN concentration at different SS values during the NPF produced 2^{nd} July 2021 using polydisperse high-time resolution variant.

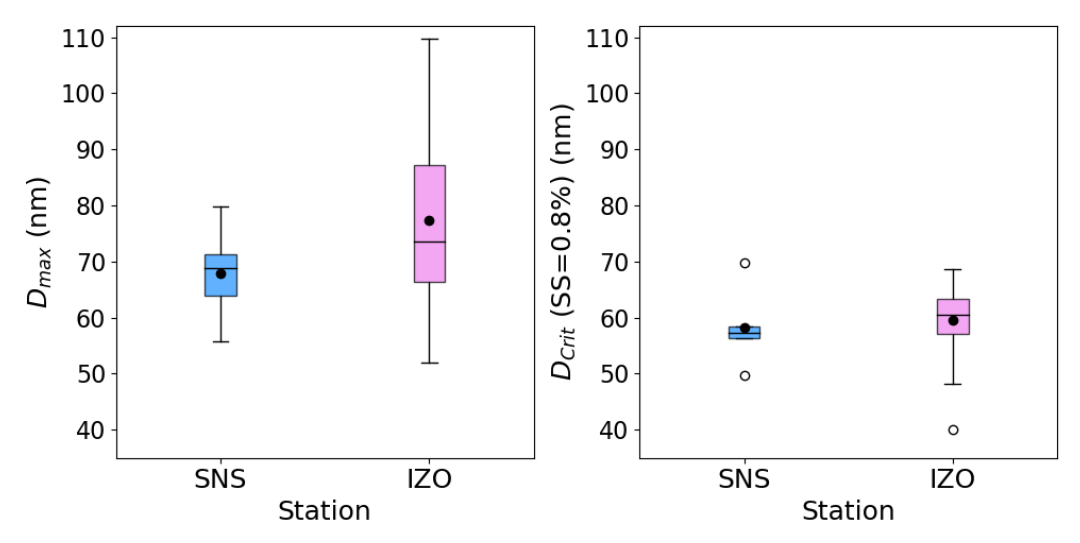


Figure 0-8. Boxplot of maximum ceiling size reached by newly formed particles (left) and critical diameters (at SS=0.8%) (right) at SNS and IZO during the analysed NPFs. Black dots and black lines represent the mean and median values, respectively. Lower and upper limits of the boxplots are the first (Q1) and third (Q3) quartiles, respectively. The difference between them is the inter-quartile range (IQR). Lower and upper whiskers show Q1-1.5·IQR and Q3+1.5·IQR, respectively. Blank dots represent the outliers.

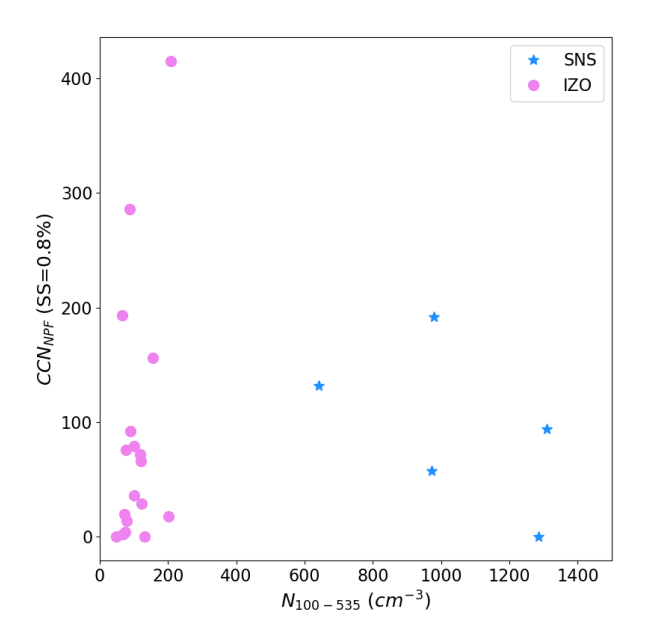


Figure 0-9. Relationship of CCN_{NPF} with $N_{100-535}$ at SNS and IZO using the polydisperse variant of the proposed method.

Abbatt, J. P. D., Broekhuizen, K., and Pradeep Kumar, P.: Cloud condensation nucleus activity of internally mixed ammonium sulfate/organic acid aerosol particles, Atmos. Environ., 39, 4767–4778, https://doi.org/https://doi.org/10.1016/j.atmosenv.2005.04.029, 2005.

Adame, J.A., Cordoba-Jabonero, C., Sorribas, M., Toledo, D., Gil-Ojeda, M. Atmospheric boundary layer and ozone-aerosol interactions under Saharan intrusions observed during AMISOC summer campaign. Atmos. Environ. 104, 205–216, https://doi.org/10.1016/j.atmosenv.2014.12.036, 2015.

Adebiyi, A., Kok, J. F., Murray, B. J., Ryder, C. L., Stuut, J.-B. W., Kahn, R. A., Knippertz, P., Formenti, P., Mahowald, N. M., Pérez García-Pando, C., Klose, M., Ansmann, A., Samset, B. H., Ito, A., Balkanski, Y., Di Biagio, C., Romanias, M. N., Huang, Y., and Meng, J.: A review of coarse mineral dust in the Earth system, Aeolian Res., 60, 100849, https://doi.org/https://doi.org/10.1016/j.aeolia.2022.100849, 2023.

Alastuey, A., Querol, X., Castillo, S., Escudero, M., Avila, A., Cuevas, E., Torres, C., Romero, P.-M., Exposito, F., García, O., Pedro Diaz, J., Dingenen, R. Van, and Putaud, J. P.: Characterisation of TSP and PM2.5 at Izaña and Sta. Cruz de Tenerife (Canary Islands, Spain) during a Saharan Dust Episode (July 2002), Atmos. Environ., 39, 4715–4728, https://doi.org/https://doi.org/10.1016/j.atmosenv.2005.04.018, 2005.

Algarra, J. A., Cariñanos, P., Herrero, J., Delgado-Capel, M., Ramos-Lorente, M. M., and Díaz de la Guardia, C.: Tracking Montane Mediterranean grasslands: Analysis of the effects of snow with other related hydro-meteorological variables and land-use change on pollen emissions, Sci. Total Environ., 649, 889–901, https://doi.org/https://doi.org/10.1016/j.scitotenv.2018.08.311, 2019.

Andreae, M. O. and Rosenfeld, D.: Aerosol–cloud–precipitation interactions. Part 1. The nature and sources of cloud-active aerosols, Earth-Science Rev., 89, 13–41, https://doi.org/10.1016/j.earscirev.2008.03.001, 2008.

Andrews, E., Ogren, J. A., Bonasoni, P., Marinoni, A., Cuevas, E., Rodríguez, S., Sun, J. Y., Jaffe, D. A., Fischer, E. V, Baltensperger, U., Weingartner, E., Coen, M. C., Sharma, S., Macdonald, A. M., Leaitch, W. R., Lin, N.-H., Laj, P., Arsov, T., Kalapov, I., Jefferson, A., and Sheridan, P.: Climatology of

aerosol radiative properties in the free troposphere, Atmos. Res., 102, 365–393, https://doi.org/10.1016/j.atmosres.2011.08.017, 2011.

Andrews, E., Zabala, I., Carrillo-Cardenas, G., Titos, G., Casquero-Vera, J.A., Hallar., G.: Harmonized aerosol size distribution, cloud condensation nuclei, chemistry and optical properties at 12 sites, Sci. Data., Under Review, 2025.

Ansmann, A., Bösenberg, J., Chaikovsky, A., Comerón, A., Eckhardt, S., Eixmann, R., Freudenthaler, V., Ginoux, P., Komguem, L., Linné, H., Márquez, M. Á. L., Matthias, V., Mattis, I., Mitev, V., Müller, D., Music, S., Nickovic, S., Pelon, J., Sauvage, L., Sobolewsky, P., Srivastava, M. K., Stohl, A., Torres, O., Vaughan, G., Wandinger, U., and Wiegner, M.: Long-range transport of Saharan dust to northern Europe: The 11–16 October 2001 outbreak observed with EARLINET, J. Geophys. Res. Atmos., 108, https://doi.org/https://doi.org/10.1029/2003JD003757, 2003.

Archer-Nicholls, S., Lowe, D., Schultz, D. M., and McFiggans, G.: Aerosol–radiation–cloud interactions in a regional coupled model: the effects of convective parameterisation and resolution, Atmos. Chem. Phys., 16, 5573–5594, https://doi.org/10.5194/acp-16-5573-2016, 2016.

Asmi, E., Freney, E., Hervo, M., Picard, D., Rose, C., Colomb, A., and Sellegri, K.: Aerosol cloud activation in summer and winter at puy-de-Dôme high altitude site in France, Atmos. Chem. Phys., 12, 11589–11607, https://doi.org/10.5194/acp-12-11589-2012, 2012.

Atkinson, J. D., Murray, B. J., Woodhouse, M. T., Whale, T. F., Baustian, K. J., Carslaw, K. S., Dobbie, S., O'Sullivan, D., and Malkin, T. L.: The importance of feldspar for ice nucleation by mineral dust in mixed-phase clouds, Nature, 498, 355–358, https://doi.org/10.1038/nature12278, 2013.

Axelrod, K., Samburova, V., and Khlystov, A. Y.: Relative abundance of saccharides, free amino acids, and other compounds in specific pollen species for source profiling of atmospheric aerosol, Sci. Total Environ., 799, 149254, https://doi.org/https://doi.org/10.1016/j.scitotenv.2021.149254, 2021.

Bahdanovich, P., Axelrod, K., Khlystov, A. Y., and Samburova, V.: Characterization of organic species and functional groups in pollen, fungi, algae and bacteria bioaerosols, Environ. Sci. Atmos., 4, 1091–1104, https://doi.org/10.1039/D4EA00083H, 2024.

Bangert, M., Nenes, A., Vogel, B., Vogel, H., Barahona, D., Karydis, V. A., Kumar, P., Kottmeier,

C., and Blahak, U.: Saharan dust event impacts on cloud formation and radiation over Western Europe, Atmos. Chem. Phys., 12, 4045–4063, https://doi.org/10.5194/acp-12-4045-2012, 2012.

Barreto, Á., Cuevas, E., García, R. D., Carrillo, J., Prospero, J. M., Ilić, L., Basart, S., Berjón, A. J., Marrero, C. L., Hernández, Y., Bustos, J. J., Ničković, S., and Yela, M.: Long-term characterisation of the vertical structure of the Saharan Air Layer over the Canary Islands using lidar and radiosonde profiles: implications for radiative and cloud processes over the subtropical Atlantic Ocean, Atmos. Chem. Phys., 22, 739–763, https://doi.org/10.5194/acp-22-739-2022, 2022.

Benavent-Oltra, J. A., Román, R., Casquero-Vera, J. A., Pérez-Ramírez, D., Lyamani, H., Ortiz-Amezcua, P., Bedoya-Velásquez, A. E., de Arruda Moreira, G., Barreto, Á., Lopatin, A., Fuertes, D., Herrera, M., Torres, B., Dubovik, O., Guerrero-Rascado, J. L., Goloub, P., Olmo-Reyes, F. J., and Alados-Arboledas, L.: Different strategies to retrieve aerosol properties at night-time with the GRASP algorithm, Atmos. Chem. Phys., 19, 14149–14171, https://doi.org/10.5194/acp-19-14149-2019, 2019.

Bianchi, F., Tröstl, J., Junninen, H., Frege, C., Henne, S., Hoyle, C. R., Molteni, U., Herrmann, E., Adamov, A., Bukowiecki, N., Chen, X., Duplissy, J., Gysel, M., Hutterli, M., Kangasluoma, J., Kontkanen, J., Kürten, A., Manninen, H. E., Münch, S., Peräkylä, O., Petäjä, T., Rondo, L., Williamson, C., Weingartner, E., Curtius, J., Worsnop, D. R., Kulmala, M., Dommen, J., and Baltensperger, U.: New particle formation in the free troposphere: A question of chemistry and timing., Science, 352, 1109–1112, https://doi.org/10.1126/science.aad5456, 2016.

Bianchi, F., Garmash, O., He, X., Yan, C., Iyer, S., Rosendahl, I., Xu, Z., Rissanen, M. P., Riva, M., Taipale, R., Sarnela, N., Petäjä, T., Worsnop, D. R., Kulmala, M., Ehn, M., and Junninen, H.: The role of highly oxygenated molecules (HOMs) in determining the composition of ambient ions in the boreal forest, Atmos. Chem. Phys., 17, 13819–13831, https://doi.org/10.5194/acp-17-13819-2017, 2017.

Bianchi, F., Junninen, H., Bigi, A., Sinclair, V. A., Dada, L., Hoyle, C. R., Zha, Q., Yao, L., Ahonen, L. R., Bonasoni, P., Buenrostro Mazon, S., Hutterli, M., Laj, P., Lehtipalo, K., Kangasluoma, J., Kerminen, V.-M., Kontkanen, J., Marinoni, A., Mirme, S., Molteni, U., Petäjä, T., Riva, M., Rose, C., Sellegri, K., Yan, C., Worsnop, D. R., Kulmala, M., Baltensperger, U., and Dommen, J.: Biogenic particles formed in the Himalaya as an important source of free tropospheric aerosols, Nat. Geosci., 14, 4–9, https://doi.org/10.1038/s41561-020-00661-5, 2021.

Birmili, W., Ries, L., Sohmer, R., Anastou, A., Sonntag, A., König, K., and Levin, I.: Fine and ultrafine aerosol particles at the GAW station Schneefernerhaus/Zugspitze | Feine und ultrafeine aerosolpartikeln an der GAW-station Schneefernerhaus/Zugspitze, Gefahrstoffe Reinhaltung der Luft, 69, 31–35, 2009.

Bougiatioti, A., Argyrouli, A., Solomos, S., Vratolis, S., Eleftheriadis, K., Papayannis, A., and Nenes, A.: CCN Activity, Variability and Influence on Droplet Formation during the HygrA-Cd Campaign in Athens, Atmosphere (Basel)., 8, 108, https://doi.org/10.3390/atmos8060108, 2017.

Boulon, J., Sellegri, K., Hervo, M., Picard, D., Pichon, J.-M., Fréville, P., and Laj, P.: Investigation of nucleation events vertical extent: a long term study at two different altitude sites, Atmos. Chem. Phys., 11, 5625–5639, https://doi.org/10.5194/acp-11-5625-2011, 2011.

Bradford, M. M.: A rapid and sensitive method for the quantitation of microgram quantities of protein utilizing the principle of protein-dye binding, Anal. Biochem., 72, 248–254, https://doi.org/https://doi.org/10.1016/0003-2697(76)90527-3, 1976.

Broekhuizen, K. E., Thornberry, T., Kumar, P. P., and Abbatt, J. P. D.: Formation of cloud condensation nuclei by oxidative processing: Unsaturated fatty acids, J. Geophys. Res. Atmos., 109, https://doi.org/https://doi.org/10.1029/2004JD005298, 2004.

Burgos, M. A., Andrews, E., Titos, G., Benedetti, A., Bian, H., Buchard, V., Curci, G., Kipling, Z., Kirkevåg, A., Kokkola, H., Laakso, A., Letertre-Danczak, J., Lund, M. T., Matsui, H., Myhre, G., Randles, C., Schulz, M., van Noije, T., Zhang, K., Alados-Arboledas, L., Baltensperger, U., Jefferson, A., Sherman, J., Sun, J., Weingartner, E., and Zieger, P.: A global model--measurement evaluation of particle light scattering coefficients at elevated relative humidity, Atmos. Chem. Phys., 20, 10231–10258, https://doi.org/10.5194/acp-20-10231-2020, 2020.

Cabrerizo-Vílchez, M. A., Wege, H. A., Holgado-Terriza, J. A., and Neumann, A. W.: Axisymmetric drop shape analysis as penetration Langmuir balance, Rev. Sci. Instrum., 70, 2438–2444, https://doi.org/10.1063/1.1149773, 1999.

Cai, M., Tan, H., Chan, C. K., Qin, Y., Xu, H., Li, F., Schurman, M. I., Liu, L., and Zhao, J.: The size-resolved cloud condensation nuclei (CCN) activity and its prediction based on aerosol hygroscopicity and composition in the Pearl Delta River (PRD) region during wintertime 2014, Atmos. Chem. Phys., 18, 16419–16437, https://doi.org/10.5194/acp-18-16419-2018, 2018.

Cai, M. F., Liang, B. L., Sun, Q. B., Zhou, S. Z., Yuan, B., Shao, M., Tan, H. B., Xu, Y. S., Ren, L. H., and Zhao, J.: Contribution of New Particle Formation to Cloud Condensation Nuclei Activity and its Controlling Factors in a Mountain Region of Inland China, J. Geophys. Res. Atmos., 126, e2020JD034302, https://doi.org/https://doi.org/10.1029/2020JD034302, 2021.

Cakmur, R. V, Miller, R. L., Perlwitz, J., Geogdzhayev, I. V, Ginoux, P., Koch, D., Kohfeld, K. E., Tegen, I., and Zender, C. S.: Constraining the magnitude of the global dust cycle by minimizing the difference between a model and observations, J. Geophys. Res. Atmos., 111, https://doi.org/https://doi.org/10.1029/2005JD005791, 2006.

Cariñanos, P., Casares-Porcel, M. & Quesada-Rubio, J. M. Estimating the allergenic potential of urban green spaces: A case-study in Granada, Spain. Landsc. Urban Plan. 123, 134–144, https://doi.org/10.1016/j.landurbplan.2013.12.009, 2014

Cariñanos, P., Foyo-Moreno, I., Alados, I., Guerrero-Rascado, J. L., Ruiz-Peñuela, S., Titos, G., Cazorla, A., Alados-Arboledas, L., and Díaz de la Guardia, C.: Bioaerosols in urban environments: Trends and interactions with pollutants and meteorological variables based on quasi-climatological series, J. Environ. Manage., 282, 111963, https://doi.org/https://doi.org/10.1016/j.jenvman.2021.111963, 2021.

Cariñanos, P., Guerrero-Rascado, J. L., Valle, A. M., Cazorla, A., Titos, G., Foyo-Moreno, I., Alados-Arboledas, L., and Díaz de la Guardia, C.: Assessing pollen extreme events over a Mediterranean site: Role of local surface meteorology, Atmos. Environ., 272, 118928, https://doi.org/https://doi.org/10.1016/j.atmosenv.2021.118928, 2022.

Cariñanos, P., Ruiz-Peñuela, S., Casans, A., Cazorla, A., Rejano, F., Ontiveros, A., Ortiz-Amezcua, P., Guerrero-Rascado, J. L., Olmo, F. J., Alados-Arboledas, L., and Titos, G.: Assessment of potential sources of airborne pollen in a high-mountain mediterranean natural environment, Atmos. Environ., 340, 120917, https://doi.org/https://doi.org/10.1016/j.atmosenv.2024.120917, 2025.

Carslaw, K. S., Boucher, O., Spracklen, D. V., Mann, G. W., Rae, J. G. L., Woodward, S., and Kulmala, M.: A review of natural aerosol interactions and feedbacks within the Earth system, Atmos. Chem. Phys., 10, 1701–1737, https://doi.org/10.5194/acp-10-1701-2010, 2010.

Casquero-Vera, J.A., Lyamani, H., Titos, G., Borrás, E., Olmo, F.J., Alados-Arboledas, L.. Impact

of primary NO2 emissions at different urban sites exceeding the European NO2 standard limit. Sci. Total Environ. 646, 1117–1125. https://doi.org/10.1016/j.scitotenv.2018.07.360, 2019.

Casquero-Vera, J. A., Lyamani, H., Dada, L., Hakala, S., Paasonen, P., Román, R., Fraile, R., Petäjä, T., Olmo-Reyes, F. J., and Alados-Arboledas, L.: New particle formation at urban and highaltitude remote sites in the south-eastern Iberian Peninsula, Atmos. Chem. Phys., 20, 14253–14271, https://doi.org/10.5194/acp-20-14253-2020, 2020.

Casquero-Vera, J. A., Pérez-Ramírez, D., Lyamani, H., Rejano, F., Casans, A., Titos, G., Olmo, F. J., Dada, L., Hakala, S., Hussein, T., Lehtipalo, K., Paasonen, P., Hyvärinen, A., Pérez, N., Querol, X., Rodríguez, S., Kalivitis, N., González, Y., Alghamdi, M. A., Kerminen, V.-M., Alastuey, A., Petäjä, T., and Alados-Arboledas, L.: Impact of desert dust on new particle formation events and the cloud condensation nuclei budget in dust-influenced areas, Atmos. Chem. Phys., 23, 15795–15814, https://doi.org/10.5194/acp-23-15795-2023, 2023.

Cazorla, A., Casquero-Vera, J. A., Román, R., Guerrero-Rascado, J. L., Toledano, C., Cachorro, V. E., Orza, J. A. G., Cancillo, M. L., Serrano, A., Titos, G., Pandolfi, M., Alastuey, A., Hanrieder, N., and Alados-Arboledas, L.: Near-real-time processing of a ceilometer network assisted with sunphotometer data: monitoring a dust outbreak\hack{\newline} over the Iberian Peninsula, Atmos. Chem. Phys., 17, 11861–11876, https://doi.org/10.5194/acp-17-11861-2017, 2017.

Cecchi L, D'Amato G, Annesi-Maesano I. Climate change and outdoor aeroallergens related to allergy and asthma: taking the exposome into account. Allergy. 75:2361–3, https://doi.org/10.1111/all.14286, 2020

Chandra, I., Kim, S., Seto, T., Otani, Y., Takami, A., Yoshino, A., Irei, S., Park, K., Takamura, T., Kaneyasu, N., Hatakeyama, S. New particle formation under the influence of the long-range transport of air pollutants in East Asia. Atmos. Environ. 141:30–40. https://doi.org/10.1016/j.atmosenv.2016.06.040, 2016

Chen, J., Budisulistiorini, S. H., Miyakawa, T., Komazaki, Y., and Kuwata, M.: Secondary aerosol formation promotes water uptake by organic-rich wildfire haze particles in equatorial Asia, Atmos. Chem. Phys., 18, 7781–7798, https://doi.org/10.5194/acp-18-7781-2018, 2018.

Chiapello, I., Bergametti, G., Chatenet, B., Dulac, F., and Soares, E. S.: Origins of African dust transported over the Eastern Tropical Atlantic, J. Geophys. Res., 102, 13701–13709,

https://doi.org/10.1029/97JD00259, 1997.

Chilson, P.: A First Course in Atmospheric Thermodynamics, Eos, Trans. Am. Geophys. Union, 90, https://doi.org/10.1029/2009EO330005, 2009.

Christiansen, S., Ickes, L., Bulatovic, I., Leck, C., Murray, B. J., Bertram, A. K., Wagner, R., Gorokhova, E., Salter, M. E., Ekman, A. M. L., and Bilde, M.: Influence of Arctic Microlayers and Algal Cultures on Sea Spray Hygroscopicity and the Possible Implications for Mixed-Phase Clouds, J. Geophys. Res. Atmos., 125, e2020JD032808, https://doi.org/10.1029/2020JD032808, 2020.

Cipoli, Y. A., Alves, C., Rapuano, M., Evtyugina, M., Rienda, I. C., Kováts, N., Vicente, A., Giardi, F., Furst, L., Nunes, T., and Feliciano, M.: Nighttime–daytime PM10 source apportionment and toxicity in a remoteness inland city of the Iberian Peninsula, Atmos. Environ., 303, 119771, https://doi.org/https://doi.org/10.1016/j.atmosenv.2023.119771, 2023.

Collaud Coen, M., Andrews, E., Aliaga, D., Andrade, M., Angelov, H., Bukowiecki, N., Ealo, M., Fialho, P., Flentje, H., Hallar, A. G., Hooda, R., Kalapov, I., Krejci, R., Lin, N.-H., Marinoni, A., Ming, J., Nguyen, N. A., Pandolfi, M., Pont, V., Ries, L., Rodr\'\iguez, S., Schauer, G., Sellegri, K., Sharma, S., Sun, J., Tunved, P., Velasquez, P., and Ruffieux, D.: Identification of topographic features influencing aerosol observations at high altitude stations, Atmos. Chem. Phys., 18, 12289–12313, https://doi.org/10.5194/acp-18-12289-2018, 2018.

Coz, E., Gómez-Moreno, F. J., Pujadas, M., Casuccio, G. S., Lersch, T. L., and Artíñano, B.: Individual particle characteristics of North African dust under different long-range transport scenarios, Atmos. Environ., 43, 1850–1863, https://doi.org/https://doi.org/10.1016/j.atmosenv.2008.12.045, 2009.

Dada, L., Paasonen, P., Nieminen, T., Buenrostro Mazon, S., Kontkanen, J., Peräkylä, O., Lehtipalo, K., Hussein, T., Petäjä, T., Kerminen, V.-M., Bäck, J., and Kulmala, M.: Long-term analysis of clear-sky new particle formation events and nonevents in Hyytiälä, Atmos. Chem. Phys., 17, 6227–6241, https://doi.org/10.5194/acp-17-6227-2017, 2017.

Dada, L., Chellapermal, R., Buenrostro Mazon, S., Paasonen, P., Lampilahti, J., Manninen, H. E., Junninen, H., Petäjä, T., Kerminen, V.-M., and Kulmala, M.: Refined classification and characterization of atmospheric new-particle formation events using air ions, Atmos. Chem. Phys.,

18, 17883-17893, https://doi.org/10.5194/acp-18-17883-2018, 2018.

Dal Maso, M., Kulmala, M., Riipinen, I., Wagner, R., Hussein, T., Aalto, P. P., and Lehtinen, K. E. J.: Formation and growth of fresh atmospheric aerosols: Eight years of aerosol size distribution data from SMEAR II, Hyytiälä, Finland, Boreal Environ. Res., 10, 323–336, 2005.

Dameto de España, C., Wonaschütz, A., Steiner, G., Rosati, B., Demattio, A., Schuh, H., and Hitzenberger, R.: Long-term quantitative field study of New Particle Formation (NPF) events as a source of Cloud Condensation Nuclei (CCN) in the urban background of Vienna, Atmos. Environ., 164, 289–298, https://doi.org/https://doi.org/10.1016/j.atmosenv.2017.06.001, 2017.

Davies, J. F., Zuend, A., and Wilson, K. R.: Technical note: The role of evolving surface tension in the formation of cloud droplets, Atmos. Chem. Phys., 19, 2933–2946, https://doi.org/10.5194/acp-19-2933-2019, 2019.

Dawson, J. N., Malek, K. A., Razafindrambinina, P. N., Raymond, T. M., Dutcher, D. D., Asa-Awuku, A. A., and Freedman, M. A.: Direct Comparison of the Submicron Aerosol Hygroscopicity of Water-Soluble Sugars, ACS Earth Sp. Chem., 4, 2215–2226, https://doi.org/10.1021/acsearthspacechem.0c00159, 2020.

Decesari, S., Facchini, M. C., Mircea, M., Cavalli, F., and Fuzzi, S.: Solubility properties of surfactants in atmospheric aerosol and cloud/fog water samples, J. Geophys. Res. Atmos., 108, https://doi.org/10.1029/2003JD003566, 2003.

Deguillaume, L., Leriche, M., Amato, P., Ariya, P. A., Delort, A.-M., Pöschl, U., Chaumerliac, N., Bauer, H., Flossmann, A. I., and Morris, C. E.: Microbiology and atmospheric processes: chemical interactions of primary biological aerosols, Biogeosciences, 5, 1073–1084, https://doi.org/10.5194/bg-5-1073-2008, 2008.

Denjean, C., Caquineau, S., Desboeufs, K., Laurent, B., Maille, M., Quiñones Rosado, M., Vallejo, P., Mayol-Bracero, O. L., and Formenti, P.: Long-range transport across the Atlantic in summertime does not enhance the hygroscopicity of African mineral dust, Geophys. Res. Lett., 42, 7835–7843, https://doi.org/https://doi.org/10.1002/2015GL065693, 2015.

Després, V., Huffman, J. A., Burrows, S. M., Hoose, C., Safatov, A., Buryak, G., Fröhlich-Nowoisky, J., Elbert, W., Andreae, M., Pöschl, U., and Jaenicke, R.: Primary biological aerosol

particles in the atmosphere: a review, Tellus B Chem. Phys. Meteorol., 64, 15598, https://doi.org/10.3402/tellusb.v64i0.15598, 2012.

Díaz, J., Linares, C., Carmona, R., Russo, A., Ortiz, C., Salvador, P., and Trigo, R. M.: Saharan dust intrusions in Spain: Health impacts and associated synoptic conditions, Environ. Res., 156, 455–467, https://doi.org/https://doi.org/10.1016/j.envres.2017.03.047, 2017.

Du, W., Cai, J., Zheng, F., Yan, C., Zhou, Y., Guo, Y., Chu, B., Yao, L., Heikkinen, L. M., Fan, X., Wang, Y., Cai, R., Hakala, S., Chan, T., Kontkanen, J., Tuovinen, S., Petäjä, T., Kangasluoma, J., Bianchi, F., Paasonen, P., Sun, Y., Kerminen, V.-M., Liu, Y., Daellenbach, K. R., Dada, L., and Kulmala, M.: Influence of Aerosol Chemical Composition on Condensation Sink Efficiency and New Particle Formation in Beijing, Environ. Sci. Technol. Lett., 9, 375–382, https://doi.org/10.1021/acs.estlett.2c00159, 2022.

Duplissy, J., Merikanto, J., Franchin, A., Tsagkogeorgas, G., Kangasluoma, J., Wimmer, D., Vuollekoski, H., Schobesberger, S., Lehtipalo, K., Flagan, R. C., Brus, D., Donahue, N., Vehkämäki, H., Almeida, J., Amorim, A., Barmet, P., Bianchi, F., Breitenlechner, M., Dunne, E., and Kulmala, M.: Effect of ions on sulfuric acid-water binary particle formation II: Experimental data and comparison with QC-normalized classical nucleation theory, J. Geophys. Res. Atmos., 121, n/a-n/a, https://doi.org/10.1002/2015JD023539, 2015.

Dusek, U., Frank, G. P., Hildebrandt, L., Curtius, J., Schneider, J., Walter, S., Chand, D., Drewnick, F., Hings, S., Jung, D., Borrmann, S., and Andreae, M. O.: Size matters more than chemistry for cloud-nucleating ability of aerosol particles., Science, 312, 1375–1378, https://doi.org/10.1126/science.1125261, 2006.

Dusek, U., Frank, G. P., Curtius, J., Drewnick, F., Schneider, J., Kürten, A., Rose, D., Andreae, M. O., Borrmann, S., and Pöschl, U.: Enhanced organic mass fraction and decreased hygroscopicity of cloud condensation nuclei (CCN) during new particle formation events, Geophys. Res. Lett., 37, https://doi.org/https://doi.org/10.1029/2009GL040930, 2010.

Eastoe, J. and Dalton, J. S.: Dynamic surface tension and adsorption mechanisms of surfactants at the air—water interface, Adv. Colloid Interface Sci., 85, 103–144, https://doi.org/https://doi.org/10.1016/S0001-8686(99)00017-2, 2000.

Ehn, M., Thornton, J. A., Kleist, E., Sipilä, M., Junninen, H., Pullinen, I., Springer, M., Rubach,

F., Tillmann, R., Lee, B., Lopez-Hilfiker, F., Andres, S., Acir, I.-H., Rissanen, M., Jokinen, T., Schobesberger, S., Kangasluoma, J., Kontkanen, J., Nieminen, T., Kurtén, T., Nielsen, L. B., Jørgensen, S., Kjaergaard, H. G., Canagaratna, M., Maso, M. D., Berndt, T., Petäjä, T., Wahner, A., Kerminen, V.-M., Kulmala, M., Worsnop, D. R., Wildt, J., and Mentel, T. F.: A large source of low-volatility secondary organic aerosol, Nature, 506, 476–479, https://doi.org/10.1038/nature13032, 2014.

Ervens, B., Cubison, M. J., Andrews, E., Feingold, G., Ogren, J. A., Jimenez, J. L., Quinn, P. K., Bates, T. S., Wang, J., Zhang, Q., Coe, H., Flynn, M., and Allan, J. D.: CCN predictions using simplified assumptions of organic aerosol composition and mixing state: a synthesis from six different locations, Atmos. Chem. Phys., 10, 4795–4807, https://doi.org/10.5194/acp-10-4795-2010, 2010.

Escudero, M., Castillo, S., Querol, X., Avila, A., Alarcón, M., Viana, M. M., Alastuey, A., Cuevas, E., and Rodríguez, S.: Wet and dry African dust episodes over Eastern Spain, J. Geophys. Res., 110, D18S08, https://doi.org/10.1029/2004JD004731, 2005.

Fan, J., Rosenfeld, D., Zhang, Y., Giangrande, S. E., Li, Z., Machado, L. A. T., Martin, S. T., Yang, Y., Wang, J., Artaxo, P., Barbosa, H. M. J., Braga, R. C., Comstock, J. M., Feng, Z., Gao, W., Gomes, H. B., Mei, F., Pöhlker, C., Pöhlker, M. L., Pöschl, U., and de Souza, R. A. F.: Substantial convection and precipitation enhancements by ultrafine aerosol particles., Science, 359, 411–418, https://doi.org/10.1126/science.aan8461, 2018.

Fontal, M., van Drooge, B. L., López, J. F., Fernández, P., and Grimalt, J. O.: Broad spectrum analysis of polar and apolar organic compounds in submicron atmospheric particles, J. Chromatogr. A, 1404, 28–38, https://doi.org/https://doi.org/10.1016/j.chroma.2015.05.042, 2015.

Forestieri, S. D., Staudt, S. M., Kuborn, T. M., Faber, K., Ruehl, C. R., Bertram, T. H., and Cappa, C. D.: Establishing the impact of model surfactants on cloud condensation nuclei activity of sea spray aerosol mimics, Atmos. Chem. Phys., 18, 10985–11005, https://doi.org/10.5194/acp-18-10985-2018, 2018.

Friedman, B., Zelenyuk, A., Beranek, J., Kulkarni, G., Pekour, M., Gannet Hallar, A., McCubbin, I. B., Thornton, J. A., and Cziczo, D. J.: Aerosol measurements at a high-elevation site: composition, size, and cloud condensation nuclei activity, Atmos. Chem. Phys., 13, 11839–11851, https://doi.org/10.5194/acp-13-11839-2013, 2013.

Fröhlich-Nowoisky, J., Kampf, C. J., Weber, B., Huffman, J. A., Pöhlker, C., Andreae, M. O., Lang-

Yona, N., Burrows, S. M., Gunthe, S. S., Elbert, W., Su, H., Hoor, P., Thines, E., Hoffmann, T., Després, V. R., and Pöschl, U.: Bioaerosols in the Earth system: Climate, health, and ecosystem interactions, Atmos. Res., 182, 346–376, https://doi.org/https://doi.org/10.1016/j.atmosres.2016.07.018, 2016.

Fuchs, N. A.: On the stationary charge distribution on aerosol particles in a bipolar ionic atmosphere, Geofis. Pura e Appl., 56, 185–193, https://doi.org/10.1007/BF01993343, 1963.

Fuentes, E., Coe, H., Green, D., and McFiggans, G.: On the impacts of phytoplankton-derived organic matter on the properties of the primary marine aerosol – Part 2: Composition, hygroscopicity and cloud condensation activity, Atmos. Chem. Phys., 11, 2585–2602, https://doi.org/10.5194/acp-11-2585-2011, 2011.

Galindo, N., Yubero, E., Nicolás, J. F., Crespo, J., Varea, M., and Gil-Moltó, J.: Regional and long-range transport of aerosols at Mt. Aitana, Southeastern Spain, Sci. Total Environ., 584–585, 723–730, https://doi.org/https://doi.org/10.1016/j.scitotenv.2017.01.108, 2017.

García, M. I., Rodríguez, S., González, Y., and García, R. D.: Climatology of new particle formation at Izaña mountain GAW observatory in the subtropical North Atlantic, Atmos. Chem. Phys., 14, 3865–3881, https://doi.org/10.5194/acp-14-3865-2014, 2014.

García, M. I., Rodríguez, S., and Alastuey, A.: Impact of North America on the aerosol composition in the North Atlantic free troposphere, Atmos. Chem. Phys., 17, 7387–7404, https://doi.org/10.5194/acp-17-7387-2017, 2017.

Garcia-Marlès, M., Lara, R., Reche, C., Pérez, N., Tobías, A., Savadkoohi, M., Beddows, D., Salma, I., Vörösmarty, M., Weidinger, T., Hueglin, C., Mihalopoulos, N., Grivas, G., Kalkavouras, P., Ondracek, J., Zikova, N., Niemi, J. V, Manninen, H. E., Green, D. C., Tremper, A. H., Norman, M., Vratolis, S., Diapouli, E., Eleftheriadis, K., Gómez-Moreno, F. J., Alonso-Blanco, E., Wiedensohler, A., Weinhold, K., Merkel, M., Bastian, S., Hoffmann, B., Altug, H., Petit, J.-E., Acharja, P., Favez, O., Santos, S. M. Dos, Putaud, J.-P., Dinoi, A., Contini, D., Casans, A., Casquero-Vera, J. A., Crumeyrolle, S., Bourrianne, E., Poppel, M. Van, Dreesen, F. E., Harni, S., Timonen, H., Lampilahti, J., Petäjä, T., Pandolfi, M., Hopke, P. K., Harrison, R. M., Alastuey, A., and Querol, X.: Source apportionment of ultrafine particles in urban Europe, Environ. Int., 194, 109149, https://doi.org/https://doi.org/10.1016/j.envint.2024.109149, 2024.

Gibson, E. R., Hudson, P. K., and Grassian, V. H.: Aerosol chemistry and climate: Laboratory

studies of the carbonate component of mineral dust and its reaction products, Geophys. Res. Lett., 33, https://doi.org/https://doi.org/10.1029/2006GL026386, 2006.

Gogoi, M. M., Babu, S. S., Jayachandran, V., Moorthy, K. K., Satheesh, S. K., Naja, M., and Kotamarthi, V. R.: Optical properties and CCN activity of aerosols in a high-altitude Himalayan environment: Results from RAWEX-GVAX, J. Geophys. Res. Atmos., 120, 2453–2469, https://doi.org/10.1002/2014JD022966, 2015.

Gong, F., Wu, X., and Wang, W.: Diversity and function of maize pollen coat proteins: from biochemistry to proteomics, Front. Plant Sci., 6, https://doi.org/10.3389/fpls.2015.00199, 2015.

Gordon, H., Kirkby, J., Baltensperger, U., Bianchi, F., Breitenlechner, M., Curtius, J., Dias, A., Dommen, J., Donahue, N. M., Dunne, E. M., Yan, C., and Carslaw, K. S.: Causes and importance of new particle formation in the present-day and preindustrial atmospheres, J. Geophys. Res. Atmos., 122, 8739–8760, https://doi.org/10.1002/2017JD026844, 2017.

Granados-Muñoz, M. J., Sicard, M., Papagiannopoulos, N., Barragán, R., Bravo-Aranda, J. A., and Nicolae, D.: Two-dimensional mineral dust radiative effect calculations from CALIPSO observations over Europe, Atmos. Chem. Phys., 19, 13157–13173, https://doi.org/10.5194/acp-19-13157-2019, 2019.

Grote, M., Valenta, R., and Reichelt, R.: Abortive pollen germination: A mechanism of allergen release in birch, alder, and hazel revealed by immunogold electron microscopy, J. Allergy Clin. Immunol., 111, 1017–1023, https://doi.org/https://doi.org/10.1067/mai.2003.1452, 2003.

Gysel, M., Weingartner, E., and Baltensperger, U.: Hygroscopicity of Aerosol Particles at Low Temperatures. 2. Theoretical and Experimental Hygroscopic Properties of Laboratory Generated Aerosols, Environ. Sci. Technol., 36, 63–68, https://doi.org/10.1021/es010055g, 2002.

Hamed, A., Birmili, W., Joutsensaari, J., Mikkonen, S., Asmi, A., Wehner, B., Spindler, G., Jaatinen, A., Wiedensohler, A., Korhonen, H., Lehtinen, K. E. J., and Laaksonen, A.: Changes in the production rate of secondary aerosol particles in Central Europe in view of decreasing SO\$_{2}\$ emissions between 1996 and 2006, Atmos. Chem. Phys., 10, 1071–1091, https://doi.org/10.5194/acp-10-1071-2010, 2010.

Hammer, E., Bukowiecki, N., Gysel, M., Jurányi, Z., Hoyle, C. R., Vogt, R., Baltensperger, U., and

Weingartner, E.: Investigation of the effective peak supersaturation for liquid-phase clouds at the high-alpine site Jungfraujoch, Switzerland (3580 m a.s.l.), Atmos. Chem. Phys., 14, 1123–1139, https://doi.org/10.5194/acp-14-1123-2014, 2014.

Han, S., Hong, J., Luo, Q., Xu, H., Tan, H., Wang, Q., Tao, J., Zhou, Y., Peng, L., He, Y., Shi, J., Ma, N., Cheng, Y., and Su, H.: Hygroscopicity of organic compounds as a function of organic functionality, water solubility, molecular weight, and oxidation level, Atmos. Chem. Phys., 22, 3985–4004, https://doi.org/10.5194/acp-22-3985-2022, 2022.

Hatch, C., Gierlus, K., Schuttlefield Christus, J., and Grassian, V.: Water adsorption and cloud condensation nuclei activity of calcite and calcite coated with model humic and fulvic acids, Atmos. Environ., 42, 5672–5684, https://doi.org/10.1016/j.atmosenv.2008.03.005, 2008.

Haynes, W.M., Lide, D.R., & Bruno, T. J.: CRC Handbook of Chemistry and Physics, 97th ed., 2670 pp., https://doi.org/https://doi.org/10.1201/9781315380476, 2016.

Herich, H., Tritscher, T., Wiacek, A., Gysel, M., Weingartner, E., Lohmann, U., Baltensperger, U., and Cziczo, D. J.: Water uptake of clay and desert dust aerosol particles at sub- and supersaturated water vapor conditions, Phys. Chem. Chem. Phys., 11, 7804–7809, https://doi.org/10.1039/B901585J, 2009.

Hess, M., Koepke, P., and Schult, I.: Optical Properties of Aerosols and Clouds: The Software Package OPAC, Bull. Am. Meteorol. Soc., 79, 831–844, https://doi.org/https://doi.org/10.1175/1520-0477(1998)079<0831:OPOAAC>2.0.CO;2, 1998.

Hoose, C. and Möhler, O.: Heterogeneous ice nucleation on atmospheric aerosols: a review of results from laboratory experiments, Atmos. Chem. Phys., 12, 9817–9854, https://doi.org/10.5194/acp-12-9817-2012, 2012.

Hoose, C., Kristjánsson, J., and Burrows, S.: How important is biological ice nucleation in clouds on a global scale, Environ. Res. Lett. v.5, 5, https://doi.org/10.1088/1748-9326/5/2/024009, 2010.

Horvath, H.: Aerosol - An introduction, https://doi.org/10.1016/S0265-931X(00)00041-2, October 2000.

Hughes, D. D., Mampage, C. B. A., Jones, L. M., Liu, Z., and Stone, E. A.: Characterization of Atmospheric Pollen Fragments during Springtime Thunderstorms, Environ. Sci. Technol. Lett., 7,

409-414, https://doi.org/10.1021/acs.estlett.0c00213, 2020.

Hussein, T., Al-Ruz, R. A., Petäjä, T., Junninen, H., Arafah, D.-E., Hämeri, K., and Kulmala, M.: Local Air Pollution versus Short-range Transported Dust Episodes: A Comparative Study for Submicron Particle Number Concentration, Aerosol Air Qual. Res., 11, 109–119, https://doi.org/10.4209/aaqr.2010.08.0066, 2011.

Hussein, T., Juwhari, H., Al Kuisi, M. *et al.* Accumulation and coarse mode aerosol concentrations and carbonaceous contents in the urban background atmosphere in Amman, Jordan. Arab J Geosci 11, 617. https://doi.org/10.1007/s12517-018-3970-z, 2018

Intergovernmental Panel on Climate Change (IPCC): IPCC: Climate Change 2021: The Physical Science Basis, Climate Change 2021: The Physical Science Basis, 42 pp., 2021.

Intergovernmental Panel on Climate Change (IPCC), 2023. Climate Change 2021 – The Physical Science Basis: Working Group I Contribution to the Sixth Assessment Report of the Intergovernmental Panel on Climate Change. Cambridge University Press, Cambridge. https://doi.org/DOI: 10.1017/9781009157896

Ischebeck, T.: Lipids in pollen — They are different, Biochim. Biophys. Acta - Mol. Cell Biol. Lipids, 1861, 1315–1328, https://doi.org/https://doi.org/10.1016/j.bbalip.2016.03.023, 2016.

Izquierdo, R., Belmonte, J., Avila, A., Alarcón, M., Cuevas, E., and Alonso-Pérez, S.: Source areas and long-range transport of pollen from continental land to Tenerife (Canary Islands), Int. J. Biometeorol., 55, 67–85, https://doi.org/10.1007/s00484-010-0309-1, 2011.

Jacobson, M. Z. and Streets, D. G.: Influence of future anthropogenic emissions on climate, natural emissions, and air quality, J. Geophys. Res. Atmos., 114, https://doi.org/https://doi.org/10.1029/2008JD011476, 2009.

Jaén, C., Titos, G., Castillo, S., Casans, A., Rejano, F., Cazorla, A., Herrero, J., Alados-Arboledas, L., Grimalt, J. O., and van Drooge, B. L.: Diurnal source apportionment of organic and inorganic atmospheric particulate matter at a high-altitude mountain site under summer conditions (Sierra Nevada; Spain), Sci. Total Environ., 167178, https://doi.org/https://doi.org/10.1016/j.scitotenv.2023.167178, 2023.

Jiang, S., Zhang, F., Ren, J., Chen, L., Yan, X., Liu, J., Sun, Y., and Li, Z.: Evaluation of the

contribution of new particle formation to cloud droplet number concentration in the urban atmosphere, Atmos. Chem. Phys., 21, 14293–14308, https://doi.org/10.5194/acp-21-14293-2021, 2021.

Jorga, S. D., Florou, K., Patoulias, D., and Pandis, S. N.: New particle formation and growth during summer in an urban environment: a dual chamber study, Atmos. Chem. Phys., 23, 85–97, https://doi.org/10.5194/acp-23-85-2023, 2023.

Jurányi, Z., Gysel, M., Weingartner, E., Bukowiecki, N., Kammermann, L., and Baltensperger, U.: A 17 month climatology of the cloud condensation nuclei number concentration at the high alpine site Jungfraujoch, J. Geophys. Res. Atmos., 116, https://doi.org/10.1029/2010JD015199, 2011.

Jurányi, Z., Tritscher, T., Gysel, M., Laborde, M., Gomes, L., Roberts, G., Baltensperger, U., and Weingartner, E.: Hygroscopic mixing state of urban aerosol derived from size-resolved cloud condensation nuclei measurements during the MEGAPOLI campaign in Paris, Atmos. Chem. Phys., 13, 6431–6446, https://doi.org/10.5194/acp-13-6431-2013, 2013.

Kaaden, N., Massling, A., Schladitz, A., MüLLER, T., Kandler, K., Schütz, L., Weinzierl, B., Petzold, A., Tesche, M., Leinert, S., Deutscher, C., Ebert, M., Weinbruch, S. and Wiedensohler, A. State of mixing, shape factor, number size distribution, and hygroscopic growth of the Saharan anthropogenic and mineral dust aerosol at Tinfou, Morocco. Tellus B: Chemical and Physical Meteorology, 61(1), 51–63. https://doi.org/10.1111/j.1600-0889.2008.00388.x, 2009

Kakavas, S., Patoulias, D., Zakoura, M., Nenes, A., and Pandis, S. N.: Size-resolved aerosol pH over Europe during summer, Atmos. Chem. Phys., 21, 799–811, https://doi.org/10.5194/acp-21-799-2021, 2021.

Kalivitis, N., Kerminen, V.-M., Kouvarakis, G., Stavroulas, I., Bougiatioti, A., Nenes, A., Manninen, H. E., Petäjä, T., Kulmala, M., and Mihalopoulos, N.: Atmospheric new particle formation as a source of CCN in the eastern Mediterranean marine boundary layer, Atmos. Chem. Phys., 15, 9203–9215, https://doi.org/10.5194/acp-15-9203-2015, 2015.

Kalkavouras, P., Bougiatioti, A., Kalivitis, N., Stavroulas, I., Tombrou, M., Nenes, A., and Mihalopoulos, N.: Regional new particle formation as modulators of cloud condensation nuclei and cloud droplet number in the eastern Mediterranean, Atmos. Chem. Phys., 19, 6185–6203,

https://doi.org/10.5194/acp-19-6185-2019, 2019.

Kammermann, L., Gysel, M., Weingartner, E., Herich, H., Cziczo, D., Holst, T., Svenningsson, B., Arneth, A., and Baltensperger, U.: Subarctic atmospheric aerosol composition: 3. Measured and modeled properties of cloud condensation nuclei, J. Geophys. Res., 115, D04202, https://doi.org/10.1029/2009JD012447, 2010.

Karydis, V. A., Kumar, P., Barahona, D., Sokolik, I. N., and Nenes, A.: On the effect of dust particles on global cloud condensation nuclei and cloud droplet number, J. Geophys. Res. Atmos., 116, https://doi.org/https://doi.org/10.1029/2011JD016283, 2011.

Karydis, V. A., Tsimpidi, A. P., Bacer, S., Pozzer, A., Nenes, A., and Lelieveld, J.: Global impact of mineral dust on cloud droplet number concentration, Atmos. Chem. Phys., 17, 5601–5621, https://doi.org/10.5194/acp-17-5601-2017, 2017.

Kaufman, Y. J. and Tanré, D.: Effect of variations in super-saturation on the formation of cloud condensation nuclei, Nature, 369, 45–48, https://doi.org/10.1038/369045a0, 1994.

Kelly, J. T., Chuang, C. C., and Wexler, A. S.: Influence of dust composition on cloud droplet formation, Atmos. Environ., 41, 2904–2916, https://doi.org/10.1016/j.atmosenv.2006.12.008, 2007.

Kerminen, V.-M., Chen, X., Vakkari, V., Petäjä, T., Kulmala, M., and Bianchi, F.: Atmospheric new particle formation and growth: review of field observations, Environ. Res. Lett., 13, 103003, https://doi.org/10.1088/1748-9326/aadf3c, 2018.

Kirkby, J., Curtius, J., Almeida, J., Dunne, E., Duplissy, J., Ehrhart, S., Franchin, A., Gagné, S., Ickes, L., Kürten, A., Kupc, A., Metzger, A., Riccobono, F., Rondo, L., Schobesberger, S., Tsagkogeorgas, G., Wimmer, D., Amorim, A., Bianchi, F., Breitenlechner, M., David, A., Dommen, J., Downard, A., Ehn, M., Flagan, R. C., Haider, S., Hansel, A., Hauser, D., Jud, W., Junninen, H., Kreissl, F., Kvashin, A., Laaksonen, A., Lehtipalo, K., Lima, J., Lovejoy, E. R., Makhmutov, V., Mathot, S., Mikkilä, J., Minginette, P., Mogo, S., Nieminen, T., Onnela, A., Pereira, P., Petäjä, T., Schnitzhofer, R., Seinfeld, J. H., Sipilä, M., Stozhkov, Y., Stratmann, F., Tomé, A., Vanhanen, J., Viisanen, Y., Vrtala, A., Wagner, P. E., Walther, H., Weingartner, E., Wex, H., Winkler, P. M., Carslaw, K. S., Worsnop, D. R., Baltensperger, U., and Kulmala, M.: Role of sulphuric acid, ammonia and galactic cosmic rays in atmospheric aerosol nucleation, Nature, 476, 429–433, https://doi.org/10.1038/nature10343,

2011.

Kirkby, J., Craven, J., Flagan, R., Seinfeld, J., and Zhang, X.: Ion-induced nucleation of pure biogenic particles, Nature, 533, https://doi.org/10.1038/nature17953, 2016.

Knippertz, P. and Stuut, J.-B.: Mineral Dust: A Key Player in the Earth System, 1–509 pp., https://doi.org/10.1007/978-94-017-8978-3, 2014.

Köhler, H.: The nucleus in and the growth of hygroscopic droplets, Trans. Faraday Soc., 32, 1152–1161, https://doi.org/10.1039/TF9363201152, 1936.

Kok, J., Storelvmo, T., Karydis, V., Adebiyi, A., Mahowald, N., Evan, A., He, C., and Leung, D.: Mineral dust aerosol impacts on global climate and climate change, Nat. Rev. Earth Environ., 4, https://doi.org/10.1038/s43017-022-00379-5, 2023.

Kok, J. F., Adebiyi, A. A., Albani, S., Balkanski, Y., Checa-Garcia, R., Chin, M., Colarco, P. R., Hamilton, D. S., Huang, Y., Ito, A., Klose, M., Leung, D. M., Li, L., Mahowald, N. M., Miller, R. L., Obiso, V., Pérez García-Pando, C., Rocha-Lima, A., Wan, J. S., and Whicker, C. A.: Improved representation of the global dust cycle using observational constraints on dust properties and abundance, Atmos. Chem. Phys., 21, 8127–8167, https://doi.org/10.5194/acp-21-8127-2021, 2021.

Korhonen, H., Carslaw, K. S., Spracklen, D. V, Mann, G. W., and Woodhouse, M. T.: Influence of oceanic dimethyl sulfide emissions on cloud condensation nuclei concentrations and seasonality over the remote Southern Hemisphere oceans: A global model study, J. Geophys. Res. Atmos., 113, https://doi.org/https://doi.org/10.1029/2007JD009718, 2008.

Kostenidou, E., Florou, K., Kaltsonoudis, C., Tsiflikiotou, M., Vratolis, S., Eleftheriadis, K., and Pandis, S. N.: Sources and chemical characterization of organic aerosol during the summer in the eastern Mediterranean, Atmos. Chem. Phys., 15, 11355–11371, https://doi.org/10.5194/acp-15-11355-2015, 2015.

Kristensen, T. B., Müller, T., Kandler, K., Benker, N., Hartmann, M., Prospero, J. M., Wiedensohler, A., and Stratmann, F.: Properties of cloud condensation nuclei (CCN) in the trade wind marine boundary layer of the western North Atlantic, Atmos. Chem. Phys., 16, 2675–2688, https://doi.org/10.5194/acp-16-2675-2016, 2016.

Kristensson, A., Rosenørn, T., and Bilde, M.: Cloud Droplet Activation of Amino Acid Aerosol

Particles, J. Phys. Chem. A, 114, 379–386, https://doi.org/10.1021/jp9055329, 2010.

Kruskal, W. H. and Wallis, W. A.: Use of ranks in one-criterion variance analysis., J. Am. Stat. Assoc., 47, 583–621, https://doi.org/10.2307/2280779, 1952.

Kulmala, M.: How Particles Nucleate and Grow, Science (80-.)., 302, 1000–1001, https://doi.org/10.1126/science.1090848, 2003.

Kulmala, M., Vehkamäki, H., Petäjä, T., Dal Maso, M., Lauri, A., Kerminen, V.-M., Birmili, W., and McMurry, P. H.: Formation and growth rates of ultrafine atmospheric particles: a review of observations, J. Aerosol Sci., 35, 143–176, https://doi.org/10.1016/j.jaerosci.2003.10.003, 2004.

Kulmala, M., Kerminen, V.-M., Petäjä, T., Ding, A. J., and Wang, L.: Atmospheric gas-to-particle conversion: why NPF events are observed in megacities?, Faraday Discuss., 200, 271–288, https://doi.org/10.1039/C6FD00257A, 2017.

Kumar, P., K, B., and Abbatt, J.: Organic acids as cloud condensation nuclei: Laboratory studies of highly soluble and insoluble species, Atmos. Chem. Phys., 3, https://doi.org/10.5194/acpd-3-949-2003, 2003.

Kumar, P., Sokolik, I., and Nenes, A.: Cloud condensation nuclei activity and droplet activation kinetics of fresh unprocessed regional dust samples and minerals, Atmos. Chem. Phys. Discuss., 10, https://doi.org/10.5194/acpd-10-31039-2010, 2010.

Kuwata, M., Kondo, Y., Miyazaki, Y., Komazaki, Y., Kim, J. H., Yum, S. S., Tanimoto, H., and Matsueda, H.: Cloud condensation nuclei activity at Jeju Island, Korea in spring 2005, Atmos. Chem. Phys., 8, 2933–2948, https://doi.org/10.5194/acp-8-2933-2008, 2008.

Kuwata, M., Shao, W., Lebouteiller, R., and Martin, S. T.: Classifying organic materials by oxygen-to-carbon elemental ratio to predict the activation regime of Cloud Condensation Nuclei (CCN), Atmos. Chem. Phys., 13, 5309–5324, https://doi.org/10.5194/acp-13-5309-2013, 2013.

Laborde, M., Crippa, M., Tritscher, T., Jurányi, Z., Decarlo, P. F., Temime-Roussel, B., Marchand, N., Eckhardt, S., Stohl, A., Baltensperger, U., Prévôt, A. S. H., Weingartner, E., and Gysel, M.: Black carbon physical properties and mixing state in the European megacity Paris, Atmos. Chem. Phys., 13, 5831–5856, https://doi.org/10.5194/acp-13-5831-2013, 2013.

Lafon, S., Sokolik, I. N., Rajot, J. L., Caquineau, S., and Gaudichet, A.: Characterization of iron oxides in mineral dust aerosols: Implications for light absorption, J. Geophys. Res. Atmos., 111, https://doi.org/https://doi.org/10.1029/2005JD007016, 2006.

Lai, S., Qi, X., Huang, X., Lou, S., Chi, X., Chen, L., Liu, C., Liu, Y., Yan, C., Li, M., Liu, T., Nie, W., Kerminen, V.-M., Petäjä, T., Kulmala, M., and Ding, A.: New particle formation induced by anthropogenic--biogenic interactions on the southeastern Tibetan Plateau, Atmos. Chem. Phys., 24, 2535–2553, https://doi.org/10.5194/acp-24-2535-2024, 2024.

Lance, S., Nenes, A., Medina, J., and Smith, J. N.: Mapping the Operation of the DMT Continuous Flow CCN Counter, Aerosol Sci. Technol., 40, 242–254, https://doi.org/10.1080/02786820500543290, 2006.

Lathem, T. L. and Nenes, A.: Water Vapor Depletion in the DMT Continuous-Flow CCN Chamber: Effects on Supersaturation and Droplet Growth, Aerosol Sci. Technol., 45, 604–615, https://doi.org/10.1080/02786826.2010.551146, 2011.

Lawson, S. P., Kennedy, K. B., and Rehan, S. M.: Pollen composition significantly impacts the development and survival of the native small carpenter bee, Ceratina calcarata, Ecol. Entomol., 46, 232–239, https://doi.org/https://doi.org/10.1111/een.12955, 2021.

Lee, Y. H., Chen, K., and Adams, P. J.: Development of a global model of mineral dust aerosol microphysics, Atmos. Chem. Phys., 9, 2441–2458, https://doi.org/10.5194/acp-9-2441-2009, 2009.

Legg, S.: IPCC, 2021: Climate Change 2021 - the Physical Science basis, Interaction, 49, 44–45, 2021.

Li, X., Dallmann, T. R., May, A. A., Stanier, C. O., Grieshop, A. P., Lipsky, E. M., Robinson, A. L., and Presto, A. A.: Size distribution of vehicle emitted primary particles measured in a traffic tunnel, Atmos. Environ., 191, 9–18, https://doi.org/https://doi.org/10.1016/j.atmosenv.2018.07.052, 2018.

Lin, J. J., Kristensen, T. B., Calderón, S. M., Malila, J., and Prisle, N. L.: Effects of surface tension time-evolution for CCN activation of a complex organic surfactant, Environ. Sci. Process. Impacts, 22, 271–284, https://doi.org/10.1039/C9EM00426B, 2020.

Lohmann, U. and Feichter, J.: Global indirect aerosol effects: a review, Atmos. Chem. Phys., 5,

715-737, https://doi.org/10.5194/acp-5-715-2005, 2005.

Lyamani, H., Olmo, F. J., and Alados-Arboledas, L.: Saharan dust outbreak over southeastern Spain as detected by sun photometer, Atmos. Environ., 39, 7276–7284, https://doi.org/https://doi.org/10.1016/j.atmosenv.2005.09.011, 2005.

Lyamani, H., Fernández-Gálvez, J., Pérez-Ramírez, D., Valenzuela, A., Antón, M., Alados, I., Titos, G., Olmo, F. J., and Alados-Arboledas, L.: Aerosol properties over two urban sites in South Spain during an extended stagnation episode in winter season, Atmos. Environ., 62, 424–432, https://doi.org/10.1016/j.atmosenv.2012.08.050, 2012.

Mahowald, N., Albani, S., Kok, J. F., Engelstaeder, S., Scanza, R., Ward, D. S., and Flanner, M. G.: The size distribution of desert dust aerosols and its impact on the Earth system, Aeolian Res., 15, 53–71, https://doi.org/https://doi.org/10.1016/j.aeolia.2013.09.002, 2014.

Maldonado-Valderrama, J., Martín-Molina, A., Gálvez-Ruiz, M. J., Martín-Rodríguez, A., and Cabrerizo-Vílchez, M. Á.: β-Casein Adsorption at Liquid Interfaces: Theory and Experiment, J. Phys. Chem. B, 108, 12940–12945, https://doi.org/10.1021/jp048388y, 2004.

Maldonado-Valderrama, J., Fainerman, V. B., Gálvez-Ruiz, M. J., Martín-Rodriguez, A., Cabrerizo-Vílchez, M. A., and Miller, R.: Dilatational Rheology of β-Casein Adsorbed Layers at Liquid–Fluid Interfaces, J. Phys. Chem. B, 109, 17608–17616, https://doi.org/10.1021/jp050927r, 2005.

Maldonado-Valderrama, J., del Castillo-Santaella, T., Gálvez-Ruiz, M. J., Holgado-Terriza, J. A., and Cabrerizo-Vílchez, M. Á.: Chapter 1 - Structure and functionality of interfacial layers in food emulsions, edited by: Galanakis, C. M. B. T.-F. S. and F., Academic Press, 1–22, https://doi.org/https://doi.org/10.1016/B978-0-12-821453-4.00010-7, 2021.

Mampage, C. B. A., Hughes, D. D., Jones, L. M., Metwali, N., Thorne, P. S., and Stone, E. A.: Characterization of sub-pollen particles in size-resolved atmospheric aerosol using chemical tracers, Atmos. Environ. X, 15, 100177, https://doi.org/https://doi.org/10.1016/j.aeaoa.2022.100177, 2022.

Manktelow, P. T., Carslaw, K. S., Mann, G. W., and Spracklen, D. V.: The impact of dust on sulfate aerosol, CN and CCN during an East Asian dust storm, Atmos. Chem. Phys., 10, 365–382,

https://doi.org/10.5194/acp-10-365-2010, 2010.

Manninen, H., Bäck, J., Sihto-Nissilä, S.-L., Huffman, J., Pessi, A.-M., Hiltunen, V., Aalto, P., Hidalgo, P., Hari, P., Saarto, A., Kulmala, M., and Petäjä, T.: Patterns in airborne pollen and other primary biological aerosol particles (PBAP), and their contribution to aerosol mass and number in a boreal forest, Boreal Environ. Res., 19, 383–405, 2014.

Mattioli, R., Palombi, N., Funck, D., and Trovato, M.: Proline Accumulation in Pollen Grains as Potential Target for Improved Yield Stability Under Salt Stress, Front. Plant Sci., 11, https://doi.org/10.3389/fpls.2020.582877, 2020.

McFiggans, G., Artaxo, P., Baltensperger, U., Coe, H., Facchini, M.C., Feingold, G., Fuzzi, S., Gysel, M., Laaksonen, A., Lohmann, U., Mentel, T.F., Murphy, D.M., O'Dowd, C.D., Snider, J.R., Weingartner, E., 2006. The effect of physical and chemical aerosol properties on warm cloud droplet activation. Atmos. Chem. Phys. 6, 2593–2649. https://doi.org/10.5194/acp-6-2593-2006, 2006

McKnight, P. E. and Najab, J.: Mann-Whitney U Test, in: The Corsini Encyclopedia of Psychology, 1, https://doi.org/https://doi.org/10.1002/9780470479216.corpsy0524, 2010.

Medeiros, P. M. and Simoneit, B. R. T.: Analysis of sugars in environmental samples by gas chromatography–mass spectrometry, J. Chromatogr. A, 1141, 271–278, https://doi.org/https://doi.org/10.1016/j.chroma.2006.12.017, 2007.

Mei, F., Hayes, P. L., Ortega, A., Taylor, J. W., Allan, J. D., Gilman, J., Kuster, W., de Gouw, J., Jimenez, J. L., and Wang, J.: Droplet activation properties of organic aerosols observed at an urban site during CalNex-LA, J. Geophys. Res. Atmos., 118, 2903–2917, https://doi.org/https://doi.org/10.1002/jgrd.50285, 2013.

Merikanto, J., Spracklen, D. V, Mann, G. W., Pickering, S. J., and Carslaw, K. S.: Impact of nucleation on global CCN, Atmos. Chem. Phys., 9, 8601–8616, https://doi.org/10.5194/acp-9-8601-2009, 2009.

Mikhailov, E. F., Ivanova, O. A., Nebosko, E. Y., Vlasenko, S. S., and Ryshkevich, T. I.: Subpollen Particles as Atmospheric Cloud Condensation Nuclei, Izv. Atmos. Ocean. Phys., 55, 357–364, https://doi.org/10.1134/S000143381904008X, 2019.

Mikhailov, E. F., Pöhlker, M. L., Reinmuth-Selzle, K., Vlasenko, S. S., Krüger, O. O., Fröhlich-Nowoisky, J., Pöhlker, C., Ivanova, O. A., Kiselev, A. A., Kremper, L. A., and Pöschl, U.: Water uptake of subpollen aerosol particles: hygroscopic growth, cloud condensation nuclei activation, and liquid-liquid phase separation, Atmos. Chem. Phys., 21, 6999–7022, https://doi.org/10.5194/acp-21-6999-2021, 2021.

Moore, R. H., Nenes, A., and Medina, J.: Scanning Mobility CCN Analysis—A Method for Fast Measurements of Size-Resolved CCN Distributions and Activation Kinetics, Aerosol Sci. Technol., 44, 861–871, https://doi.org/10.1080/02786826.2010.498715, 2010.

Moulin, C., Lambert, C. E., Dayan, U., Masson, V., Ramonet, M., Bousquet, P., Legrand, M., Balkanski, Y. J., Guelle, W., Marticorena, B., Bergametti, G., and Dulac, F.: Satellite climatology of African dust transport in the Mediterranean atmosphere, J. Geophys. Res. Atmos., 103, 13137–13144, https://doi.org/https://doi.org/10.1029/98JD00171, 1998.

Myhre, G., Lund Myhre, C., Samset, B. H., and Storelvmo, T.: Aerosols and their Relation to Global Climate and Climate Sensitivity, Nat. Educ. Knowl., 4, 7, 2013.

de Nascimento, L., Nogué, S., Fernández-Lugo, S., Méndez, J., Otto, R., Whittaker, R. J., Willis, K. J., and Fernández-Palacios, J. M.: Modern pollen rain in Canary Island ecosystems and its implications for the interpretation of fossil records, Rev. Palaeobot. Palynol., 214, 27–39, https://doi.org/https://doi.org/10.1016/j.revpalbo.2014.11.002, 2015.

Nenes, A., Murray, B., and Bougiatioti, A.: Mineral Dust and its Microphysical Interactions with Clouds, in: Mineral Dust: A Key Player in the Earth System, edited by: Knippertz, P. and Stuut, J.-B. W., Springer Netherlands, Dordrecht, 287–325, https://doi.org/10.1007/978-94-017-8978-3_12, 2014.

Nguyen, Q. T., Kjær, K. H., Kling, K. I., Boesen, T., and Bilde, M.: Impact of fatty acid coating on the CCN activity of sea salt particles, Tellus B Chem. Phys. Meteorol., 69, 1304064, https://doi.org/10.1080/16000889.2017.1304064, 2017.

Nicolás, J., Chiari, M., Crespo, J., Orellana, I. G., Lucarelli, F., Nava, S., Pastor, C., and Yubero, E.: Quantification of Saharan and local dust impact in an arid Mediterranean area by the positive matrix factorization (PMF) technique, Atmos. Environ., 42, 8872–8882, https://doi.org/https://doi.org/10.1016/j.atmosenv.2008.09.018, 2008.

Nozière, B., Baduel, C., and Jaffrezo, J.-L.: The dynamic surface tension of atmospheric aerosol surfactants reveals new aspects of cloud activation, Nat. Commun., 5, 3335, https://doi.org/10.1038/ncomms4335, 2014.

Oros, D. R. and Simoneit, B. R. T.: Identification and emission factors of molecular tracers in organic aerosols from biomass burning Part 1. Temperate climate conifers, Appl. Geochemistry, 16, 1513–1544, https://doi.org/https://doi.org/10.1016/S0883-2927(01)00021-X, 2001.

Ovadnevaite, J., Zuend, A., Laaksonen, A., Sanchez, K. J., Roberts, G., Ceburnis, D., Decesari, S., Rinaldi, M., Hodas, N., Facchini, M. C., Seinfeld, J. H., and O' Dowd, C.: Surface tension prevails over solute effect in organic-influenced cloud droplet activation, Nature, 546, 637–641, https://doi.org/10.1038/nature22806, 2017.

Paasonen, P., Peltola, M., Kontkanen, J., Junninen, H., Kerminen, V.-M., and Kulmala, M.: Comprehensive analysis of particle growth rates from nucleation mode to cloud condensation nuclei in boreal forest, Atmos. Chem. Phys., 18, 12085–12103, https://doi.org/10.5194/acp-18-12085-2018, 2018.

Pacini, E. and Hesse, M.: Pollenkitt - Its composition, forms and functions, Flora - Morphol. Distrib. Funct. Ecol. Plants, 200, 399–415, https://doi.org/10.1016/j.flora.2005.02.006, 2005.

Pacini, E., Guarnieri, M., and Nepi, M.: Pollen carbohydrates and water content during development, presentation, and dispersal: a short review, Protoplasma, 228, 73, https://doi.org/10.1007/s00709-006-0169-z, 2006.

Paramonov, M., Kerminen, V.-M., Gysel, M., Aalto, P. P., Andreae, M. O., Asmi, E., Baltensperger, U., Bougiatioti, A., Brus, D., Frank, G. P., Good, N., Gunthe, S. S., Hao, L., Irwin, M., Jaatinen, A., Jurányi, Z., King, S. M., Kortelainen, A., Kristensson, A., Lihavainen, H., Kulmala, M., Lohmann, U., Martin, S. T., McFiggans, G., Mihalopoulos, N., Nenes, A., O'Dowd, C. D., Ovadnevaite, J., Petäjä, T., Pöschl, U., Roberts, G. C., Rose, D., Svenningsson, B., Swietlicki, E., Weingartner, E., Whitehead, J., Wiedensohler, A., Wittbom, C., and Sierau, B.: A synthesis of cloud condensation nuclei counter (CCNC) measurements within the EUCAARI network, Atmos. Chem. Phys., 15, 12211–12229, https://doi.org/10.5194/acp-15-12211-2015, 2015.

Park, J., Kang, H., Gim, Y., Jang, E., Park, K.-T., Park, S., Jung, C. H., Ceburnis, D., O'Dowd, C., and Yoon, Y. J.: New particle formation leads to enhanced cloud condensation nuclei concentrations

at Antarctic Peninsula, EGUsphere, 2023, 1–37, https://doi.org/10.5194/egusphere-2023-707, 2023.

Patrón, D., Lyamani, H., Titos, G., Casquero-Vera, J. A., Cardell, C., Močnik, G., Alados-Arboledas, L., and Olmo, F. J.: Monumental heritage exposure to urban black carbon pollution, Atmos. Environ., 170, 22–32, https://doi.org/10.1016/j.atmosenv.2017.09.030, 2017.

Perry, K. D., Cliff, S. S., and Jimenez-Cruz, M. P.: Evidence for hygroscopic mineral dust particles from the Intercontinental Transport and Chemical Transformation Experiment, J. Geophys. Res. Atmos., 109, https://doi.org/https://doi.org/10.1029/2004JD004979, 2004.

Petters, M. D. and Kreidenweis, S. M.: A single parameter representation of hygroscopic growth and cloud condensation nucleus activity, Atmos. Chem. Phys., 7, 1961–1971, https://doi.org/10.5194/acp-7-1961-2007, 2007.

Petters, M. D. and Kreidenweis, S. M.: A single parameter representation of hygroscopic growth and cloud condensation nucleus activity – Part 2: Including solubility, Atmos. Chem. Phys., 8, 6273–6279, https://doi.org/10.5194/acp-8-6273-2008, 2008.

Petters, M.D., Carrico, C.M., Kreidenweis, S.M., Prenni, A.J., DeMott, P.J., Collett Jr., J.L., Moosmüller, H. Cloud condensation nucleation activity of biomass burning aerosol. J. Geophys. Res. Atmos. 114. https://doi.org/https://doi.org/10.1029/2009JD012353, 2009

Petters, M. D. and Kreidenweis, S. M.: A single parameter representation of hygroscopic growth and cloud condensation nucleus activity – Part 3: Including surfactant partitioning, Atmos. Chem. Phys., 13, 1081–1091, https://doi.org/10.5194/acp-13-1081-2013, 2013.

Petters, S. S. and Petters, M. D.: Surfactant effect on cloud condensation nuclei for two-component internally mixed aerosols, J. Geophys. Res. Atmos., 121, 1878–1895, https://doi.org/10.1002/2015JD024090, 2016.

Pey, J., Querol, X., Alastuey, A., Forastiere, F., and Stafoggia, M.: African dust outbreaks over the Mediterranean Basin during 2001–2011: PM\$_{10}\$ concentrations, phenomenology and trends, and its relation with synoptic and mesoscale meteorology, Atmos. Chem. Phys., 13, 1395–1410, https://doi.org/10.5194/acp-13-1395-2013, 2013.

Pfeifer, S., Müller, T., Weinhold, K., Zikova, N., dos Santos, S., Marinoni, A., Bischof, O. F., Kykal,

C., Ries, L., Meinhardt, F., Aalto, P., Mihalopoulos, N., and Wiedensohler, A.: Intercomparison of 15 aerodynamic particle size spectrometers (APS 3321): uncertainties in particle sizing and number size distribution, Atmos. Meas. Tech., 9, 1545–1551, https://doi.org/10.5194/amt-9-1545-2016, 2016.

Pöhlker, M. L., Pöhlker, C., Ditas, F., Klimach, T., de Angelis, I., Araújo, A., Brito, J., Carbone, S., Cheng, Y., Chi, X., Ditz, R., Gunthe, S. S., Kesselmeier, J., Könemann, T., Lavrič, J. V, Martin, S. T., Mikhailov, E., Moran-Zuloaga, D., Rose, D., Saturno, J., Su, H., Thalman, R., Walter, D., Wang, J., Wolff, S., Barbosa, H. M. J., Artaxo, P., Andreae, M. O., and Pöschl, U.: Long-term observations of cloud condensation nuclei in the Amazon rain forest -- Part 1: Aerosol size distribution, hygroscopicity, and new model parametrizations for CCN prediction, Atmos. Chem. Phys., 16, 15709–15740, https://doi.org/10.5194/acp-16-15709-2016, 2016.

Pöschl, U., Martin, S. T., Sinha, B., Chen, Q., Gunthe, S. S., Huffman, J. A., Borrmann, S., Farmer, D. K., Garland, R. M., Helas, G., Jimenez, J. L., King, S. M., Manzi, A., Mikhailov, E., Pauliquevis, T., Petters, M. D., Prenni, A. J., Roldin, P., Rose, D., Schneider, J., Su, H., Zorn, S. R., Artaxo, P., and Andreae, M. O.: Rainforest aerosols as biogenic nuclei of clouds and precipitation in the Amazon., Science, 329, 1513–1516, https://doi.org/10.1126/science.1191056, 2010.

Pósfai, M., Axisa, D., Tompa, É., Freney, E., Bruintjes, R., and Buseck, P. R.: Interactions of mineral dust with pollution and clouds: An individual-particle TEM study of atmospheric aerosol from Saudi Arabia, Atmos. Res., 122, 347–361, https://doi.org/https://doi.org/10.1016/j.atmosres.2012.12.001, 2013.

Prisle, N. L., Raatikainen, T., Laaksonen, A., and Bilde, M.: Surfactants in cloud droplet activation: mixed organic-inorganic particles, Atmos. Chem. Phys., 10, 5663–5683, https://doi.org/10.5194/acp-10-5663-2010, 2010.

Prisle, N. L., Lin, J. J., Purdue, S., Lin, H., Meredith, J. C., and Nenes, A.: Cloud condensation nuclei activity of six pollenkitts and the influence of their surface activity, Atmos. Chem. Phys., 19, 4741–4761, https://doi.org/10.5194/acp-19-4741-2019, 2019.

Prisle, N.L., Raatikainen, T., Sorjamaa, R., Svenningsson, B., Laaksonen, A.R.I., Bilde, M. Surfactant partitioning in cloud droplet activation: a study of C8, C10, C12 and C14 normal fatty acid sodium salts. Tellus B 60, 416–431. https://doi.org/10.1111/j.1600-0889.2008.00352.x., 2008

Prospero, J. M.: Long-term measurements of the transport of African mineral dust to the southeastern United States: Implications for regional air quality, J. Geophys. Res. Atmos., 104, 15917–15927, https://doi.org/https://doi.org/10.1029/1999JD900072, 1999.

Prospero, J. M. and Lamb, P. J.: African droughts and dust transport to the Caribbean: climate change implications., Science, 302, 1024–1027, https://doi.org/10.1126/science.1089915, 2003.

Prospero, J. M., Glaccum, R. A., and Nees, R. T.: Atmospheric transport of soil dust from Africa to South America, Nature, 289, 570–572, https://doi.org/10.1038/289570a0, 1981.

Prospero, J. M., Ginoux, P., Torres, O., Nicholson, S. E., and Gill, T. E.: Environmental characterization of global sources of atmospheric soil dust identified with the Nimbus 7 Total Ozone Mapping Spectrometer (TOMS) absorbing aerosol product, Rev. Geophys., 40, 2–31, https://doi.org/https://doi.org/10.1029/2000RG000095, 2002.

Querol, X., Pey, J., Pandolfi, M., Alastuey, A., Cusack, M., Pérez, N., Moreno, T., Viana, M., Mihalopoulos, N., Kallos, G., and Kleanthous, S.: African dust contributions to mean ambient PM10 mass-levels across the Mediterranean Basin, Atmos. Environ., 43, 4266–4277, https://doi.org/https://doi.org/10.1016/j.atmosenv.2009.06.013, 2009a.

Querol, X., Alastuey, A., Pey, J., Cusack, M., Pérez, N., Mihalopoulos, N., Theodosi, C., Gerasopoulos, E., Kubilay, N., and Koçak, M.: Variability in regional background aerosols within the Mediterranean, Atmos. Chem. Phys., 9, 4575–4591, https://doi.org/10.5194/acp-9-4575-2009, 2009b.

Querol, X., Alastuey, A., Pandolfi, M., Reche, C., Perez, N., Minguillon, M.C., Moreno, T., Viana, M., Escudero, M., Orio, A., Pallares, M., Reina, F. 2001-2012 trends on air quality in Spain. Sci. Total Environ. 490, 957–969, https://doi.org/10.1016/j.scitotenv.2014.05.074, 2014.

Quinn, P. K., Bates, T. S., Baynard, T., Clarke, A. D., Onasch, T. B., Wang, W., Rood, M. J., Andrews, E., Allan, J., Carrico, C. M., Coffman, D., and Worsnop, D.: Impact of particulate organic matter on the relative humidity dependence of light scattering: A simplified parameterization, Geophys. Res. Lett., 32, https://doi.org/https://doi.org/10.1029/2005GL024322, 2005.

Quinn, P.K., Bates, T.S., Coffman, D.J., Covert, D.S., 2008. Influence of particle size and chemistry on the cloud nucleating properties of aerosols. Atmos. Chem. Phys. 8, 1029–1042.

https://doi.org/10.5194/acp-8-1029-2008

Raoult, F.-M.: Loi générale des tensions de vapeur des dissolvants, CR Hebd. Seances Acad. Sci, 104, 1430–1433, 1887.

Rathnayake, C. M., Metwali, N., Jayarathne, T., Kettler, J., Huang, Y., Thorne, P. S., O'Shaughnessy, P. T., and Stone, E. A.: Influence of rain on the abundance of bioaerosols in fine and coarse particles, Atmos. Chem. Phys., 17, 2459–2475, https://doi.org/10.5194/acp-17-2459-2017, 2017.

Raymond, T. M. and Pandis, S. N.: Cloud activation of single-component organic aerosol particles, J. Geophys. Res. Atmos., 107, AAC 16-1-AAC 16-8, https://doi.org/10.1029/2002JD002159, 2002.

Raza, M. A., Hallett, P. D., Liu, X., He, M., and Afzal, W.: Surface Tension of Aqueous Solutions of Small-Chain Amino and Organic Acids, J. Chem. Eng. Data, 64, 5049–5056, https://doi.org/10.1021/acs.jced.9b00026, 2019.

Reid, J. S., Jonsson, H. H., Maring, H. B., Smirnov, A., Savoie, D. L., Cliff, S. S., Reid, E. A., Livingston, J. M., Meier, M. M., Dubovik, O., and Tsay, S.-C.: Comparison of size and morphological measurements of coarse mode dust particles from Africa, J. Geophys. Res. Atmos., 108, https://doi.org/https://doi.org/10.1029/2002JD002485, 2003.

Rejano, F., Titos, G., Casquero-Vera, J. A., Lyamani, H., Andrews, E., Sheridan, P., Cazorla, A., Castillo, S., Alados-Arboledas, L., and Olmo, F. J.: Activation properties of aerosol particles as cloud condensation nuclei at urban and high-altitude remote sites in southern Europe, Sci. Total Environ., 762, 143100, https://doi.org/https://doi.org/10.1016/j.scitotenv.2020.143100, 2021.

Rejano, F., Casquero-Vera, J. A., Lyamani, H., Andrews, E., Casans, A., Pérez-Ramírez, D., Alados-Arboledas, L., Titos, G., and Olmo, F. J.: Impact of urban aerosols on the cloud condensation activity using a clustering model, Sci. Total Environ., 858, 159657, https://doi.org/https://doi.org/10.1016/j.scitotenv.2022.159657, 2023.

Rejano, F., Casans, A., Via, M., Casquero-Vera, J. A., Castillo, S., Lyamani, H., Cazorla, A., Andrews, E., Pérez-Ramírez, D., Alastuey, A., Gómez-Moreno, F. J., Alados-Arboledas, L., Olmo, F. J., and Titos, G.: CCN estimations at a high-altitude remote site: role of organic aerosol variability and

hygroscopicity, Atmos. Chem. Phys., 24, 13865–13888, https://doi.org/10.5194/acp-24-13865-2024, 2024.

Ren, J., Chen, L., Fan, T., Liu, J., Jiang, S., and Zhang, F.: The NPF Effect on CCN Number Concentrations: A Review and Re-Evaluation of Observations From 35 Sites Worldwide, Geophys. Res. Lett., 48, https://doi.org/10.1029/2021GL095190, 2021.

Rissanen, T., Hyötyläinen, T., Kallio, M., Kronholm, J., Kulmala, M., and Riekkola, M.-L.: Characterization of organic compounds in aerosol particles from a coniferous forest by GC–MS, Chemosphere,

64,

1185–1195,
https://doi.org/https://doi.org/10.1016/j.chemosphere.2005.11.079, 2006.

Riipinen, I., Rastak, N., Pandis, S.N., 2015. Connecting the solubility and CCN activation of complex organic aerosols: a theoretical study using solubility distributions. Atmos. Chem. Phys. 15, 6305–6322. https://doi.org/10.5194/acp-15-6305-2015.

Rissler, J., Vestin, A., Swietlicki, E., Fisch, G., Zhou, J., Artaxo, P., and Andreae, M. O.: Size distribution and hygroscopic properties of aerosol particles from dry-season biomass burning in Amazonia, Atmos. Chem. Phys., 6, 471–491, https://doi.org/10.5194/acp-6-471-2006, 2006.

Ro, C.-U., Hwang, H., Kim, H., Chun, Y., and Van Grieken, R.: Single-Particle Characterization of Four "Asian Dust" Samples Collected in Korea, Using Low-Z Particle Electron Probe X-ray Microanalysis, Environ. Sci. Technol., 39, 1409–1419, https://doi.org/10.1021/es049772b, 2005.

Roberts, G. C. and Nenes, A.: A Continuous-Flow Streamwise Thermal-Gradient CCN Chamber for Atmospheric Measurements, Aerosol Sci. Technol., 39, 206–221, https://doi.org/10.1080/027868290913988, 2005.

Rodríguez, S., González, Y., Cuevas, E., Ramos, R., Romero, P. M., Abreu-Afonso, J., and Redondas, A.: Atmospheric nanoparticle observations in the low free troposphere during upward orographic flows at Izaña Mountain Observatory, Atmos. Chem. Phys., 9, 6319–6335, https://doi.org/10.5194/acp-9-6319-2009, 2009.

Rodríguez, S., Cuevas, E., Prospero, J. M., Alastuey, A., Querol, X., López-Solano, J., García, M. I., and Alonso-Pérez, S.: Modulation of Saharan dust export by the North African dipole, Atmos. Chem. Phys., 15, 7471–7486, https://doi.org/10.5194/acp-15-7471-2015, 2015.

Rose, C., Sellegri, K., Moreno, I., Velarde, F., Ramonet, M., Weinhold, K., Krejci, R., Andrade, M., Wiedensohler, A., Ginot, P., Laj, P., Ginot, P., and Laj, P.: CCN production by new particle formation in the free troposphere, Atmos. Chem. Phys., 17, 1529–1541, https://doi.org/10.5194/acp-17-1529-2017, 2017.

Rose, C., Foucart, B., Picard, D., Colomb, A., Metzger, J.-M., Tulet, P., and Sellegri, K.: New particle formation in the volcanic eruption plume of the Piton de la Fournaise: specific features from a long-term dataset, Atmos. Chem. Phys., 19, 13243–13265, https://doi.org/10.5194/acp-19-13243-2019, 2019.

Rose, D., Gunthe, S. S., Mikhailov, E., Frank, G. P., Dusek, U., Andreae, M. O., and Pöschl, U.: Calibration and measurement uncertainties of a continuous-flow cloud condensation nuclei counter (DMT-CCNC): CCN activation of ammonium sulfate and sodium chloride aerosol particles in theory and experiment, Atmos. Chem. Phys., 8, 1153–1179, https://doi.org/10.5194/acp-8-1153-2008, 2008.

Rose, D., Nowak, A., Achtert, P., Wiedensohler, A., Hu, M., Shao, M., Zhang, Y., Andreae, M. O., and Pöschl, U.: Cloud condensation nuclei in polluted air and biomass burning smoke near the mega-city Guangzhou, China – Part 1: Size-resolved measurements and implications for the modeling of aerosol particle hygroscopicity and CCN activity, Atmos. Chem. Phys., 10, 3365–3383, https://doi.org/10.5194/acp-10-3365-2010, 2010.

Rose, D., Gunthe, S.S., Jurányi, Z., Gysel, M., Frank, G.P., Schneider, J., Curtius, J., Pöschl, U., 2013. Size-resolved and integral measurements of cloud condensation nuclei (CCN) at the high-alpine site Jungfraujoch. Atmos. Chem. Phys. Discuss. 13, 32575–32624. https://doi.org/10.5194/acpd-13-32575-2013

Rosenørn, T., Kiss, G., and Bilde, M.: Cloud droplet activation of saccharides and levoglucosan particles, Atmos. Environ., 40, 1794–1802, https://doi.org/https://doi.org/10.1016/j.atmosenv.2005.11.024, 2006.

Ruehl, C. R., Chuang, P. Y., and Nenes, A.: How quickly do cloud droplets form on atmospheric particles?, Atmos. Chem. Phys., 8, 1043–1055, https://doi.org/10.5194/acp-8-1043-2008, 2008.

Ruehl, C. R., Chuang, P. Y., and Nenes, A.: Aerosol hygroscopicity at high (99 to 100%) relative humidities, Atmos. Chem. Phys., 10, 1329–1344, https://doi.org/10.5194/acp-10-1329-2010, 2010.

Ruehl, C. R., Chuang, P. Y., Nenes, A., Cappa, C. D., Kolesar, K. R., and Goldstein, A. H.: Strong evidence of surface tension reduction in microscopic aqueous droplets, Geophys. Res. Lett., 39, https://doi.org/https://doi.org/10.1029/2012GL053706, 2012.

Ruehl, C. R., Davies, J. F., and Wilson, K. R.: An interfacial mechanism for cloud droplet formation on organic aerosols, Science (80-.)., 351, 1447–1450, https://doi.org/10.1126/science.aad4889, 2016.

Salvador, P., Artíñano, B., Querol, X., and Alastuey, A.: A combined analysis of backward trajectories and aerosol chemistry to characterise long-range transport episodes of particulate matter: the Madrid air basin, a case study., Sci. Total Environ., 390, 495–506, https://doi.org/10.1016/j.scitotenv.2007.10.052, 2008.

Salvador, P., Alonso-Pérez, S., Pey, J., Artiñano, B., de Bustos, J. J., Alastuey, A., and Querol, X.: African dust outbreaks over the western Mediterranean Basin: 11-year characterization of atmospheric circulation patterns and dust source areas, Atmos. Chem. Phys., 14, 6759–6775, https://doi.org/10.5194/acp-14-6759-2014, 2014.

Salvador, P., Pey, J., Pérez, N., Querol, X., and Artíñano, B.: Increasing atmospheric dust transport towards the western Mediterranean over 1948–2020, npj Clim. Atmos. Sci., 5, 34, https://doi.org/10.1038/s41612-022-00256-4, 2022.

Schmale, J., Henning, S., Henzing, B., Keskinen, H., Sellegri, K., Ovadnevaite, J., Bougiatioti, A., Kalivitis, N., Stavroulas, I., Jefferson, A., Park, M., Schlag, P., Kristensson, A., Iwamoto, Y., Pringle, K., Reddington, C., Aalto, P., Äijälä, M., Baltensperger, U., Bialek, J., Birmili, W., Bukowiecki, N., Ehn, M., Fjæraa, A. M., Fiebig, M., Frank, G., Fröhlich, R., Frumau, A., Furuya, M., Hammer, E., Heikkinen, L., Herrmann, E., Holzinger, R., Hyono, H., Kanakidou, M., Kiendler-Scharr, A., Kinouchi, K., Kos, G., Kulmala, M., Mihalopoulos, N., Motos, G., Nenes, A., O'Dowd, C., Paramonov, M., Petäjä, T., Picard, D., Poulain, L., Prévôt, A. S. H., Slowik, J., Sonntag, A., Swietlicki, E., Svenningsson, B., Tsurumaru, H., Wiedensohler, A., Wittbom, C., Ogren, J. A., Matsuki, A., Yum, S. S., Myhre, C. L., Carslaw, K., Stratmann, F., and Gysel, M.: Collocated observations of cloud condensation nuclei, particle size distributions, and chemical composition, Sci. Data, 4, 170003, https://doi.org/10.1038/sdata.2017.3, 2017.

Schmale, J., Henning, S., Decesari, S., Henzing, B., Keskinen, H., Sellegri, K., Ovadnevaite, J.,

Pöhlker, M., Brito, J., Bougiatioti, A., Baltensperger, U., and Gysel, M.: Long-term cloud condensation nuclei number concentration, particle number size distribution and chemical composition measurements at regionally representative observatories, Atmos. Chem. Phys., 18, 2853–2881, https://doi.org/10.5194/acp-18-2853-2018, 2018.

Seidl, W.: Model for a surface film of fatty acids on rain water and aerosol particles, Atmos. Environ., 34, 4917–4932, https://doi.org/https://doi.org/10.1016/S1352-2310(00)00198-9, 2000.

Seinfeld, J. H. and Pandis, S. N.: From air pollution to climate change, Atmos. Chem. Phys., 1326, 1998.

Seinfeld, J. H., Bretherton, C., Carslaw, K. S., Coe, H., DeMott, P. J., Dunlea, E. J., Feingold, G., Ghan, S., Guenther, A. B., Kahn, R., Kraucunas, I., Kreidenweis, S. M., Molina, M. J., Nenes, A., Penner, J. E., Prather, K. A., Ramanathan, V., Ramaswamy, V., Rasch, P. J., Ravishankara, A. R., Rosenfeld, D., Stephens, G., and Wood, R.: Improving our fundamental understanding of the role of aerosol-cloud interactions in the climate system., Proc. Natl. Acad. Sci. U. S. A., 113, 5781–90, https://doi.org/10.1073/pnas.1514043113, 2016.

Shantz, N. C., Pierce, J. R., Chang, R. Y.-W., Vlasenko, A., Riipinen, I., Sjostedt, S., Slowik, J. G., Wiebe, A., Liggio, J., Abbatt, J. P. D., and Leaitch, W. R.: Cloud condensation nuclei droplet growth kinetics of ultrafine particles during anthropogenic nucleation events, Atmos. Environ., 47, 389–398, https://doi.org/https://doi.org/10.1016/j.atmosenv.2011.10.049, 2012.

Shen, X., Sun, J., Che, H., Zhang, Y., Zhou, C., Gui, K., Xu, W., Liu, Q., Zhong, J., Xia, C., Hu, X., Zhang, S., Wang, J., Liu, S., Lu, J., Yu, A., and Zhang, X.: Characterization of dust-related new particle formation events based on long-term measurement in the North China Plain, Atmos. Chem. Phys., 23, 8241–8257, https://doi.org/10.5194/acp-23-8241-2023, 2023.

Sokolik, I. N., Winker, D. M., Bergametti, G., Gillette, D. A., Carmichael, G., Kaufman, Y. J., Gomes, L., Schuetz, L., and Penner, J. E.: Introduction to special section: Outstanding problems in quantifying the radiative impacts of mineral dust, J. Geophys. Res. Atmos., 106, 18015–18027, https://doi.org/10.1029/2000JD900498, 2001.

Sorjamaa, R., Svenningsson, B., Raatikainen, T., Henning, S., Bilde, M., and Laaksonen, A.: The role of surfactants in Köhler theory reconsidered, Atmos. Chem. Phys., 4, 2107–2117, https://doi.org/10.5194/acp-4-2107-2004, 2004.

Sorribas, M., Ogren, J. A., Olmo, F. J., Quirantes, A., Fraile, R., Gil-Ojeda, M., and Alados-Arboledas, L.: Assessment of African desert dust episodes over the southwest Spain at sea level using in situ aerosol optical and microphysical properties, Tellus B Chem. Phys. Meteorol., 67, 27482, https://doi.org/10.3402/tellusb.v67.27482, 2015.

Spracklen, D. V, Carslaw, K. S., Merikanto, J., Mann, G. W., Reddington, C. L., Pickering, S., Ogren, J. A., Andrews, E., Baltensperger, U., Weingartner, E., Boy, M., Kulmala, M., Laakso, L., Lihavainen, H., Kivekäs, N., Komppula, M., Mihalopoulos, N., Kouvarakis, G., Jennings, S. G., O'Dowd, C., Birmili, W., Wiedensohler, A., Weller, R., Gras, J., Laj, P., Sellegri, K., Bonn, B., Krejci, R., Laaksonen, A., Hamed, A., Minikin, A., Harrison, R. M., Talbot, R., and Sun, J.: Explaining global surface aerosol number concentrations in terms of primary emissions and particle formation, Atmos. Chem. Phys., 10, 4775–4793, https://doi.org/10.5194/acp-10-4775-2010, 2010.

Stafoggia, M., Zauli-Sajani, S., Pey, J., Samoli, E., Alessandrini, E., Basagaña, X., Cernigliaro, A., Chiusolo, M., Demaria, M., Díaz, J., Faustini, A., Katsouyanni, K., Kelessis, A. G., Linares, C., Marchesi, S., Medina, S., Pandolfi, P., Pérez, N., Querol, X., Randi, G., Ranzi, A., Tobias, A., Forastiere, F., and null null: Desert Dust Outbreaks in Southern Europe: Contribution to Daily PM₁₀ Concentrations and Short-Term Associations with Mortality and Hospital Admissions, Environ. Health Perspect., 124, 413–419, https://doi.org/10.1289/ehp.1409164, 2016.

Steiner, A. L., Brooks, S. D., Deng, C., Thornton, D. C. O., Pendleton, M. W., and Bryant, V.: Pollen as atmospheric cloud condensation nuclei, Geophys. Res. Lett., 42, 3596–3602, https://doi.org/10.1002/2015GL064060, 2015.

Stone, E. A., Mampage, C. B. A., Hughes, D. D., and Jones, L. M.: Airborne sub-pollen particles from rupturing giant ragweed pollen, Aerobiologia (Bologna)., 37, 625–632, https://doi.org/10.1007/s10453-021-09702-x, 2021.

Su, P., Joutsensaari, J., Dada, L., Zaidan, M. A., Nieminen, T., Li, X., Wu, Y., Decesari, S., Tarkoma, S., Petäjä, T., Kulmala, M., and Pellikka, P.: New particle formation event detection with Mask R-CNN, Atmos. Chem. Phys., 22, 1293–1309, https://doi.org/10.5194/acp-22-1293-2022, 2022.

Sullivan, R. C., Moore, M. J. K., Petters, M. D., Kreidenweis, S. M., Roberts, G. C., and Prather, K. A.: Effect of chemical mixing state on the hygroscopicity and cloud nucleation properties of

calcium mineral dust particles, Atmos. Chem. Phys., 9, 3303–3316, https://doi.org/10.5194/acp-9-3303-2009, 2009.

Sun, J., Hermann, M., Weinhold, K., Merkel, M., Birmili, W., Yang, Y., Tuch, T., Flentje, H., Briel, B., Ries, L., Couret, C., Elsasser, M., Sohmer, R., Wirtz, K., Meinhardt, F., Schütze, M., Bath, O., Hellack, B., Kerminen, V.-M., Kulmala, M., Ma, N., and Wiedensohler, A.: Measurement report: Contribution of atmospheric new particle formation to ultrafine particle concentration, cloud condensation nuclei, and radiative forcing -- results from 5-year observations in central Europe, Atmos. Chem. Phys., 24, 10667–10687, https://doi.org/10.5194/acp-24-10667-2024, 2024a.

Sun, N., Wu, L., Zheng, F., Liang, D., Qi, F., Song, S., Peng, J., Zhang, Y., and Mao, H.: Atmospheric environment characteristic of severe dust storms and its impact on sulfate formation in downstream city, Sci. Total Environ., 922, 171128, https://doi.org/https://doi.org/10.1016/j.scitotenv.2024.171128, 2024b.

Tanarhte, M., Bacer, S., Burrows, S., Huffman, J., Pierce, K., Pozzer, A., Sarda-Estève, R., Savage, N., and Lelieveld, J.: Global modeling of primary biological particle concentrations with the EMAC chemistry-climate model, Atmos. Chem. Phys. Discuss., 1–33, https://doi.org/10.5194/acp-2018-361, 2018.

Tao, J., Kuang, Y., Luo, B., Liu, L., Xu, H., Ma, N., Liu, P., Xue, B., Zhai, M., Xu, W., Xu, W., and Sun, Y.: Kinetic Limitations Affect Cloud Condensation Nuclei Activity Measurements Under Low Supersaturation, Geophys. Res. Lett., 50, e2022GL101603, https://doi.org/10.1029/2022GL101603, 2023.

Tao, J., Luo, B., Meng, Z., Xie, L., Zhang, S., Hong, J., Zhou, Y., Kuang, Y., Wang, Q., Huang, S., Cheng, P., Yuan, B., Yu, P., Su, H., Cheng, Y., and Ma, N.: A New Method for Size-Resolved Aerosol CCN Activity Measurement at Low Supersaturation in Pristine Atmosphere, J. Geophys. Res. Atmos., 129, e2023JD040357, https://doi.org/https://doi.org/10.1029/2023JD040357, 2024.

Taylor, P. E., Flagan, R. C., Miguel, A. G., Valenta, R., and Glovsky, M. M.: Birch pollen rupture and the release of aerosols of respirable allergens., Clin. Exp. allergy J. Br. Soc. Allergy Clin. Immunol., 34, 1591–1596, https://doi.org/10.1111/j.1365-2222.2004.02078.x, 2004.

Thalman, R., de Sá, S. S., Palm, B. B., Barbosa, H. M. J., Pöhlker, M. L., Alexander, M. L., Brito, J., Carbone, S., Castillo, P., Day, D. A., Kuang, C., Manzi, A., Ng, N. L., Sedlacek III, A. J., Souza, R.,

Springston, S., Watson, T., Pöhlker, C., Pöschl, U., Andreae, M. O., Artaxo, P., Jimenez, J. L., Martin, S. T., and Wang, J.: CCN activity and organic hygroscopicity of aerosols downwind of an urban region in central Amazonia: seasonal and diel variations and impact of anthropogenic emissions, Atmos. Chem. Phys., 17, 11779–11801, https://doi.org/10.5194/acp-17-11779-2017, 2017.

Titos, G., Foyo-Moreno, I., Lyamani, H., Querol, X., Alastuey, A., and Alados-Arboledas, L.: Optical properties and chemical composition of aerosol particles at an urban location: An estimation of the aerosol mass scattering and absorption efficiencies, J. Geophys. Res. Atmos., 117, https://doi.org/https://doi.org/10.1029/2011JD016671, 2012.

Titos, G., Jefferson, A., Sheridan, P. J., Andrews, E., Lyamani, H., Alados-Arboledas, L., and Ogren, J. A.: Aerosol light-scattering enhancement due to water uptake during the TCAP campaign, Atmos. Chem. Phys., 14, 7031–7043, https://doi.org/10.5194/acp-14-7031-2014, 2014a.

Titos, G., Lyamani, H., Cazorla, A., Sorribas, M., Foyo-Moreno, I., Wiedensohler, A., and Alados-Arboledas, L.: Study of the relative humidity dependence of aerosol light-scattering in southern Spain, Tellus B Chem. Phys. Meteorol., 66, 24536, https://doi.org/10.3402/tellusb.v66.24536, 2014b.

Titos, G., del Águila, A., Cazorla, A., Lyamani, H., Casquero-Vera, J. A., Colombi, C., Cuccia, E., Gianelle, V., Močnik, G., Alastuey, A., Olmo, F. J., and Alados-Arboledas, L.: Spatial and temporal variability of carbonaceous aerosols: Assessing the impact of biomass burning in the urban environment, Sci. Total Environ., 578, 613–625, https://doi.org/10.1016/j.scitotenv.2016.11.007, 2017.

Topping, D. O., McFiggans, G. B., and Coe, H.: A curved multi-component aerosol hygroscopicity model framework: Part 1 – Inorganic compounds, Atmos. Chem. Phys., 5, 1205–1222, https://doi.org/10.5194/acp-5-1205-2005, 2005.

Trovato, M., Forlani, G., Signorelli, S., and Funck, D.: Proline Metabolism and Its Functions in Development and Stress Tolerance, 41–72, https://doi.org/10.1007/978-3-030-27423-8-2, 2019.

Twomey, S.: The Influence of Pollution on the Shortwave Albedo of Clouds, J. Atmos. Sci., 34, 1149–1152, https://doi.org/10.1175/1520-0469(1977)034<1149:TIOPOT>2.0.CO;2, 1977.

Usher, C. R., Al-Hosney, H., Carlos-Cuellar, S., and Grassian, V. H.: A laboratory study of the

heterogeneous uptake and oxidation of sulfur dioxide on mineral dust particles, J. Geophys. Res. Atmos., 107, ACH 16-1-ACH 16-9, https://doi.org/https://doi.org/10.1029/2002JD002051, 2002.

Valenzuela, A., Olmo, F. J., Lyamani, H., Antón, M., Quirantes, A., and Alados-Arboledas, L.: Aerosol radiative forcing during African desert dust events (2005–2010) over Southeastern Spain, Atmos. Chem. Phys., 12, 10331–10351, https://doi.org/10.5194/acp-12-10331-2012, 2012.

Varga, Z., Kiss, G., and Hansson, H.-C.: Modelling the cloud condensation nucleus activity of organic acids on the basis of surface tension and osmolality measurements, Atmos. Chem. Phys., 7, 4601–4611, https://doi.org/10.5194/acp-7-4601-2007, 2007.

Vlasenko, A., Sjogren, S., Weingartner, E., Stemmler, K., Gäggeler, H. W., and Ammann, M.: Effect of humidity on nitric acid uptake to mineral dust aerosol particles, Atmos. Chem. Phys., 6, 2147–2160, https://doi.org/10.5194/acp-6-2147-2006, 2006.

Wagner, F., Bortoli, D., Pereira, S., Costa, M. Jo., Maria Silva, A., Weinzierl, B., Esselborn, M., Petzold, A., Rasp, K., Heinold, B., and Tegen, I.: Properties of dust aerosol particles transported to Portugal from the Sahara desert, Tellus B Chem. Phys. Meteorol., 61, 297–306, https://doi.org/10.1111/j.1600-0889.2008.00393.x, 2009.

Walser, A.: On the Saharan air layer aerosol and its role as a reservoir of cloud condensation nuclei, http://nbn-resolving.de/urn:nbn:de:bvb:19-216647, 2017.

Wang, J., Shilling, J. E., Liu, J., Zelenyuk, A., Bell, D. M., Petters, M. D., Thalman, R., Mei, F., Zaveri, R. A., and Zheng, G.: Cloud droplet activation of secondary organic aerosol is mainly controlled by molecular weight, not water solubility, Atmos. Chem. Phys., 19, 941–954, https://doi.org/10.5194/acp-19-941-2019, 2019.

Wang, X., Gordon, H., Grosvenor, D. P., Andreae, M. O., and Carslaw, K. S.: Contribution of regional aerosol nucleation to low-level CCN in an Amazonian deep convective environment: results from a regionally nested global model, Atmos. Chem. Phys., 23, 4431–4461, https://doi.org/10.5194/acp-23-4431-2023, 2023.

Wiedensohler, A., Cheng, Y. F., Nowak, A., Wehner, B., Achtert, P., Berghof, M., Birmili, W., Wu, Z. J., Hu, M., Zhu, T., Takegawa, N., Kita, K., Kondo, Y., Lou, S. R., Hofzumahaus, A., Holland, F., Wahner, A., Gunthe, S. S., Rose, D., Su, H., and Pöschl, U.: Rapid aerosol particle growth and increase

of cloud condensation nucleus activity by secondary aerosol formation and condensation: A case study for regional air pollution in northeastern China, J. Geophys. Res. Atmos., 114, https://doi.org/https://doi.org/10.1029/2008JD010884, 2009.

Wiedensohler, A., Wiesner, A., Weinhold, K., Birmili, W., Hermann, M., Merkel, M., Müller, T., Pfeifer, S., Schmidt, A., Tuch, T., Velarde, F., Quincey, P., Seeger, S., and Nowak, A.: Mobility particle size spectrometers: Calibration procedures and measurement uncertainties, Aerosol Sci. Technol., 52, 146–164, https://doi.org/10.1080/02786826.2017.1387229, 2018.

Williamson, C. J., Kupc, A., Axisa, D., Bilsback, K. R., Bui, T., Campuzano-Jost, P., Dollner, M., Froyd, K. D., Hodshire, A. L., Jimenez, J. L., Kodros, J. K., Luo, G., Murphy, D. M., Nault, B. A., Ray, E. A., Weinzierl, B., Wilson, J. C., Yu, F., Yu, P., Pierce, J. R., and Brock, C. A.: A large source of cloud condensation nuclei from new particle formation in the tropics, Nature, 574, 399–403, https://doi.org/10.1038/s41586-019-1638-9, 2019.

Xu, J. Z., Mei, F., Zhang, X. H., Zhao, W. H., Zhai, L. X., Zhong, M., and Hou, S. G.: Impact of Anthropogenic Aerosol Transport on Cloud Condensation Nuclei Activity During Summertime in Qilian Mountain, in the Northern Tibetan Plateau, J. Geophys. Res. Atmos., 129, e2023JD040519, https://doi.org/https://doi.org/10.1029/2023JD040519, 2024.

Yang, F., Xue, H., Deng, Z., Zhao, C., and Zhang, Q.: A closure study of cloud condensation nuclei in the North China Plain using droplet kinetic condensational growth model, Atmos. Chem. Phys., 12, 5399–5411, https://doi.org/10.5194/acp-12-5399-2012, 2012.

Yao, L., Garmash, O., Bianchi, F., Zheng, J., Yan, C., Kontkanen, J., Junninen, H., Mazon, S. B., Ehn, M., Paasonen, P., Sipilä, M., Wang, M., Wang, X., Xiao, S., Chen, H., Lu, Y., Zhang, B., Wang, D., Fu, Q., Geng, F., Li, L., Wang, H., Qiao, L., Yang, X., Chen, J., Kerminen, V.-M., Petäjä, T., Worsnop, D. R., Kulmala, M., and Wang, L.: Atmospheric new particle formation from sulfuric acid and amines in a Chinese megacity, Science (80-.)., 361, 278–281, https://doi.org/10.1126/science.aao4839, 2018.

Yu, F., Luo, G., Nair, A. A., Schwab, J. J., Sherman, J. P., and Zhang, Y.: Wintertime new particle formation and its contribution to cloud condensation nuclei in the Northeastern United States, Atmos. Chem. Phys., 20, 2591–2601, https://doi.org/10.5194/acp-20-2591-2020, 2020.

Zhang, S., Xing, J., Sarwar, G., Ge, Y., He, H., Duan, F., Zhao, Y., He, K., Zhu, L., and Chu, B.:

Parameterization of heterogeneous reaction of SO(2) to sulfate on dust with coexistence of NH(3) and NO(2) under different humidity conditions., Atmos. Environ. (1994)., 208, 133–140, https://doi.org/10.1016/j.atmosenv.2019.04.004, 2019.

Zhang, Y. and Steiner, A. L.: Projected climate-driven changes in pollen emission season length and magnitude over the continental United States, Nat. Commun., 13, 1234, https://doi.org/10.1038/s41467-022-28764-0, 2022.

Zhao, B., Donahue, N. M., Zhang, K., Mao, L., Shrivastava, M., Ma, P.-L., Shen, J., Wang, S., Sun, J., Gordon, H., Tang, S., Fast, J., Wang, M., Gao, Y., Yan, C., Singh, B., Li, Z., Huang, L., Lou, S., Lin, G., Wang, H., Jiang, J., Ding, A., Nie, W., Qi, X., Chi, X., and Wang, L.: Global variability in atmospheric new particle formation mechanisms, Nature, 631, 98–105, https://doi.org/10.1038/s41586-024-07547-1, 2024.

Zhao, X., Huang, K., Fu, J. S., and Abdullaev, S. F.: Long-range transport of Asian dust to the Arctic: identification of transport pathways, evolution of aerosol optical properties, and impact assessment on surface albedo changes, Atmos. Chem. Phys., 22, 10389–10407, https://doi.org/10.5194/acp-22-10389-2022, 2022.

Zhu, Y., Sabaliauskas, K., Liu, X., Meng, H., Gao, H., Jeong, C.-H., Evans, G. J., and Yao, X.: Comparative analysis of new particle formation events in less and severely polluted urban atmosphere, Atmos. Environ., 98, 655–664, https://doi.org/10.1016/j.atmosenv.2014.09.043, 2014.

Zieger, P., Fierz-Schmidhauser, R., Weingartner, E., and Baltensperger, U.: Effects of relative humidity on aerosol light scattering: results from different European sites, Atmos. Chem. Phys., 13, 10609–10631, https://doi.org/10.5194/acp-13-10609-2013, 2013.

Zieger, P. C.: Effects of relative humidity on aerosol light scattering, ETH, Zürich, https://doi.org/10.3929/ethz-a-006668068, 2011.

Ziska, L. H., Makra, L., Harry, S. K., Bruffaerts, N., Hendrickx, M., Coates, F., Saarto, A., Thibaudon, M., Oliver, G., Damialis, A., Charalampopoulos, A., Vokou, D., Heidmarsson, S., Gudjohnsen, E., Bonini, M., Oh, J.-W., Sullivan, K., Ford, L., Brooks, G. D., Myszkowska, D., Severova, E., Gehrig, R., Ramón, G. D., Beggs, P. J., Knowlton, K., and Crimmins, A. R.: Temperature-related changes in airborne allergenic pollen abundance and seasonality across the northern hemisphere:

a retrospective data analysis, Lancet Planet. Heal., 3, e124–e131, https://doi.org/https://doi.org/10.1016/S2542-5196(19)30015-4, 2019.



Instituto Interuniversitario de Investigación del Sistema Tierra en Andalucía

Grupo de Física de la Atmósfera





